UNIVERSITY OF CALIFORNIA
RIVERSIDE

Solidification, Thermodynamics, and Mechanical Properties of Multi-Principal Element Alloys

A Dissertation submitted in partial satisfaction
of the requirements for the degree of

Doctor of Philosophy

in

Materials Science & Engineering

by

Nicholas Alexander Derimow

June 2019

Dissertation Committee:

Dr. Reza Abbaschian, Chairperson
Dr. Suveen Nigel Mathaudhu
Dr. Peter Alexander Greaney

The Dissertation of Nicholas Alexander Derimow is approved:

Committee Chairperson

University of California, Riverside

Acknowledgments

I would like to dedicate this thesis to my parents, Jacqueline and Rudy Derimow, as well as my brother Alexander Derimow. Without their continued love and support I would not have been able to accomplish any of the degrees I have obtained, nor have the stability to pursue higher education. As for making it through the PhD program in one piece, I would not have survived it if wasn't for the enormous emotional support from my fiance (and soon to be wife) Jillian Foster, whom I met at UCR.

I have enormous thanks for support I have received from my network of friends and colleagues I've made while at UCR. I believe the most important aspects to graduate school is work-life balance and a network of friends. During extremely stressful and tiring times, the people that I was able to call my friends really kept my spirits up, therefore I feel that it is necessary to acknowledge everyone who has been a good friend to me at UCR, who I will list here: Christian Roach, Trevor Clark, The Coleman Family (Devin, Ece, Mike, Peri, Ryan Corrine, Tori), Fabian Villalobos and Anoush Shahidzadeh, Darren Dewitt, Joe Martinez, Kyle Chan, Velveth Klee, Max Mayther, Steven Herrera, Sina Shahrezaei, Austin Woodard, Thomas Dugger, Andy Patalano, Alex and Sara Frie Vliet, Chithra Asokan, Wenny Wong, Sami and Paul Lou, Marissa Giroux, Benjamin Sommerkorn, Jedediah Kistner-Morris, Melina Fuentes, Alex Ross, Josh Plank, Sherrie Huo, Vitaly Fedotov, Marcus Asaro, Heather Salvador, Erik Sease, Evander Ramos, Kendrick Mensink, Daisy Patino, Amir Ardalan Rezaie, Johny Quan, Lauren Ficarelli, Michelle Wurch, Tyler Hunter, GT Harraka, Tori Stempniewicz, Deborah Nelson, Ravdeep Pasricha, Jason and Shelley Ott, Steve Cook, Aalekhya Reddam, Adric Jones, Gabe Ceccini, Alyssa Vollaro,

Steph Miller, Will Agnew-Svoboda, Gaurav Jhaveri, Navaneet Ramabadran, Nichole Ginnan, Erin Sternburg, Derreck Adam Carter-House, Kevin Myhro, Adam Arnot, Lauren Holloway, Paul Bogie, Pedro Piqueras, Maria Cordoba Otero, Claudia Chaves Villarreal, Aleksey and Grissel Volodchenkov, Pranee Pairs, Tanner Zerrin, Morgan Dundon, Luz Cruz, Holly Mayton, Jan Scheifers, Giorgio Nava, Alejandro Alvarez, Chris Rudnicki, Dipankar Baisya, Paulo Fonseca, Arash Mirjalili, Kimia Claudia Yaghoubi, Stephen Exarhos and Melissa Klocke, Isabel Davila, Carys Layton, Soren Weber, Brandon Davis, Sahar Naghibi, Ahmad Darki, Sara Allec, Nicholas Rajen, Tammy Huang, Ingrid Liao, Aditya Dhakal, Ramya Mohan, Maiko Le Lay, Scott Coffin, J. C. Leapman, Chad Warren, Noam Hart, Maria Patino, Yvonne Willis, Anqi Yu.

I would like to thank my student mentees for putting up with me and always providing me feedback on how to be a better mentor: Zaira Alibay, Yige Li, Melody Buscagan, Bryce de Camara, Qingsong Fan, Irem Ergun, Tung Dinh, and Somchate Wasantwisut. I would also like to thank my undergraduate students in the laboratory for their invaluable efforts: Bryan Le, Alex Haduong, and Raquel Jaime.

I would like to thank the academic help I've received while pursuing my PhD: The late Abraham Munitz, Louis J. Santodonato, Hassina and Jean Bilheux, Ercan Balikci, Alexander Davis Dupuy, Ben MacDonald, Brady Butler, James Paramore, my qualifying exam committee members Krassimir Bozhilov and Monica Martinez-Wilhemus, my PhD committee members Suveen Mathaudhu and P. Alex Greaney, and lastly, none of this would have been possible without the excellent guidance of my PhD advisor Reza Abbaschian.

A special thanks to the UCR/Greater Riverside area rock climbing community for keeping me sane and exploring the outdoors with me, as well as belaying me on all the routes I've climbed and have keeping me alive: Stephen Zimmerman, Duncan Ashby and Michelle Tom, Bryan Woo, Jimmy Guilinger and Kylie Morse, Clare Stephens, Tucker Adams, Marisa Clagett and Richard Eastburn, Win Cowger and Tori McGruer, William Morales, Samuel Odiakosa, Valarie Williams Booth, Julia Harreshou, Brent Webster.

If it wasn't for martial arts, specifically Brazilian Jiu-Jitsu, I would not have been able to balance my life and truly appreciate the things that matter most to me. My eternal gratitude goes out to my coaches, training partners, and teammates: Joe Alayra, Arto Mercado, Don Kim, Geoff Obst, Amanda Hodson, Ivan Serrano, Josh Galvan, Matt Jewett, James Jewett, Kevin Jewett, Alex Aung, Seth Johnston, Mark Holford, Big Tony Tesone, Owen Francis, JR Bermuda, Ryan Olsen, Israel Santana, Tim Derosiers, Shaun Nelson, Santiago Maldonado, Sean Benggon, Rob Kim, Carlisle Salcedo, Vicki Kha, Art Minas, Andrew Tran, Matt Soliz, Jordan Leon, Stephen Hernandez, Will Reed, Mauro Samayoa, James Brooks, Juan Sosa, David Escarsega, Victor Rivera, my old training partners from Academy of Martial Science whose last names escape me: Gilbert, Rodrigo, Mario, Alex, Hector, Luis, my old judo instructors Ron Shuebert and Mike Higashi.

I would not have had the ability to apply to PhD programs if not for the CSULA MORE Programs. Being a MBRS-RISE MS-to-PhD scholar taught me how to navigate the waters of graduate school, as well as what it would take to submit a successful application package to PhD programs. My sincerest thanks to everyone involved in the program who helped me get this far: Carlos Gutierrez, Vicki Kubo-Anderson, Linda Tunstad, Maria Man-

zanares, and Lisa Bautista. I would also like to acknowledge all of my friends and colleagues who were part of my journey studying physics at CSULA: Marie Bruno, Stephanie Pham, Joby Marfori, Tzitlaly Barajas, David Guzman, Min Liu, Raul Herrera, Benji Macaulay, Oliver Ta, Karen Garcia, Velveth Klee, Carmen Quen, Sophia Iqbal, Victor Aguilar, AJ Cressman, Mary Kalayejian, Edith Soto, Jay Chiang, Clare Abreu, Ian McGregor, Ariana Valdez, Madeline Monroy, Herwick Mok, Tino Troung, Armond Khogdagulyan, Smbat Avetyan, Jacob Labry, Lamar Glover, Dea Flores, my MS advisor Guo-meng (Peter) Zhao, Konrad Aniol, Radi Jishi, Edward Rezayi, and the late Linda Alviti. I would also like to acknowledge the friends I have made in the MORE program and from other departments, such as Jhen Lumbres and Aldo Corona, Abigail Tadle, Israel Santana, Maria Escamilla, Edgar Perez, Rigoberto Arenas, Maria Flores, Antonia Flores, Leo Castro, Adrian Gomez, Alejandra Rios, Esay Monzon, Carla Gonsalez, Frank Navarrete, Marlene Macias, Natalia De Vries, Hugo Avila, Luis Rosa, Andrew Martinez, Jameka Jefferson, Jeremiah Heredia, Oscar Diaz, Norbert Godinez, Miguel Pinto, Megan Franklin, Rafael Rincon, Daniel Delgado, Jonathan Ma, Brittany Ulloa, Bridgette Spencer, Calista Lyon, Gaby Villasenor, the late Sevak (Sam) Gazarian, Narek Darabedian, Mary Darbinian, Ryan Cundiff, Mable Hua. I also had many friends during my community college days, and really helped shape the person I was growing up to be: Rehevolew Shiao, Hein Soe, Heeyup Kim, Suzanne Takamoto, Sima Guyumdzhyan, Julian Villa, Jeff Aronhalt, Eylene Pirez, Anthony Flores.

I was not always a career scientist, but a musician as well. I would like thank my long time band members who were patient with me during my bachelor's and master's degrees, who have become some of my best friends Sean Baumgartner and Jesus

Galvan. I would also like to acknowledge other musicians, friends from this period of my life, people in the scene, and just general long time friends with no specific affiliation that have been part of my journey: Damien Valdez, Mario (Moz) Martinez, Christian Cardenas, Tita Marquez, Ulises Galvan, Jose Renteria, Tana Cheth, Christian Esqueda, Reyman Villegas, Raul Fregoso, Melyssa Vides-Montes, Loretta Ramos, Jeanette Araya and Ron Baumgartner, Robert Vreugdenhil, John Araya, Tom Araya, Robert and Misty Madriaga, Gino Gabuardi and Cypress Esparza, Jimmy Craig, Chris Hutchings, Robert Martinez, Jennifer Martinez, Yesenia Loza, Larry Lopez, Ryan Carrasco, Eddie Gonzalez Caamano, Barbara Guerra Torres, Erik Lee, Bianca Oceguera, Altair Padilla, Rosalinda Padilla, Miguel Negrete, Kelvin Sabando, the late Paulo Aldebaran Centeno, Alan Villalobos and Shalita Castaneda, Andy Co and Novella, John Henry Barboza, Andrew and Francis Barboza, Larry Baca, Lisa and Oliver, Jonathan Cruz, Melissa Gastelum, Kat Martinez, Louis Garza, Anette Jimenez, Nancy Gutierrez, Manual Robles, Adrian Mendoza, Derek Rosales, Leonardo Murillo, George Jr., George Sr., and Yadira Diaz, Juan Diaz-Infante, Ehecatl Negrete, Andrew Serrato, M. Rahman, Malcolm Ramirez, Jessica Ceniceros.

And lastly, I wish to acknowledge my remainder of my extended family, who helped raise me to be who I am today: Isabel and Oleg Derimow, Louis and Celia Jones, John Derimow Sr., John Jr. and Corrina Derimow, Joanne Jones, Carolyn and Richard Matusiewicz, my cousins Jimmy, Katie, Mike Matusiewicz, Dana and Tim Scroggins, Joey Cressler, Karyn Shishmanian, Diane and Ken Simonds, Chris Simonds, Robert Jones, Brittany Jones, Erica Valdez, Tony Scopellite.

"Nature is no doubt simpler than all our thoughts about it now... and the question is, what way do we have to think about it so that we understand its simplicity?"

–Richard P. Feynman

ABSTRACT OF THE DISSERTATION

Solidification, Thermodynamics, and Mechanical Properties of Multi-Principal Element Alloys

by

Nicholas Alexander Derimow

Doctor of Philosophy, Graduate Program in Materials Science & Engineering
University of California, Riverside, June 2019
Dr. Reza Abbaschian, Chairperson

Structure and solidification of CoCrCu-X with X = Fe, Mn, Ni, Ti, V, FeMn, FeNi, FeTi, FeV, MnNi, MnTi, MnV, NiTi, NiV, and TiV were studied via arc-melting and electromagnetic levitation melting. The ternary mixture of CoCrCu was found to form no single phase liquid, however by systematically introducing the remaining 3d transition metals, it was found that Ni and Ti promote single phase liquid formation, eventually leading to dendritic microstructures as opposed to the highly phase separated microstructures found in ten of the alloys. The thermodynamics of the liquid phase separation in these alloys is largely dictated by the positive mixing enthalpy contributions of Cu in these systems. Of the six dendritically solidifying alloys, CoCrCuNi, CoCrCuFeNi, and CoCrCuMnNi solidified with a face-centered cubic (FCC) crystal structure for both the dendritic and interdendritic phases while CoCrCuTi and CoCrCuTiV solidified with FCC and body-centered cubic (BCC) phases. In contrast CoCrCuMnTi solidified with a hexagonal closed packed Laves C14 dendritic phase and FCC interdendritic matrix. The three FCC alloys were then prepared via powder metallurgy and processed via spark plasma sintering (SPS)

to compare microstructure, crystal structure, and mechanical properties with the solidification processed alloys. It was found that the powder metallurgical processing and SPS led to a doubling of the hardness in these alloys due to the nanocrystallinity of the powder being preserved. Liquid phase separation was further investigated by neutron imaging techniques. It was found that the technique not only allows for the direct observations of molten metals, but also shows mixing and de-mixing in the liquid for these alloys. The neutron imaging technique was applied to the CoCrCuNi high-entropy alloy to study the remixing of the de-mixed liquid with the addition of Ni to CoCrCu. The CoCrCuMnTi alloys were systematically studied by varying the amount of Mn in order to find the critical Mn concentration for the formation of the Laves C14 phase in these alloys. The particular composition of $Co_{22}Cr_{18}Cu_{20}Mn_{16}Ti_{24}$ has high hardness of 996.6 HV 0.01 for the dendritic phase, while the hardness of the interdendritic phase is 457.3 HV 0.01. In this alloy, there is also a small dispersed Ti-rich phase. The effects of varied cooling rates on this alloy were studied, and it was found that higher cooling rates led to the suppression of the tertiary Ti-rich phase.

Contents

List of Figures

List of Tables

Chapter 1

Introduction

The goal of this work is to gain a better understanding of the solidification, phase formation, and liquid phase separation of the high-entropy alloys (HEAs). In a nutshell, high-entropy alloys are metal alloys that have no base element, but rather a near-equal proportion of three or more elements. Since their discovery in 2004 [1–6], there has been an great number of research dedicated to studying equiatomic alloy combinations due to their tendency to form single phase crystal structures. Research articles have described these alloys in a different manner of ways, however the general core concepts behind design are relatively the same. Some prefer to call these alloys:

- High-Entropy Alloys (HEAs) [2] – Original definition, used for compositions with an ideal entropy of $S_{ideal} \geq 1.61R$ that are comprised solely of a single phase solid solution. However, $S_{ideal} \geq 1.5R$ has also been frequently used to define an alloy has having 'high entropy'.

- Multiprincipal Element Alloys (MPEAs) [5] – Broader definition loosely used to generalize all multicomponent alloy systems that stray away from the traditional alloying route.

- Complex Concentrated Alloys (CCAs) [7] – typically interchangeable with multiprincipal element alloys. Sometimes used interchangeably with Compositionally Complex Alloys (CCAs) [8, 9]

- Medium-Entropy Alloys (MEAs) [10] – used for compositions with an ideal entropy of $0.69R < S_{ideal} \geq 1.61R$

- Low-Entropy Alloys (LEAs) [10] – used for compositions with an ideal entropy of

$S_{ideal} < 0.69R$

- Lightweight High-Entropy Alloys (LWHEAs) [11] – HEAs that consist of lightweight elements
- Eutectic High-entropy Alloys (EHEAs) [12] – HEAs/MPEAs/CCAs that have a eutectic microstructure.
- Baseless Alloys [7] – Simplest classification, implies no base metal element in the alloy.

Regardless of what these alloys are called or referred to, the research in this field seeks to understand these materials' tendency for simple phase formation as well explore the interior regions of these alloys' complex hyperdimensional phase space. These multicomponent alloys show considerable potential for uses as structural and functional materials, and many studies have show that these alloy systems are coming close to the mechanical properties for some commercial alloys.

This dissertation covers the author's work over several different experiments and approaches, where the majority of these alloys are described as MPEAs. The experimentation begins with the study of MPEA combinations using the 3-d transition metals that contain equiatomic ternary CoCrCu to understand the effects of the 3d transition metals on liquid phase separation and miscibility. The next investigation into these alloys were in-situ neutron imaging of the liquid phase separation in CoCrCu to investigate whether it can be observed with this technique, and if it lead to a better scientific understanding of the solidification process when paired with the thermal history of the system. This experiment demonstrates that neutron imaging can be utilized as a characterization technique

for solidification research with the potential for imaging the liquid phases of more complex alloys, such as the MPEAs, which is a new characterization technique developed in part by the present author. This neutron imaging technique was applied to the CoCrCuNi system, where CoCrCu and Ni were alloyed and imaged in-situ during melting, remixing, and solidification. Three of the dendritically solidifying alloys from the initial study outlining liquid phase separation in the CoCrCu system were studied via powder metallurgical processing and spark plasma sintering to elucidate the effect of processing on the phases of the alloys. Lastly, the duplex hexagonal (HCP)/face-centered cubic (FCC) CoCrCuMnTi alloy was studied via varying the amount of Mn concentration in the alloy as well as the use of electromagnetic levitation processing to understand phase formation in this alloy system.

1.1 Background of Multicomponent Alloys

The discovery of the high-entropy alloys (HEAs) [1–6] has inspired an enormous amount of research into multicomponent alloy design. Since their inception, there has been numerous reviews [9, 13–23] and several books [24–29] which summarize the state of the art for the materials community. These reviews compile and assess the microstructural developments, mechanical properties, crystallography, and thermodynamics of the high-entropy, complex concentrated, and multi-principal element alloy systems.

One of the first HEAs contained equal parts Co, Cr, Fe, Mn, and Ni, often written alphabetically as CoCrFeMnNi and referred to as the 'Cantor Alloy' after the alloy's inventor Brian Cantor [1]. Subsequent studies of the Cantor alloy involved substitution of various elements in place of the original five equiatomic elements in the alloy. One of the most

popular substitutions is often Cu for Mn [3], as well as the addition of Al to create the widely studied AlCoCrCuFeNi HEAs [30–33]. Since their inception, the majority of the high entropy alloys that are synthesized consist mostly of the 3d transition metals with other elements substituted into the well-studied systems in the search for new stable phases, mechanical properties, and reproducible microstructures [22]. There have been several research papers that prescribe methodologies for computationally screening HEAs for those that are likely to create single phase solid solutions [8, 34–41].

The underlying motivation for the vast amount of work that has been carried out on the high-entropy alloys has essentially not changed since their initial discovery. As quoted from Brian Cantor, the central theme of this explorative alloy research is "to investigate the unexplored central region of multicomponent alloy phase space." [1]. An example of an isothermal ternary phase diagram cross section in Fig. 1.1 depicts where traditional alloys used in industry tend to lie in terms of composition, whereas the HEAs, MPEAs, and CCAs are designed such that the compositions are equiatomic or near-equiatomic, with the goal to explore the phase space of these multicomponent alloys' multidimensional phase diagrams. By using less restrictive terms such as MPEAs or CCAs to classify these alloys, the goal of the research is not hindered by adhering to strict definitions of what constitutes a 'high-entropy' alloy. Therefore, this allows the researcher to cultivate the original scientific curiosity that was employed during the founding research that led to the development of these alloys in the first place. As there are billions of alloy combinations that can exist, there remains an enormous amount of work to be done in terms of developing high-throughput methods for screening these alloys for their phases, mechanical properties, and potential

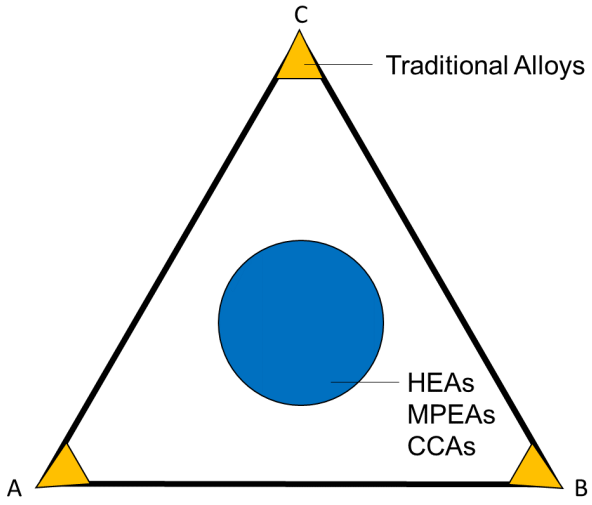

Figure 1.1: Diagram depicting the alloy design of HEAs, MPEAs, and CCAs when compared to traditional alloys.

applications.

The primary reason why HEAs, CCAs, and MPEAs are such an attractive alternative to traditional alloy design is arguably for a single reason, that being these alloys tend to form solid solutions with simple crystal structures. It is this reason that these alloys have displayed considerable potential as engineering materials, as the increasing demand for stronger materials drives research into new unexplored directions. As demonstrated by the work of Cantor [1] and Yeh [3], the CoCrFeMnNi and CoCrCuFeNi alloys solidify dendritically with FCC crystal structures, where the dendritic phase is a disordered solid solution of the alloying elements in the single phase. In both cases for CoCrFeMnNi and CoCrCuFeNi, the interdendritic phase was also FCC. These disordered solid solution phases differ however from traditional room temperature crystal structures of the individual alloying elements. For example, Fig. 1.2 displays a drawing of the close-packing in Co, while

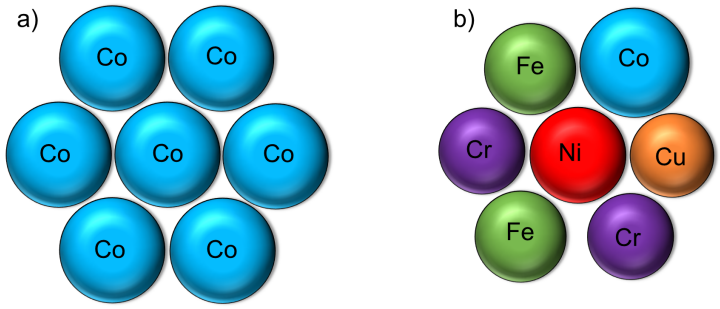

Figure 1.2: a) Close-packing of cobalt (Co) b) Close-packing of CoCrCuFeNi

the close-packing of a high entropy alloy CoCrCuFeNi containing equal amounts of Co, Cr, Cu, Fe, and Ni is shown to be slightly distorted due to the differences in atomic size of the constituent elements. There are many HEAs in the literature that also display ordered crystal structures, which will be discussed in this work, however the central theme is that these multicomponent alloys form stable crystal structures without the presence of a base element, but rather collectively form the base.

Due to the solid solutions displayed by the high-entropy alloys, four hypotheses denoted as 'core-effects' were outlined by Yeh in 2006 [10]. These are outlined as such:

- **High-entropy Effect** – the high entropy of mixing stabilizes the solid solutions into simple phases.
- **Lattice Distortion Effect** – The lattice distortion from the different atomic sizes in an HEA leads to solid solution hardening, thermal resistance, electrical resistance, and X-ray diffuse sccattering.
- **Sluggish Diffusion Effect** – hindered atomic movement due to the the lattice dis-

tortion.

- **Cocktail Effect** – If the HEAs are viewed as an 'atomic composite', then the composite effects will come from the basic features and interactions between the alloying elements and can be tailored for desired mechanical, thermodynamic, and functional properties.

A recent review by Miracle and Senkov [22] critically analyzes these 'core-effects', and provides an in-depth discussion regarding the validity of these hypotheses. The summary of the comments on the four 'core-effects' in HEAs by Miracle and Senkov are presented below:

- *High-entropy Effect* – Vibrational entropy is significantly larger than the ideal configurational entropy, and that there are typically four major competing thermodynamic quantities such as the enthalpy of solid solution and intermetallic phases and the entropy of the solid solution and intermetallic phases.

- *Lattice Distortion Effect* – Lattice distortion is indeed present in these alloy systems, however there is much need in the development of approaches to experimentally quantify lattice distortion in these systems as well as systematically isolate the lattice distortion effects from the other features these alloys exhibit.

- *Sluggish Diffusion Effect* – More diffusion studies are needed to systematically test this hypothesis

- *Cocktail Effect* – While not necessarily a hypothesis, Miracle and Senkov seek to remind the reader to remain "open to non-linear, unexpected results that can come

from unusual combinations of elements and microstructures in the vast composition space of MPEAs." [22].

The literature reviews thus far catalog the hundreds of HEAs, MPEAs, and CCAs that have been made to date. These reviews have included comprehensive viewpoints and observations [9, 16, 20, 22, 23], phase formation and predictions [18, 21, 42–46], microstructures and mechanical properties [17,47], fracture resistance [48], lightweight high-entropy alloys [11], fatigue behavior [49], deformation behavior [50], high-temperature properties [51], corrosion resistance [52], films and coatings [53, 54], liquid phase separation [55], and modeling of stacking faults [56].

To date, there have been no recorded HEAs, CCAs, or MPEAs that outperform the Ni-based superalloys, however, these alloys show significant promise for not only high-temperature or structural applications, but also in their potential for thin films and coatings, their exceptional wear-resistance, fatigue behavior,and deformation behavior. There are significant advancements being made in the ability for high-throughput calculations and screening for stable compounds. The amount of scientific publications in this new field of metallurgy and materials science continues to grow exponentially by the year, with new alloys being developed every single day. In order to systematically understand how phase formation occurs in these systems, more exploratory research needs to be carried out in order to understand what parameters influence the phase formation in these systems.

1.2 Alloy Combinations

1.2.1 3d Transition Metal High Entropy Alloys

From the reviews of the HEAs, CCAs, and MPEAs, the majority of the alloys are composed of the 3d transition metals, often with substitutions of one or two of the elements in various permutations. According to the Intnernational Union of Pure and Applied Chemistry (IUPAC) definition [57], a transition metal is an element whose atom has a partially filled d sub-shell, or which can give rise to cations with an incomplete d sub-shell. Not all d block elements count as transition metals as they are defined as one or more stable ions which have incompletely filled d orbitals. Scandium has the electronic Structure $[Ar]3d^1 4s^2$. When it forms ions, it loses the 3 outer electrons and ends up with an [Ar] structure which as an empty d sub-level. The Sc^{3+} has no d electrons and so does not meet the definition. Zinc has the electronic structure $[Ar]3d^{10}4s^2$. When it forms ions, it always loses the two 4s electrons to give a 2+ ion with the electronic structure $[Ar]3d^{10}$. In order to preserve similar chemistry among the metals used in this study, Sc and Zn were excluded from the possible combinations of alloys that could occur. From a practical standpoint, Sc is a very expensive material ($\approx$ \$20,000/kg) while Zn has a very low boiling point (907 ^{o}C), making it difficult to alloy using methods such as arc-melting, levitation casting, and induction melting.

The 3d transition metals Ti, V, Cr, Mn, Fe, Co, Ni, and Cu are highlighted in Fig. 1.3. A collection of the properties of these elements is present in Table 1.1. All possible equiatomic alloy combinations of these elements have been compiled below with references

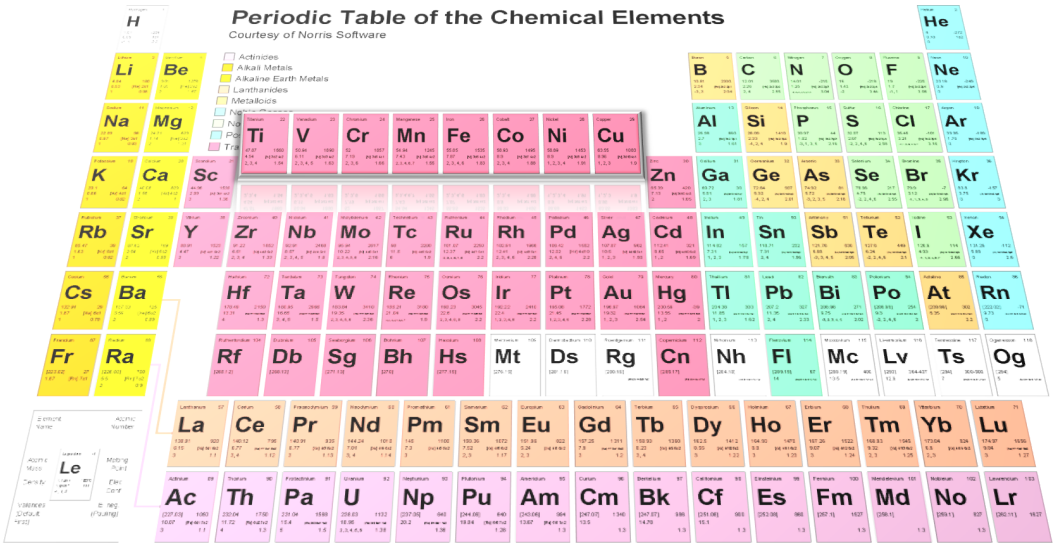

Figure 1.3: Periodic table of the elements highlighting the 3d transition metal row.

to each of the systems that have been studied in the literature. These combinations are listed alphabetically for consistency in reading. Note that these alloy systems are not all equiatomic, and serve to only illustrate the amount of exploration into complex alloy design. Tables 1.2 and 1.3 are collections of the binary and ternary alloys that can be constructed using Co, Cr, Cu, Fe, Mn, Ni, Ti, and V. Almost all of the binary alloy systems have been studied prior to the discovery of HEAs, while the ternary alloys have a mixed history of development, all except for the CrCuV system, which is yet to be studied. Tables 1.4 and 1.5 represent the quaternary and quinary alloys that contain the 3d transition metals with citations to the relevant literature. Alloy combinations without a citation indicate that the alloy has yet to be studied. Note, there are many HEA/MPEA/CCA systems that contain aluminum in similar ratios to the other alloying elements. For the purposes of this study, similar chemistry of the alloying elements was preserved so that relationships between miscibility of the systems can be understood with elements of similar atomic radii.

Table 1.1: Properties of the 3d transition metals from Ti through Cu. $\chi \equiv$ Pauling electronegativity, VEC = Valence Electron Concentration, Cryst. $\equiv$ Crystal structure at room temperature.

Elem.	m (g/mol)	ρ (g/cm^3)	T_m (°C)	χ	VEC	r_a (pm)	Cryst.	Magnetism
Ti	47.69	4.51	1668	1.54	4	147	HCP	Paramagnetic
V	50.94	6.11	1910	1.63	5	134	BCC	Paramagnetic
Cr	52.00	7.14	1907	1.66	6	128	BCC	Antiferromagnetic
Mn	54.94	7.47	1246	1.55	7	127	αMn (A12)	Paramagnetic
Fe	55.85	7.87	1538	1.83	8	126	BCC	Ferromagnetic
Co	55.93	8.90	1495	1.88	9	125	HCP	Ferromagnetic
Ni	58.69	8.91	1455	1.91	10	124	FCC	Ferromagnetic
Cu	63.55	8.92	1085	1.90	11	128	FCC	Diamagnetic

Tables 1.6, 1.7, and 1.8 represent the senary, septary, and octonary combinations of the 3d transition metals that have been studied in the literature. Note that there is no literature on the septary combinations of the 3d transition metals.

Table 1.2: Binary Combinations of Co, Cr, Cu, Fe, Mn, Ni, Ti, V

CoCr	[58]	CrCu	[59]	CuMn	[60]	FeV	[61]
CoCu	[62]	CrFe	[63]	CuNi	[64]	MnNi	[65]
CoFe	[66]	CrMn	[67]	CuTi	[68]	MnTi	[69]
CoMn	[70]	CrNi	[71]	CuV	[72]	MnV	[73]
CoNi	[74]	CrTi	[75]	FeMn	[76]	NiTi	[77]
CoTi	[78]	CrV	[79]	FeNi	[80]	NiV	[81]
CoV	[82]	CuFe	[83]	FeTi	[84]	TiV	[85]

Table 1.3: Ternary Combinations of Co, Cr, Cu, Fe, Mn, Ni, Ti, V

CoCrCu	[86]	CoFeV	[87]	CrFeTi	[88]	CuMnV	[89]
CoCrFe	[90]	CoMnNi	[91]	CrFeV	[92]	CuNiTi	[93]
CoCrMn	[94]	CoMnTi	[95]	CrMnNi	[96]	CuNiV	[97]
CoCrNi	[98]	CoMnV	[99]	CrMnTi	[100]	CuTiV	[101]
CoCrTi	[102]	CoNiTi	[103]	CrMnV	[104]	FeMnNi	[105]
CoCrV	[106]	CoNiV	[107]	CrNiTi	[108]	FeMnTi	[109]
CoCuFe	[110]	CoTiV	[111]	CrNiV	[112]	FeMnV	[113]
CoCuMn	[114]	CrCuFe	[115]	CrTiV	[116]	FeNiTi	[117]
CoCuNi	[118]	CrCuMn	[119]	CuFeMn	[114]	FeNiV	[120]
CoCuTi	[121]	CrCuNi	[122]	CuFeNi	[123]	FeTiV	[124]
CoCuV	[125]	CrCuTi	[126]	CuFeTi	[127]	MnNiTi	[128]
CoFeMn	[129]	CrCuV		CuFeV	[115]	MnNiV	[113]
CoFeNi	[130]	CrFeMn	[131]	CuMnNi	[132]	MnTiV	[133]
CoFeTi	[134]	CrFeNi	[135]	CuMnTi	[136]	NiTiV	[137]

Table 1.4: Quaternary Combinations of Co, Cr, Cu, Fe, Mn, Ni, Ti, V. *Note, * indicates calculation only.*

CoCrCuFe	[138–140]	CoCrTiV		CoFeNiTi	[141]	CrCuNiTi		CuFeMnTi	
CoCrCuMm	[138, 140]	CoCuFeMn*	[138]	CoFeNiV		CrCuNiV		CuFeMnV	
CoCrCuNi	[138, 140]	CoCuFeNi	[138, 142]	CoFeTiV		CrCuTiV		CuFeNiTi	
CoCrCuTi	[140]	CoCuFeTi		CoMnNiTi		CrFeMnNi	[143, 144]	CuFeNiV	
CoCrCuV	[140]	CoCuFeV		CoMnNiV		CrFeMnTi		CuFeTiV	
CoCrFeMn*	[138]	CoCuMnNi*	[138]	CoMnTiV		CrFeMnV		CuMnNiTi	
CoCrFeNi	[145–147]	CoCuMnTi		CoNiTiV		CrFeNiTi		CuMnNiV	
CoCrFeTi		CoCuMnV		CrCuFeMn*	[138]	CrFeNiV		CuMnTiV	
CoCrFeV		CoCuNiTi		CrCuFeNi*	[138]	CrFeTiV		CuNiTiV	
CoCrMnNi*	[138]	CoCuNiV		CrCuFeTi		CrMnNiTi		FeMnNiTi	
CoCrMnTi		CoCuTiV		CrCuFeV		CrMnNiV		FeMnNiV	
CoCrMnV		CoFeMnNi	[142]	CrCuMnNi*	[138]	CrMnTiV		FeMnTiV	
CoCrNiTi		CoFeMnTi		CrCuMnTi		CrNiTiV		FeNiTiV	
CoCrNiV		CoFeMnV		CrCuMnV		CuFeMnNi*	[138]	MnNiTiV	

Table 1.5: Quinary Combinations of Co, Cr, Cu, Fe, Mn, Ni, Ti, V. *Note, * indicates calculation only.*

CoCrCuFeMn	[140, 148]	CoCrFeNiV	[149]	CoCuMnTiV		CrCuMnNiV	
CoCrCuFeNi	[2, 31, 139, 150–153]	CoCrFeTiV		CoCuNiTiV		CrCuMnTiV	
CoCrCuFeTi	[140]	CoCrMnNiTi		CoFeMnNiTi		CrCuNiTiV	
CoCrCuFeV	[139, 140]	CoCrMnNiV	[148]	CoFeMnNiV	[148]	CrFeMnNiTi	[148]
CoCrCuMnNi	[138, 140]	CoCrMnTiV		CoFeMnTiV		CrFeMnNiV	
CoCrCuMnTi	[140]	CoCrNiTiV		CoFeNiTiV		CrFeMnTiV	
CoCrCuMnV	[140]	CoCuFeMnNi*	[138]	CoMnNiTiV		CrFeNiTiV	
CoCrCuNiTi	[140]	CoCuFeMnTi		CrCuFeMnNi	[154]	CrMnNiTiV	
CoCrCuNiV	[140]	CoCuFeMnV		CrCuFeMnTi		CuFeMnNiTi	
CoCrCuTiV	[140]	CoCuFeNiTi	[155]	CrCuFeMnV		CuFeMnNiV	
CoCrFeMnNi	[1]	CoCuFeNiV	[156]	CrCuFeNiTi		CuFeMnTiV	
CoCrFeMnTi		CoCuFeTiV		CrCuFeNiV		CuFeNiTiV	
CoCrFeMnV		CoCuMnNiTi		CrCuFeTiV		CuMnNiTiV	
CoCrFeNiTi	[157]	CoCuMnNiV		CrCuMnNiTi		FeMnNiTiV	

Table 1.6: Senary Combinations of Co, Cr, Cu, Fe, Mn, Ni, Ti, V

CoCrCuFeMnNi [1]	CoCrCuMnNiV	CoCrMnNiTiV	CrCuFeMnNiTi
CoCrCuFeMnTi	CoCrCuMnTiV	CoCuFeMnNiTi	CrCuFeMnNiV
CoCrCuFeMnV	CoCrCuNiTiV	CoCuFeMnNiV [158]	CrCuFeMnTiV
CoCrCuFeNiTi [159]	CoCrFeMnNiTi [1]	CoCuFeMnTiV	CrCuFeNiTiV
CoCrCuFeNiV	CoCrFeMnNiV [160]	CoCuFeNiTiV	CrCuMnNiTiV
CoCrCuFeTiV	CoCrFeMnTiV	CoCuMnNiTiV	CrFeMnNiTiV
CoCrCuMnNiTi	CoCrFeNiTiV	CoFeMnNiTiV	CuFeMnNiTiV

Table 1.7: Septary Combinations of Co, Cr, Cu, Fe, Mn, Ni, Ti, V

CoCrCuFeMnNiTi
CoCrCuFeMnNiV
CoCrCuFeMnTiV
CoCrCuFeNiTiV
CoCrCuMnNiTiV
CoCrFeMnNiTiV
CoCuFeMnNiTiV
CrCuFeMnNiTiV

Table 1.8: Octonary Combination of Co, Cr, Cu, Fe, Mn, Ni, Ti, V

CoCrCuFeMnNiTiV [161]

1.3 Empirical Approaches For Single Phase Prediction

There are currently several empirical approaches for predicting single phase formation in MPEAs such as the configurational entropy, enthalpy of mixing (ΔH_{mix}), composition weighted parameters for differences in atomic radii and electronegativity (δr, $\delta \chi$), and valence electron concentration (VEC) [42]. Recent studies have included criterions for the formation of σ phase in many alloy systems to help the accuracy of prediction when distinguishing between potential phases that can form [41].

1.3.1 Atomic Size Mismatch, Configurational Entropy, Electronegativity Difference, and Valenece Electron Concentration

Some of the earlier theories suggested that the stability of the simple single phase solid solutions were due to the high configurational entropy of these alloys, however by that same reasoning the 20 component alloy from Ref. [1] should have been a single solid solution, which was not the case as Yeh describes that the competition between mixing enthalpy and entropy can be used as a design parameter for HEAs [10]. Guo et al. initially reported parameters for characterizing the behavior of the constituent elements within multicomponent alloys, defined by using the Hume-Rothery rules for atomic size difference (δ) and mixing entropy (ΔS_{mix}) Eqs. 1.1 and 1.2:

$$\delta = 100\sqrt{\sum_{i=1}^{n} c_i(1 - r_i/\bar{r})^2} \tag{1.1}$$

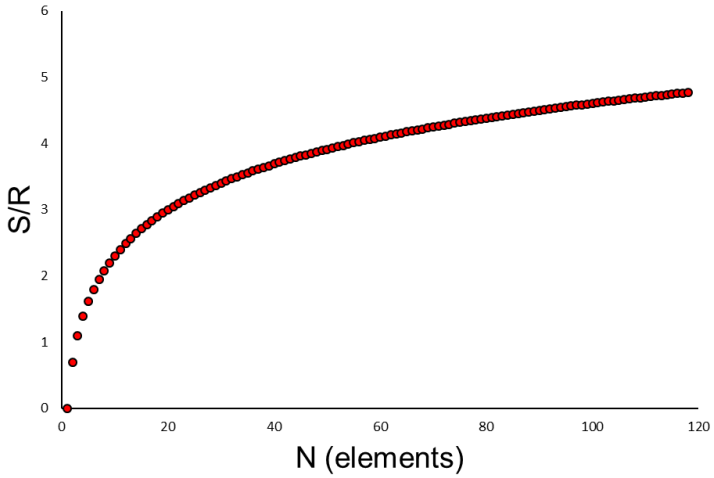

Figure 1.4: Configurational entropy as an integer function of elements in the periodic table.

$$\Delta S_{mix} = -R \sum_{i=1}^{n} c_i \ln c_i = R \ln N \tag{1.2}$$

where $\bar{r} = \sum_{i=1}^{n} c_i r_i$, and c_i and r_i are the atomic percentage and atomic radius of the ith element, and R is the gas constant. A plot of Eq. 1.2 such that configurational entropy is plotted against equiatomic additions of elements of periodic table is presented in Fig. 1.4. Most of the HEAs/MPEAs/CCAs in the literature contain from 3 – 8 elements, which equates to a configurational entropy of $\sim 1R$ to $2R$. The configurational entropy for the equiatomic 20 element alloy from Cantor's original work is $\sim 3R$ [1], yet we see that these high mixing entropies do not necessarily lead to single phase solid solutions.

Additional parameters for electronegativity difference $\Delta\chi$ [162] and valence electron concentration, VEC [163] have also been adapted to determine the phase stability in HEAs:

$$\Delta\chi = \sqrt{\sum_{i=1}^{n} c_i(\chi_i - \bar{\chi})^2} \tag{1.3}$$

$$\text{VEC} = \sum_{i=1}^{n} c_i(\text{VEC})_i \tag{1.4}$$

where $\bar{\chi} = \sum_{i=1}^{n} c_i\chi_i$, and χ_i is the Pauling electronegativity for the ith element and $(\text{VEC})_i$ is the VEC for the ith element. Guo et al. point out that VEC in this case is different than the average number of itinerant electrons per atom $e/a = \sum_{i=1}^{n} x_i e/a_i$, in that VEC counts the total electrons including the d-electrons accommodated in the valence band [42]. Valence electron concentrations (VEC) for 3d transition metals are often calculated from the tables in Ref. [164] using (1.4) where Guo suggests that FCC phases are found when VEC ≥ 8 while BCC occurs when VEC <6.87.

Guo et al. suggests that high mixing entropy is not sufficient to form solid solution phases in equiatomic multi-component alloys. There exists a possibility that when the system gets confused is to form an amorphous phase. To form stable metallic glass phases, the more negative enthalpy has to be coupled with the large atomic size difference of elements in the alloy. Guo statistically analyzes the effects of atomic size difference, mixing enthalpy, mixing entropy, electronegativity, and valence electron concentration on the formation of solid solution and amorphous phases. They conclude that the most significant difference between high-entropy alloy and bulk metallic glasses formation is the atomic size difference, while the requirements for complete solid solution are,

- $-22 \leq \Delta H_{mix} \leq 7$ kJ/mol

- $0 \leq \Delta S_{mix} \leq 8.5$ J/(K·mol)
- $11 \leq \Delta S_{mix} \leq 19.5$ J/(K·mol)

However, bulk metallic glass has the tendency to form when $\delta \geq 9$, $-49 \leq \Delta H_{mix} \leq -5.5$ kJ/mol and $7 \leq \Delta S_{mix} \leq 16$ J/(K·mol).

1.3.2 Entropy

In the review by Miracle et al. they suggest that the configurational entropy hypothesis for these alloy systems is not a good indicator for predicting the formation of stable single phases alloys. The authors suggest that there are many other contributions to the entropy of these systems, and that by using only the configurational entropy term (i.e. Boltzmann equation) can lead to erroneous results when calculating free energies. The total molar entropy outlined in Ref. [22] is given by Eq. 1.5:

$$S^{\phi} = S^{\phi,\text{ideal}} + {}^{conf}S^{\phi} + {}^{\text{vib}}S^{\phi} + {}^{\text{elec}}S^{\phi} + {}^{\text{mag}}S^{\phi} \tag{1.5}$$

where S^{ϕ} is the total molar entropy of phase ϕ, S^{ideal} is the atomic configurational entropy for solid solution phases via the Boltzmann equation, ${}^{conf}S^{\phi}$ is the excess configurational entropy term which can arise from short range ordering, and ${}^{vib}S^{\phi}$, ${}^{mag}S^{\phi}$, and ${}^{elec}S^{\phi}$ are the entropy terms from atomic vibrations, magnetic moments, and electronic effects respectively. The significance of these terms relative to S^{ideal} vary across alloy systems, and the literature suggests that the "excess entropy terms can make important contributions to the total entropy in competition between phases." [22]. This ultimately leads to difficulty when calculating free energies of these systems.

1.3.3 Enthalpy

The Gibbs free energy of a system can be defined as:

$$\Delta G = \Delta H - T\Delta S \tag{1.6}$$

where ΔG is the Gibbs free energy, ΔH is the enthalpy contribution and $T\Delta S$ is the entropy contribution. As described earlier, the entropy term can be difficult to calculate based on the number of factors that can influence the entropy of the system. The ability for a solid or liquid solution of an alloy to form highly depends on the interplay between enthalpy and entropy.

Due to the lack of experimental data for mixing enthalpies of many binary alloys, a model for generating approximate mixing enthalpies was first developed by Miedema et al. in 1973 [165], which uses the electron density at the Wigner-Seitz cell boundary and the chemical potential of electronic charge of pure metals as input and can be written as $\Delta H_{\text{mix}} = \sum_{i=1,i\neq j}^{n} \Delta H_{c_i,c_j}^{\text{mix}}$. This model was used by Takeuchi et al. in 2005 for the classification of bulk metallic glasses by atomic size difference and heat of mixing [166] and later revisited by Takeuchi in 2010 [167] for mixing enthalpies of binary alloys, which includes an additional model for sub-regular solutions [168]. The ΔH_{mix} of the binary alloys from Ref. [167] serve as a starting point for calculations of ΔH_{mix} for HEAs, MPEAs, and CCAs.

$$\Delta H_{\text{mix}} = \sum_{i=1,i\neq j}^{n} \Delta H_{c_i,c_j}^{\text{mix}} \tag{1.7}$$

In equiatomic MPEA systems, there can be $\sum_{k=1}^{n-1} \binom{n}{k+1}$ elemental combinations that may arise during the overall mixture, not taking into account the enormous amount of non-equiatomic combinations that may also arise. For context, in an equiatomic quinary alloy mixture, there can be 5 quarternary combinations, 10 ternary combinations, and 10 binary combinations of the elements used in the alloys. By generating a table of the possible combinations that can arise from binary, ternary, quaternary, and quinary 3-d transition metal MPEAs of a specific combination, we may roughly investigate the ΔH_{mix} of phase separated regions to draw comparisons between the resulting compositions in the solid or liquid phase separated regions with the nominal values for the possible combinations. This way we may begin to elucidate the relationship between miscibility and mixing enthalpy.

1.3.4 Additional Parameters

Yang et al. presents a theoretical prediction for phase formation for a wide array of multi-component alloys with assumed normal casting or casting into copper mold [34]. They conclude that the number of the phases and their structures depend on processing conditions other than atomic size difference parameter δ and a solid-solution formation parameter Ω defined as,

$$\Omega = \frac{T_m \Delta S_{mix}}{|\Delta H_{mix}|} \tag{1.8}$$

Yang suggests that processing such as splat quenching with rapid cooling rate could facilitate the formation of simple structures. Their calculations for the formation of bulk-metallic glasses have larger values of δ and smaller values of Ω than multi-component

HEAs. They claim that the calculation of δ and Ω can provide two key factors in the prediction of solid-solution formation of HEAs. They suggest that $\Omega \geq 1.1$ and $\delta \geq 6.6\%$ as criterion for forming solid-solution phase while Guo et al. suggested that $\delta \leq 6.5$ with $\Delta H_{mix} \geq -12$ kJ/mol favors solid solution phase [42]. Ren et al. further refine these values with investigations into the formation of solid solution structures of seventeen different kinds of high-entropy alloys [149]. The phase compositions and microstructures of the alloys that were analyzed favored $\delta \leq 2.77$ and $\Delta H_{mix} \geq -8.8$ kJ/mol for simple solid solution. Otherwise intermetallic compounds tended to form.

King et al. presents a new method for predicting the formation of single phase high-entropy alloys [169]. Two new values are compared to assess the suppression of an ordered phase through the formation of a random solid solution: the change in Gibbs free energy for the formation of a fully disordered solid solution from a mixture of its individual elements ΔG_{ss} , and the lowest intermetallic or highest segregated possible Gibbs free energy obtainable from the formation of binary systems from the constituents of the mixture ΔG_{max}. Thus, a new parameter Φ, defined as the ratio of these two values (Eq. 1.9), where a value of $\Phi \geq 1$ suggests a stable solid solution at the systems' melting temperature while $\Phi < 0$ suggests the system has a positive formation enthalpy and will not form a solid solution.

$$\Phi = \frac{\Delta G_{ss}}{-|\Delta G_{max}|} \tag{1.9}$$

There were a few exceptions to this method, however density functional theory (DFT) calculations suggest that partial atomic ordering may explain the discrepancies.

The authors suggest this parameter Φ, can be used to predict the temperature at which the single phase solid solution will begin to precipitate.

Using the CALPHAD approach, the stability of phase was determined by the systems Gibbs energy which includes contributions from both enthalpy and entropy. Using phase diagrams, a two step approach is proposed to face the challenge of having a complete database for the entire compositional range of the ever evolving HEAs. Zhang proposes that a thermodynamic database can be developed for the limited number of matching elements [170].

Recently, work by Toda-Caraballo et al. suggests that the lattice distortion is related to the high solid solution hardening effect in HEAs. Along with the previously discussed solid solution forming parameters, two new parameters are introduced: interatomic spacing distribution s_m and bulk modulus distribution K_m [37]. These parameters are suggested to be used in conjunction with the existing parameters, and can approximately describe separate regions displaying solid solutions, intermetallics, bulk metallic glasses, and other crystal structures. Full mathematical representation of s_m and K_m can be found in Ref [37].

1.4 Liquid Phase Separation

It has been 14 years since the discovery of the high-entropy alloys (HEAs), an idea of alloying which has reinvigorated materials scientists to explore unconventional alloy compositions and multicomponent alloy systems. Many authors have referred to these alloys as multi-principal element alloys (MPEAs) or complex concentrated alloys (CCAs)

in order to place less restrictions on what constitutes an HEA. Regardless of classification, the research is rooted in the exploration of structure-properties and processing relations in these multicomponent alloys with the aim to surpass the physical properties of conventional materials. More recent studies show that some of these alloys undergo liquid phase separation, a phenomenon largely dictated by low entropy of mixing and positive mixing enthalpy. Studies posit that positive mixing enthalpy of the binary and ternary components contribute substantially to the formation of liquid miscibility gaps. The objective of this review is to bring forth and summarize the findings of the experiments which detail liquid phase separation (LPS) in HEAs, MPEAs, and CCAs and to draw parallels between HEAs and the conventional alloy systems which undergo liquid-liquid separation. Positive mixing enthalpy if not compensated by the entropy of mixing will lead to liquid phase separation. It appears that Co, Ni, and Ti promote miscibility in HEAs/CCAs/MPEAs while Cr, V, and Nb will raise the miscibility gap temperature and increase LPS. Moreover, addition of appropriate amounts of Ni to CoCrCu eliminates immiscibility, such as in cases of dendritically solidifying CoCrCuNi, CoCrCuFeNi, and CoCrCuMnNi.

Liquid phase separation (LPS), a widely observed phenomenon in metals is related directly to the Gibbs free energy of the system, and the most prevailing cases are often two distinct immiscible liquids of varying compositions. Although there is often some degree of solubility between the alloying elements in a metallic system exhibiting LPS, each liquid will have its own equilibrium vapor pressure, such that the vapor pressure of both phases are the same, with a positive deviation from Raoult's Law. When positive deviations from Raoult's Law are large, phase segregation tends to occur.

The occurrence of liquid phase separation in an alloy can lead to heterogeneous microstructures which may or may not be desirable depending on the intended application. For example, an alloy exhibiting liquid phase separation would not be suited for use as a structural material due to the heterogeneity of the microstructure, however may have potential use as a self-lubricating bearing material, such as the case with Cu-Pb. There have been several comprehensive reviews of immisicible metal systems of common alloys about the phenomenon [171–175]. Therefore the scope of this review will focus particularly on the liquid phase separation in the high-entropy alloy (HEA), complex concentrated alloy (CCA), and multi-principal element alloy (MPEA) systems.

1.4.1 Thermodynamics of Liquid Phase Separation

Factors such as positive deviations from Raoult's Law, positive heat of mixing, and atomic size mismatch in some cases do not overcome the entropy term in the overall Gibbs free energy and, cause overall immiscibility in the liquid, as is the case of miscibility between Au-Bi [175]. B. Mott in the late 1950s put together a review of the immiscible liquid metal systems as well as the corresponding thermodynamic data for each material at the time. The immiscible alloys Mott compiled in the study contained many of the known immiscible binary monotectic alloys of the time [171]. Nearly ten years later, Mott compiled another review detailing the thermodynamics of these metal systems as well as provided models for predictions of immiscibility in metals [172]. In Table 1.9, we provide a non-exhaustive table of binary alloys with miscibility gaps in the liquid state. The table is expands the tables from Mott's reviews [171,172] by adding alloys from binary phase diagrams from the Centre for Research in Computational Thermochemistry using the FactSage databases [176].

The molar Gibbs free energy of a system of stable unmixed liquids is represented additively via the atomic fraction of the free energies of the constituent liquids,

$$G^{\mathrm{L}}_{\mathrm{A\ +\ B\ +\ C\ ...}} = \sum_{i=\mathrm{A,B,C...}} x_{\mathrm{i}} G^{\mathrm{L}}_{\mathrm{i}} \tag{1.10}$$

where $x_{i=\mathrm{A,B,C...}}$ are the molar fractions of elements A, B, C etc. The molar Gibbs free energy of mixing is classically defined as,

$$\Delta G_{\mathrm{mix}} = \Delta H_{\mathrm{mix}} - T\Delta S_{\mathrm{mix}} \tag{1.11}$$

where the entropy of mixing is given as,

$$\Delta S_{\mathrm{mix}} = -R \sum_{i} x_i \ln x_i \tag{1.12}$$

and the enthalpy of mixing is

$$\Delta H_{\mathrm{mix}} = \sum_{i=1, i\neq j}^{n} \Delta H^{\mathrm{mix}}_{x_i, x_j} \tag{1.13}$$

where $\Delta H^{\mathrm{mix}}_{x_i, x_j}$ is the interatomic interaction between concentrations of 'i' and 'j' elements in the system. Immiscible alloys typically have a positive value of ΔH_{mix}, which implies a preference of nearest neighbors of similar atoms as opposed to compound formation with different atoms. Many of the immiscible binary systems can be categorized by their liquid state miscibility gaps and positive enthalpy of mixing, $\Delta H_{\mathbf{mix}}$, of which extensive thermodynamic treatments are presented in Ref. [173, 175].

The region of a phase diagram where there is non-mixing of the constituents is defined as a miscibility gap. The liquid miscibility gap in many of the monotectic binary systems assumes a dome-like shape; the shape and location of which may shift with the addition of more alloying elements. For example, one of the most well studied ternary systems with a stable liquid miscibility gap is the Co-Cu-Fe system [110, 115, 177–185] while equiatomic additions of Cr and Ni, the CoCrCuFeNi high-entropy alloy solidifies dendritically from a single phase liquid, as observed by Yeh et al. in 2004 [3].

A generalized equilibrium monotectic phase diagram is present in Fig. 1.5, where the miscibility gap in the liquid state is present as a dome with label $L_1 + L_2$. The size and width of the immiscibility gap varies from system to system, however the concept is the same. That is, cooling the alloy system from a liquid state in the concentrations that fall within the miscibility gap will lead to the liquid decomposing into two compositionally different liquids, the temperature of which is known as the critical temperature (labeled T_c in Fig. 1.5).

As the temperature decreases to T_1 in Fig. 1.5, the entropy term $T\Delta S$, is smaller than the enthalpy of mixing ΔH_{mix} in the free energy of the system (Fig. 1.6), therefore the free energy of the liquid G_L with respect to concentration of the B element in A will also assume a dome shape, presented in Fig. 1.5. If the temperature T_1 is held, the equilibrium phases will be L_1, $L_1 + L_2$, or L_2 dependent on composition X_B. Cooling the system through T_2 until the monotectic temperature, T_3, the monotectic reaction will take place and we will start to see α precipitate out of the liquid as L_1 is no longer stable until we reach T_4, where the remaining equilibrium phases are the solidified α and liquid L_2. Cooling through

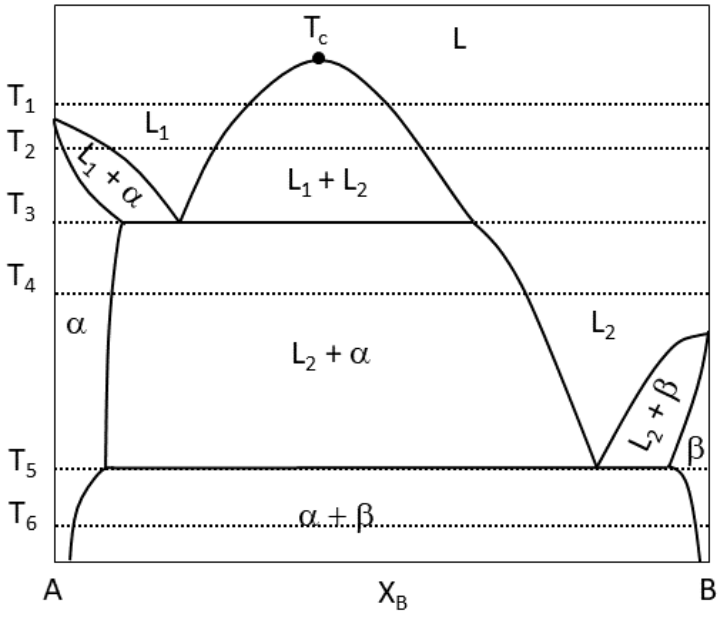

Figure 1.5: Generalized equilibrium monotectic binary phase diagram.

the eutectic temperature at T_5 to reach T_6 we are ultimately left with $\alpha + \beta$ solid phases.

Due to the lack of experimental data for mixing enthalpies of many binary alloys, a model for generating approximate mixing enthalpies was first developed by Miedema et al. in 1973 [165], which uses the electron density at the Wigner-Seitz cell boundary and the chemical potential of electronic charge of pure metals as input and can be written as $\Delta H_{\text{mix}} = \sum_{i=1, i\neq j}^{n} \Delta H_{c_i, c_j}^{\text{mix}}$. This model was used by Takeuchi et al. in 2005 for the classification of bulk metallic glasses by atomic size difference and heat of mixing [166] and later revisited by Takeuchi in 2010 [167] for mixing enthalpies of binary alloys, which includes an additional model for sub-regular solutions [168]. The ΔH_{mix} of the binary alloys from Ref. [167] serve as a starting point for many of the recent calculations of ΔH_{mix} for HEAs, MPEAs, and CCAs. Using the calculated binary mixing enthalpies (ΔH_{mix}) from Takeuchi et al. [167], ΔH_{mix} much of the values used for determining the mixing enthalpies

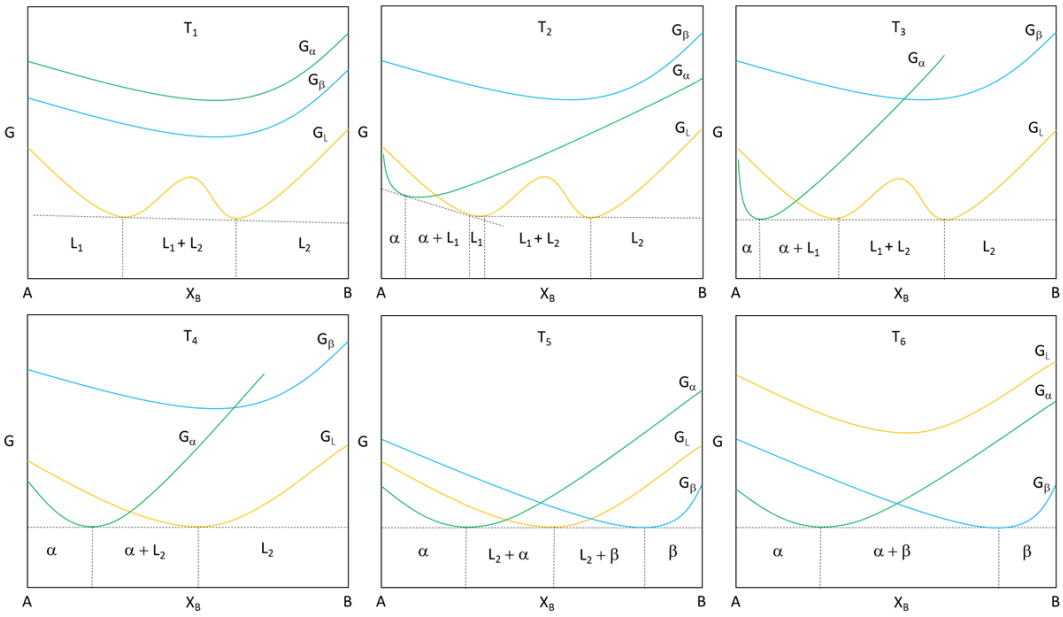

Figure 1.6: Gibbs free energy corresponding to the monotectic phase diagram.

for HEAs/CCAs/MPEAs were calculated using equation (3.1) where $\Delta H^{\text{mix}}_{x_i,x_j} = 4\Omega_{0_{ij}} x_i x_j$ for the i$^{\text{th}}$ and j$^{\text{th}}$ elements at $A_{0.50}B_{0.50}$ concentrations from the tables in Ref. [167]. The values for c_i and c_j are the normalized atomic concentrations in the multicomponent alloy.

1.4.2 Metastable Liquid Phase Separation

Unlike the stable liquid state immiscibility observed in the monotectic binary alloys, there are certain cases where a completely miscible liquid alloy can de-mix in the presence of impurities or when supercooled below the freezing temperature of the alloy, as demonstrated for Co-Cu and Cu-Fe by Nakagawa in 1958 [186]. Since then, there has been an enormous amount of LPS studies on metastable Co-Cu [177, 183, 184, 187–197] and Cu-Fe [83, 183, 198–205], as well as the stable LPS that occurs in the combination of all three

Table 1.9: Binary systems that contain a stable miscibility gap in the liquid state.

Ag - B	Au - Ru	Bi - V	Ce - Cr	Cs - Fe	Fe - Na	K - Mo	Li - Tb	Na - Y	Sr - Tm
Ag - Co	B - Ge	Bi - Zn	Ce - Eu	Cu - K	Fe - Pb	K - Nd	Li - Ti	Na - Yb	Sr - V
Ag - Cr	B - Sn	C - Cu	Ce - K	Cu - Mo	Fe - Rb	K - Ni	Li - V	Na - Zn	Sr - Y
Ag - Fe	Ba - Ce	C - Sn	Ce - Li	Cu - Na	Fe - Sn	K - Pb	Li - Yb	Na - Zr	Sr - Zr
Ag - Ir	Ba - Cr	Ca - Cd	Ce - Mo	Cu - Pb	Fe - Sr	K - Pm	Li - Zr	Nd - Sr	Tb - Ti
Ag - K	Ba - Fe	Ca - Ce	Ce - Na	Cu - Ru	Fe - Tl	K - Pr	Lu - Na	Nd - Ti	Tb - V
Ag - Mn	Ba - Gd	Ca - Cr	Ce - Sr	Cu - Se	Ga - Hg	K - Sc	Lu - Sr	Nd - V	Te - Tl
Ag - Nb	Ba - K	Ca - Dy	Ce - Ti	Cu - Tl	Ga - Pb	K - Sm	Lu - V	Nd - Yb	Th - U
Ag - Nb	Ba - La	Ca - Er	Ce - U	Cu - Tu	Ga - Te	K - Sr	Lu - Yb	Ni - Pb	Ti - Yb
Ag - Ni	Ba - Mn	Ca - Fe	Ce - V	Cu - U	Ga - Tl	K - Tb	Mg - Mn	Ni - Sr	Tl - Zn
Ag - Os	Ba - Nd	Ca - Gd	Ce - Zr	Cu - V	Ge - Tl	K - Ti	Mg - Mo	Ni - Tl	Tm - V
Ag - Os	Ba - Pm	Ca - Ho	Co - In	Cu - W	Gd - K	K - Tm	Mg - Na	Pb - Se	V - Y
Ag - Rh	Ba - Pr	Ca - K	Co - K	Cr - Pb	Gd - Li	K - V	Mg - Nb	Pb - Si	V - Yb
Ag - Rh	Ba - Ru	Ca - La	Co - Li	Cr - Sn	Gd - Mo	K - Y	Mg - Ru	Pb - Zn	W - Zn
Ag - Se	Ba - Sc	Ca - Lu	Co - Pb	Dy - K	Gd - Na	K - Yb	Mg - Ru	Pb - Zr	
Ag - Ta	Ba - Sm	Ca - Mn	Co - Tl	Dy - Li	Gd - Sr	K - Zn	Mg - Ta	Pm - Sr	
Ag - U	Ba - Ti	Ca - Na	Cr - Dy	Dy - Na	Gd - Ti	K - Zr	Mg - Ti	Pm - Ti	
Ag - V	Ba - Y	Ca - Nd	Cr - Er	Dy - Sr	Gd - V	La - Li	Mg - W	Pm - V	
Ag - W	Ba - Zr	Ca - Pm	Cr - Eu	Dy - Ti	Gd - Yb	La - Mn	Mg - Zr	Pr - Sr	
Al - Bi	Be - K	Ca - Pr	Cr - Gd	Dy - V	Hg - Nb	La - Na	Mn - Na	Pr - Ti	
Al - Cd	Be - Li	Ca - Ru	Cr - K	Er - K	Hg - Si	La - Sr	Mn - Pb	Pr - V	
Al - In	Be - Mg	Ca - Sc	Cr - La	Er - K	Hf - Mg	La - Ti	Mn - Sr	Pr - Zr	
Al - K	Be - Na	Ca - Sm	Cr - Li	Er - Na	Ho - K	La - V	Mn - Tl	Sc - V	
Al - Na	Be - Se	Ca - Tb	Cr - Mg	Er - Sr	Ho - Mo	La - Zr	Mn - Yb	Sc - Sr	
Al - Pb	Be - Sn	Ca - Ti	Cr - Na	Er - V	Ho - Na	Li - Cs	Mo - Na	Sc - V	
Al - Tl	Be - Sr	Ca - Tm	Cr - Nd	Eu - Li	Ho - Sr	Li - Fe	Na - Nd	Se - Tl	
As - Tl	Be - Zn	Ca - V	Cr - Pb	Eu - Mn	Ho - Ti	Li - K	Na - Ni	Si - Tl	
Au - B	Bi - Co	Ca - Y	Cr - Pm	Eu - Na	Ho - V	Li - Na	Na - Pm	Sm - Sr	
Au - Ir	Bi - Cr	Ca - W	Cr - Pr	Eu - T I	In - Te	Li - Nd	Na - Pr	Sm - Ti	
Au - Mo	Bi - Fe	Ca - Zr	Cr - Sm	Eu - V	In - V	Li - Ni	Na - Sc	Sm - V	
Au - Rh	Bi - Ga	Cd - Cr	Cr - Sn	Eu - Zr	K - La	Li - Pm	Na - Sm	Sn - V	
Au - Rh	Bi - Mn	Cd - Fe	Cr - Sr	Fe - In	K - Li	Li - Pr	Na - Tb	Sn - W	
Au - Se	Bi - Rb	Cd - Ga	Cr - Tm	Fe - K	K - Lu	Li - Rb	Na - Ti	Sn - Zr	
Au - W	Bi - Se	Cd - K	Cr - Y	Fe - Li	K - Mg	Li - Sc	Na - Tm	Sr - Tb	
Au - Ru	Bi - Si	Cd - Na	Cr - Yb	Fe - Mg	K - Mn	Li - Sm	Na - V	Sr - Ti	

elements in Co-Cu-Fe [110, 115, 177–185]. Metastable liquid phase separation is defined as the liquid phase separation that occurs when undercooling an alloy such that it enters a miscibility gap that would not have been observed if solidified via conventional methods, presented in the phase diagram from Ref. [188] in Fig. 1.7. These studies have shown that when undercooling past freezing, the single phase alloy liquid will then split into two liquids (L1 + L2), specifically in these cases into Cu-rich and Cu-lean liquids, which solidify often as spherical globules trapped in the frozen regions of the other liquid (the microstructure of such will be discussed later). This metastable LPS implies that there exists a dome shape

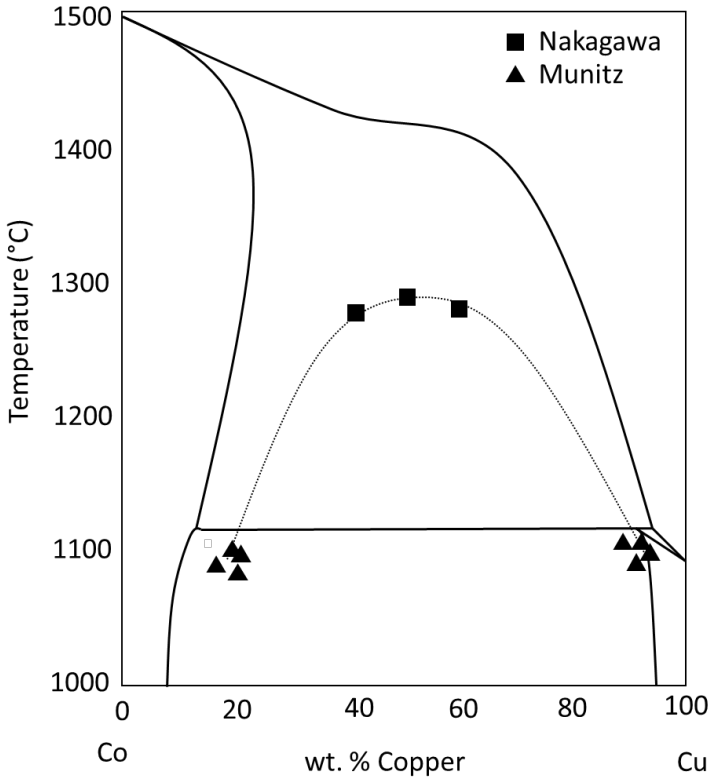

Figure 1.7: The Co-Cu phase diagram with dashed line indicating the metastable liquid miscibility gap beneath the liquidus.

similar to the monotectic alloys beneath the liquidus curves in their respective equilibrium phase diagrams.

1.4.3 LPS in Ternary systems

Many of the ternary alloys that exhibit liquid phase separation contain Cu as it has a low affinity for mixing with other elements, however, there are a number of other non Cu-containing ternary alloys with liquid miscibility gaps as well. Table 1.10 is a non-exhaustive list of the studied ternary alloys with liquid phase miscibility gaps, many of which contain

Cu. As was the case with many binary alloys, the ΔH_{mix} of these systems are typically positive. One can think of the HEAs/CCAs/MPEAs as the addition of alloying elements to preexisting ternary alloys, some of which may actually contain a stable miscibility gap in the liquid, which is the case with CoCrCu [86] and many of the HEAs that contain Co, Cr, and Cu in equal parts with respect to the other alloying elements in the HEA. It would appear that the increase in the entropy of mixing ΔS_{mix} with additional alloying elements stabilizes the solution, however this strongly depends on the enthalpy of mixing ΔH_{mix} as well as other factors that determine miscibility [22].

Table 1.10: Ternary alloy systems that contain a liquid miscibility gap

Ag - Al - Pb	[176]	Al - Mg - Mn	[176]
Ag - Co - Pd	[176]	Au - Cu - Pb	[176]
Ag - Cu - Fe	[206]	Au - In - Pb	[176]
Ag - Cu - Mn	[206]	Au - In - Pb	[176]
Ag - Cu - Ni	[206]	B - Cu - Fe	[181, 207]
Ag - Cu - Pb	[206]	Bi - Ga - Zn	[176]
Ag - Cu - Se	[206]	Co - Cr - Cu	[86, 140, 208, 209]
Ag - Cu - Ti	[206]	Co - Cr - Nb	[86]
Ag - Fe - Mn	[176]	Co - Cu - Fe	[110, 115, 177–180, 182–185, 210]
Ag - Fe - Ni	[176]	Cr - Cu - Fe	[115, 211]
Ag - Nb - Ti	[212]	Cu - Fe - Mo	[213]
Ag - Ni - Sn	[176]	Cu - Fe - Nb	[213]
Al - Bi - Cu	[214]	Cu - Fe -Si	[115, 181]
Al - Bi - Sb	[215]	Cu - Fe - Sn	[216]
Al - Bi - Sn	[217–220]	Cu - Fe - V	[115]
Al - Cu - Sn	[221]	Cu - Ni - Pb	[176]
Al - Ga - In	[176]	Fe - Si - Zn	[176]
Al - Ga - Sn	[176]	Pb - Pd - Sn	[176]

There is much debate as to what exactly constitutes a high-entropy alloy (HEA), complex concentrated alloy (CCA), or multi-principal element alloy (MPEA). In essence, the core idea is very similar behind each definition: multicomponent, "baseless" alloys greater than 3 elements designed with the goal of surpassing the mechanical properties of traditional alloys. Whether or not which composition will solidify into a single, duplex, or multiple phases is not what this review is concerned with, but rather the observance of liquid

phase separation in these multicomponent alloy systems. Approximately 85% of HEAs in the literature to date are made up of predominantly 3d transition metals, many of which contain Al [22]. As it is impossible to visualize the phase diagram space of multicomponent alloy systems that contain 5+ elements, it can be difficult to know whether these alloy systems will phase separate in the liquid. Many of the well studied HEA systems, such as CoCrCuFeNi for example [2], contain equiatomic CoCrCu which has a very large liquid miscibility gap [86, 208].

1.5 Solidification Microstructures

1.5.1 Dendritic Microstructure

Alloy solidification morphology and as-cast microstructure can have many forms depending on the solidification process. The most common microstructures of a solidified alloy can vary from plane front solidification, dendritic morphology, and eutectic microstructures, among others. Many of the solidification microstructures present in HEA literature consist of dendritic growth, which is typically indicative of crystal growth from a liquid with an imposed thermal gradient, as is the case with most arc-melting processes. Dendrites are solid tree-like, branching cellular structures that grow from a liquid phase. The conglomeration of atoms during solidification typically form a nucleus of spherical shape, which then becomes unstable due to perturbations. The solid shape then begins to express the preferred growth directions of the underlying crystal and consumes atoms from the overall liquid to form a stable solidifying phase [222]. The liquid that is leftover after dendritic solidification is referred to as the interdendritic liquid which solidifies last, and is referred

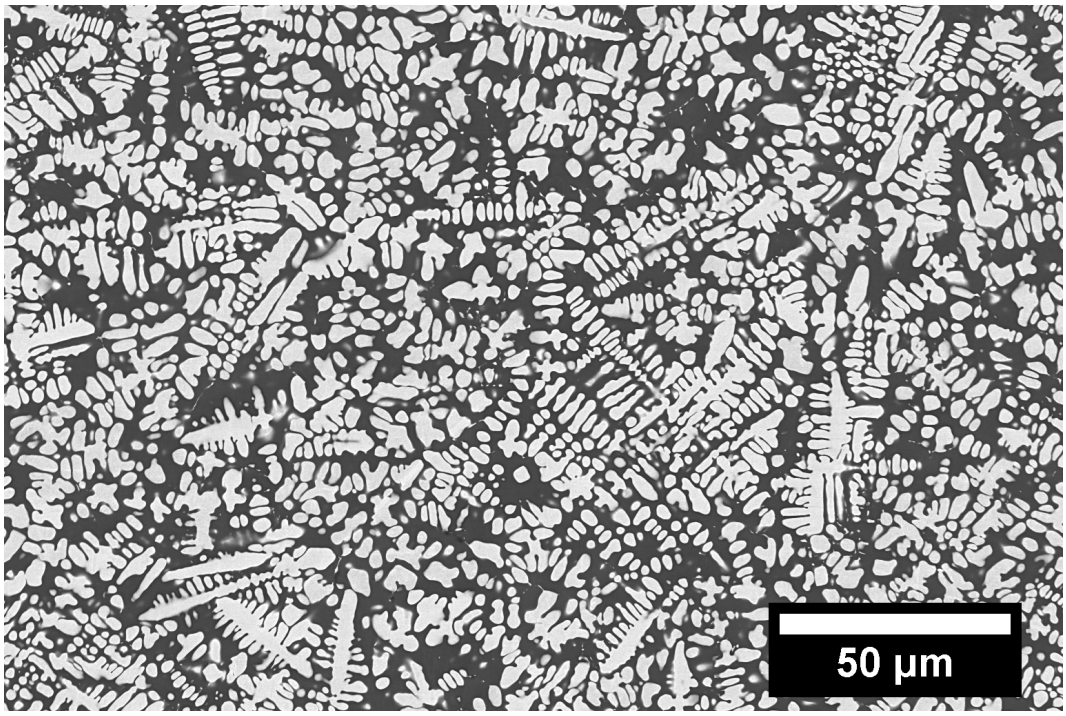

Figure 1.8: Backscattered electron image of an as-cast AlMoNi alloy with a dendritic microstructure.

to as the interdendritic region or interdendrite.

The preferred dendritic growth directions for most cubic systems (FCC/BCC) are in the $< 100 >$ directions, which leads to the secondary dendrite arms to grow perpendicular from the primary arm. This is often an easy way to differentiate between cubic and noncubic crystal structure of the dendritic phase.

Typical dendritic microstructure of an electromagnetically levitated and solidified alloy is presented in Fig. 1.8. The dendritic morphology usually indicates that the microstructure evolved from a single phase liquid if the dendritic morphology is uniform, however if the alloy has a small volume fraction of LPS, the remaining L2 globules may be

pushed to the edge of the sample by the growing dendrites. There have been cases where liquid phase separation has occurred in the interdendritic liquid after the growth of primary dendrites [223, 224], however the general morphology of dendritic microstructures indicate that there were no large scale liquid-liquid immiscibility between the alloying elements.

Many HEAs/CCAs/MPEAs solidify with a duplex microstructure, where the dendritic and interdendritic regions have a large compositional and crystallographic differences [9, 17, 22, 23, 27]. These have been shown to have interesting mechanical properties however, have yet to surpass the mechanical properties of commercial alloys.

1.5.2 Microstructures Resulting From Liquid Phase Separation

Alloys that undergo either stable or metastable LPS also have very distinct microstructures that can vary based on the solidification process. Slow cooling rates paired with a static environment can lead to the liquids separating. If the system is a little more dynamic, such as in the case of casting, the process can lead to trapping of the primary liquids in one another, referred to as emulsion (Fig. 1.9). The separated liquids tend to be trapped as spherical globules inside the other liquid, and solidify as such, as is the case of the equiatomic CoCrCu alloy present in Fig. 1.10. As these liquids can be slightly different in composition than the primary liquid, they are referred to as secondary liquids. Based on morphology alone, one can distinguish the first phase to solidify from the interface between the the two liquids as the higher melting point liquid will solidify at a higher temperature, and will most of the time solidify with protrusions into the other liquid, as is the case with the solidification of CoCrCu present in Fig. 1.11. The backscattered electron image in Figs. 1.10,1.11 display emulsion of the lighter (Cu-rich) and darker (CoCr-rich) liquids, as well

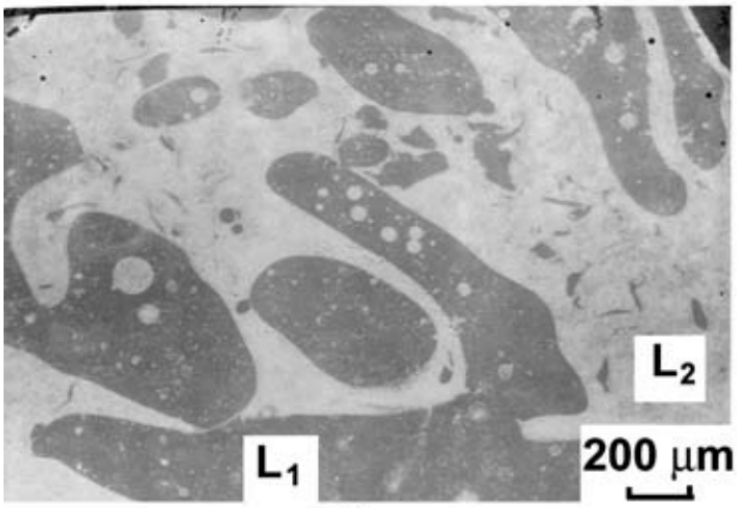

Figure 1.9: SEM image of liquid phase separation and emulsion of two immiscible liquids L1 and L2 in an undercooled CoCuFe alloy. Image presented with permission from the original authors.

as small protrusions coming from the CoCr-rich secondary liquid in Fig. 1.11.

There have been several efforts to create uniform microstructures of immiscible liquid melts, such that the LPS is evenly distributed. These techniques include free directional and directional solidification [225], rheomixing [226], microgravity experiments [191, 227, 228], electromagnetic levitation processing [202] and rapid solidification [229]. Much of this work is aimed at the tailoring of the immiscible liquid droplets such that microstructure has a uniform spread of the immiscible phase [173]. There have also been experiments aimed at the suppression of LPS with additional alloying elements [230].

Traditionally, observing LPS in metallic systems was done via post-mortem analysis via metallography and microscopy, as metals are not transparent to light and have

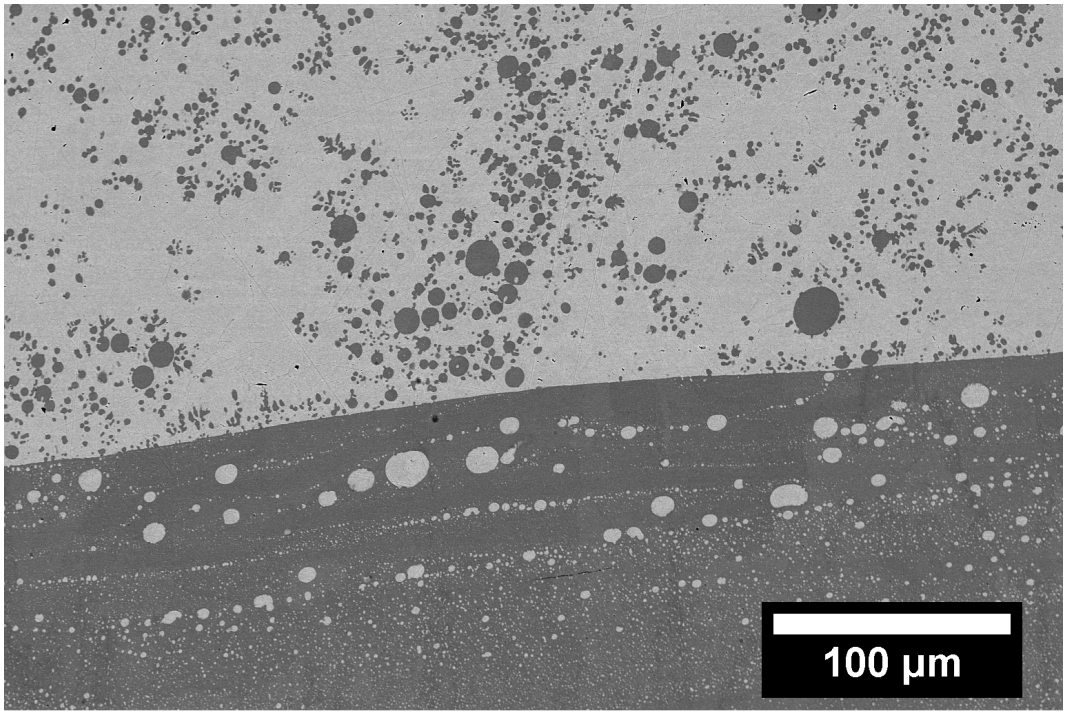

Figure 1.10: Backscattered electron image displaying emulsion of CoCr-rich (darker) and Cu-rich (lighter) liquids in an as-cast alloy of CoCrCu.

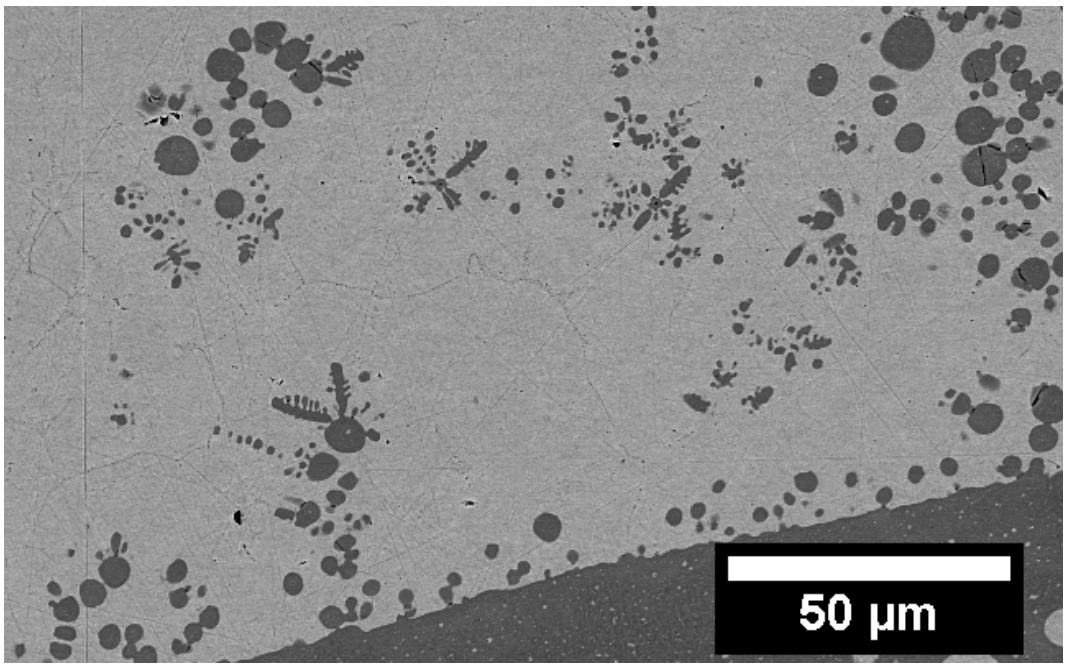

Figure 1.11: Backscattered electron image displaying emulsion and protrusions of the CoCr-rich (darker) phase into the Cu-rich (lighter) phase in an as-cast alloy of CoCrCu.

a very small transparency for X-rays. Recently through the use of neutron transmission imaging techniques, the direct observation of liquid phase separation in metals was made possible via neutron radiographs taken during heating and cooling of immiscible CoCrCu alloys [209]. These experiments show for the first time an in-situ observation of macroscopic LPS in metals, and can be applied to any metallic system such that the neutron transmission through the each phase can provide enough contrast between them. Fig. 1.13 displays neutron radiographs of two stacked CoCrCu arc-melted buttons in a small Al_2O_3 crucible with inner diameter of 8 mm. Prior to the in-situ testing, the arc-melted CoCrCu buttons underwent stable LPS and solidified with very heterogeneous Cu-rich and Cu-depleted regions, as presented in Fig. 1.12. The resulting as-cast button consists of a non-uniform mix of the two solidified Cu-rich and Cu-depleted phases, and can be seen as the lighter (Cu-rich) and darker (Cu-depleted) regions in Fig. 1.13a. During melting (Figs. 1.13b–d), the two liquid phases separate and stack according to density (Cu being the lighter contrast, more dense liquid phase). Note that the solid Cu-rich and CoCr-rich phases were already separated in the arc-melted buttons, but at a finer scale. The stable liquid phases then agglomerated and separated at the macro-scale. A full sequence of images in the form of a movie can be found in Ref. [209].

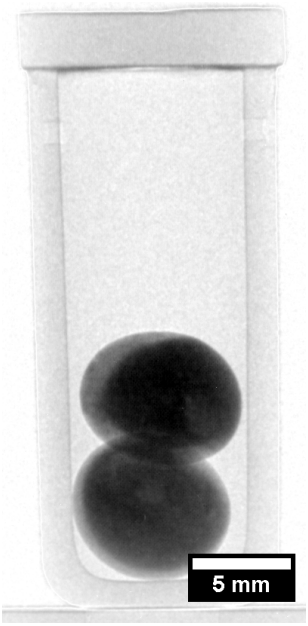

Figure 1.12: Neutron radiograph of two stacked arc-melted CoCrCu buttons in an alumina crucible with brighter regions corresponding to Cu-rich phases and darker regions corresponding to CoCr-rich phases.

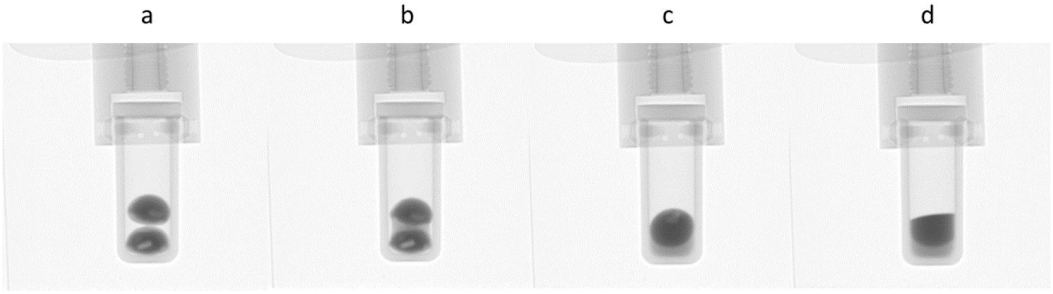

Figure 1.13: Melting and liquid phase separation of stacked CoCrCu samples. (a) During initial heating, the two as-cast buttons are intact. (b) The Cu-rich phase melts first between 1075 and 1100 °C, and (c) pools at the bottom of the crucible. (d) The Cu-lean phase fully melts upon heating to 1500 °C and stack based on density due to the influence of gravity.

1.6 High-Entropy Alloys Exhibiting Liquid Phase Separation

1.6.1 HEAs containing Cu

The first occurrence of LPS in HEAs was observed by Hsu et al. in 2007 with a study of the alloying behavior of AlCoCrCuNi-based HEAs with additions of Fe, Ag, and Au [231]. The addition of Ag to the AlCoCrCuNi HEA to create AgAlCoCrCuNi was found to phase separate in the liquid which resulted in the solidification microstructure consisting of Cu-rich globules embedded in Cu-depleted phases, contrary to the typical dendritic solidification microstructures observed for AlCoCrCuNi. Hsu suggested that in order to achieve effective mixing in the liquid, the ΔH_{mix} for atom pairs should not exceed 10 kJ/mol, and that "mutual interaction between elements, based on their mixing enthalpies, should be taken into account when designing high-entropy alloys" [231].

These alloys were then revisited by Munitz et al. in 2013 where AgAlCoCrCuNi and AgAlCoCrCuFeNi were synthesized to study the melt separation behavior [232]. It was observed that the Cu-rich immiscible liquid tended to flow to the bottom of the buttons udring arc-melting, as well as residual Cu-rich liquid being trapped in the interdendritic region of the Cu-depleted dendritic phase. Undercooling experiments were also carried out for a similar alloy of $Al_{1.8}CoCrCu_{3.5}FeNi$, however no metastable liquid miscibility gap was found at the undercoolings obtained in the study ($\sim$ 150 K) [184, 232].

A similar alloy composition of $AlCoCrCuFeNiSi_{0.5}$ doped with Y_2O_3 was synthesized via laser cladding with the intention to form a core-shell structure in HEAs, inspired by the LPS observed in HEAs and binary monotectics. The undoped $AlCoCrCuFeNiSi_{0.5}$ did not undergo LPS, while the addition of 1 wt.% nanosized Y_2O_3 caused the liquids to

separate into egg like globules of Cu-rich liquids inside the Cu-depleted liquid [233]. This is similar LPS phenomena that has been seen in the aforementioned alloy compositions.

Recent studies into Co-free $Al_{2.2}CrCuFeNi_2$ revealed what the authors referred to as anomalous "sunflower-like" solidification microstructures [234], where it was suggested that LPS occurs in the no longer stable-depleted interdendritic liquid, occurring due to changes in the composition. Munitz et al. suggest that the liquid phase separation is due to constitutional changes and not temperature changes, where the authors refer to this phenomena as "constitutional LPS" (CLPS) [224]. For the $Al_{2.2}CrCuFeNi_2$ alloy, constitutional LPS occurred in the interdendritic liquid , where the interdendritic liquid decomposed into a CrFe-rich L_1 and a Cu-rich L_2. As the dendritic skeleton was already formed, the heavier Cu-rich liquid accumulated in the interdendritic region and the cast bottom, while the CrFe-rich spheres underwent solidification emulsed in the Cu-rich liquid.

A large study of several HEAs by Munitz et al. in 2017 was undertaken to explore the effects of Al, Co, Cr, Ni, Ti, and V on the miscibility gap temperature of several HEA systems. It was shown that Al, Co, Ni, and Ti lowered the miscibility gap temperature while Cr, V, and Nb will raise the miscibility gap temperature and increase LPS in these systems, alloys of which are found in Table 1.11. Many of the HEAs studied by Munitz et al. contained equiatomic CoCrCu, which was experimentally determined to have a large liquid miscibility gap [86]. It is peculiar that systems such as CoCrCuFeNi will solidify dendritically [3] while similar alloys of CoCrCu [86, 140, 209] and CoCuFe [110, 115, 177–180, 182–185, 210] have been shown to have large liquid miscibility gaps. A recent study by Derimow et al. investigated the solidification microstructures of equiatomic CoCrCu with

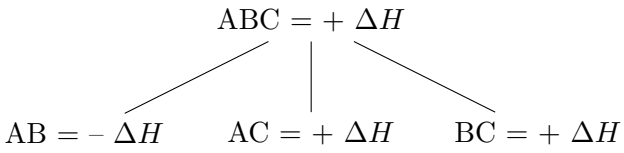

Figure 1.14: Tree diagram representing probability of clustering based on the mixing enthalpies of binary combinations of elements ABC

added Fe, Mn, Ni, V, FeMn, FeNi, FeV, MnNi, MnV, and NiV to the composition. It was found that only three of the alloys solidified dendritically (CoCrCuNi, CoCrCuFeNi, and CoCrCuMnNi), while the remaining combinations underwent stable LPS [140]. Derimow et al. also suggest that the positive mixing enthalpy of each of the systems were responsible for the LPS, and presented a tree diagram for approximating the likelihood of which elements will cluster together in the melt, present in Fig. 1.14.

The tree diagram in Fig. 1.14 indicates that AB atoms are more likely to cluster than ABC, AC, or BC, thereby rejecting the C element. This can be seen in case of the ternary CoCrCu where the LPS consists of CoCr-rich and Cu-rich liquids [86, 140] and solidifies with the microstructure shown in Fig. 1.10.

Table 1.11 compiles the multicomponent alloys found in the literature that have been shown to undergo LPS. Each of these systems have solidification morphology similar to the microstructure present in Fig. 1.10. From this table, the common component in all but one of these systems is equiatomic Cu. This is in part due to the positive mixing enthalpy Cu has with many of the alloying elements in the system. It should be noted that although Ni appears to promote miscibility in Cu-containing HEAs, however may be ineffective if the

Table 1.11: Multcomponent alloy systems with reported liquid miscibility gaps.

System	Classification	Type of LPS	Ref.
Ag - Al - Co - Cr - Cu - Fe - Ni	HEA	Stable	[232]
Ag - Al - Co - Cr - Cu - Ni	HEA	Stable	[231, 232]
Al - Co - Ce - La - Zr	Bulk Metallic Glass	Stable/Metastable	[235]
$Al_{0.5}$ - Co - Cr - Cu - Fe - V	HEA	Stable	[139]
Al - Cr - Cu - Fe - Ni	HEA	Stable	[224]
Al - Cu - La - Ni - Zr	Bulk Metallic Glass	Stable	[236]
B - Cu - Fe - P - Si	Fe-Cu-alloy	Stable	[237]
Co - Cr - Cu - Fe	HEA	Stable	[139, 140]
Co - Cr - Cu - Fe - Mn	HEA	Stable	[140]
Co - Cr - Cu - Fe - Mo - Ni	HEA	Stable	[238]
Co - Cr - Cu - Fe - Ni	HEA	Metastable	[151–153, 239]
Co - Cr - Cu - Fe - Ni - Nb	HEA	Stable	[139]
Co - Cr - Cu - Fe - Ti - V	HEA	Stable	[139]
Co - Cr - Cu - Fe - V	HEA	Stable	[139, 140]
Co - Cr - Cu - Mn	HEA	Stable	[140]
Co - Cr - Cu - Mn - V	HEA	Stable	[140]
Co - Cr - Cu - Ni - V	HEA	Stable	[140]
Co - Cr - Cu - V	HEA	Stable	[140]
Cr - Cu - Fe - Mn - V	HEA	Stable	[139]
Cr - Cu - Fe - Mo - Ni	HEA	Stable	[240]
Cr - Cu - Fe -Ni	Cu-alloy	Stable/Metastable	[110]

repulsion between Cu and the majority of the alloying elements is too great.

1.6.2 CoCrCuFeNi

One of the seminal HEAs synthesized by Yeh et al. was the CoCrCuFeNi HEA [3]. Along with the Cantor alloy (CoCrFeMnNi) [1], these alloys served as many a starting point for the addition and subtraction of alloying elements. The first study to note the liquid phase separation in HEAs in a similar composition of AgAlCoCrCuNi attributed the presence of LPS to the positive mixing enthalpies between Ag and the rest of the alloying elements [231].

An induction melting study by Wu et al. involving CoCrCuFeNi demonstrated the first occurrences of LPS in this alloy [153]. In Wu's study, several combinations of the CoCrCuFeNi alloy with varied Fe and Ni were studied to investigate the effects on microstructure and crystallography of the system. When Fe and Ni were varied to create $CoCrCuFe_{0.5}Ni$

and $CoCrCuFeNi_{0.5}$, spherical Cu-rich separations were observed postmortem analysis of the solidified samples [153]. The authors rationalized that the two alloy compositions positive mixing enthalpies were too great to be overcome by the entropy of the system which would thereby lower the overall Gibbs energy of the system in the molten state.

Previous studies of supercooling and rapid solidification via electromagnetic levitation melting by Elder et al. characterize large undercoolings of 150 K for Cu-Fe and 75 K for Co-Cu that produce the LPS microstructures for these metastable alloys [241]. Elder et al. list several techniques to achieve high undercoolings such as melt emulsification, melting in molten slag or fused silica (glass fluxing), free fall in a drop tube, and electromagnetic levitation techniques to achieve undercooled temperatures [241]. Using the molten fused silica technique, rapid solidification studies of CoCrCuFeNi by Liu et al. were carried out to investigate rapid solidification effects on the microstructure and phase stability of $CoCrCuFe_xNi$ HEAs (where x = 1, 1.5, and 2.0) [151]. It was found that LPS occurred in all three compositions below critical undercooling temperature, ΔT_{crit}, where $\Delta T_{\text{crit}}^{x=1.0} =$ 160 K, $\Delta T_{\text{crit}}^{x=1.5} = 190$ K, and $\Delta T_{\text{crit}}^{x=2.0} = 293$ K. When $\Delta T > \Delta T_{\text{crit}}$, the microstructure is consistent with that of LPS, such that there were Cu-rich spheres present throughout the material. Due to the dendritic solidification behavior of CoCrCuFeNi through regular solidification routes [3], this alloy is classified as having a metastable liquid phase miscibility gap that is present when undercooled past ΔT_{crit} [151]. The metastable liquid miscibility gap was also confirmed by Wang et al. for CoCrCuFeNi where the authors also achieved an exceptionally high degree of undercooling of 381 K ($0.23T_m$) for the alloy [152]. The ΔT_{crit} for equiatomic CoCrCuFeNi was also studied by Guo et al., and it was found that metastable

LPS occurs when $\Delta T > \Delta T_{\text{crti}} = 100$ K [239]. The authors also show that the yield strength and elongation of equiatomic CoCrCuFeNi significantly decrease when the alloy undergoes liquid phase separation due to the non-uniformity of the resultant microstructure [239].

Recently, Wang et al. show that with the addition of 3 at.% Sn to CoCrCuFeNi, the alloy undergoes the same characteristic liquid phase separation when undercooled past $\Delta T_{\text{crti}} = 100$K [242]. The study showed that the LPS produced an increase in hardness of the Cu-depleted phases due to the separation of Cu and Sn in the liquid [242].

Previous studies on similar alloys have shown that Mo improves the strength in the AlCoCrFeNi and AlCoCrCuFeNi HEAs [243–245]. However, it has been shown that with varied Cu concentrations in CoCrCu$_x$FeMoNi where x $\geq$ 0.5, LPS occurs in similar fashion to the other Cu-containing HEAs [238].The addition of Mo to the CoCrCuFeNi alloy was investigated by Wu et al. to elucidate the solidification process in these alloys, as there had been a lack of thorough studies on the solidification microstructures of these alloys [238]. Due to the Cu-rich sphere emulsion in Cu-depleted phases, likely due to the positive mixing enthalpy between Cu and the remaining alloying elements, Wu et al. suggested that the ΔH_{mix} criteria for the prediction of single phase formation be amended to include the possibility of liquid phase separation in the liquid when $\Delta H_{\text{mix}} > 0$. In order to further study the Mo-containing HEAs, Peng et al. synthesized a Co-depleted CrCu$_x$FeMo$_y$Ni HEA to further elucidate the effects of the large positive ΔH_{mix} between Cu and Mo on the solidification process and microstructure. It was found that Cu-rich and Cu-depleted LPS occurs in the CrCu$_x$FeMo$_y$Ni when x and y = 0.5 and 1, attributed to $\Delta H_{\text{mix}} > 0$ for these alloy combinations [240].

The field of high-entropy alloys, complex concentrated alloys, and multi-principal element alloys continues to grow, with new studies producing valuable insights to the materials community with the overarching goal of creating new alloys that exceed the properties of conventional materials. This relatively new class of material is not much different from the conventional alloys, being that they are still subject to the same thermodynamic rules that are imposed on them. The main caveats are that with the increase of alloying elements, orthogonal element phase diagram visualization becomes impossible, therefore creative ideas are warranted to help understand the nature solidification of these alloys. Positive mixing enthalpy if not compensated by the entropy of mixing will cause liquid phase separation. It appears that Co, Ni, and Ti promote miscibility in multicomponent alloys,while Cr, V, and Nb will raise the miscibility gap temperature and increase LPS. Moreover, for equiatomic CoCrCu, which has a large liquid miscibility gap, addition of appropriate amounts of Ni eliminates immiscibility. Indications of such for example is the CoCrCuFeNi alloy, which will solidify dendritically while similar alloys of CoCrCu and CoCuFe show strong immiscibility. Moreover, when Fe, Mn, Ni, V, FeMn, FeNi, FeV, MnNi, MnV, and NiV are added to to equiatomic CoCrCu, only three of the alloys solidify dendritically (CoCrCuNi, CoCrCuFeNi, and CoCrCuMnNi), while the remaining combinations underwent stable LPS. In the case of CoCrCuNiV, it appears that the addition of Ni in equiatomic amounts was not enough to overcome the positive mixing enthalpy interaction between Cu and V, as the CoCrCuV alloy also exhibits stable LPS. From the table of listed multicomponent alloys that undergo LPS, Cu is found in all but one of these combinations, which indicates that Cu containing HEAs may contain a metastable liquid miscibility similarly to CoCrCuFeNi.

Chapter 2

Experimental Procedure

2.1 Arc Melting

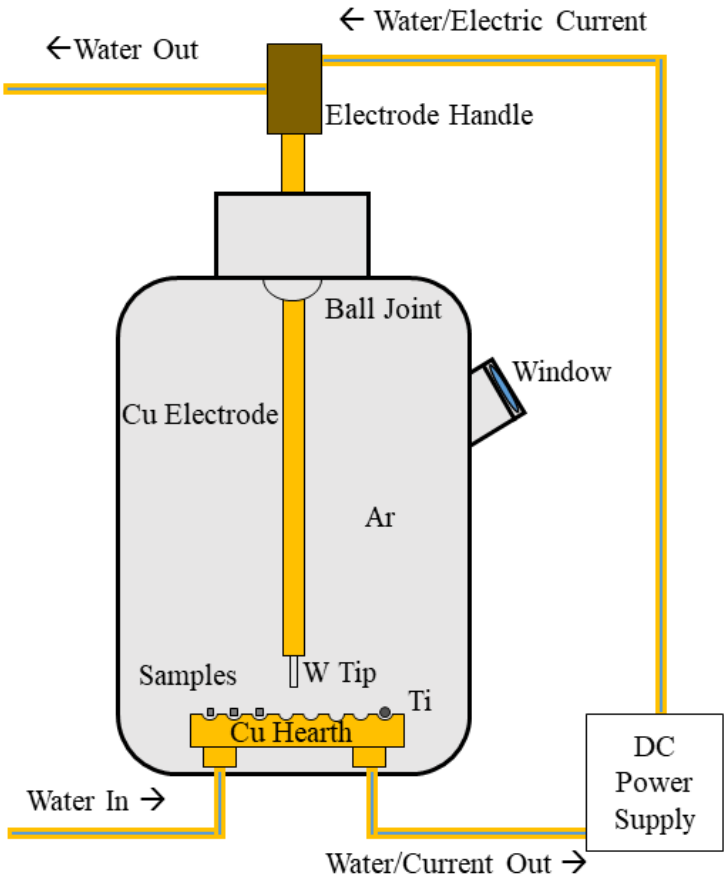

Figure 2.1: Schematic of Arcmelting System

The first melting of metal on a water-cooled metal substrate was performed over 100 years ago for the invention of ductile tantalum [246]. The water cooled substrates became more elaborate nearly 50 years later when researchers began to carve grooves into water filled Cu tubes to hold the starting metallic material [247,248]. This process eventually led to the modern hearths we have today that can have a variety of shapes. As opposed to consumable electrode melting, inert or nonconsumable electrode melting is what is mainly

used in laboratories for current research purposes. In this method, the arc is maintained by a refractory material, such as thoriated tungsten. The schematic in Fig. 2.1 displays the modern arc melting unit, such as the one used for these experiments. The system is a fairly simple circuit with half of it being encapsulated inside of a water-cooled bell jar; a direct current (DC) power supply provides current through water-cooled Cu wires surrounded by insulated tubing into the electrode to where the current travels through the electrode and to the thoriated tungsten tip. An arc is an extremely hot body of ionized elemental species (5000-50,000K) which the current passes through, typically over 100 A with a voltage drop between the limits of 20-45 V [249]. Once the arc is started, the current completes the circuit through the water-cooled Cu-hearth and back to the DC power supply, melting the metal inside the hearth in the process. To remove impurities in the atmosphere of the bell jar, a piece of titanium is melted in between sample melts to act as an oxygen getter. The arc-melting device used throughout this work was a Centor Series 5 BJ arc-melter, depicted in Fig. 2.2.

Compositions in the following studies were prepared with elemental purities of the base metals: Co $\geq$ 99.9%, Cr $\geq$ 99.99%, Cu $\geq$ 99.9%, Fe $\geq$ 99.97%, Mn $\geq$ 99.7%, Ni $\geq$ 99.99%, Ti $\geq$ 99.7% and V $\geq$ 99.7% all purchased from Alfa Aesar (Ward Hill, Massachusetts). Elemental manganese used in the experiments was pickled prior to alloying to remove unwanted oxide layers from the manufacturer. Bulk pieces of Co and Ti received from the manufacturer were cut into 4x4x8 mm pieces via wire EDM. Elemental metals were cut to specific sample stoichiometry with SiC griding discs on a rotary tool, followed by sonic bath in isopropyl alcohol to remove dust and oils. Each sample with elemental

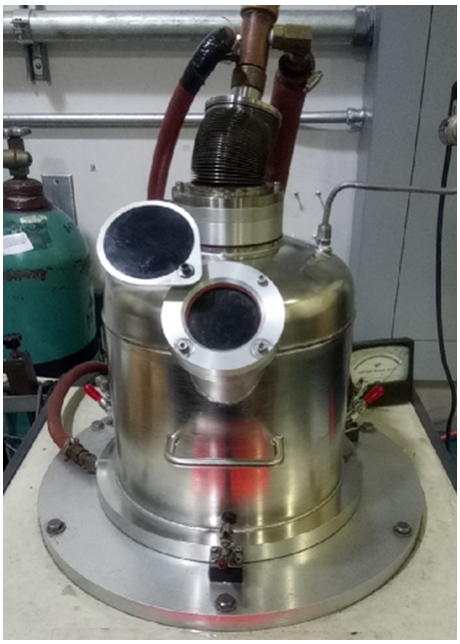

Figure 2.2: Centorr Series 5BJ Arc-melting unit.

metal pieces weighing a total of ≈ 1.5g, were then placed into the water-cooled Cu hearth of the arcmelting furnace in Fig. 2.1 and melted three to five times in a Ti-gettered argon atmosphere.

2.2 Electromagnetic Levitation

The use of induction coils to achieve levitation of conducting materials was first proposed by O. Muck in 1923 [250], but not fully realized until 1951 where it was suggested that sample levitation could be achieved without melting [251, 252]. Shortly after, the process was further theoretically and experimentally developed by researchers at the Westinghouse Research Laboratory who were able to achieve sample levitation in a container-less

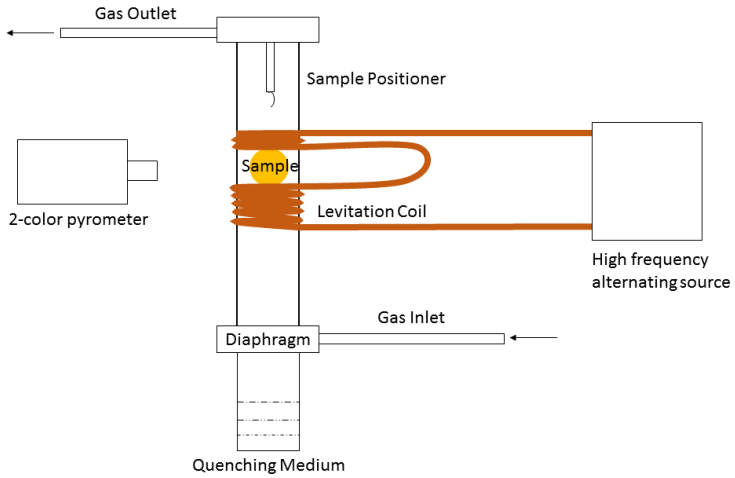

Figure 2.3: Schematic of Levitation System

environment [253–255].

The force required for sample levitation and heat input are influenced by [253]:

- Size, shape, and construction of the induction coil.
- Size, shape, and material of the charge relative to the coil.
- Physical properties of the charge, such as the rate of variation of surface tension, electrical, and magnetic properties with temperature.
- Type of power supply and frequency.
- Thermal history of the melt as influenced by the gas environment.

The ratio of levitation force to weight of the sample, and power absorbed by the sample is given by,

$$\frac{\mathbf{F}}{W} = -\frac{\frac{2}{3}G(x)}{\rho\mu_0}(\mathbf{B}\cdot\nabla)\mathbf{B} \tag{2.1}$$

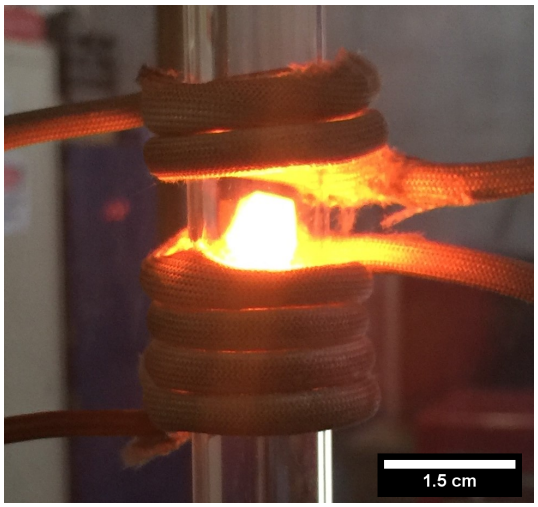

Figure 2.4: Photograph of a metal suspended in the magnetic field of the EML apparatus

$$P = \frac{3\pi RH(x)}{\sigma\mu_0^2}\mathbf{B}\cdot\mathbf{B} \tag{2.2}$$

where x is defined as the ratio of the radius of the metal sphere R to the skin depth δ (x = R/δ) , G(x) and H(x) are functions of x, **F** is the levitating force, W is the weight of the sphere, **B** is the magnetic induction, P is the power absorbed by the sample, μ_0 is the permeability of free space, σ is the electrical conductivity of the metal and ρ is the density of the metal [249]. The high frequency current supplied by the power source produces an alternating magnetic field in the induction coil, which induces eddy currents in the sample that are 180^o out of phase with the applied field. This both heats the sample and creates an opposing magnetic flux that moves the sample to the weaker part of the applied field. For levitation to occur there must be a lifting force equal to the weight of the sample, which can be achieved by using a conical induction coil with one or two opposing turns at the top to provide horizontal stability and dampen oscillations. The samples are typically levitated

within quartz tubing under Ar cover gas, while temperature of the sample can be controlled via flow of gasses with high thermal conductivity (such as He) [241]. A schematic for this system can be seen in Fig. 2.3.

Successful electromagnetic levitation experiments in the 1980s and 90s utilized this technique to manipulate undercooling effects, grain refinement, reduced gravity environments, levitation of paramagnetic materials, and rapid solidification in metallic samples [241, 256–261].

Electromagnetic levitation processing was carried out using a LEPEL 20 kW, 300 kHz - 8 MHz high-frequency generator in an Ar/He environment inside of a 5/8" OD quartz tube with slightly conical induction coils, which were prepared via the prescribed coil preparation method in Ref. [262]. Heating and cooling of the levitating metallic samples were controlled via passing a combination of He and Ar gasses through the quartz tube. The gasses were first passed through a Centorr Model 2A gas purifier prior to entering the quartz tube. Heating is achieved when He gas is reduced, while cooling is achieved by increasing the flow of He and reducing the flow of Ar. For fast cooling rates, the samples were dropped from levitation to quench on a room temperature piece of copper. Temperature measurements were made with Process Sensors M3 2-color pyrometers of temperature ranges 500 - 1800 °C and 800 – 3000 °C.

2.3 Metallography

The cast samples were cut in half using a diamond wafering blade and subsequently mounted face down in BPA epoxy resin or Conducto Mount conductive mounting powder.

The specimens were then abraded using SiC paper up to 1200 grit, and polished using 1μ, 0.3μ, and 0.05μ Al_2O_3 powder or colloidal silica. As the colloidal silicon is slightly alkaline, no additional etchant was used prior to electron microscopy.

2.4 Characterization

X-ray diffraction patterns were taken using a PANalytical Empyrean Series 2 diffractometer with Cu K_α radiation. The data was acquired from 20° to 100° with a step size of 0.02° and step time of 30s/step. Backscattered electron images (BEIs) and energy-dispersive X-ray spectroscopy (EDS) were obtained with NovaNanoSEM 450 and TEESCAN MIRA3 GMU scanning electron microscopes. Semi-quantitative analysis was carried out on the X-ray spectra obtained from the primary liquid regions and dendritic/interdendritic regions. With the magnification being on the order of several microns, we can estimate the average elemental composition based on the semiquantitative analysis of the Kα and Lα X-ray emission peaks of the elements with approximate error in atomic composition $\pm$ 2-3 at.%.

Chapter 3

Solidification Microstructures and Calculated Mixing Enthalpies in CoCrCu Containing Alloys

3.1 Abstract

We report on observations of the as-cast microstructures of equiatomic quaternary and quinary multiprincipal element alloys (MPEAs) containing equiatomic ternary CoCrCu-X with X being Fe, Mn, Ni, Ti, V, FeMn, FeNi, FeTi, FeV, MnNi, MnTi, MnV, NiTi, NiV and TiV. Out of the 15 MPEA combinations studied, CoCrCuNi, CoCrCuTi, CoCrCuFeNi, CoCrCuMnNi, CoCrCuMnTi, and CoCrCuTiV displayed solid solution dendritic microstructures while the remaining 10 displayed a liquid phase separation into Cu-lean and Cu-rich liquids which solidified into highly phase separated regions. Calculations for enthalpy of mixing (ΔH_{mix}) were carried out on the possible equiatomic combinations of these alloys using Miedema's scheme for sub-regular solutions. The calculated ΔH_{mix} for the nominal combinations were then compared to the ΔH_{mix} for the atomic percentages of the actual compositions determined via EDS. It was found that stable Cu-lean microstructures all have lower ΔH_{mix} than the calculated ΔH_{mix} for their equiatomic ratios, indicating a positive correlation between ΔH_{mix} and stable phase formation. The FCC structures observed for CoCrCuNi, CoCrCuFeNi, and CoCrCuMnNi dendrites are in agreement with the model for valence electron concentration described in the literature. The following work was published in part in Ref. [140].

3.2 Background

Since the discovery of high-entropy alloys (HEAs) in 2004 [1–6], several efforts have been made to fully understand the formation mechanisms of these alloys as well as to what extent their mechanical, thermal, and electric properties could be exploited through

various processing techniques. Recent literature has been heading in the direction of using less restrictive definitions for these complex alloy systems, leading to more inclusive terms such as multi-principal element alloys (MPEAs), baseless alloys, and complex concentrated alloys (CCAs) [22]. Not withstanding, much of the research in the field of HEAs, CCAs, and MPEAs has conformed to the idea that HEAs must be composed of five or more principal elements in equimolar ratios which lead to the formation of a single phase solid solution in [1, 2]. As such, previous studies have mostly skipped equiatomic ternary and quaternary alloys due to them being considered medium-entropy alloys based on the classifications outlined by Yeh in 2006 [10]. Almost all of the literature pertaining to high-entropy alloys refer to many of the alloys being found to be single-phase solid solutions while neglecting the interdendritic regions with elementally different compositions, such as the Cantor alloy CoCrFeMnNi [1] and CoCrCuFeNi [2, 139, 150–153]. The interdentritic regions also fundamentally lower the overall melting temperature of the alloy, which should be taken into consideration when designing materials for high-temperature applications.

The process of designing engineering materials is complex when different metallurgical methods are employed for synthesizing alloys such as HEAs, MPEAs or CCAs. For example, a single-phase solid solution with desirable properties may be obtainable via powder metallurgy, yet vanishes if these alloys undergo stable liquid phase separation (LPS) during casting. In the recent review of HEAs, CCAs, and MPEAs by D. Miracle and O. Senkov, approximately 85% of all HEAs contained the 3d transition metal elements plus Al [22]. Alloys that have been shown to have stable liquid phase separation have been mostly the Cu alloy systems such as, Cu-Fe [83,181,199,201,204,263], Co-Cu [62,184,187,188,194,195,202],

Cu-Nb [184, 264], Co-Cu-Fe [110, 178, 180, 184], Co-Cr-Cu [86], Cr-Cu-Nb [86] and Cr-Cu-Fe-Ni [110]. The single phase HEA CoCrCuFeNi solidifies dendritically but undergoes Cu-segregation when solidified at undercooled temperatures [152].

It has been experimentally found that equiatomic CoCrCu leads to two distinct liquids with a very large miscibility gap [86]. Out of the alloys listed in the review by Miracle et al. [22], over 100 systems contained equimolar Co, Cr, and Cu. The percentage of CoCrCu ranges from approximately 30-75% of the entire alloy in these systems. Cu-segregation has been observed in many of these HEA systems, of which contain equiatomic CoCrCu and are listed in Table 3.1. In each of these phase-separated alloys, primary Cu-rich and Cu-lean phases have been observed. Cu segregation occurs typically in the interdendritic regions as well as large globule like separation. Table 3.1 represents a compilation of HEAs/MPEAs/CCAs with Cu-segregation that could be be due to the liquid phase separation of Cu in the CoCrCu. The additional alloying elements preferentially mix with the CoCr-rich liquids forming compounds that reject Cu. as observed in Table 3.1.

The data in the literature suggests that configurational entropy does not have as strong an influence on the formation of single-phase alloys or simple crystal structures as previously thought [22], therefore more fundamental experiments must be carried out to understand the formation mechanisms of these alloy systems. This work seeks to fill in the gaps in experimental data for 3-d transition metal MPEAs containing the ternary base of CoCrCu in order to elucidate any effects of the 3-d transition metals on single phase formation. Although there are many variables that could be responsible for stable phase formation, this study focuses on relating the enthalpy of mixing ΔH_{mix} and valence

electron concentration VEC to the observed phases from the equiatomic combinations of these alloys to understand the correlations between each alloying element and the miscibility of the system.

In addition, the study focuses on the miscibility of liquid phases of these complex alloys at different compositions, while varying solidification parameters. In this study, we report on the solidification microstructures obtained from arcmelted CoCrCu-X, with X being Fe, Mn, Ni, Ti, V, FeMn, FeNi, FeTi, FeV, MnNi, MnTi, MnV, NiTi, NiV, and TiV. In addition, some samples of CoCrCu, CoCrCuFe, CoCrCuV, and CoCrCuFeV were electromagnetically levitated and cast to further investigate the LPS observed in the systems. It should be noted that since these alloys explore the interior regions of hyper-dimensional composition space [22], which does not necessarily place requirement on the presence of a single-phase solid solution, hereafter referred to the alloys in this study as MPEAs.

There are currently several empirical approaches for predicting single phase formation in MPEAs, such as the Hume-Rothery rules, enthalpy of mixing (ΔH_{mix}), composition weighted parameters for differences in atomic radii and electronegativity (δr, $\delta \chi$), and valence electron concentration (VEC) [42]. When used in conjunction, their predictive capabilities are approximations at best due to the complex hyperdimensional composition space that arises in systems with greater than 3 components [22]. Due to the lack of experimental data for mixing enthalpies of many binary alloys, a model for generating approximate mixing enthalpies was first developed by Miedema et al. in 1973 [165], which uses the electron density at the Wigner-Seitz cell boundary and the chemical potential of electronic charge of pure metals as input and can be written as $\Delta H_{\text{mix}} = \sum_{i=1, i\neq j}^{n} \Delta H_{c_i, c_j}^{\text{mix}}$. This model was

Table 3.1: Near-equiatomic MPEAs containing CoCrCu. AC = as-cast, MA + SPS = mechanically alloyed with spark plasma sintering, SS = solid solution, IM = intermetallic, U = unknown. Calculated predictions using CALPHAD neglect the possibility of complex phases.

Composition	Processing	Phase	Crystal Structure	Cu Seg.	Ref.
AgAlCoCrCuFeNi	AC	–	–	Yes	[265]
AgAlCoCrCuNi	AC	SS + IM	2FCC + B2	Yes	[231, 265]
AlAuCoCrCuNi	AC	SS + IM	FCC + $L1_0$	Yes	[231]
AlCoCrCuFe	MA + SPS	SS + IM	FCC + B2	Yes	[266]
$Al_{0.5}$CoCrCuFeV	AC	–	–	Yes	[139]
AlCoCrCuFeMnNi	AC	SS + IM	FCC + B2 + σ	Yes	[267]
$Al_{0.25}$CoCrCuFeMnNiTiV	AC	SS	BCC	No	[161]
AlCoCrCuFeMoNi	AC	–	BCC + U	Yes	[245]
AlCoCrCuFeNi	AC	SS	BCC + FCC	Yes	[231, 268]
AlCoCrCuFeNiSi	AC	SS	BCC + FCC	–	[269]
AlCoCrCuFeNiTi	AC	SS + IM	BCC + FCC + B2	Yes	[267]
AlCoCrCuFeNiTiV	AC	SS	BCC + FCC	–	[3]
AlCoCrCuFeNiV	AC	SS	BCC + FCC	Yes	[267]
AlCoCrCuMnFe	AC	SS	2BCC + FCC	Yes	[270]
AlCoCrCuMnTi	AC	SS + IM	2BCC + FCC + $AlCu_2Mn$	Yes	[270]
AlCoCrCuNi	AC	SS + IM	BCC + FCC	Yes	[231, 269]
AlCoCrCuNiTi	AC	SS	2BCC + FCC	Yes	[271]
AlCoCrCuNiTiY	AC	SS + IM	BCC + C15 +$L2_1$ + U	Yes	[271]
CoCrCu	AC	SS + IM	BCC + FCC + σ	Yes	[86]
CoCrCuFe	AC	–	–	Yes	[139]
CoCrCuFeMn	AC + $\frac{1123\ C}{72\ Hr}$	SS	2FCC +B2	Yes	[148]
CoCrCuFeMnNi	AC	SS	FCC	Yes	[1]
CoCrCuFeMnNiTiV	AC	SS + IM	2BCC + FCC + σ + U	Yes	[161]
CoCrCuFeMoNi	AC	SS	BCC + FCC	Yes	[238]
CoCrCuFeNi	AC	SS	FCC	Yes	[2]
CoCrCuFeNiTi	AC	SS + IM	FCC + C14	–	[159]
$CoCrCuFeTi_{0.5}$	AC	–	–	Yes	[139]
CoCrCuFeV	AC	–	–	Yes	[139]
CoCrCuMn	Calculated	SS	BCC + FCC + 2HCP	Yes	[138]
CoCrCuMnNi	Calculated	SS	BCC + 2FCC + HCP	Yes	[138]
CoCrCuNi	MA	SS	BCC + 2FCC	Yes	[138, 142]

used by Takeuchi et al. in 2005 for the classification of bulk metallic glasses based on atomic size difference and heat of mixing [166] and later revisited by the same authors in 2010 [167] to include an additional model for sub-regular solutions [168]. The ΔH_{mix} of the binary alloys from Ref. [167] serve as a starting point for calculations of ΔH_{mix} in this study.

3.3 Experimental Procedure

Fifteen equiatomic compositions were prepared: CoCrCu, CoCrCuFe, CoCrCuMn, CoCrCuNi, CoCrCuTi, CoCrCuV, CoCrCuFeMn, CoCrCuFeNi, CoCrCuFeTi, CoCrCuFeV, CoCrCuMnNi, CoCrCuMnTi CoCrCuMnV, CoCrCuNiTi, CoCrCuNiV, and CoCrCuTiV. Elemental purities used were Co $\geq$ 99.9%, Cr $\geq$ 99.99%, Cu $\geq$ 99.9%, Fe $\geq$ 99.97%, Mn $\geq$ 99.7%, Ni $\geq$ 99.99%, Ti $\geq$ 99.7%, and V $\geq$ 99.7% all purchased from Alfa Aesar (Ward Hill, Massachusetts). Each sample, weighing about 1.5g, was arcmelted three times (flipped twice) on a water-cooled Cu hearth in a Ti-gettered argon atmosphere. Elemental manganese used in the experiments was etched prior to alloying using 12 M HCl to remove unwanted oxide layers from the manufacturer. The cast samples were cut vertically in half using a diamond wafering blade and subsequently mounted face down in BPA epoxy resin. The specimens were then abraded using SiC paper up to 1200 grit, and polished using 1μ, 0.3μ, and 0.05μ Al_2O_3 powder.

X-ray diffraction patterns were taken of the remaining halves of the unetched samples using a PANalytical Empyrean Series 2 diffractometer with Cu K_α radiation. The data was acquired from 20 $^\circ$ to 100 $^\circ$ with a step size of 0.02 $^\circ$ and step time of 30s/step. Backscattered electron images (BEIs) and energy-dispersive X-ray spectroscopy (EDS) were obtained

with NovaNanoSEM 450 and TEESCAN MIRA3 GMU scanning electron microscopes. Duplicate samples of CoCrCu, CoCrCuFe, CoCrCuV, and CoCrCuFeV were chosen to be electromagnetically levitated, melted in a continuous purified argon flow environment.The electromagnetically levitated, melted, and cast samples CoCrCu, CoCrCuFe, CoCrCuV, and CoCrCuFeV were cast onto a flat Cu chill. Alloy temperatures were measured with a Metis M3 2-color pyrometer. Once complete sample melting was achieved, each sample was then dropped out of the magnetic field and cast onto a flat Cu-surface with the exception of CoCrCuV, which was solidified in the magnetic field. Semi-quantitative analysis was carried out on the X-ray spectra obtained from the primary liquid regions and dendritic/interdendritic regions. With the magnification being on the order of several microns, we can estimate the average elemental composition based on the semiquantitative analysis of the Kα and Lα X-ray emission peaks of the elements with approximate error in atomic composition $\pm$ 2-3 at.%.

3.4 Thermodynamic Calculations

The calculated binary mixing enthalpies (ΔH_{mix}) from Takeuchi et al. [167] for liquid binary alloys, which were compiled to study amorphous systems, were used in the present investigation for calculating ΔH_{mix} for equiatomic ternary, quaternary, and quinary 3-d transition metal MPEAs were calculated using equation (3.1) where $\Delta H^{\text{mix}}_{c_i,c_j} = 4\Omega_{0_{ij}} c_i c_j$ for the i$^{\text{th}}$ and j$^{\text{th}}$ elements at $A_{0.50}B_{0.50}$ concentrations from the tables in Ref. [167], and are collected in Table 3.2. The values for c_i and c_j are the normalized atomic concentrations in the multicomponent alloy. Many HEA, MPEA, and CCA studies have used

the Miedema method to approximate ΔH_{mix} [42, 138, 164, 238, 268, 270] and are frequently used in conjunction with other parameters such as configurational entropy ΔS_{mix}, atomic size mismatch δ, electronegativity $\Delta\chi$ and valence electron concentration (VEC) to predict phase in HEA systems [42]. A comprehensive table of thermodynamic calculations using these parameters for systems previously studied in the literature can be found in Ref. [34].

Table 3.2 represents the ΔH_{mix} for the alloy combinations that can arise when producing quinary alloys containing CoCrCu. The equiatomic combinations of 3d transition metals Co, Cr, Cu, Fe, Mn, Ni, Ti, and V constructed from their binary mixing enthalpies. Although the 3d transition metals have similar chemistry, equiatomic combinations are thermodynamically different and can be seen in Table 3.2 from the range in values of ΔH_{mix}.

Guo et al. [163] proposed using valence electron concentration (VEC), defined as the number of valence electrons per atom, as an additional parameter for predicting phase stability, citing its usefulness in earlier studies of intermetallic compounds [272,273]. Recent work by Poletti and Battezzati [274] also uses VEC in conjunction with electronegativity $\Delta\chi$ and itinerant electron concentration (e/a) with atomic size mismatch in order to improve the methodology for improving HEAs. These authors state that the enthalpy of mixing depends on the electron concentration, such that the d electron band and the heat of formation of an alloy are strongly correlated [274]. VEC for the alloys in this study were calculated from the tables in Ref. [164] using equation (3.2), where it is suggested that FCC phases are found in HEAs when VEC ≥ 8 while BCC occurs when VEC <6.87 [163].

$$\Delta H_{\text{mix}} = \sum_{i=1, i\neq j}^{n} \Delta H_{c_i,c_j}^{\text{mix}} \tag{3.1}$$

$$\text{VEC} = \sum_{i=1}^{n} c_i (\text{VEC})_i \tag{3.2}$$

In equiatomic MPEA systems, there can be $\sum_{k=1}^{n-1} \binom{n}{k+1}$ elemental combinations that may arise during the overall mixture, not taking into account the enormous amount of non-equiatomic combinations that may also arise. For context, in an equiatomic quinary alloy mixture, there can be 5 quarternary combinations, 10 ternary combinations, and 10 binary combinations of the elements used in the alloys. By generating a table of the possible combinations that can arise from binary, ternary, quaternary, and quinary 3-d transition metal MPEAs, we may roughly investigate the ΔH_{mix} of phase separated regions to draw comparisons between the resulting compositions in the phase separated regions with the nominal values for the possible combinations. This way we may begin to elucidate the relationship between miscibility and mixing enthalpy.

CoCrCu was chosen to remain present in all of the alloys in this study as there is no ternary compound formed in the equimolar state, leading to Cu-rich and Cu-lean phases [86]. By doing so, we can investigate the effects of the 3d transition metals solubility in Cu-rich and Cu-lean phases. It is interesting that the equimolar addition of FeNi to CoCrCu makes single phase CoCrCuFeNi with primary dendrites that have FCC structure [2]. It is peculiar that by adding more elements (FeNi) to this ternary lead to the metastable FCC CoCrCuFeNi [150–153] while the addition of Fe, $FeTi_{0.5}$, and FeV resulted in stable liquid phase separation [139]. For binary liquids, if ΔH_{mix} is more negative, it implies

Table 3.2: ΔH_{mix} (kJ/mol) of all binary to quaternary equiatomic 3-d transition metal MPEAs and quinary MPEAs containing CoCrCu calculated using Miedema's scheme for sub-regular solutions.

Binary [167]		CoFeNi	-1.0	MnTiV	-4.6	CrCuMnNi	10.3
CoCr	-4.5	CoFeTi	-19.9	NiTiV	-23.6	CrCuMnTi	-1.6
CoCu	6.4	CoFeV	-9.5	**Quaternary**		CrCuMnV	5.2
CoFe	-0.6	CoMnNi	-5.9	CoCrCuFe	6.3	CrCuNiTi	-10.4
CoMn	-5.2	CoMnTi	-18.2	CoCrCuMn	3.8	CrCuNiV	-1.4
CoNi	-0.2	CoMnV	-8.7	CoCrCuNi	2.4	CrCuTiV	-0.7
CoTi	-28.3	CoNiTi	-27.4	CoCrCuTi	-7.6	CrFeMnNi	-3.9
CoV	-14.0	CoNiV	-14.0	CoCrCuV	3.4	CrFeMnTi	-7.9
CrCu	12.5	CoTiV	-19.2	CoCrFeMn	-2.4	CrFeMnV	-2.3
CrFe	-1.5	CrCuFe	10.4	CoCrFeNi	-3.8	CrFeNiTi	-17.2
CrMn	2.1	CrCuMn	8.0	CoCrFeTi	-14.8	CrFeNiV	-9.2
CrNi	-6.7	CrCuNi	4.1	CoCrFeV	-7.4	CrFeTiV	-9.2
CrTi	-7.5	CrCuTi	-1.7	CoCrMnNi	-5.7	CrMnNiTi	-15.8
CrV	-2.0	CrCuV	6.8	CoCrMnTi	-12.9	CrMnNiV	-8.4
CuFe	12.9	CrFeMn	0.3	CoCrMnV	-6.1	CrMnTiV	-4.5
CuMn	3.8	CrFeNi	-4.3	CoCrNiTi	-20.4	CrNiTiV	-17.6
CuNi	3.6	CrFeTi	-11.2	CoCrNiV	-11.4	CuFeMnNi	2.7
CuTi	-8.9	CrFeV	-4.6	CoCrTiV	-14.5	CuFeMnTi	-4.3
CuV	5.0	CrMnNi	-5.6	CoCuFeMn	3.9	CuFeMnV	3.5
FeMn	0.2	CrMnTi	-5.9	CoCuFeNi	5.1	CuFeNiTi	-11.3
FeNi	-1.6	CrMnV	-0.3	CoCuFeTi	-8.8	CuFeNiV	10.7
FeTi	-16.8	CrNiTi	-21.2	CoCuFeV	0.7	CuFeTiV	-4.2
FeV	-7.1	CrNiV	-11.6	CoCuMnNi	0.1	CuMnNiTi	-13.1
MnNi	-8.2	CrTiV	-4.9	CoCuMnTi	-10.1	CuMnNiV	-3.6
MnTi	-8.2	CuFeMn	7.4	CoCuMnV	-1.2	CuMnTiV	-2.7
MnV	-0.7	CuFeNi	6.5	CoCuNiTi	-15.5	CuNiTiV	-13.6
NiTi	-34.5	CuFeTi	-5.6	CoCuNiV	-4.3	FeMnNiTi	-17.3
NiV	-18.0	CuFeV	4.7	CoCuTiV	-10.4	FeMnNiV	-13.0
TiV	-1.7	CuMnNi	-0.3	CoFeMnNi	-3.9	FeMnTiV	-8.6
Ternary		CuMnTi	-5.8	CoFeMnTi	-14.7	FeNiTiV	-19.9
CoCrCu	6.3	CuMnV	3.5	CoFeMnV	-6.9	MnNiTiV	-17.8
CoCrFe	-2.9	CuNiTi	-17.3	CoFeNiTi	-20.5	**Quinary**	
CoCrMn	-3.3	CuNiV	-4.1	CoFeNiV	-10.4	CoCrCuFeMn	4.2
CoCrNi	-5.0	CuTiV	-2.4	CoFeTiV	-17.1	CoCrCuFeNi	3.2
CoCrTi	-17.6	FeMnNi	-4.2	CoMnNiTi	-12.5	CoCrCuFeTi	-5.8
CoCrV	-8.9	FeMnTi	-10.8	CoMnNiV	-11.6	CoCrCuFeV	1.1
CoCuFe	8.1	FeMnV	-3.3	CoMnTiV	-14.5	CoCrCuMnNi	0.6
CoCuMn	2.2	FeNiTi	-23.0	CoNiTiV	-24.2	CoCrCuMnTi	-6.0
CoCuNi	4.3	FeNiV	-11.6	CrCuFeMn	7.5	CoCrCuMnV	0.5
CoCuTi	-13.4	FeTiV	-11.2	CrCuFeNi	4.8	CoCrCuNiTi	-10.9
CoCuV	-1.1	MnNiTi	-22.2	CrCuFeTi	-2.3	CoCrCuNiV	-2.9
CoFeMn	-2.4	MnNiV	-11.7	CrCuFeV	5.0	CoCrCuTiV	-6.9

more probability of A-B bonds (clustering of A and B) than random mixing of A and B. Conversely, positive ΔH_{mix} means a repulsive interaction between unlike atoms. For CoCrCu, ΔH_{mix} is calculated to be +6.3 $\frac{\text{kJ}}{\text{mol}}$. If we break CoCrCu into its three constituent binaries as seen in Fig. 3.1, CoCr has the lowest mixing enthalpy of -4.5 kJ/mol out of the possible combinations that can occur.

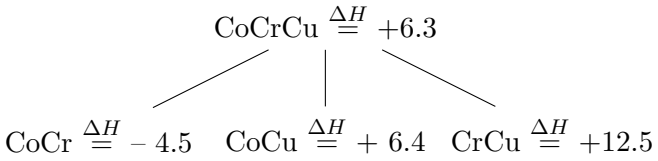

Figure 3.1: Mixing Enthalpies of binary combinations of elements within CoCrCu in $\frac{kJ}{mol}$.

By creating an enthalpy combination tree we can make approximate predictions as to which elements undergo liquid phase separation, and in the case of CoCrCu, the mixing enthalpy of CoCr is significantly lower than that of the rest of the combinations, indicating that the Co-Cr bonds will preferentially cluster. Using this basic algorithm, rough predictions for liquid phase separation of the alloys in this study are made in Table 3.3.

3.5 Results

Out of the 15 alloys in this study, 6 of them solidified dendritically: CoCrCuNi, CoCrCuTi, CoCrCuFeNi, and CoCrCuMnNi, CoCrCuMnTi, and CoCrCuTiV. The typical dendritic solidification of the alloys is indicative of no major liquid phase separations occurring in the melt. The following figures will describe the microstructure of each of the

Table 3.3: List of quaternary and quinary 3-d transition metal MPEAs containing CoCrCu in this study. Liquid phase separation predictions are made via comparing the possible combinations of mixing enthalpies for a given system and are approximations of possible Cu-rich and Cu-lean phases.

Composition	ΔH_{mix} (kJ/mol)	VEC	Seg. Prediction (kJ/mol)
CoCrCu	6.3	8.6	CoCr (-4.5) + Cu
CoCrCuFe	6.3	8.5	CoCrFe (-2.9) + Cu
CoCrCuMn	3.8	8.3	CoCrMn (-3.3) + Cu
CoCrCuNi	2.4	9.0	CoCrNi (-5.0) + Cu
CoCrCuTi	-7.6	7.5	CoCrTi (-13.4) + Cu
CoCrCuV	3.4	7.8	CoCrV (-8.9) + Cu
CoCrCuFeMn	4.2	8.2	CoCrFeMn (-2.4) + Cu
CoCrCuFeNi	3.2	8.8	CoCrFeNi (-3.8) + Cu
CoCrCuFeTi	-5.8	7.6	CoCrFeTi (-14.8) + Cu
CoCrCuFeV	1.1	7.8	CoCrFeV (-7.4) + Cu
CoCrCuMnNi	0.6	8.6	CoCrMnNi (-5.7) + Cu
CoCrCuMnTi	-6.0	7.4	CoCrMnTi (-12.9) + Cu
CoCrCuMnV	0.5	7.6	CoCrMnV (-6.1) + Cu
CoCrCuNiTi	-10.9	8.0	CoCrNiTi (-20.4) + Cu
CoCrCuNiV	-2.9	8.2	CoCrNiV (-11.4) + Cu
CoCrCuTiV	-6.9	7.0	CoCrTiV (-14.5) + Cu

dendritically solidifying alloy system.

The alloys CoCrCuFe, CoCrCuMn, CoCrCuV, CoCrCuFeMn, CoCrCuFeTi, CoCrCuFeV, CoCrCuMnV, CoCrCuNiTi, and CoCrCuNiV, shown in the following figures displayed almost identical LPS to CoCrCu with P-L1 and P-L2 boundary with secondary liquids exsolved into the matrix of the other primary liquid. EDS measurements of the separated regions for the samples reveal that the regions of P-LX and S-LX have the same composition with the exception of CoCrCuMnV, where S-L1 was Cr-rich. The P-L1 regions had the stoichiometric ratio of similar to the nominal equiatomic compositions devoid of Cu, while P-L2 was mostly Cu with trace amounts of the other alloying elements. The electromagnetically levitated and cast alloys CoCrCu, CoCrCuFe, CoCrCuV, and CoCrCuFeV displayed macrostructures similar to samples that were prepared via arcmelting, indicating

that the liquid phase separation that occurs in these alloys is stable and not a result of the arcmelting process. A table of all of the chemical compositions of the phases in these alloys can be found in Table 3.4.

3.5.1 CoCrCu

Microstructures of phase separated and dendrtically solidified MPEAs are shown in following figures as noted. The phase separated liquids are labeled as primary (P-LX) while the secondary liquids are labeled as (S-LX), with X pertaining two either 1 or 2 for Primary liquid 1 or Primary Liquid 2.The Cu-lean phases in these systems are labeled as dendritic D, primary and secondary liquids P-L1 and S-L1, while Cu-rich phases segregated to the interdendritic ID, and primary liquid P-L2. The CoCrCu alloy in Fig. 3.4 displays a boundary of Cu-lean and Cu-rich regions, labeled P-L1 and P-L2 respectively. Two distinct regions were seen in the backscattered electron image of the CoCrCu alloy in Fig. 3.4. The darker region was Cu-lean (P-L1), containing mostly equiatomic Co and Cr while the lighter contrast region, P-L2 contains over 96% Cu. There were globules of each region inside of the other which were elementally equal to the colored region they correspond to. Small dendritic arms are seen extending from the P-L1 composition into the P-L2 region along the boundary as well as near the segregated globules (extending from S-L1) while no dendritic structures of P-L2 are present. The X-ray diffraction patterns (Fig. 3.3) obtained on the flat piece of polished surface for this alloy displayed (2) sets of FCC peaks corresponding to two phase separated regions, as well as σ phase peaks that are most likely resulting from the P-L1

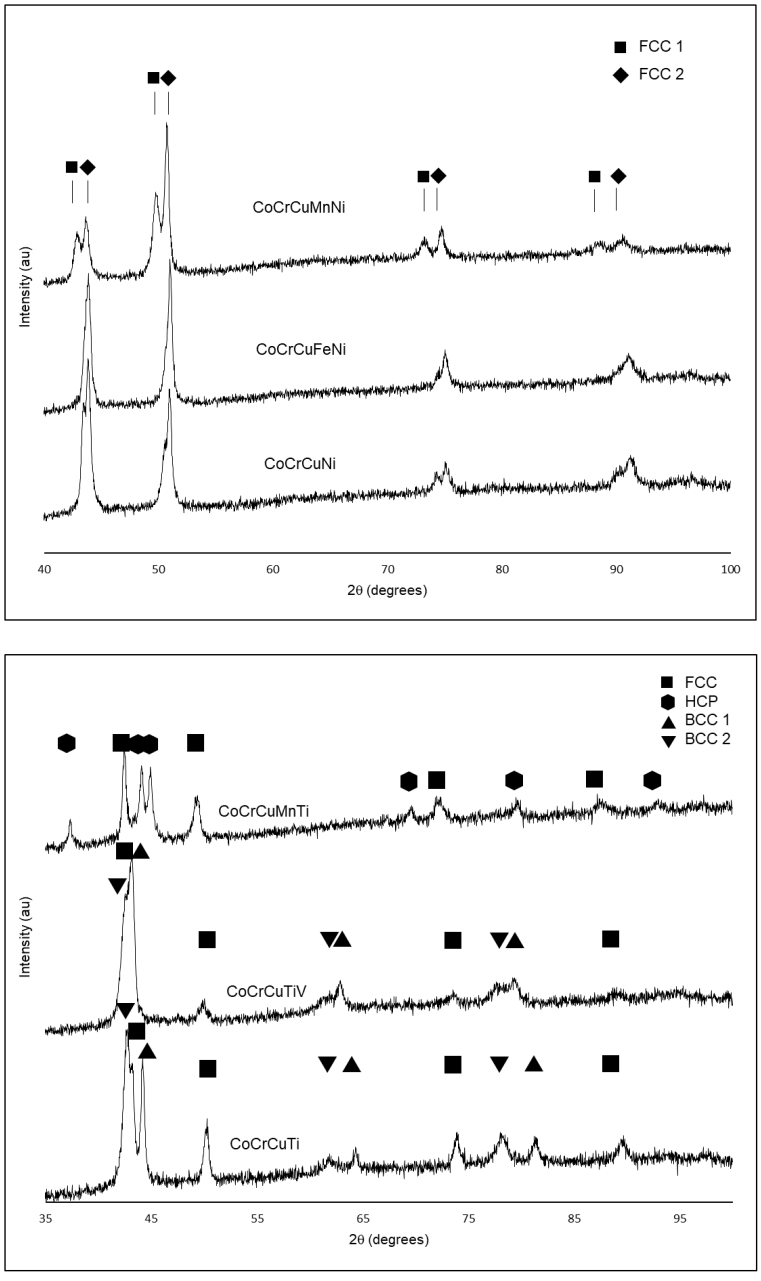

Figure 3.2: X-ray diffraction patterns of CoCrCuNi, CoCrCuFeNi, & CoCrCuMnNi displaying 2 sets of FCC peaks

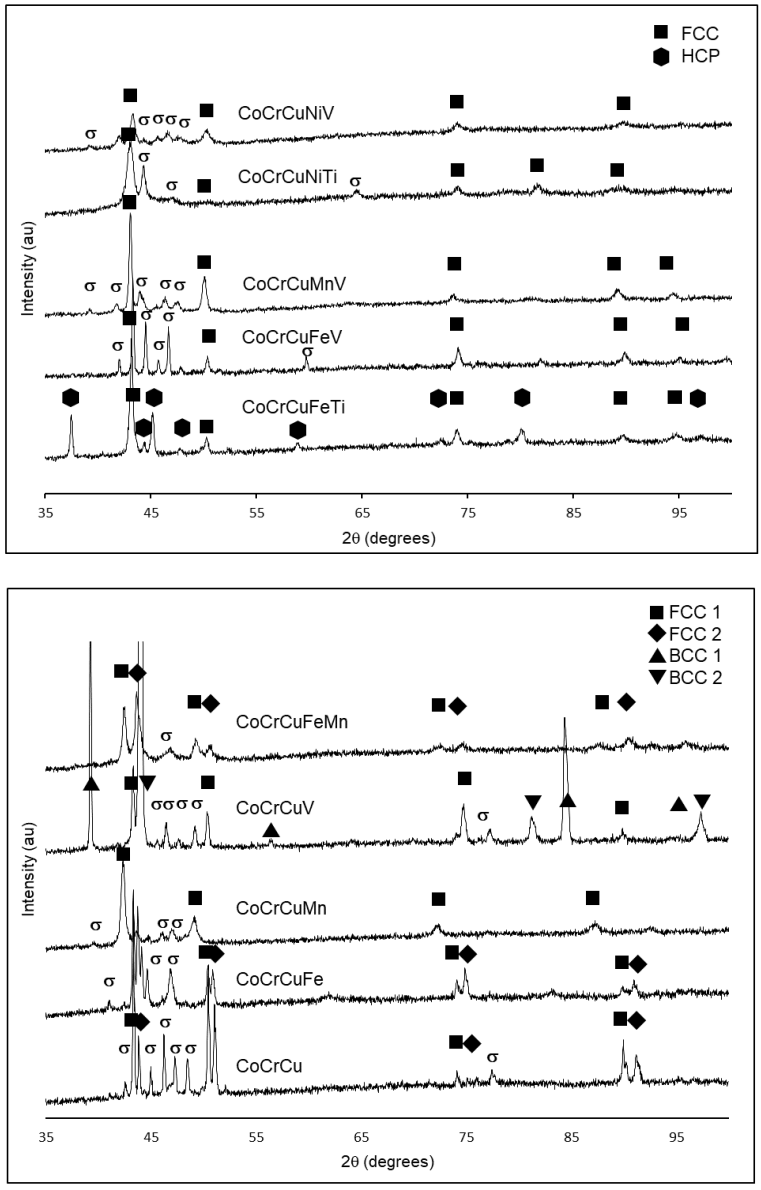

Figure 3.3: X-ray diffraction patterns of liquid phase separated samples displaying FCC, BCC, HCP, and σ phases.

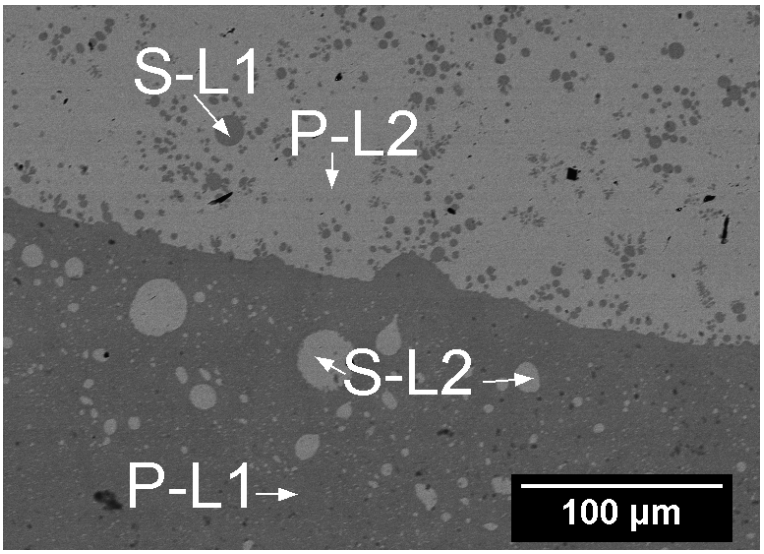

Figure 3.4: Liquid phase separation of electromagnetically levitated ternary CoCrCu. P-L1/L2 and S-L1/S-L2 indicate primary and secondary liquids. P-L1/S-L1 represent Cu-lean phases while P-L2/S-L2 are Cu-rich.

region.

3.5.2 CoCrCuFe

The microstructure of the CoCrCuFe alloy is very similar to that of the CoCrCu alloy. That is, P-L1 and S-L1 are both Cu-lean, with atomic percentages resulting in an approximate stoichiometry of $CoCrCu_{0.42}Fe$ whereas the P-L2/S-L2 Cu-rich regions are $\sim$ 97 at. % Cu.

As presented in Fig. 3.5a for CoCrCuFe, the P-L1 Cu-lean liquid appears to solidfy first, enclosing Cu-rich spheres inside the region while forming dendrites through the boundary into the P-L2 region. These compositions are similar to those of CoCrCu in terms of CoCr separating from Cu, while the Mn present in the system distributes almost evenly with the two liquids. Fig. 3.5b shows the Cu-rich P-L2 region with microstructure of S-L1 liquid that solidified with dendrite arms pushing freely into the liquid P-L2.

Atomic compositions differences are shown more drastically in Fig. 3.6, where the difference in chemical composition is denoted by the colors present in the EDS maps. From the EDS maps in Fig. 3.6 we can confirm the chemical segregation of the Cu from the other elements in the system. Based on the morphology of the microstructure, this is clear indication of liquid phase separation. These results confirm the LPS in this system as previously observed by Munitz et al. [139].

Similarly to the CoCrCu alloy, the XRD pattern for the CoCrCuFe also shows (2) sets of FCC peaks corresponding to P-L1/L2, and the presence of σ phase, likely in the CoCrFe-rich P-L1 phase.

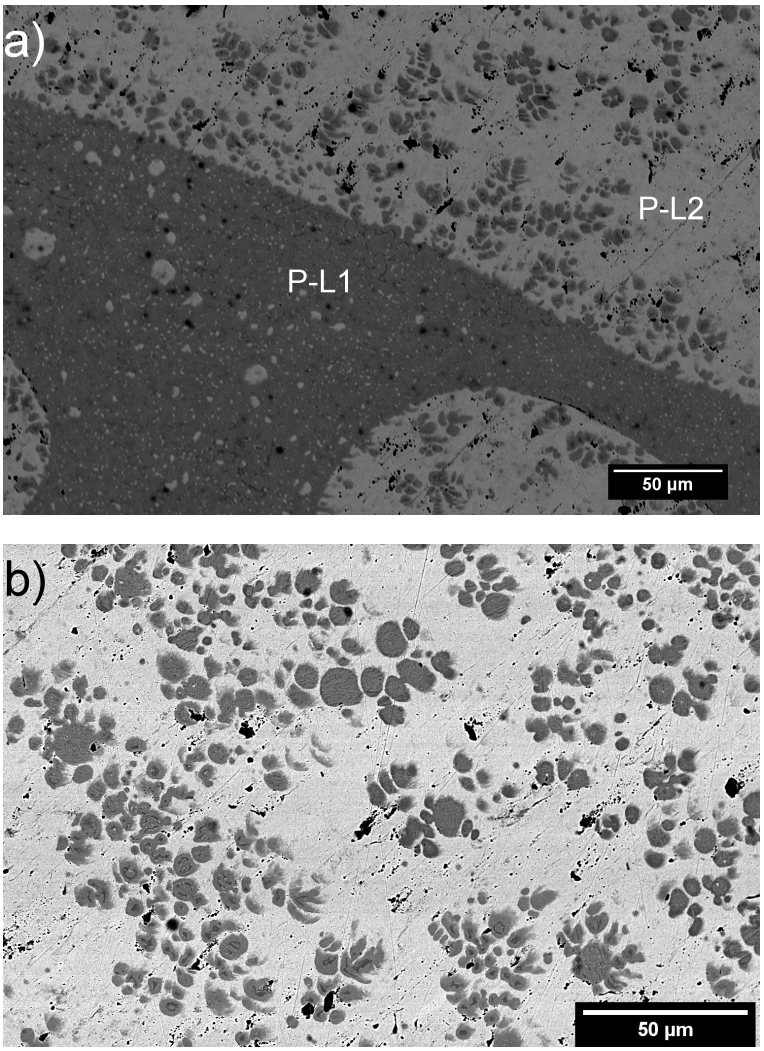

Figure 3.5: Liquid phase separation of CoCrCuFe. P-L1/L2 and S-L1/S-L2 indicate primary and secondary liquids. P-L1/S-L1 represent Cu-lean phases while P-L2/S-L2 are Cu-rich. a) Boundary between P-L1 and P-L2 showing emulsion of the S-L1/L2 liquids, b) P-L2 region showing S-L1 LPS and dendritic arms branching from the spherical phase separations.

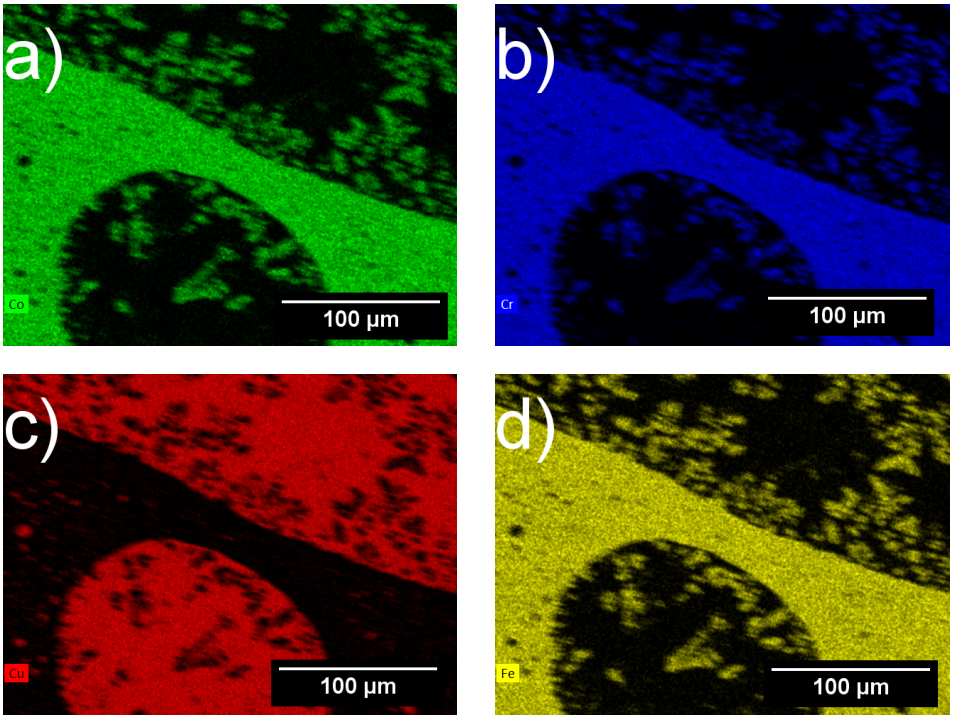

Figure 3.6: Energy dispersive X-ray spectroscopy (EDS) maps of the CoCrCuFe phase separated boundary.

3.5.3 CoCrCuMn

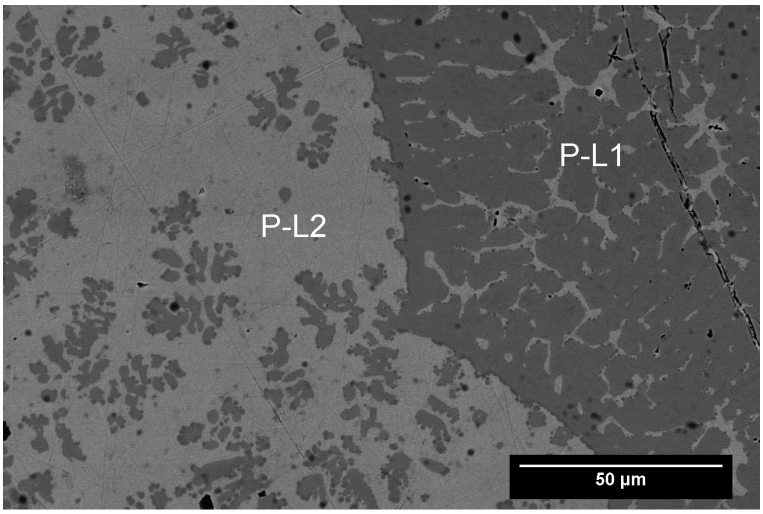

Figure 3.7: Liquid phase separation of CoCrCuMn. P-L1/L2 and S-L1/S-L2 indicate primary and secondary liquids. P-L1/S-L1 represent Cu-lean phases while P-L2/S-L2 are Cu-rich.

A representative portion of the microstructure of the arc-melted CoCrCuMn alloy is presented in Fig. 3.7 where the boundary of P-L1 and P-L2 is highlighted. Unlike the large Cu chemical segregation that occurred in CoCrCu and CoCrCuFe, the P-L1 and P-L2 liquids share Mn concentrations, as opposed to a complete rejection of Cu into a liquid by itself. The Cu-rich liquid P-L2 contains $\sim$ 26 at. % Mn while the Cu-rich liquid contained only $\sim$ 15 at. % Mn. There are no microstructural features that indicate secondary liquid phase separation present in the CoCrCuMn cross-section that was characterized via SEM.

The region indicated by P-L1 appears to have some semblance of dendritic solidification due to the presence primary dendrite arms. The right hand side of the primary dendrite arms contain secondary dendrite arms that appear to break off and become spher-

ical. The pieces of the dendrite arms to the left of the phase separation boundary contains floating dendrites as well, and it is not immediately clear if these broken dendrites are a result of broken secondary dendrite arms or from free floating spherical globules of P-L1. This microstructure is an indication of liquid phase separation during melting.

Due to the relatively small volume fraction of the P-L2 Cu-rich phase, the XRD pattern for CoCrCuMn only shows (1) FCC peak and σ phase. These FCC and σ phase peaks are likely due to the P-L1 phase.

3.5.4 CoCrCuNi

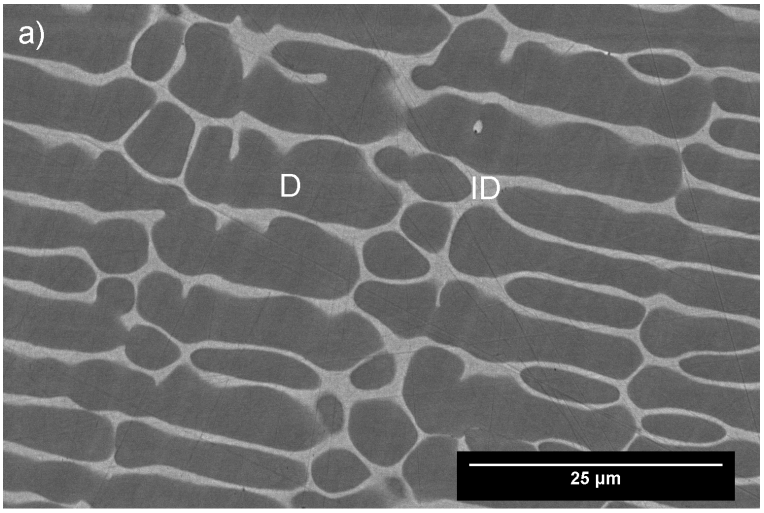

Figure 3.8: As-cast dendritic microstructure of CoCrCuNi.

The CoCrCuNi alloy solidified with a typical dendritic microstructure, with a CoCrNi-rich dendritic phase and a Cu-rich interdendritic phase. No features in the microstructure indicate that there were phase separations in the liquid. The composition of the dendritic phase is similar to that of the composition of the P-L1 phase of the CoCr-

CuFe alloy, except for Fe there is Ni in solution with Co and Cr. The composition of the CoCrNi-rich phase is $\sim CoCrCu_{0.5}Ni$ while the interdendritic liquid is $\sim$ 84 at. % Cu. The equiatomic addition of Ni to the equiatomic CoCrCu remixes the immiscible CoCr-rich and Cu-rich liquids and leads to the formation of a single phase liquid CoCrCuNi, where uniform dendritic solidification could take place.

The XRD pattern for this alloy shows (2) sets of FCC peaks, corresponding to the dendritic and interdendritic phase.

3.5.5 CoCrCuTi

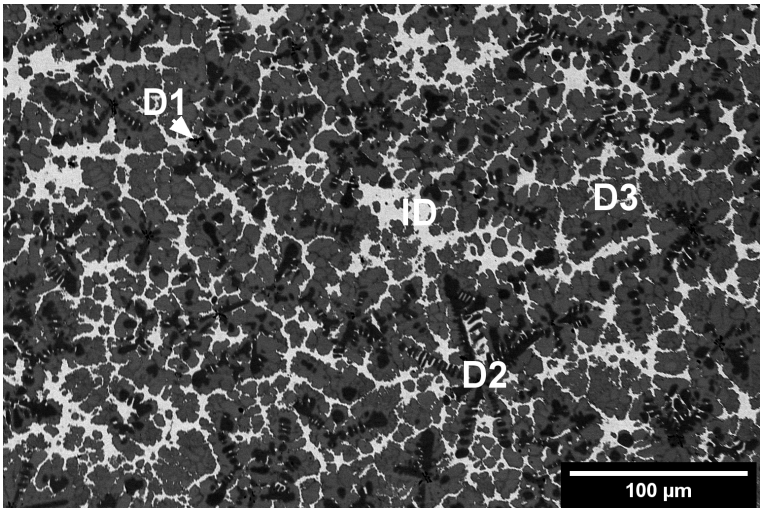

Figure 3.9: As-cast dendritic microstructure of CoCrCuTi.

Like the CoCrCuNi alloy, the addition of Ti to equiatomic CoCrCu to form equiatomic CoCrCuTi leads to a dendritic microstructure, which is usually an indication of the alloy solidifying from a single phase liquid as there are no spherical globules or emulsion like microstructures. It appears that the very small darkest shaded dendrites (D1) in Fig.

3.9 solidified first from the overall melt, followed peritectically by the large dark gray dendrites (D2) that surround the tiny black phase. A medium-gray phase (D3) also appears to peritectically surround the large dark gray D2 phase, followed by the Cu-rich interdendritic phase labeled ID. The chemical composition of each phase is presented in Table 3.4, in contrast to the previous alloys, the brightest phase in the backscattered electon image is due to the higher Z number of Cu, which was segregated to the interdendritic liquid prior to overall solidification.

The XRD pattern for the CoCrCuTi contained (2) BCC peaks and (1) FCC peak. The FCC peak is most likely the ID phase which is $\sim$ 93 at. % Cu, while the D2 and D3 phases have a large enough volume fraction within the alloy to be attributable to the remaining BCC peaks. The small black Ti-rich D1 phase is too small for the X-ray diffraction pattern to show any peaks.

3.5.6 CoCrCuV

The CoCrCuV system in Fig. 3.10 displays slightly different solidification microstructures compared to that of CoCrCu, CoCrCuFe, and CoCrCuMn while still containing primary liquids P-L1 and P-L2, but also containing a Cr/V-rich dendritic structure labeled D within P-L1. The dendritic structures were seen mostly between the boundaries of P-L1 and P-L2, indicating that D solidified before P-L1. Comparing the microstructures to those obtained via arc-melting indicate a stable liquid phase separation occuring, indicating the presence of a stable miscibility gap for equiatomic CoCrCuV. EDS maps for the CoCrCuV alloy are presented in Fig. 3.11 where the Cu segregation can be seen by the

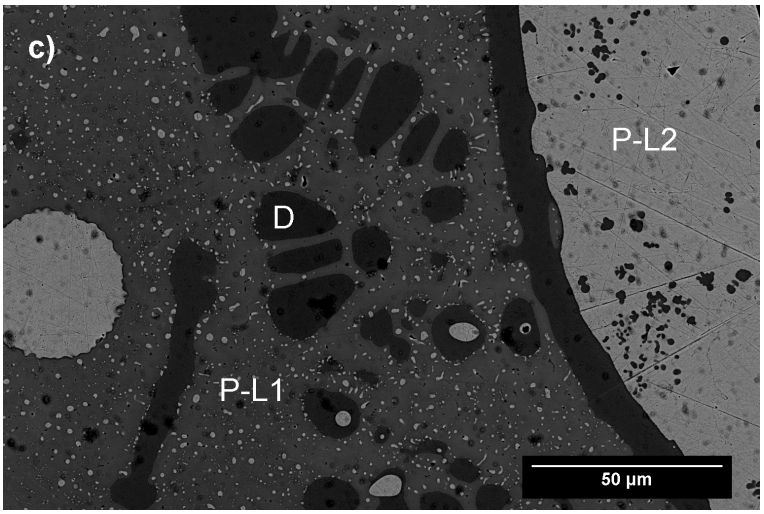

Figure 3.10: Liquid phase separation of electromagnetically levitated ternary CoCrCuV. P-L1/L2 and S-L1/S-L2 indicate primary and secondary liquids. P-L1/S-L1 represent Cu-lean phases while P-L2/S-L2 are Cu-rich. A floating dendritic phase D is labeled.

color red, while the Cr/V-rich phase D can be seen for the blue Cr and pink V maps. The difference in brightness for the Co map for the D phase indicates that this phase is depleted in Co when compared to the P-L1 phase.

The XRD patterns for the CoCrCuV phase show (2) sets of BCC peaks, (1) set of FCC peaks, and σ phase. The Cu-rich P-L2 phase is attributable to the FCC peaks, while the remaining phases are likely the BCC phases whereas the σ phase is likely part of the P-L1 region.

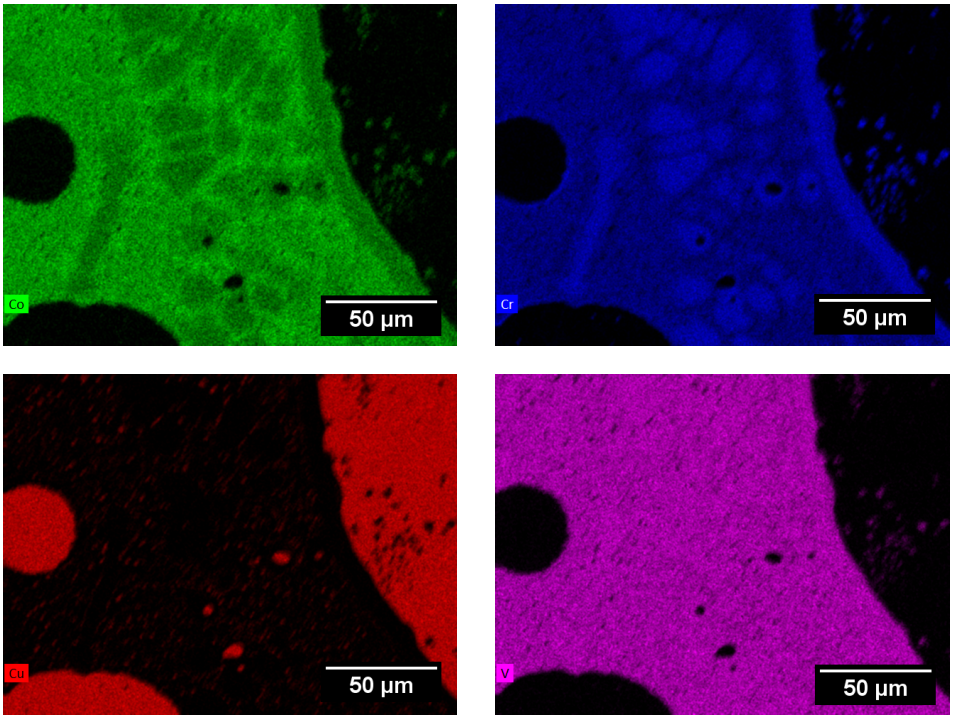

Figure 3.11: EDS maps of the CoCrCuV alloy depicted in Fig. 3.10.

3.5.7 CoCrCuFeMn

Equiatomic additions of Fe and Mn to CoCrCu lead to the CoCrCuFeMn shown in Fig. 3.12. The alloy exhibited LPS emulsion-like structures very similarly to the CoCrCu, CoCrCuFe, CoCrCuMn, and CoCrCuV systems. The melt separated into Cu-lean (P-L1) and Cu-rich (P-L2) liquids, having similar LPS to CoCrCu. Like CoCrCuMn, the Cu-rich region P-L2 also contained about 25 at. % Mn.

The XRD pattern for the CoCrCuFeMn alloy displays (2) sets of FCC peaks (P-L1/P-L2) and the presence of σ phase.

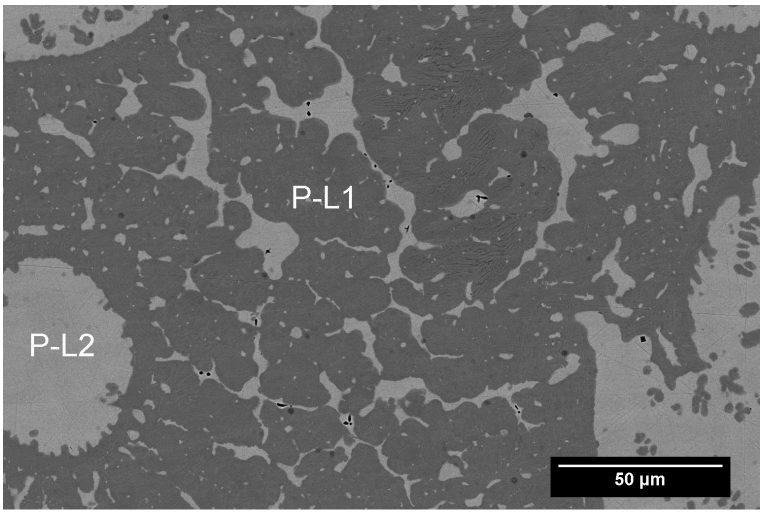

Figure 3.12: Emulsion-like microstructure showing LPS in CoCrCuFeMn between the P-L1 and P-L2 phases.

3.5.8 CoCrCuFeNi

Like the CoCrCuNi alloy, equiatomic additions of Fe also lead to typical dendritic microstructure, as shown in Fig. 3.13. The dendritic phase labeled D is CoCrFeNi-rich, wheres the ID phase is $\sim$ 84 at. % Cu. This microstructure indicates that the melt was a single phase liquid, and confirms the observations for this alloy from Ref. [139]. The XRD pattern for this alloy is presented in Fig. 3.2, and is also similar to that of CoCrCuNi. There are (2) sets of FCC peaks present, corresponding the the dendritic and interdendritic phases.

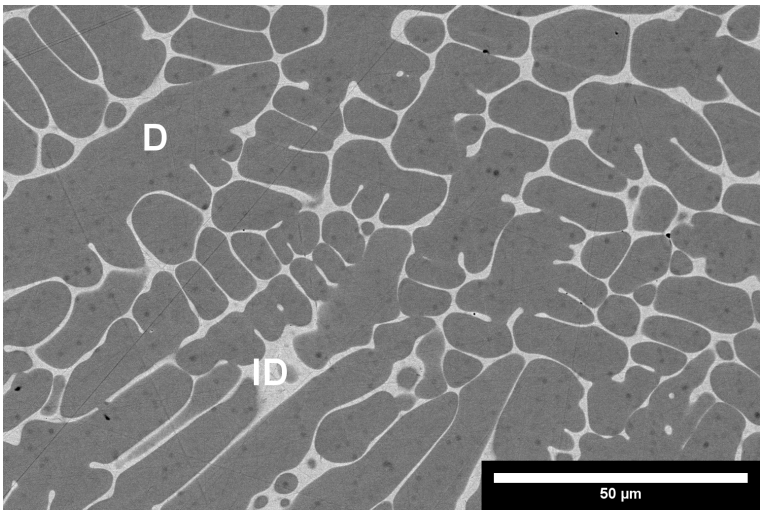

Figure 3.13: Backscattered electron image of the CoCrCuFeNi alloy displaying typical dendritic microstructure. Note that the small black specs are pores from polishing.

3.5.9 CoCrCuFeTi

The CoCrCuFeTi alloy is depicted in Fig. 3.14. The alloy underwent dendritic solidification towards the bottom of the chill surface (Fig. 3.14a) as well as large globule like liquid phase separation that occurred near the top of the sample (Fig. 3.14b). A small dendritic phase labeled D is present in higher resolution in Fig. 3.14c, and is composed of $\geq$ 50 at. % Ti. The majority dendritic/P-L1 phase is mostly CoCrFeTi whereas the ID/P-L2 regions are $\sim$ 95 at. % Cu.

The XRD pattern for the CoCrCuFeTi (Fig. 3.3) shows both the presence of a hexagonal crystal structure as well as FCC peaks. The FCC peaks are due to the Cu-rich phase separated regions, while the hexagonal peaks are due to the P-L1 phase. This can also be determined via the morphology of the P-L1 dendrites, such that the secondary dendrite arms are not extending perpendicularly to the primary dendrite arms (which is

the solidification morphology in cubic systems). Rather at an approximate 35angle from the primary dendrite arm which is typical of hexagonal dendrite arm spacing.

3.5.10 CoCrCuFeV

The levitated and cast CoCrCuFeV shown in Fig. 3.15, a very clear liquid phase separation of Cu-lean and Cu-rich liquids with secondary liquid separation as spherical globules in the other's matrix was observed. Primary and secondary liquids had the same atomic concentrations, where the Cu-rich P-L2/S-L2 regions contained $\sim$ 97 at. % Cu. The observations are also in agreement with the arc-melted samples of CoCrCuFeV from Ref. [139]. EDS Maps displaying the presence of each of the alloying element in the P-LX/S-LX phases are presented in Fig. 3.16.

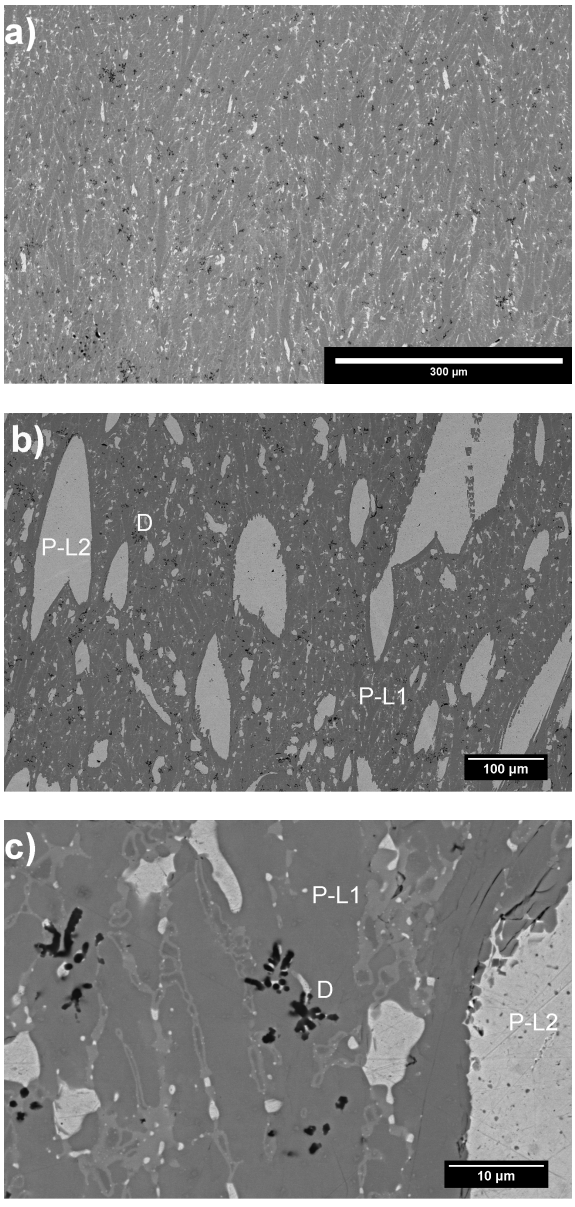

Figure 3.14: Backscattered electron images of the CoCrCuFeTi alloy. a) Bottom portion of the sample nearest the chill zone of the arc-melter, b) top layer of the sample exhibiting LPS, and c) higher resolution image of the small Ti-rich dendritic phase.

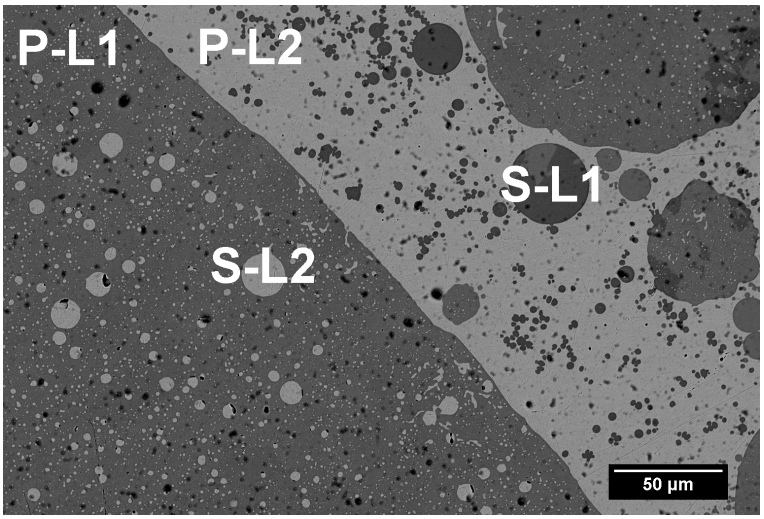

Figure 3.15: Liquid phase separation of electromagnetically levitated ternary CoCrCuFeV. P-L1/L2 and S-L1/S-L2 indicate primary and secondary liquids. P-L1/S-L1 represent Cu-lean phases while P-L2/S-L2 are Cu-rich.

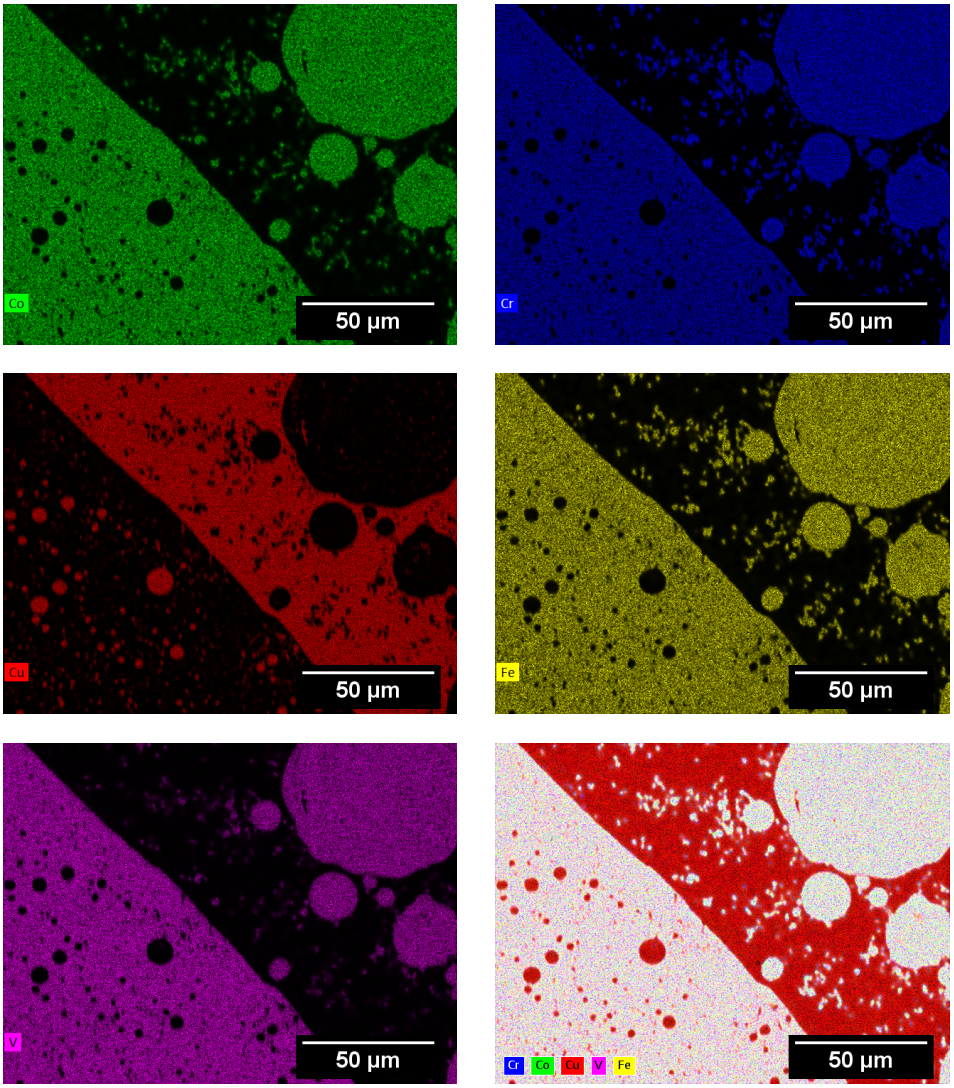

Figure 3.16: Energy dispersive X-ray spectroscopy (EDS) maps of the CoCrCuFeV system.

3.5.11 CoCrCuMnNi

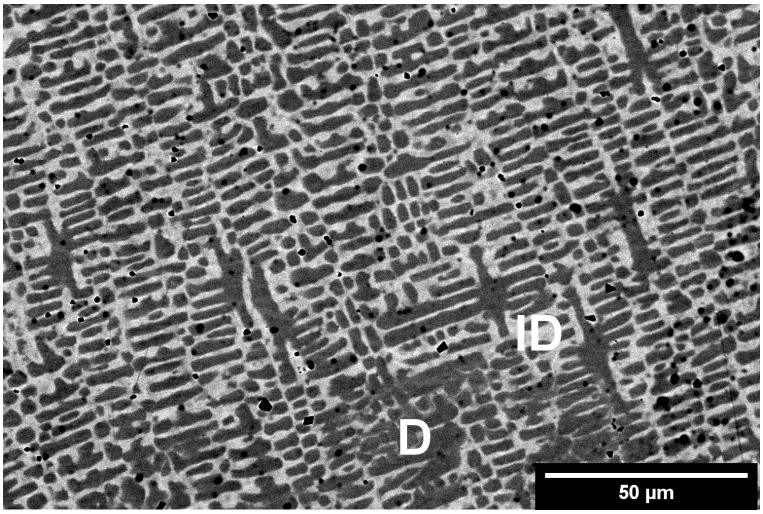

Figure 3.17: As-cast dendritic microstructure of arc-melted CoCrCuMnNi. Note that the black spots are pores generated from polishing.

Similarly to the CoCrCuNi and CoCrCuFeNi alloys, the CoCrCuMnNi alloy shown in Fig. 3.17 displays typical dendritic solidification indicative of the melt being a single phase liquid. In Table 3.4 we can see that Cu and Mn are present in large quantities in both phases, however much more present in the ID than in the D phase. Just as the CoCrCuNi and CoCrCuFeNi alloys, CoCrCuMnNi also solidified with both phases being FCC, as shown from the two sets of FCC peaks in Fig. 3.2.

3.5.12 CoCrCuMnTi

The equiatomic CoCrCuMnTi alloy solidified with a typical dendritic microstructure similarly to the other dendritically solidifying MPEAs CoCrCuNi, CoCrCuFeNi, and

CoCrCuMnNi and is presented in Fig. 3.18. However, the dendritic morphology in this alloy is non-cubic, which was verified to be a HCP phase from XRD, presented in Fig. 3.2. There are small floating dark contrast dendrites labeled D1 in Fig. 3.18, and consist of $\geq$ 50 at. % Ti. The majority dendritic phase has approximate stoichiometry of $CoCrCu_{0.1}Mn_{0.3}Ti$, whereas the single phase ID contains $\sim$ 77 at. % Cu. The small dark dendrites labeled D3 were too small for accurate compositional analysis within the EDS detector, therefore $\geq$ at. % Ti is reported from the measured elements in this phase. Aside from the HCP peaks present in the XRD pattern of Fig. 3.2, there is also a set of FCC peaks which is attributable to the Cu-rich ID.

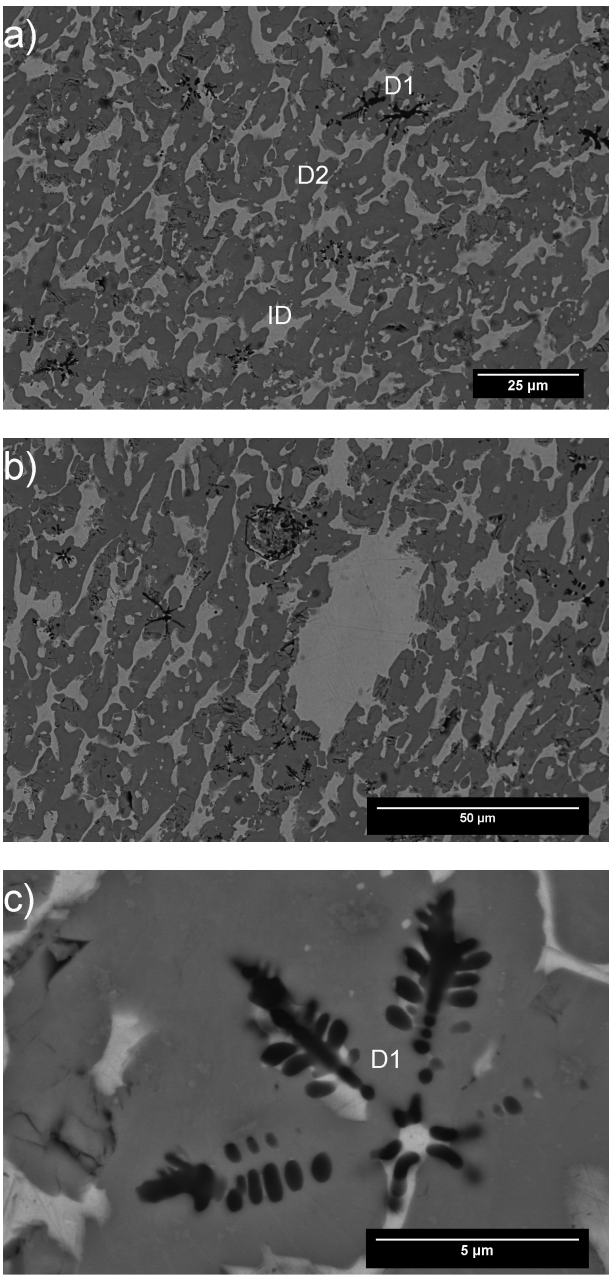

Figure 3.18: As-cast dendritic microstructure of arc-melted CoCrCuMnTi. a) Dendritic microstructure with labeled small Ti-rich dendrites (D1), followed by the majority hexagonal dendrite (D2) and interdendritic region ID b) Large irregular ID region, c) Higher resolution of the small Ti-rich (D1) dendrites.

3.5.13 CoCrCuMnV

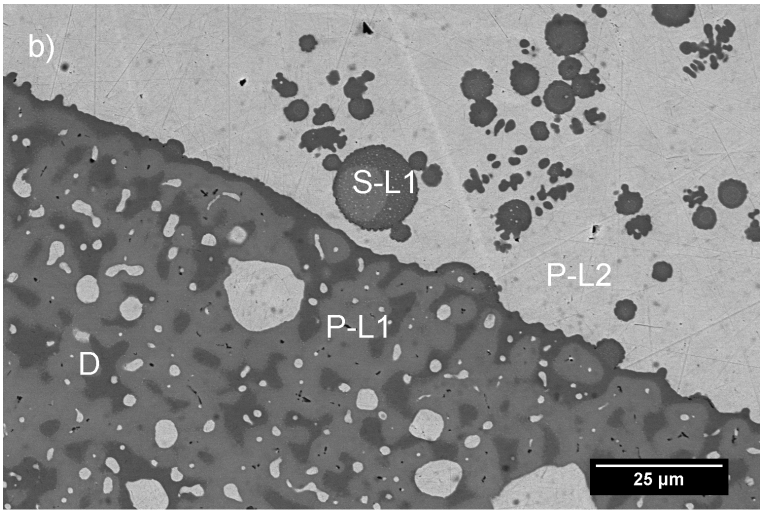

Figure 3.19: Backscattered electron images of the liquid phase separation in CoCrCuMnV.

Figure 3.19 displays the equiatomic CoCrCuMnV alloy solidified with the same liquid phase separation microstructures to that of CoCrCu, CoCrCuFe, and CoCrCuFeV where a very distinct boundary can be seen between the two liquid phase separated regions P-L1 and P-L2, with secondary LPS regions S-L1 and S-L2 trapped in the other's matrix. This is the only MPEA combination exhibiting LPS where the composition of S-L1 varied significantly from P-L1, with S-L1 containing more Cr and less V, which is tabulated in Table 3.4.

The XRD pattern for the CoCrCuMnV alloy is present in Fig. 3.3, where FCC and σ phase are present.

3.5.14 CoCrCuNiTi

The CoCrCuNiTi alloy combination displayed both liquid phase separation and dendritic solidification microstructures. There are a total of (5) solidification microstructures noticeable from the micrograph depicted in Fig. 3.20a, and are labeled D1, D2, ID1, ID2, and Cu-LPS in Fig. 3.20b. Similarly to the the other Ti-containing alloys CoCrCuFeTi and CoCrCuMnTi, small dark floating dendrites with $\geq$ at. % Ti are present in the microstructure, which pertain to the D1 label. Then the next phase that appears to solidify from the melt is D2, with $\sim$ 84 at. % Cr, then an interdendritic phase ID1 which is a depleted in Cr and rich in Co, Cu, Ni, and Ti, followed what appears to be a peritectic transformation of ID1 to the remaining interdendritic liquid ID2 which is similar in composition to ID1, and is tabulated in Table 3.4. Amongst these phases, there are also spherical Cu-rich globules present in Fig. 3.20, and are labeled Cu-LPS and contain $\sim$ 90 at. % Cu.

The XRD pattern present in Fig. 3.3 only displays the presence of FCC and σ phase, and it is not clear if there are missing peaks from the many phases in this alloy due to small volume fraction or peak overlap.

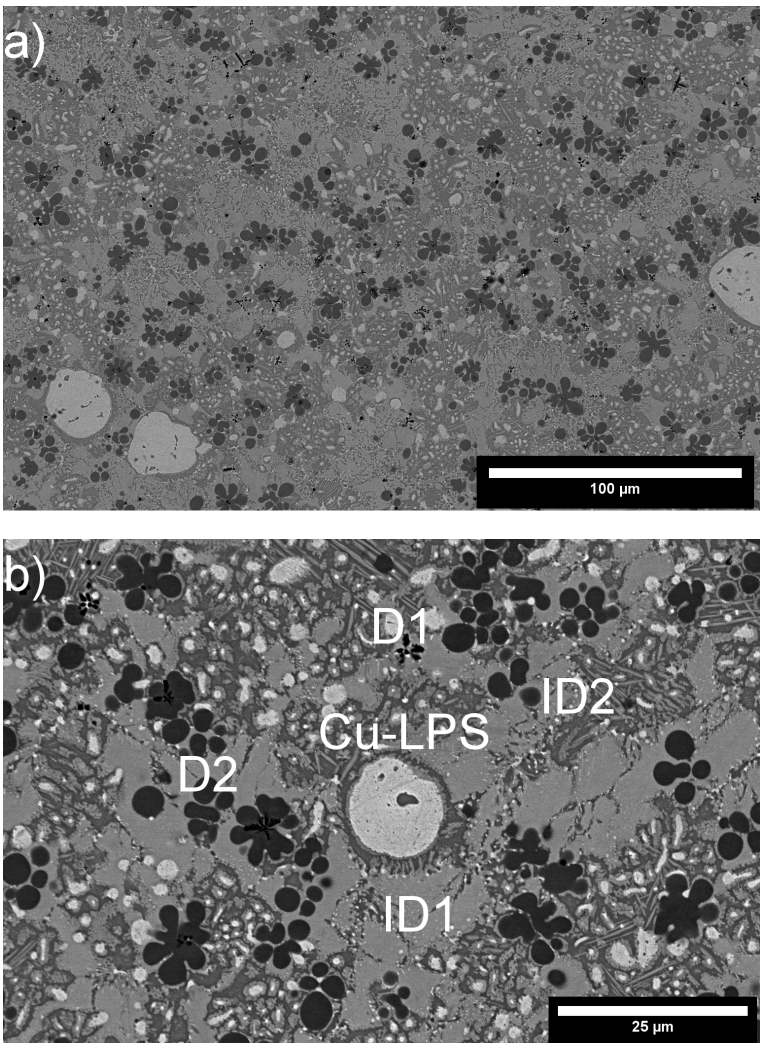

Figure 3.20: Backscattered electron images of the microstructure of CoCrCuNiTi a) macroscopic view b) higher resolution with all 5 phases with corresponding labels.

3.5.15 CoCrCuNiV

The CoCrCuNiV alloy in Fig. 3.21 similarly separated into two distinct liquids P-L1 and P-L2, which solidified into Cu-lean and Cu-rich phases, respectively. Unlike the other alloys exhibiting LPS, the boundaries between P-L1 and P-L2 are jagged. The S-L2 globule inside of P-L1 n Fig. 3.21a does not have a spherical shape and is much more jagged compared to the S-L1 globules in P-L2 in Fig. 3.21b which are much more rounded. The jagged edges from the P-L1 phase that push into the the P-L2 phase may be due to the dendritic solidification of the P-L1 phase. The XRD pattern for this alloy displays a set of FCC peaks and σ phase.

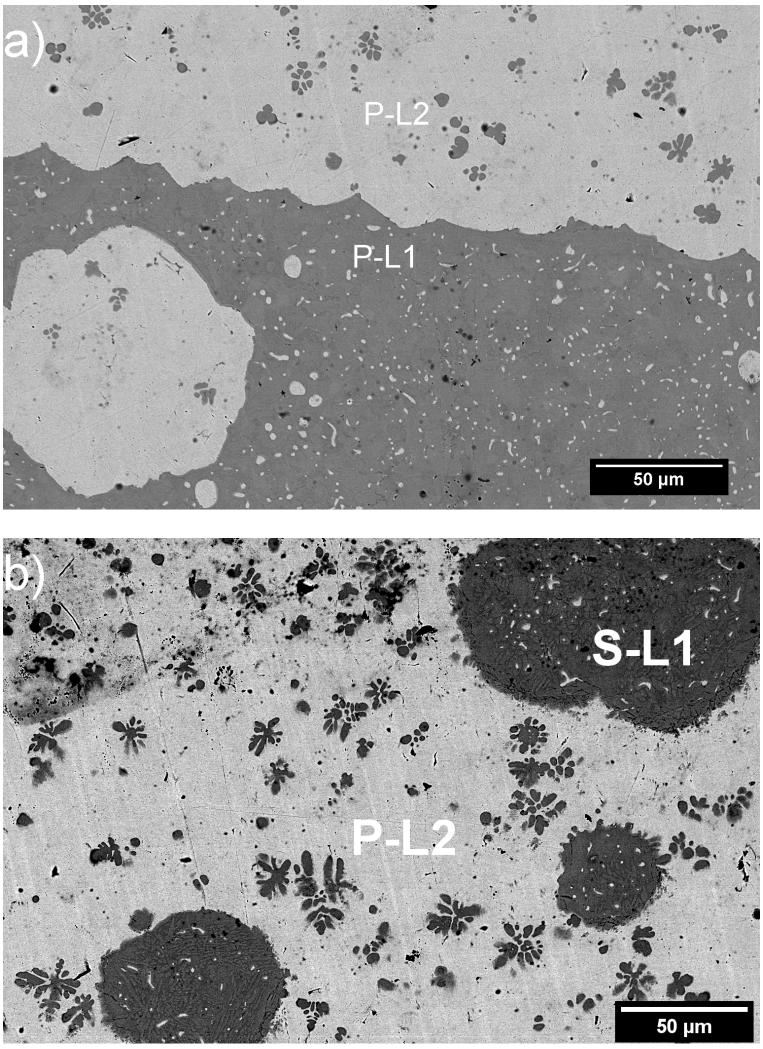

Figure 3.21: Backscattered electron images of the CoCrCuNiV alloy. P-L1/L2 and S-L1/S-L2 indicate primary and secondary liquids. P-L1/S-L1 represent Cu-lean phases while P-L2/S-L2 are Cu-rich.

3.5.16 CoCrCuTiV

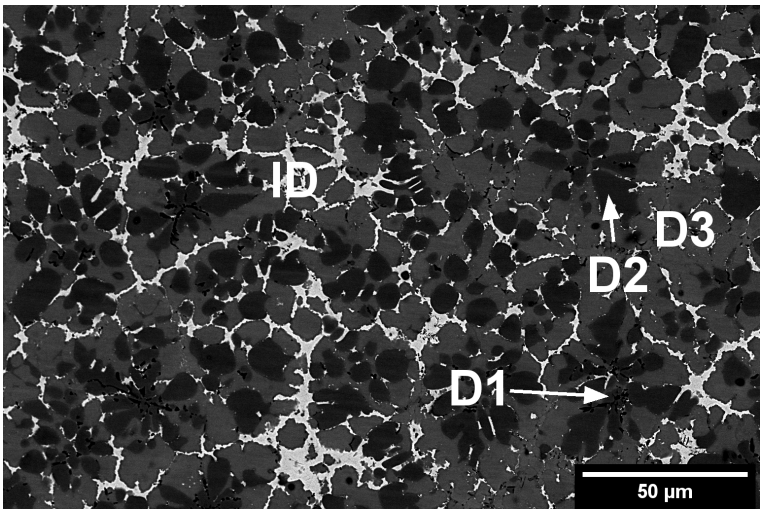

Figure 3.22: Dendritic microstructure of the as-cast CoCrCuTiV alloy.

The microstructure and phase of the CoCrCuTiV alloy is similar to that of the quaternary CoCrCuTi alloy and is presented in Fig. 3.22. The first phase to solidify is the small dark phase D1 that is similar to the D1 phase present in the other Ti-containing alloys in this study (CoCrCuTi – Fig. 3.9, CoCrCuFeTi – Fig. 3.14, CoCrCuMnTi – Fig. 3.18, and CoCrCuNiTi – Fig. 3.20), followed by the D2 and D3 phase labeled in the micrograph of Fig. 3.22. It appears that D2 forms peritectically from D1, and D3 forms peritectically from D2 as indicated by the morphology of these phases. The last phase to solidify is a Cu-rich interdendritic liquid labeled ID. The XRD pattern for this alloy is also very similar to that of CoCrCuTi, that is, it displays nearly identical peaks of two BCC and FCC. The FCC phase is likely the $\sim$ 87 at. % Cu ID phase, therefore leaving the two large volume fraction Cu-lean phases to be attributable to the remaining BCC peaks. The small Ti-rich phase did not have enough volume fraction to produce XRD peaks in the diffraction pattern and

may be overshadowed by the larger FCC and BCC peaks if present above the background noise of the measurement.

3.6 Discussion

3.6.1 Microstructures and Observations

The structures observed in this investigation display both dendritic solidification as well as liquid phase separation which leads to the solidification of compositionally different regions inside the samples. These structures and their compositions are summarized in Table 3.4. All of the separated regions in the alloys studied consisted of Cu-lean and Cu-rich phases. Table 3.4 summarizes the phases that formed for the solidification of the alloys in this study. The alloys that solidified dendritically include CoCrCuNi, CoCrCuFeNi, CoCrCuMnNi, CoCrCuTi, CoCrCuMnTi, and CoCrCuTiV. The remaining 10 alloy combinations CoCrCu, CoCrCuFe, CoCrCuMn, CoCrCuV, CoCrCuFeMn, CoCrCuFeTi, CoCrCuFeV, CoCrCuMnV, CoCrCuNiV, CoCrCuNiTi exhibit liquid phase separation, indicative of the presence of a stable miscibility gap.

Thermodynamic calculations of mixing enthalpy ΔH_{mix} were carried out on the experimental phases obtained in this investigation to try and elucidate the effect of chemically similar alloying elements on single phase formation and liquid phase separation. From the alloys in this study, those that underwent liquid phase separation split into Cu-rich and Cu-lean phases. The calculated mixing enthalpy for each of the Cu-lean phases was lower than the calculated mixing enthalpy for the nominal equiatomic concentrations. All

Table 3.4: EDS data and semi-quantitative analysis of elemental composition of MPEAs in this study. D = dendrite, ID = interdendrite, P-LX = Primary liquids, S-LX = Secondary liquids. Rough values for ΔH_{mix} (kJ/mol) are recalculated from the experimental atomic concentrations of the resultant microstructures and are compared to ΔH_{nom} which are the calculated mixing enthalpies for the nominal equiatomic concentrations.

MPEA	ΔH_{nom}	Region	Co	Cr	Cu	Fe	Mn	Ni	Ti	V	ΔH_{mix}
CoCrCu	6.3	PL1	48.8	45.3	5.9	–	–	–	–	–	-1.9
		PL2	2.0	1.2	96.8	–	–	–	–	–	–
CoCrCuFe	6.3	PL1	30.5	28.3	12.4	28.8	–	–	–	–	2.3
		PL2	1.1	0.7	96.9	1.3	–	–	–	–	–
CoCrCuMn	3.8	PL1	37.5	42.2	4.7	–	14.6	–	–	–	-1.9
		PL2	3.6	1.0	68.9	–	26.5	–	–	–	3.6
CoCrCuNi	2.4	D	31.4	30.0	14.3	–	–	24.3	–	–	0.1
		ID	4.1	4.0	84.1	–	–	7.9	–	–	3.4
CoCrCuTi	-7.6	D1	–	–	–	–	–	–	≥ 50	–	–
		D2	25.4	45.5	4.7	–	–	–	24.4	–	-11.5
		D3	29.8	34.4	6.1	–	–	–	29.7	–	-14.1
		ID	2.8	1.0	93.4	–	–	–	2.8	–	–
CoCrCuV	3.4	D	25.9	40	3.6	–	–	–	–	30.5	-6.1
		PL1	34.6	27.8	7.8	–	–	–	–	29.8	-5.9
		PL2	0.5	1.3	98.2	–	–	–	–	0	–
CoCrCuFeMn	4.2	PL1	25.9	27.5	7.1	26.7	12.7	–	–	–	0.3
		PL2	1.8	1.0	72.7	0.9	23.6	–	–	–	3.6
CoCrCuFeNi	3.2	D	20.8	21.1	18.5	19.7	–	19.3	–	–	2.8
		ID	3.6	2.6	84.6	3.3	–	5.9	–	–	4.4
CoCrCuFeTi	-5.8	D	–	–	–	–	–	–	≥ 50	–	–
		PL1	23.2	21.6	3.4	24.0	–	–	27.9	–	-14.3
		PL2	0.6	1.4	95.1	0.6	–	–	2.3	–	–
CoCrCuFeV	1.1	PL1	23.8	21.3	9.7	–	22.7	–	–	22.5	-3.0
		PL2	0.5	1.1	97.6	0.7	–	–	–	0.1	–
CoCrCuMnNi	0.6	D	30.9	33.8	6.9	–	9.3	19.2	–	–	-2.6
		ID	8.7	6.6	42.6	–	21.6	20.5	–	–	2.8
CoCrCuMnTi	-6.0	D1	–	–	–	–	–	–	≥ 50	–	–
		D2	30.1	27.6	3.8	–	9.3	–	29.3	–	-14.7
		ID	2.6	1.7	77.6	–	16.0	–	2.1	–	1.9
CoCrCuMnV	0.5	PL1	32.7	28.3	4.7	–	1.4	–	–	32.9	-7.1
		SL1	27.8	37.7	8.3	–	1.8	–	–	24.4	-3.9
		PL2	1.0	1.0	90.3	–	7.6	–	–	0.1	1.9
		D	26.9	35.7	4.5	–	1.3	–	–	31.7	-6.0
CoCrCuNiTi	-10.9	D1	–	–	–	–	–	–	≥ 50	–	–
		D2	8.6	83.6	2.1	–	–	2.5	3.1	–	-2.1
		ID1	21.5	7.7	24.1	–	–	26.1	20.6	–	-12.4
		ID2	25.5	9.0	14.0	–	–	23.9	27.6	–	-18.2
		Cu-LPS	2.0	1.9	90.4	–	–	3.8	1.9	–	1.0
CoCrCuNiV	-2.9	PL1	22.5	25.0	8.4	–	–	18.9	–	25.2	-7.2
		PL2	1.6	2.0	88.2	–	–	7.9	–	0.2	2.2
CoCrCuTiV	-6.9	D1	–	–	–	–	–	–	≥ 50	–	–
		D2	9.8	39.4	3.8	–	–	–	5.4	41.5	-4.6
		D3	28.3	4.1	27.8	–	–	–	29.9	10.0	-11.8
		ID	3.6	0.7	86.9	–	–	–	7.8	1.0	-1.5

Table 3.5: Summary of phases of the alloys studied.

MPEA	Crystal Structure	VEC
CoCrCu	2FCC + σ	8.6
CoCrCuFe	2FCC + σ	8.5
CoCrCuMn	FCC + σ	8.3
CoCrCuNi	2FCC	9.0
CoCrCuTi	2BCC + FCC	7.5
CoCrCuV	2BCC+ FCC + σ	7.8
CoCrCuFeMn	2FCC + σ	8.2
CoCrCuFeNi	2FCC	8.8
CoCrCuFeTi	FCC + HCP	7.6
CoCrCuFeV	FCC + σ	7.8
CoCrCuMnNi	2FCC	8.6
CoCrCuMnTi	FCC + HCP	7.4
CoCrCuMnV	FCC + σ	7.6
CoCrCuNiTi	FCC + σ	8.0
CoCrCuNiV	FCC + σ	8.2
CoCrCuTiV	2BCC + FCC	7.0

of the alloys rejected Cu to an extent, which demonstrates an approximate predictive capability when comparing the possible mixing enthalpies between the combinations of the alloying elements for estimating phase separation in Cu-containing MPEAs. As seen from the dendritic structures of CoCrCuNi, CoCrCuTi, CoCrCuFeNi, and CoCrCuMnNi, CoCrCuMnTi, and CoCrCuTiV, this method requires further investigation as it does not make a distinction between globule-like separation and segregation in the form of interdendrites.

3.6.2 MPEAs Exhbiting Dendritic Solidification

Alloys displaying dendritic solidifcation:

- CoCrCuNi
- CoCrCuTi

- CoCrCuFeNi
- CoCrCuMnNi
- CoCrCuMnTi
- CoCrCuTiV

It appears that CoCrCuNi serves as a type of foundation group, or base system for Fe and Mn while CoCrCuTi serves as a base system for for CoCrCuMnTi and CoCrCuTiV. Calculations of the CoCrNi ternary phase diagram show that in equiatomic concentrations that there is ternary solid solubility for CoCrNi [98]. With the addition of Cu, dendrites are observed in Fig. 3.8, leaving the excess Cu to the interdendritic regions. All of the dendritic phases of the six alloys that did not undergo LPS had lower calculated mixing enthalpies than the nominal compositions.

Calculated VEC using Eq. 3.2 for all the dendritically solidyfing FCC alloys are ≥ 8. The diffraction patterns of each dendritically solidifying sample display FCC crystal structures, which is in agreement with Ref. [163] for alloy combinations with VECs ≥ 8. The 2 FCC peaks can be identified by the bulk dendrite/interdendrite structures which are uniform throughout the sample. As there are only 2 visible phases from the SEM images, it is our observation that the dendritic and interdendritic regions are both FCC. Caution must be taken when analyzing X-ray diffraction data with MPEAs that contain Cu due to Cu-rich regions producing FCC diffraction peaks which may be overlooked due to peak overlap by a majority FCC phase. While similar microstructures are observed in the CoCrFeNi [146, 147, 275], there exists the possibility that the ternary bases CoCrFe and CoCrNi may also serve as foundation groups for MPEA design due to their low mixing enthalpy.

The MPEAs CoCrCuNi and CoCrCuMnNi were found to exhibit similar solid solution dendritic microstructures to CoCrCuFeNi. Much of the literature in the HEA/MPEA/CCA community refers to these structures as single phase solid solutions however, it must be noted that the interdendritic regions are separate phases that also have FCC structure.

As for the Ti-containing CoCrCuTi, CoCrCuMnTi, and CoCrCuMnTi alloys, the appearance of the HCP phase is quite rare in MPEAs, whereas the BCC phases found in CoCrCuTi and CoCrCuTiV are also worth noting as BCC or HCP phases encapsulated in a Cu-rich FCC matrix may have interesting mechanical properties.

3.6.3 MPEAs Exhibiting Liquid Phase Separation

Alloys displaying liquid phase separation:

- CoCrCu
- CoCrCuFe
- CoCrCuMn
- CoCrCuV
- CoCrCuFeMn
- CoCrCuFeTi
- CoCrCuFeV
- CoCrCuMnV
- CoCrCuNiV
- CoCrCuNiTi

The liquid phase separation of CoCrCu in Fig. 3.4 is agreement with the solidification of CoCrCu in Ref. [86]. Elemental analysis carried out on the exsolved globules had the same atomic composition. The macrostructures of CoCrCuFe and CoCrCuFeV display liquid phase separation which verifies the previous work done on these alloys by Munitz et al. [139]. The presence of near-equiatomic Co, Cr, and Fe within the Cu-lean P-L1 region

of CoCrCuFe in Fig. 3.5 a as a stable liquid is similar to the single liquid phase in the isothermal CoCrFe ternary diagram at 1450 ^{o}C for equiatomic concentrations of Co, Cr, and Fe [90]. The calculated mixing enthalpy of CoCrCuFe is more positive compared to the resultant P-L1 region CoCrCu$_{0.5}$Fe as shown in Table 3.4, indicating that the elements in P-L1 preferentially clustered to each other as opposed to equally mixing with Cu. The Co-Cr-rich region P-L1 of the CoCrCuMn system is primarily Co-Cr, with atomic percentages near the eutectic for the binary Co-Cr system ($T_m \approx 1400\,^{\circ}$C) [58]. This large difference in melting temperature results in the Co-Cr-rich P-L1 region solidifying first, with dendrites being pushed into the Cu-Mn-rich P-L2 region. The Cu-Mn-rich region labeled P-L2 has the approximate composition of Cu-40 at.%Mn, which is near the congruent freezing point of the Cu-Mn system. The Cr-V-rich dendrites present in CoCrCuV within the primarily Co-Cr-V-rich primary liquid P-L1 agrees with the previous experimental determination of phase equilibria in the Co-Cr-V system in which Cr-V-rich phases form in the near-equiatomic molar concentrations of the ternary alloy [106].

The calculated mixing enthalpy of the atomic ratios in P-L1 for CoCrCuFeMn yield a much lower ΔH_{mix} of 0.3 kJ/mol compared to the nominal value of 4.2 kJ/mol indicating that not only is the P-L1 preferentially clustered in the alloy, but also positively correlates with a lower mixing enthalpy compared to its nominal value. The relatively uniform atomic composition of the elements within the P-L1 regions for CoCrCuFeMn and CoCrCuFeV may indicate that a single liquid phases could form from CoCrFeMn$_{0.5}$ and CoCrFeV. The presence of small amounts of Cu in each of the Cu-lean regions may indicate a solubility limit of Cu for Cu-lean phase separated regions. The mixing enthalpy of CoCrCuNiV P-

L1 was calculated to be -7.2 kJ/mol compared to the nominal value of -2.9 kJ/mol for equiatomic CoCrCuNiV indicating the possible presence of a "closed miscibility gap" in these alloys [276].

Valence electron concentration calculations for comparing the nominal mixtures to the phase separated regions become difficult when trying to distinguish which phases are responsible for the observed peaks in the X-ray diffraction patterns. The above alloys separated into two primary liquids, Cu-lean and Cu-rich (P-L1 and P-L2). Each of the Cu-lean separated liquids had a calculated lower ΔH_{mix} than the calculations for their equiatomic concentrations. This indicates that the approximations for ΔH_{mix} using Miedema's scheme for sub-regular solutions can at least demonstrate a correlation between a qualitative probability for single phase liquids and liquid phase separation when comparing the mixing enthalpies for the possible combinations that can arise from multi-principal element alloys in the liquid state. Due to the stable liquid phase separation of CoCrCu into Co-Cr-Cu_{lean} and Co-Cr-Cu_{rich} liquids, it is our hypothesis that MPEAs containing CoCrCu form stable liquid phases based on the miscibility between the other alloying elements and their interactions with liquid species of Cu_{lean} and Cu_{rich}. This may have to do with the system being more energetically stable when $\Delta H_{\text{mix}} < 0$, as elemental combinations with $\Delta H_{\text{mix}} > 0$ could require much higher superheated temperatures for the liquids to mix and become a single-phase liquid that could subsequently separate during cooling.

3.7 Summary

Out of the MPEA samples studied in this investigation CoCrCuNi, CoCrCuTi, CoCrCuFeNi, CoCrCuMnNi, CoCrCuMnTi, and CoCrCuTiV solidified dendritically resulting in FCC solid solutions of both the dendritic and interdendritic regions for the Ni containing alloys, but BCC, HCP, and FCC phases for the Ti-containing alloys. Through normal solidification processing, CoCrCuNi and CoCrCuMnNi resulted in dendritic FCC crystal structure with FCC interdendrites, while our study of CoCrCuFeNi is in agreement with the literature as it also is a dual-phase FCC MPEA. The alloys of CoCrCuTi and CoCrCuTiV were found to have (2) sets of BCC dendritic phases, with a Cu-rich FCC interdendritic matrix. CoCrCuMnTi was found to be dual-phase HCP/FCC, while CoCrCuFeTi also contained the HCP phase but exhibited severe liquid phase separation. The remaining samples all underwent a melt separation into Cu-rich and Cu-lean liquids. The presence of the Cu-lean liquids indicate that although the entire mixture exhibited liquid phase separation, the separated regions are expected to solidify into solid solutions independent of the other. The compositions of the Cu-lean phase separated regions gathered from the EDS data seem to indicate the potential for single phase solid solutions. Although the compositions of the Cu-lean phase separated regions are not equiatomic and fall out of the realm of traditional HEA design, they may qualify as complex concentrated alloys or multiprincipal element alloys and could yield interesting microstructures and properties.

The calculated ΔH_{mix} for each of the dendritic regions are more negative than the calculations for their nominal equiatomic concentrations, indicating that the approximation for ΔH_{mix} using Miedema's scheme for sub-regular solutions displays a correlation between

negative mixing enthalpy and liquid phase separation in MPEAs. However, we note that even though the summation of binary alloy mixing enthalpies may have a negative ΔH_{mix}, binaries within the calculation that have a very large positive mixing enthalpy (such as alloys with Cu) may lead to liquid phase separation of the compositions that has the most positive mixing enthalpy across the binaries. When comparing the mixing enthalpies of the possible combinations of mixing enthalpies of all the alloying elements, approximations can be made as to whether the resulting mixture will contain Cu-rich and Cu-lean phases, however cannot distinguish if this separation will occur in the interdendritic region or a completely phase separated globule.

Chapter 4

In-Situ Imaging of Liquid Phase Separation in Molten Alloys Using Cold Neutrons

4.1 Abstract

Understanding the liquid phases and solidification behaviors of multicomponent alloy systems becomes difficult as modern engineering alloys grow more complex, especially with the discovery of high-entropy alloys (HEAs) in 2004. Information about their liquid state behavior is scarce, and potentially quite complex due to the presence of perhaps five or more elements in equimolar ratios. These alloys are showing promise as high strength materials, many composed of solid-solution phases containing equiatomic CoCrCu, which itself does not form a ternary solid solution. Instead, this compound solidifies into highly phase separated regions, and the liquid phase separation that occurs in the alloy also leads to phase separation in systems in which Co, Cr, and Cu are present. The present study demonstrates that in-situ neutron imaging of the liquid phase separation in CoCrCu can be observed. The neutron imaging of the solidification process may resolve questions about phase separation that occurs in these alloys and those that contain Cu. These results show that neutron imaging can be utilized as a characterization technique for solidification research with the potential for imaging the liquid phases of more complex alloys, such as the HEAs which have very little published data about their liquid phases. This imaging technique could potentially allow for observation of immiscible liquid phases becoming miscible at specific temperatures, which cannot be observed with ex-situ analysis of solidified structures. The following work was published in Ref. [209].

4.2 Introduction

The continuous search for better engineering alloys has given rise to the superalloys, bulk metallic glasses, and more recently, the high-entropy alloys (HEAs), also referred to as complex concentrated alloys (CCAs), and multiprincipal element alloys (MPEAs). Introduced in 2004, a "high-entropy" alloy was first considered to be an equiatomic combination of 3 to 5 elements that form a single-phase solid solution, with a large configurational entropy of mixing [1–6]. The definition has since been relaxed somewhat, as researchers have been synthesizing these alloys with many components in non-equiatomic combinations to form dual-phase materials and intermetallic compounds. Enormous efforts have been made to understand their potential as engineering materials as many of the 3d transition metal HEAs/CCAs/MPEAs are comparable to austenitic steels, precipitation hardened steels, austenitic nickel alloys, and other superalloy classes–many having non-equiatomic 3d transition metal combinations which can be classified as CCAs [22]. To harness the potential of these alloys, researchers must reliably understand the thermodynamics and formation mechanisms of these materials during various processing routes. It is extremely difficult to visualize the hyperdimensional phase diagrams of multicomponent alloys containing more than 3 base elements, and efforts have been made to accelerate the discovery of single-phase HEAs by using computational methods [35, 37, 169]. These methods are useful for refining the search for single-phase and dual-phase HEAs, and along with experimental studies of new HEA systems, the field is moving in the direction of getting a better understanding of how these alloys form. However, information about HEA behavior in the liquid state is scarce, specifically pertaining to liquid phase separation.

In order to investigate the possible liquid phase separation in more complex alloys such as the HEAs in Reference [22], in-situ studies of liquid phase separation in "medium entropy" alloy CoCrCu were carried out to verify that the technique can identify distinct phase-separated liquids, which in turn can be applied to the other CoCrCu-containing systems. This work would provide a novel characterization technique for investigating the thermodynamics and phase formation mechanics of new and existing metals used throughout industry. Liquid phase separation has been recorded in many alloy systems such as Co-Cu [62, 184, 187, 188, 194, 195, 202], Cu-Fe [83, 181, 199, 201, 204, 263, 264], Cu-Nb [184, 264], Co-Cr-Cu [86], and Co-Cu-Fe [110, 178, 180, 184]. More recently, Munitz et al. show that HEA systems CoCrCuFe, CoCrCuFeNiNb, CoCrCuFeV, CoCrCuFeTi0.5V, CoCrCuFeTiV, and CrCuFeMnV undergo stable liquid phase separation into Cu-rich and Cu-lean phases [139]. The previous experiments have not measured real time liquid phase separation, but rather the resultant microstructures of the Cu-rich and Cu-lean phases. Many of the HEAs in the literature contain Co, Cr, and Cu and have distinct regions that are rich in Cu, examples of which being the alloys in Table 4.1. As the field of HEAs continues to grow, the understanding of phase formation and separation will continue to be problematic as these alloys phase diagrams will be very complex. Post-mortem analysis can sometimes lead to difficulty when trying to understand how certain phases form, therefore using cold neutrons to image a solidification process can potentially lead to better understanding of the solidification behavior of the alloy in question.

In-situ neutron imaging provides a unique opportunity to image liquid phase separation in the form of a carefully constructed sequence of neutron radiographs throughout

Table 4.1: High-entropy alloys studied in the literature that contain equiatomic CoCrCu with Cu-rich phase separation.

HEA	References
CoCrCuFeMn	[148]
CoCrCuFeNi	[139, 150–153]
CoCrCuFeMnNiTiV	[161]
CoCrCuFeMoNi	[238]
CoCrCuFeNiTi	[159]

sample heating and cooling. This technique could be utilized to provide insight into bulk molten alloy behavior, and can potentially be used for studying solid state phases which subsequently form and whether macro separation takes place. Real-space imaging with $\approx$ 80 μm spatial resolution, sufficient to see globule-like separation in materials such as the present CoCrCu alloys, (where the phase separation can be on the order of 200 + μm [86]), is routinely available at several neutron user facilities worldwide. Although the spatial resolution of neutron imaging instruments will continue to become more precise, other significant challenges may arise when combining standard neutron imaging capabilities with the in situ heating and melting of an alloy as crucible size, furnace distance to the detector, and dimensions of the detector will influence the amount of sample that can be melted.

The neutron transmission through the elements used in this study (Table 4.2) is suitable for studying phase separation within mm-size crucibles. The neutron transmission values are calculated based upon the expression,

$$I(\lambda) = I_0(\lambda)e^{-\mu(\lambda)\Delta x} \tag{4.1}$$

where $I(\lambda)$ and $I_0(\lambda)$ are the transmitted and incident neutron intensities, respectively, for

Table 4.2: Table of neutron transmission through the elements, and the CoCr-rich phas, used in this study.

Composition	Density (g/cm^3)	Transmission $\Delta x = 4$ mm	Transmission $\Delta x = 8$ mm
Co	8.9	12%	1%
Cr	7.2	77%	59%
Cu	9.0	63%	40%
CoCr	8.0	31%	10%

the wavelength λ, and path length Δx, through the attenuating material. The wavelength-dependent attenuation coefficient $\mu(\lambda)$ is given by,

$$\mu(\lambda) = \sigma_{tot}(\lambda)\frac{\rho N_A}{M} \tag{4.2}$$

where $\sigma_{tot}(\lambda)$ is the total (absorption plus scattering) neutron cross section of the material, ρ is the mass density, N_A is Avogadro's number, and M is the molar mass [277].

The neutron wavelengths for the present study were in the "cold" range, with a distribution peaking at about 2.6 Å. Thus, for the purpose of estimating transmission and contrast among the elements, a fixed value of $\lambda = 2.6$ Åwas used in the equation above. The densities ρ and molar masses M, of the room-temperature metals were used in the calculations.

Indications of liquid phase separation can be deduced by the difference in contrast of the regions inside the melt. Due to the elements in Table 4.2 having different neutron transmission percentages, it is predicted that the different phases can be distinguished from the other, as the CoCrCu melt separates into Cu-rich and Cu-lean liquids. Liu et al. provided an experimental determination and thermodynamic calculation for the CoCrCu

system where a stable liquid phase miscibility gap of Cu-rich and Cu-lean liquids should exist at 1500 °C, especially in near-equiatomic concentrations of each element in the melt [86].

4.3 Materials and Methods

4.3.1 Sample Preparation and Microstructural Characterization

Identical samples of CoCrCu were prepared with elemental purity of Co $\geq$ 99.9%, Cr $\geq$ 99.99%, and Cu $\geq$ 99.9%. Each sample weighing approximately 1.5 g and was arc-melted three times (flipped twice) on a water-cooled Cu hearth in a Ti-gettered argon atmosphere. Sample dimensions were semi-spherical buttons (Fig. 4.1) and were approximately 6 mm in diameter and 3 – 4 mm tall. For microstructural characterization, an arc-melted button of CoCrCu was electromagnetically levitated and remelted to temperatures within the liquid miscibility gap (1130–1630 °C). After visual confirmation that the system was molten, the sample was cast onto a flat Cu surface from $\approx$ 1500 °C. Sample melting was also confirmed due to the flat (coin-like) shape of the splat sample not retaining any of the spherical shape of an arc-melted button. Temperature of the alloy system was recorded with a Metis M3 2-color pyrometer with temperature range of (500 to 1800 °C). The flat cast sample was cut vertically in half using a diamond wafering blade and subsequently mounted face down in BPA epoxy resin. The mounted sample was then abraded using SiC paper up to 1200 grit, and polished using 1 μm, 0.3 μm and 0.05 μm Al_2O_3 powder. Backscattered electron images and energy dispersive X-ray spectroscopy (EDS) of the mounted sample were obtained with a NovaNanoSEM 450 scanning electron microscope.

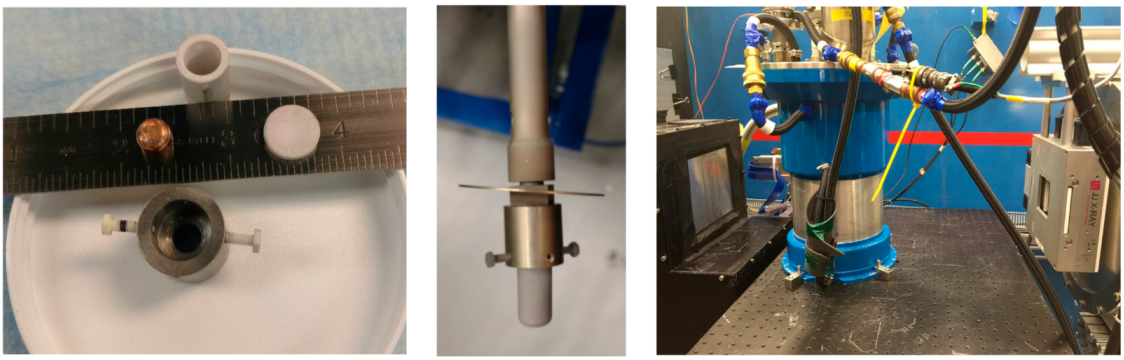

(a) (b) (c)

Figure 4.1: Images of the experimental setup at the CG-1D beamline at the High-Flux Isotope Reactor (HFIR) at Oak Ridge National Laboratory. (a) sample of CoCrCu, Al_2O_3 crucible, lid, and Nb mounting adaptor placed near a ruler for scale. (b) The crucible-mounted to the sample stick. (c) The high-vacuum Institut Laue-Langevin (ILL) furnace placed between the detector and incident neutron beam slits.

4.3.2 Neutron Imaging

The CG-1D Neutron Imaging Instrument at Oak Ridge National Laboratory uses a polychromatic "cold" neutron beam, obtained by passing the beam through a liquid hydrogen cold source, giving a wavelength range of $0.8 < \lambda < 6$ Å, peaking at 2.6 Å. As the neutron beam enters the CG-1D instrument, it passes through one of four user-selectable circular apertures with diameters, D = 3.3, 4.1, 8.2, 11, or 16 mm. This set of apertures allows users to make the trade off between higher neutron flux (larger D), or greater spatial resolution (greater L/D ratio, where L = 6.59 m is the distance between the aperture and detector). The intermediate aperture size of 8.2 mm was chosen for the present furnace work, where the large sample-to-detector distance ($\sim$ 20 cm) caused significant image blurring

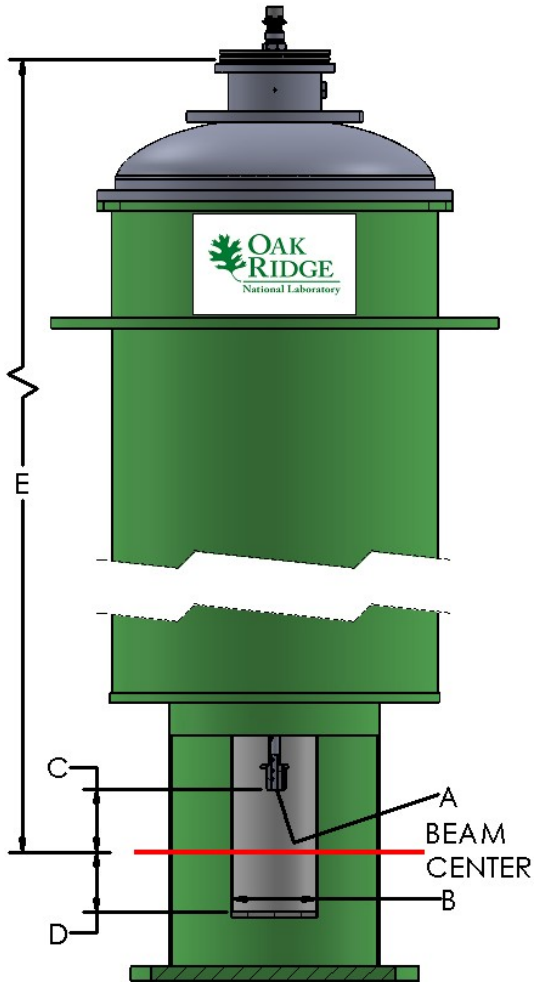

Figure 4.2: ILL Niobium Foil Vacuum Furnace. Temperature range of 30–1500 °C (A) Interface connection M8 × 1.25 (male) (B) Bore size diameter = 50 mm (C) Distance interface to beam center = 31.75 mm (D) Beamcenter to sample space bottom= 11.862 cm(E) Distance stick flange to beamcenter = 41.275 cm. Image of ILL furnace "HOT-A" courtesy of Oak RidgeNational Laboratory Sample Environment Group.

with large apertures. The present detector assembly is capable of 80 μm spatial resolution. The working resolution, however, changes depending upon the experimental configuration. Under the present experimental setup, the working resolution was $\sim$ 200 μm, because the sample-to-detector distance is relatively large ($\sim$ 20 cm) when using the furnace. This resolution degradation was mitigated by choosing a relatively small aperture (8.2 mm). The scintillators are routinely changed among different thicknesses (25, 50, and 100 μm). The 50 μm thickness was used for the present work. The detector field-of-view (FOV) is a 75 mm square region on the scintillator screen. The working FOV of the sample slightly decreases from 75 mm with sample-to-detector distance, according to a 2-degree beam divergence.

Neutron radiographs were acquired using a ^{6}LiF/ZnS scintillator viewed by a CCD detector with 20, 40, and 55 s, exposure times for the various heating curves described below. The heterogeneous alloy of CoCrCu was inserted into the furnace (Fig. 4.2) for heating. The image acquisition was set to acquire 5 images every 50 °C from 900 – 1500 °C with a 1 °C tolerance and ramp rate of 17 °C/min. Each image was acquired for 40 s, and the images were only captured once 1 °C tolerance had been reached for each temperature. At the maximum temperature of 1500 °C, 10 images were taken before the temperature script entered the cooling. Ten dark field and ten open beam images were acquired under the same conditions for image normalization. Computed tomography (CT) scans were carried out at room temperature of the samples inside the crucible on a rotating stage from 0 to 183° in steps of 0.20° at a rate of 1 image/step and an exposure time of 55 s per image.

This in situ heating process was refined with two samples of CoCrCu stacked inside the small style alumina crucible in Fig. 4.1a so that the flow of liquids toward the crucible

bottom could be observed. The stacked sample system is what is discussed throughout the rest of the text. The image acquisition for the stacked CoCrCu system was refined to produce a more movie-like series of radiographs, and therefore set to acquire 10 images every 25 °C from 900 – 1500 °C with a 5 °C tolerance and ramp rate of 17 °C/min. Each image was acquired for 20 s in order to maintain good resolution while maintaining the same time (200 s) at each temperature before the continuing in the heating curve. This allowed for more images to be captured at each temperature of the heating curve (Fig. 4.3) while maintaining enough resolution to distinguish between the separated liquid phases. At the maximum temperature of 1500 °C, 20 images were taken before the script entered the cooling portion of the curve. This temperature of the system can be seen in Fig. 4.3. After the sample cooled, computed tomography (CT) scans were again carried out at room temperature of the solid in the crucible on a rotating stage from 0 to 183° in steps of 0.20° at a rate of 1 image/step and an exposure time of 55 s per image ($\sim$ 14 h scan). The images were then normalized in the standard fashion, by subtracting the the dark field from the raw images, and dividing by (open beam-dark field) radiographs.

4.4 Results

4.4.1 Microstructural Characterization Using Electron Microscopy

The ex situ microstructural characterization of the levitated sample revealed Cu-rich and Cu-lean phases, as seen in Figure 4a by the different colored grayscale regions. The amount of electrons that are scattered back to the detector is proportional to the atomic

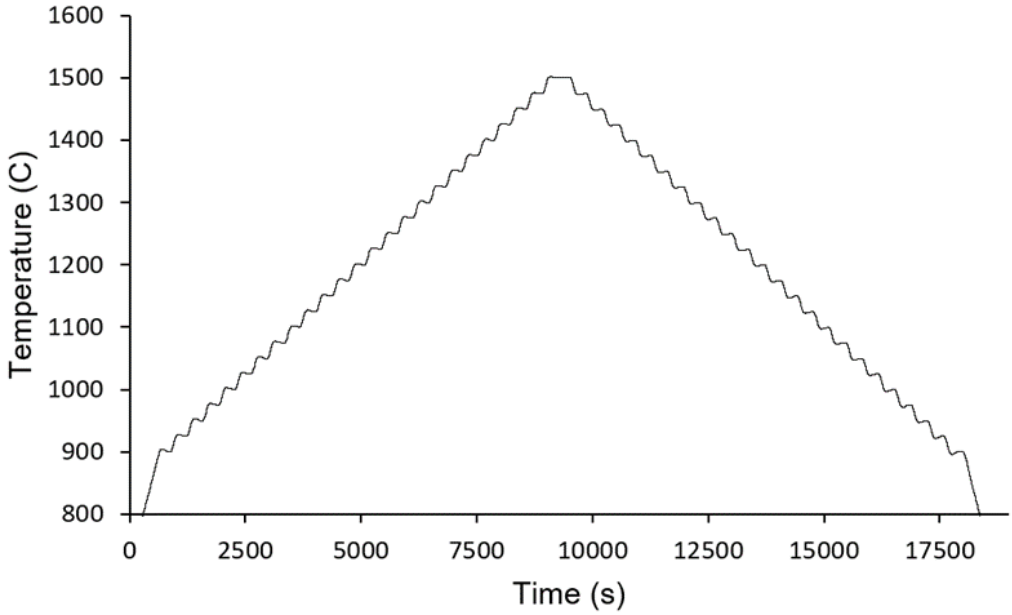

Figure 4.3: Temperature vs. time of the stacked CoCrCu system heating from 900 to 1500 °C and back to 900 °C in 25 °C increments.

number of the material (brighter regions higher Z), therefore, the brighter region at the top is a Cu-rich phase (2.8% Co, 1.2% Cr, and 96.0% Cu), while the bottom region is Cu-lean, containing $\geq$ 90% CoCr (45.6% Co, 46.6% Cr, and 7.8% Cu), confirmed by energy dispersive X-ray spectroscopy (EDS). The bottom dark-gray region of the micrograph in Fig. 4.4a displays a CoCr-rich phase that appears to solidify first, with small dendrites seen protruding into the lighter Cu-rich region. According to the isothermal phase diagram in Ref. [86], the CoCr-rich liquid solidifies first resulting in the eutectic (Cr) + (αCo) phases near equiatomic concentrations. Fig. 4.4b displays an optical micrograph of an arc-melted button of CoCrCu. This button was cross-sectioned vertically, and the two distinct phases can be seen, represented by the different colored regions. The Cu-phase retains its distinct orange color and can be seen in along the edges of Fig. 4.4b.

Maps of atomic composition were collected for the distinct regions, revealing the large phase separation between the Cu-rich and CoCr-rich liquids, and can be seen in Fig. 4.5. The globule-like separation is indicative of liquid phase separation, as seen in the previous work on these and similar alloys with stable liquid miscibility gaps [86, 139]. In energy dispersive X-ray mapping, each element emits a characteristic X-ray upon electrons returning to the ground state, therefore this technique allows for analysis of specific atomic concentrations of specific areas within a sample. This can be seen in Fig. 4.5a-b, where the cobalt and chromium maps correspond to the CoCr-rich region, while the separated spheres to the left are mostly copper (Fig. 4.5c). The total elemental map is present in Fig. 4.5d, displaying an equal mixed presence of Co and Cr, while the red Cu sphere is its own separated phase.

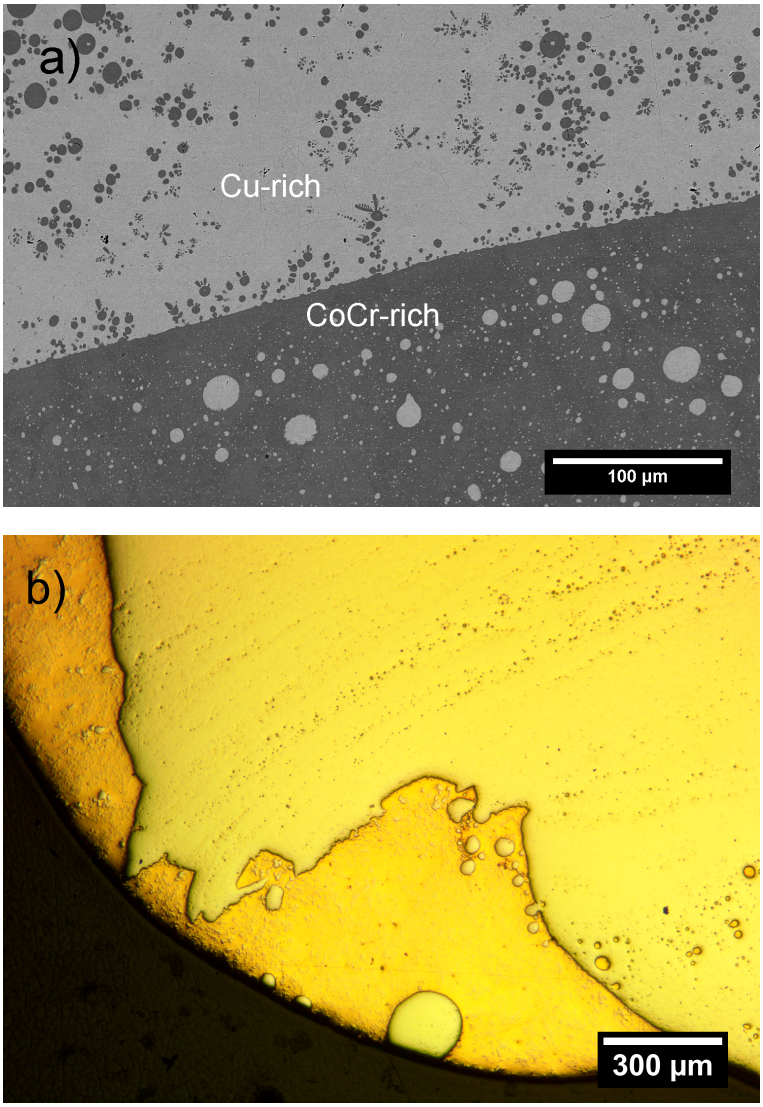

Figure 4.4: (a) Backscattered electron image of CoCrCu displaying 2 distinct phases: Cu-rich (top), CoCr-rich (bottom). Note, tiny black spots are pores generated from the initial grinding/polishing process. (b) Optical micrograph of the bottom-half cross-section of an arc-melted CoCrCu button.

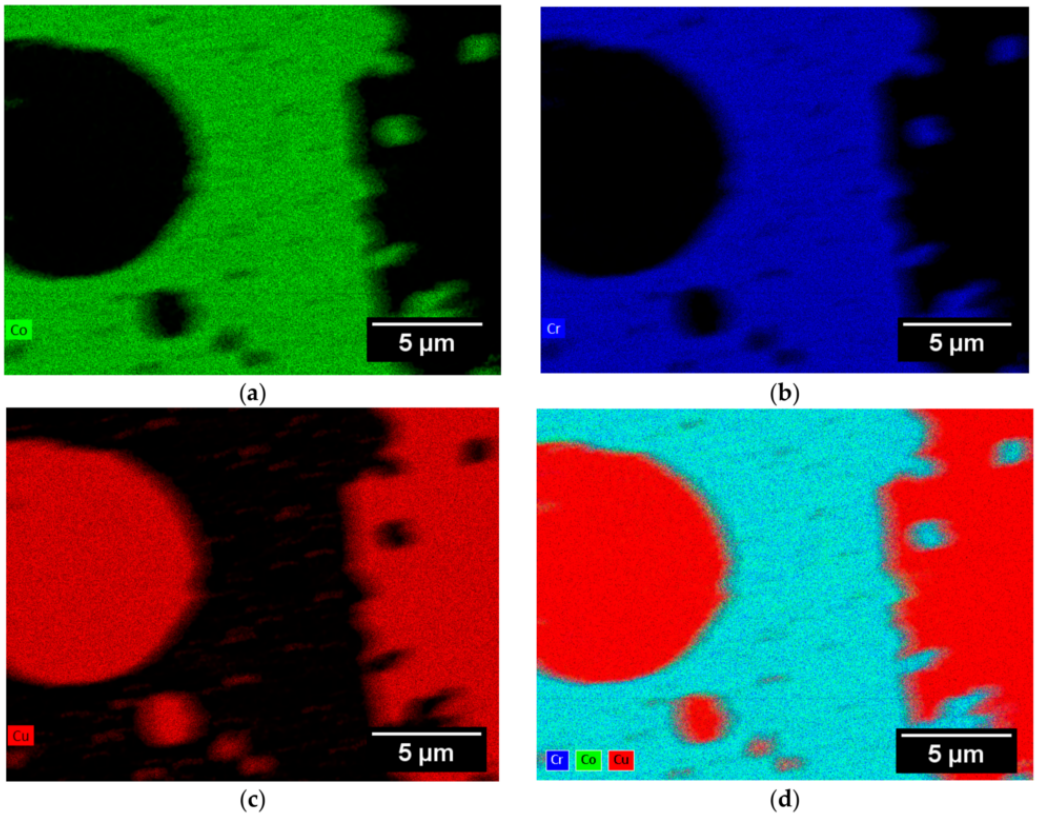

Figure 4.5: Energy dispersive X-ray spectroscopy (EDS) maps of the phase separated regions of the electromagnetically levitated and cast CoCrCu alloy. The colored regions correspond to the atomic composition present in the material: (a) Cobalt only (b) Chromium only (c) Copper only (d) Map of all elements in the system.

4.4.2 Neutron Imaging

For the initial imaging, a solitary CoCrCu was placed inside of the furnace and heated to 1500 °C and cooled according to the step function described for this system in the methods section. Additional experiments were conducted with two samples stacked inside the crucible (Fig. 4.6) so that a more drastic flow can be observed. The CoCrCu sample itself does not form a solid solution with the alloying elements Co, Cr, and Cu, in contrast to some HEAs containing these elements [2]. The arc-melted CoCrCu buttons have a random distribution of Cu-rich globules that solidify alongside of the CoCr-rich species. Due to this alloy's nature for phase separation, it was the ideal candidate for neutron imaging as the Cu-rich species has a higher neutron transmission than the CoCr-rich liquid. As can be seen in Fig. 4.6, the distribution of the Cu-rich species inside of the sample button is identified as the lighter region of the spherical shapes, as Cu allows for more transmission of neutrons compared to much darker CoCr-rich regions (Fig. 4.6).

The stacked CoCrCu samples in Fig. 4.7 show two heterogeneous buttons of CoCrCu placed inside of the alumina crucible and radiographed from 900 to 1500 °C (and eventually back to 900 °C). The brighter Cu-rich regions in the 2 buttons are the first to melt and travel downward due to gravity until the CoCr-rich dark region melts and collapses into a single liquid held together by surface tension. The remaining Cu-rich (lighter phase) inside of the CoCr-rich liquid can be seen travelling out towards the top of the system, possibly as a pocket trapped by the surrounding CoCr-rich solid/liquid. Once the system was allowed to reach equilibrium, this lighter region disappears and could have made its way to the bottom of the crucible either along the sides or through the CoCr-rich liquid

due to the different liquid densities. As the system reaches overall solidification, a void grows from the bottom left of the crucible. This void expands as Cu-rich liquid contracts until a low enough temperature is ultimately reached, allowing for the solidification of the Cu-rich phase (Fig. 4.8). As heating proceeds to overall sample melting in Fig. 4.7, the lighter-appearing Cu-rich region flows from the sides of the buttons to the bottom of the crucible. The two liquids remain separated in the molten state until solidification of the higher melting point species. The first to solidify is the CoCr-rich region as it cools from 1500 °C and contracts next to the Cu-rich liquid (Fig. 4.8) in between 1400 and 1350 °C, as inferred by the CoCr binary phase diagram and the isothermal sections of the CoCrCu ternary diagrams [86]. As the environment is cooled down to 900 °C the Cu-rich liquid solidifies between 1100 and 1075 °C and we are left with the two distinctly separated regions in Fig. 4.8. Overall, two types of phase separations have been directly observed using neutron imaging. At the highest temperatures, above the liquidus, Cu-rich and Cu-lean liquids co-exist.

4.5 Disucssion

4.5.1 Microstructure

The microstructure and macrosegregation of CoCrCu from Fig. 4.4 displays the Cu-rich and Cu-lean phases described previously by [86]. During the initial arc-melting, the alloy either formed a single phase liquid and underwent decomposition into two distinct liquids, or there existed a stable liquid phase separation overall throughout the melt. There

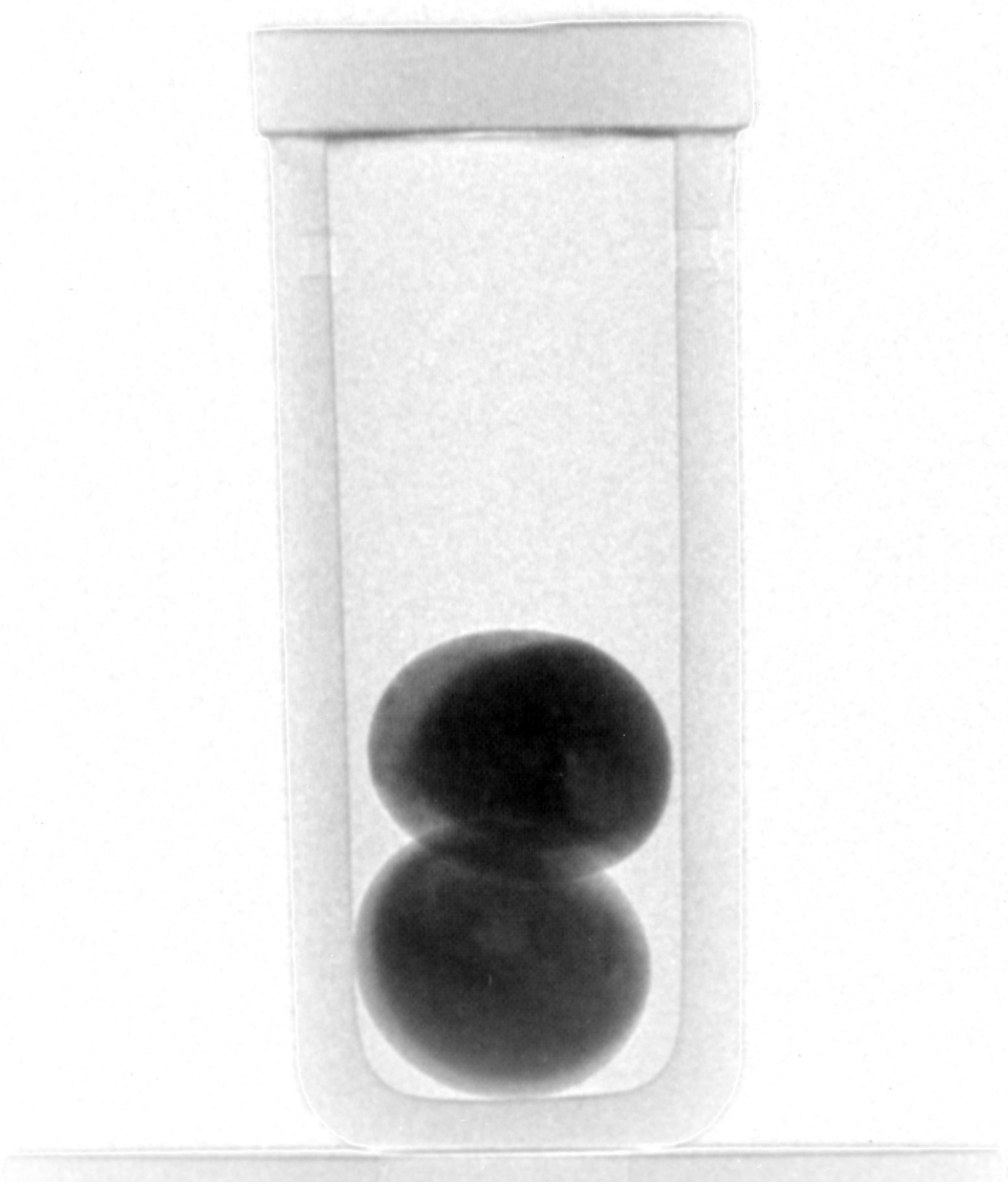

Figure 4.6: Room temperature radiograph of two heterogeneous arc-melted CoCrCu samples stacked inside a small crucible. The lighter regions are the Cu-rich phase ($> 95\%$) and are segregated to the surface of the buttons as well as randomly distributed globules inside the bulk. The darker regions are Co-Cr-rich and make up the rest of the arc-melted button.

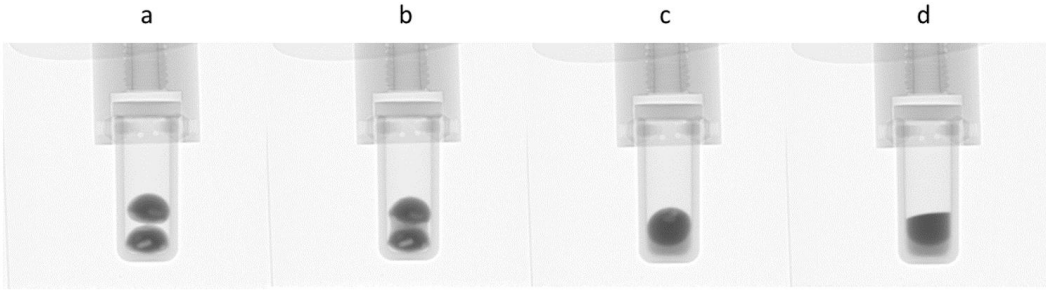

Figure 4.7: Melting and liquid phase separation of stacked CoCrCu samples. (a) During initial heating, the two as-cast buttons are intact. (b) The Cu-rich phase melts first between 1075 and 1100 °C, and (c) pools at the bottom of the crucible. (d) The Cu-lean phase fully melts upon heating to 1500 °C. Full video available in original publication.

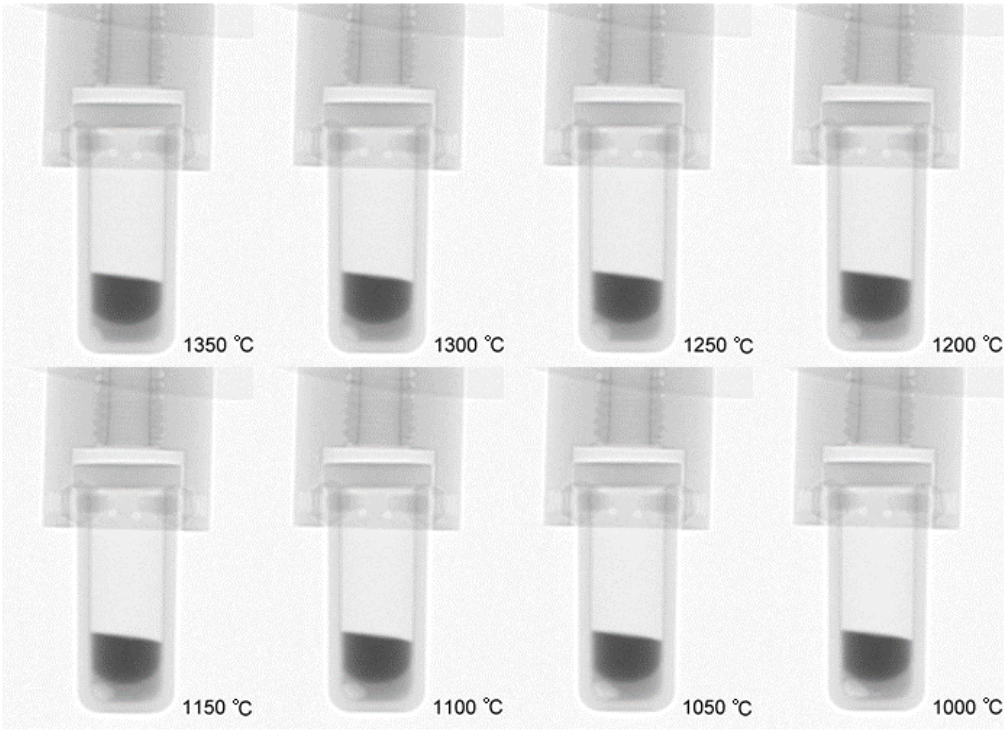

Figure 4.8: Cooling, macroscopic void formation, and solidification.

is currently no literature for this ternary system regarding the miscibility gap past 1627 °C detailing the presence of a single phase liquid, however with higher temperatures it may be possible to image approximately where this demixing occurs with cold neutrons. Further experimentation is needed to understand the thermodynamics of the CoCrCu system. The two liquids appear to remain immiscible throughout melting and solidify independently of the other, indicating the presence of a stable miscibility gap and is agreement with the miscibility gap studies of Liu et al. [86].

4.5.2 Neutron Imaging

In Fig. 4.7, as temperature increases, the entire system becomes molten and reaches a thermodynamic equilibrium with a stable liquid phase miscibility gap containing Cu-rich and Cu-lean liquids. The difference in brightness between the two liquids is consistent with the expected phase separation, the brighter being the Cu-rich liquid (see Table 4.2,where the neutron transmission through Cu is about twice that of CoCr mixture). The phase separation is also consistent with the relative volumes, inferred from the bright versus dark image areas, such that the Cu-rich region accounts for one third of the volume determined by analyzing the areas from the CT scans with image processing software. The phase diagram suggests that the solidification of the CoCr-liquid will have a very small solubility with Cu, and vice-versa [86]. As the concentrations of the elements in the system are in equal parts, it is easy to see the separated Cu-liquid correspond to its approximate volume fraction of 1/3rd, which was verified with image analysis software (ImageJ v. 1.50b, National Institutes of Health (NIH), Bethesda, MA, USA).A final confirmation was made by visual inspection of the sample as they are copper-rich on the surface, retaining the color of pure copper, as

seen in Fig. 4.1a. As shown in Table 4.2, the Cu-rich and CoCr-rich species have enough contrast to be able to determine the phases based on volume fraction.

The neutron radiography experiments conducted on the stacked CoCrCu button display an optimized number of radiographs and temperature steps to capture a representative melt-solidification process. Fig. 4.7 displays specific radiographs taken from the overall collection of images which forms a movie of 500 images, which can be found at Ref. [209]. The movie of the melting and solidification process is formatted to play at 10 frames per second (fps), such that each second displays a 25 °C step. The Cu that surrounded the surface of the button melts first and flows to the bottom of the crucible. The Co-Cr rich center collapses and forms a spherical shape in Fig. 4.7c, likely due to surface tension of the liquid. As the temperature was increased to 1500 °C, both liquid phases were present within the miscibility gap of the system and the temperature was held for 200 s until entering the cooling portion of the temperature curve.

At 1350 °C, a void began to grow into the molten pool of Cu-rich liquid at the bottom of the crucible which can be observed in Fig. 4.8. The void continued to grow as the Cu-rich liquid solidified between 1050 and 1000 °C. The radiograph of the solidified system at room temperature and photograph of the void can be seen in Fig. 4.9. The reconstructed computed tomography is present in Fig. 4.10, where the Cu-rich phase is represented by the green while the CoCr-rich phase is atop in red.

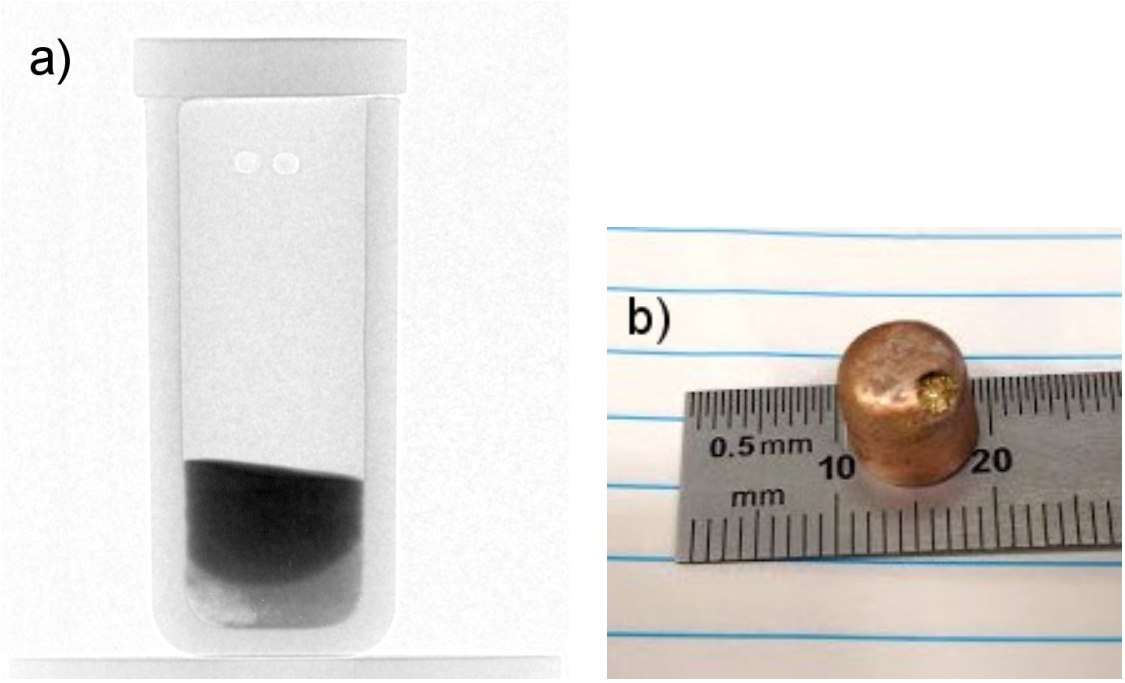

Figure 4.9: (a) Room temperature radiograph of CoCrCu after the melt cycle. The darkest region atop is the Co-Cr-rich phase, while the lighter region to the bottom right was the formation of a void. The lighter gray region toward the bottom right is the Cu-rich phase. (b) Photograph of the sample after removal from the crucible, displaying the void that formed during solidification

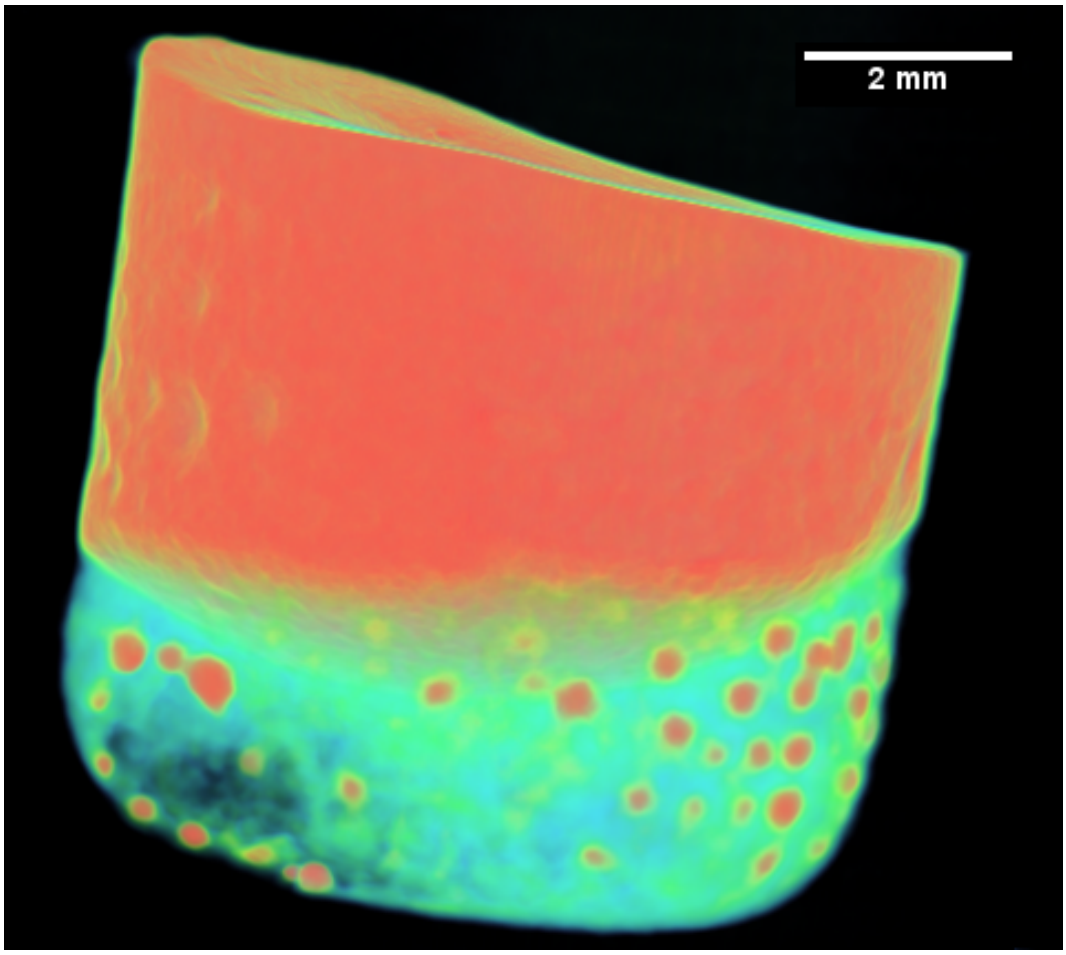

Figure 4.10: Reconstructed computed tomography of the CoCrCu system with void present in the bottom left, and CoCr-rich (red) globules dispersed throughout Cu-rich (green) phase.

4.6 Summary

With the growing number of complex alloy systems being studied, understanding their liquid behavior becomes crucial when designing materials for applications across industries. During casting processes, it is very hard to distinguish liquid phase separation, as most metals are not transparent. By utilizing cold neutron imaging, liquid phase separation of the CoCrCu system was able to be observed, demonstrating that this technique can be applied to other metal systems provided that the neutron transmission of the alloying elements are dissimilar enough to see a contrast between the multiple phases. This technique has the potential to be improved for future work, for example, by utilizing a smaller furnace with better transparency for neutrons such that the sample is closer to the detector with better resolution. This technique also provides a way to potentially image casting processes by constructing crucibles that simulate various cast shapes. After solidification has finished, the use of computed tomography (CT) can be applied with the cold neutrons and a rotating sample stage to look for impurities or voids within the cast. This method can be applied to study fundamental liquid state behavior in complex alloy systems, such as the high-entropy alloys. By using neutron imaging of the liquid phase, it can provide invaluable information about the alloy system as well as other systems that contain miscibility gaps and is not solely specific to liquid metals.

Chapter 5

In-Situ Imaging of Molten High-Entropy Alloys Using Cold Neutrons

Real-time neutron imaging was utilized to produce a movie-like series of radiographs for in-situ observation of the remixing of liquid state immiscibility that occurs in equiatomic CoCrCu with the addition of Ni. A previous neutron imaging study demonstrated that liquid state immiscibility can be observed in-situ for the equiatomic CoCrCu alloy. In this follow-up study, equiatomic buttons of CoCrCu were placed alongside small Ni buttons inside an alumina crucible in a high-temperature vacuum furnace. The mass of the Ni buttons was specifically selected such that when melted in the same crucible as the CoCrCu buttons, the overall composition would become equiatomic CoCrCuNi. Neutron imaging was simultaneously carried out to capture 10 radiographs in 20 °C steps from

1000 °C to 1500 °C and back down to 1000 °C. This, in turn, produced a movie-like series of radiographs that allow for the observation of the buttons melting, the transition from immiscible to miscible as Ni is alloyed into the CoCrCu system, and solidification. This novel imaging process showed the phase-separated liquids remixing into a single-phase liquid when Ni dissolves into the melt, which makes this technique crucial for understanding the liquid state behavior of these complex alloy systems. As metals are not transparent to X-ray imaging techniques at this scale, neutron imaging of melting and solidification allows for the observation of liquid state phase changes in real time. Thermodynamic calculations of the isopleth for $CoCrCuNi_x$ were carried out to compare the observed results to the predictions resulting from the current Thermo-Calc TCHEA3 thermodynamic database. The calculations show a very good agreement with the experimental results, as the calculations indicate that the $CoCrCuNi_x$ alloy solidifies from a single-phase liquid when $x \geq 0.275$, which is close to the nominal concentration of the CoCrCuNi alloy ($x = 0.25$). The neutron imaging shows that the solidification of CoCrCuNi results from a single-phase liquid. This is evident as no changes in the neutron attenuation were observed during the solidification of the CoCrCuNi alloy. The following work was published in Ref. [278].

5.1 Introduction

The equiatomic CoCrCuFeNi has been extensively studied since its discovery by Yeh et al. in 2004 due to it dendritically solidifying into primary face-centered cubic (FCC) dendrites with FCC interdendrites [3]. These studies include magnetization [159], compressive strength [159, 238], calculation of phase diagrams (CALPHAD) [138], recrystal-

lization [150], thermodynamic properties [279], cold rolling [150, 280], and rapid solidification [151].

Liquid phase separation (LPS) in CoCrCuFeNi has also been observed during supercooling [151, 152, 239, 242], or by varying concentrations of Fe/Ni [139, 140, 153]. LPS resulting from additions of Mo [238] and Sn [242] has also been investigated.

The components present in CoCrCuFeNi have been shown to phase separate when present in ternary or quaternary combinations. For example, the equiatomic ternary CoCrCu has been shown to phase separate in the liquid [55, 86], indicating the existence of a stable miscibility gap. Equiatomic additions of Ni to CoCrCu have been shown to eliminate LPS and lead to typical dendritic solidification in the CoCrCuNi alloy [140]. In contrast, additions of Fe to CoCrCu have led to stable LPS which is characterized by macroscopic globule-like phase separations present in the microstructure [139, 140]. This would lead one to believe that the Ni addition in the CoCrCuFeNi alloy is what stabilizes the solution into a single-phase liquid as CoCrCu [140] and CoCrCuFe [139, 140] exhibit stable LPS. However, LPS has also been observed in induction-melted CoCrCuFe$_x$Ni when x = 0.5 [153] but not when x = 0 (CoCrCuNi, arc-melted) [140] or x = 1 (CoCrCuFeNi, arc-melted) [3]. When Ni is varied, in the case of arc-melted CoCrCuFeNi$_{0.5}$, stable LPS is also observed [153]. It is not immediately clear whether the LPS observed in these alloys is a result of processing parameters or from elemental concentration.

In an effort to elucidate the liquid state behavior of high-entropy and related alloys, the present authors utilized the CG-1D Neutron Imaging Instrument at the High-Flux Isotope Reactor (HFIR) at Oak Ridge National Laboratory to image the melt separation

process in-situ [209]. The technique utilizes a high-temperature furnace between a neutron beam and a detector, and was successfully implemented for the in-situ imaging of the liquid phase separation that occurs in equiatomic CoCrCu [209] as this compound has been shown to exhibit a stable liquid phase separation into CoCr-rich and Cu-rich liquids [86,140]. The experiment consisted of arc-melted CoCrCu buttons placed in a small alumina crucible inside a high-temperature vacuum furnace, which were then heated to 1500 °C, and slowly cooled back to room temperature with simultaneous neutron imaging being carried out in 25 °C steps. The technique requires that the neutron transmission percentage between the alloying elements is different enough such that a contrast between the phases can be seen during imaging. The experiment demonstrated that while at high temperatures, the melt separation can be observed in-situ as the CoCr-rich and Cu-rich layers separated and stacked similarly to the classic observations of oil and water [209].

The aim of this follow-up investigation was to apply the techniques for in-situ neutron imaging of melting and solidification to the CoCrCu alloy with buttons of Ni placed alongside the CoCrCu buttons in the crucible, so as to image in-situ mixing of the added Ni to the previously immiscible CoCr-rich and Cu-rich liquid phases. The slow cooling rate paired with neutron imaging of the solidification process will help elucidate the equilibrium solidification behavior of this alloy, as well as image the remixing of the immiscible CoCr-rich and Cu-rich liquids. As neutrons can penetrate through metals, this technique provides a novel solution for observing the liquid state behavior of HEAs.

5.2 Experimental

5.2.1 Sample Preparation and Furnace Setup

Two buttons of CoCrCu were prepared such that their atomic concentrations would remain equiatomic upon the melting of the two Ni buttons added into the crucible to form equiatomic CoCrCuNi (the CoCrCu + Ni buttons were doubled to increase the volume of material inside the crucible). The samples were prepared from elemental purities of Co $\geq$ 99.9%, Cr $\geq$ 99.99%, Cu $\geq$ 99.9%, and Ni $\geq$ 99.99%. The CoCrCu buttons were arc-melted two times (flipped once) on a water-cooled Cu hearth in a Ti-gettered argon atmosphere. CoCrCu button dimensions were $\sim$ 8 mm while the elemental Ni was remelted from chunk form into a smaller spherical shape of $\sim$ 5 mm, presented in Figure 5.1.

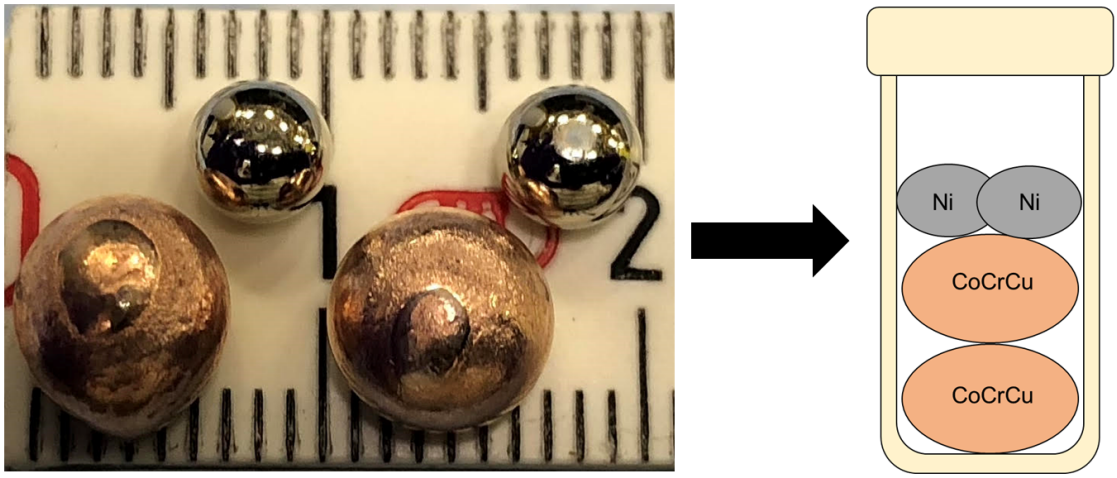

Figure 5.1: Photograph of the arc-melted CoCrCu buttons next to the remelted Ni buttons prior to the neutron imaging and melting.

The two CoCrCu and two Ni buttons weighing 1.14 g, 1.12 g and 0.38 g, 0.38

g, respectively, were stacked in a small alumina crucible of dimensions 27 mm height, 8 mm inner diameter, and 12 mm outer diameter. The crucible was then closed with a lid of 13 mm in diameter with a height of 3 mm (no vacuum seal). The crucible was then placed inside a top-loading "ILL-type" vacuum furnace customized at Oak Ridge National Laboratory (referred to as the HOT-A furnace), which was then placed between the neutron source and the detector (Figure 5.2). A more detailed description of the high-temperature furnace is presented in Figure 5.3. The buttons were heated up to the maximum operating temperature of the furnace (1500 °C) which was continuously pumped during heating to maintain a vacuum of $\approx 1 \times 10^{-6}$ mbar.

5.2.2 Neutron Imaging

The calculations for the transmission of neutrons through the elements/phases in these alloys are presented in Table 5.1, where Δx is the path length through the attenuating material. The neutron transmission values are calculated from,

$$I(\lambda) = I_0(\lambda)e^{-\mu(\lambda)\Delta x} \tag{5.1}$$

where $I(\lambda)$ and $I_0(\lambda)$ are the transmitted and incident neutron intensities, respectively, for wavelength λ. A more comprehensive description of the attenuation percentage calculation can be found in Ref. [277].

The CG-1D Neutron Imaging Instrument uses a polychromatic neutron beam, which is referred to as "cold" neutrons. The beam passes through a liquid hydrogen cold source which results in a wavelength range of $0.8 < \lambda < 6$ Å, which peaks at 2.6 Å. This

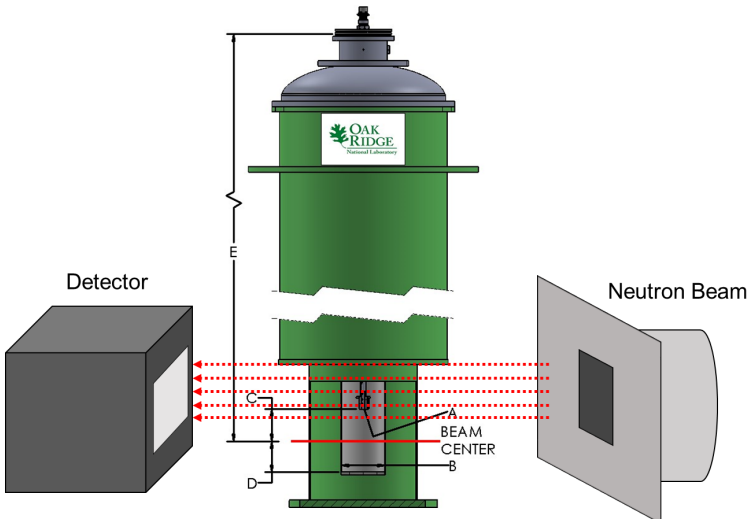

Figure 5.2: Diagram of the experimental setup at the CG-1D beamline at the High Flux Isotope Reactor (HFIR) at Oak Ridge National Laboratory. The image depicts the high-vacuum Institut Laue-Langevin (ILL) HOT-A furnace placed between the detector and the incident neutron beam slits. (A) Interface connection M8 $\times$ 1.25 (male), (B) Bore size diameter = 50 mm, (C) Distance interface to beam center = 31.75 mm, (D) Beam center to sample space bottom = 11.862 cm, E) Distance stick flange to beam center = 41.275 cm. Image of ILL furnace 'HOT-A' courtesy of Oak Ridge National Laboratory Sample Environment Group.

wavelength range gives sufficient transmission and contrast for imaging the present elements (Table 5.1, calculated assuming a peak wavelength of $\lambda = 2.6$ Å). Neutron radiographs were acquired using a ^{6}LiF/ZnS scintillator viewed by an ANDOR DW936 CCD detector. The detector field of view was a 75 mm square region on the 100 μm thick scintillator screen. The distance from the aperture to the detector, L, was 6.49 m, while the aperture diameter, D, was 11 mm. Therefore, the L/D ratio for this experiment was 599.1. Sample distance

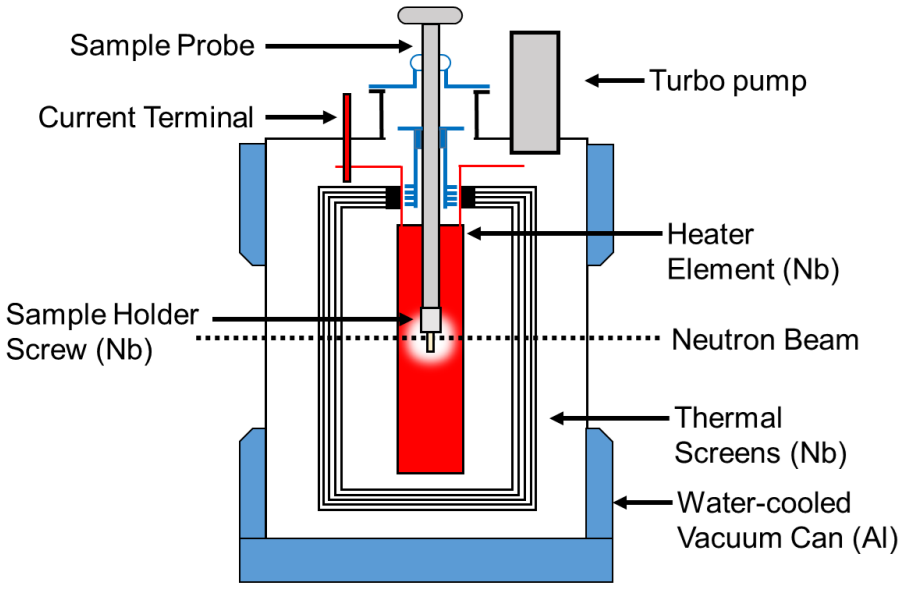

Figure 5.3: Top loading neutron furnace layout and description of furnace elements.

Table 5.1: Table of neutron transmission through the CoCr, Cu, Ni, and CoCrCuNi phases.

Composition	**Density (g/cm^3)**	**Δx (mm)**	**Transmission**
CoCr	8.01	8	10%
Cu	8.96	8	40%
Ni	8.91	5	34%
CoCrCuNi	8.47	8	16%

to scintillator was approximately 13 cm, resulting in a working spatial resolution on the order of $\sim$ 200 μm. The image acquisition was set to acquire 10 radiographs with an acquisition time of 10 s/radiograph (with a 4 second delay between radiographs) every 20 °C from 1000 °C $\rightarrow$ 1500 °C $\rightarrow$ 1000 °C with a 5 °C tolerance and ramp rate of 20 °C/min. The acquisition of images in these steps allows for a movie-like series of radiographs to display melting events in-situ [209]. The maximum temperature of 1500 °C was held for an additional 150 radiographs, so there would be sufficient time for mixing before entering the cooling portion of the image acquisition program.

After the heating/cooling cycle, the solidified CoCrCuNi alloy + crucible was removed from the furnace and placed on a rotating stage for additional radiographs such that computed tomography (CT) could be carried out on the solidified alloy. The CT scan was performed at room temperature on the rotating stage from 0 to 360° in steps of 0.20° at a rate of 1 image/step and an exposure time of 20 s per image.

5.3 Results

The radiograph in Figure 5.4 displays a negative image of the two CoCrCu buttons stacked with two spherical pieces of Ni placed on top of the two CoCrCu buttons. The two Ni buttons sat in the same path as the neutron beam, therefore there is a slight overlap between the two buttons which causes a slight increase in contrast. The CoCrCu buttons at the bottom of Figure 5.4 are heterogeneous from the arc-melting process, as indicated by brightness fluctuations in the bottom two buttons in Figure 5.4. The lighter region pertains to the CoCr-rich solid phase while the darker sides and portions of the inner regions are Cu-rich. This miscibility gap in CoCrCu [86] leads to macroscopic-phase segregation of CoCr-rich and Cu-rich phases during solidification. The differences in phase are distinguishable from the other in Figure 5.4 due to differences in brightness based on the attenuation of neutrons through each phase in the CoCrCu buttons [209]. The alumina crucible as well as the niobium sample stick are also visible in Figure 5.4 however do not interfere with the neutron transmission through the buttons.

Heating of the samples began from room temperature up to 1000 °C without any radiographs being taken. Once 1000 °C was reached, the programmed image acquisition

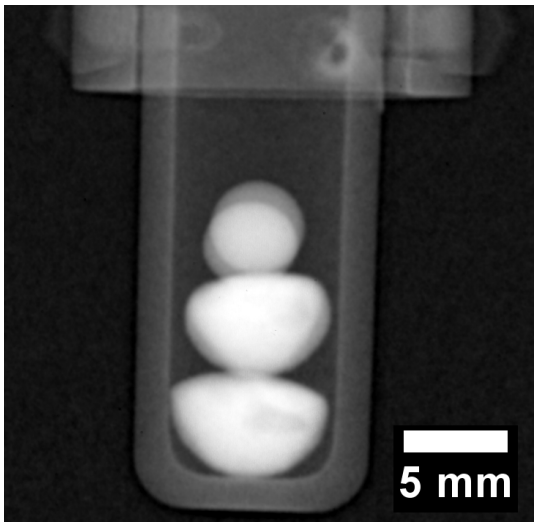

Figure 5.4: Radiograph of the four buttons stacked inside an alumina crucible such that the heterogeneous CoCrCu are placed on the bottom while the spheres of Ni are placed at the top (the Ni buttons are oriented in the direction of the beam such that they overlap). The darker regions present randomly in the bottom two buttons are the Cu-rich phase that separated in the liquid during arc-melting of the CoCrCu buttons.

process was carried out as described in the experimental details. The heating and cooling cycle is presented in Figure 5.5 with labels corresponding to the onset of melting at approximately 1100 °C, complete dissolution at $\sim$ 1420 °C, followed by solidification at $\sim$ 1320 °C. The onset of melting and subsequent thermal contraction due to solidification are indicated by the change in shape of the buttons/melt, and is presented in Figure 5.6, which is labeled with red arrows to indicate the changes that occurred in the samples during measurement. For the onset of melting, the red arrow in Figure 5.6 points from the very first slight changes in shape at a 1100 °C radiograph to a radiograph taken at 1120 °C where a red circle outlines the Cu-rich phase on the surface of the CoCrCu buttons that begins to fully melt and

spread outwards. As the melting point of pure Cu is 1085 °C, the visual onset of Cu melting at 1100 °C furnace temperature suggests that, during heating, the furnace thermocouple is about 15 °C higher than the sample during heating. If a similar trend holds during cooling, the sample will be approximately 15 °C hotter than the furnace. As such, the accuracy of the temperature measurements is within ±15 °C.

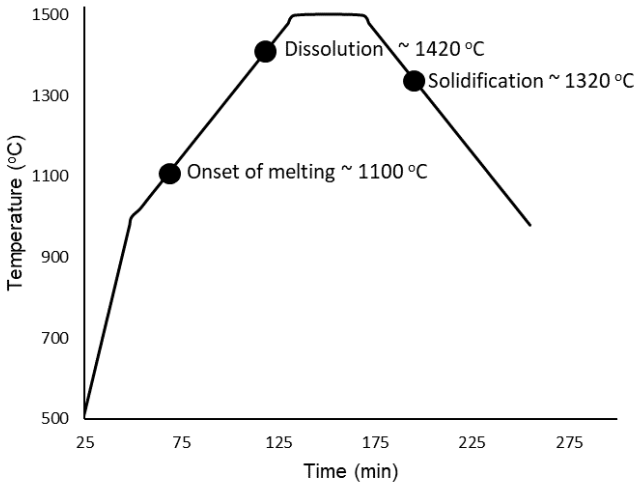

Figure 5.5: Temperature vs. time of the CoCrCu + Ni samples heated and imaged from 1000 °C to 1500 °C and back down to 1000 °C.

Radiographs taken at different temperatures during the heating process are presented in Figure 5.7. The buttons are in the solid state at 1000 °C, while the subsequent radiographs show different stages of melting as well as the final temperature of 1500 °C which was held for approximately 35 min to ensure sufficient mixing had taken place. Full dissolution of the phases occurred at 1420 °C which is noticeable due to the uniform contrast of the molten pool in the crucible at 1420 °C when compared to the darker (Cu-rich) phases

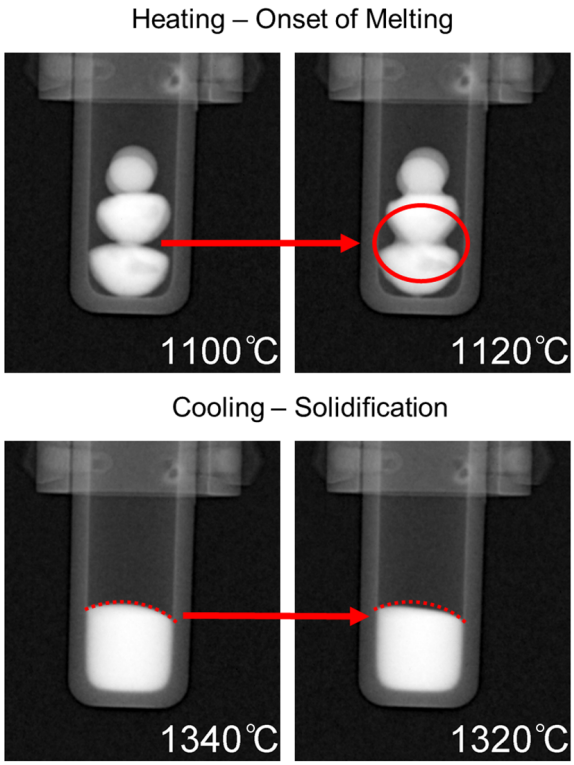

Figure 5.6: Top: Onset of melting as depicted via the dark phase spreading downwards outlined by a red circle. Bottom: Solidification as indicated by thermal contraction inside the dotted red line.

that are present throughout the CoCrCu buttons at the lower temperatures during heating. A full movie-like sequence of the radiographs (recorded in 10 fps → 20 °C steps/s) can be found in the Supplemental.

After the heating and cooling neutron imaging cycle finished, the samples were taken out of the furnace and radiographed on a 360° rotating stage for CT neutron imaging. The reconstructed CT image of the solidified CoCrCuNi alloy solid is presented in Figure 5.8. The surface roughness is likely due to thermal contraction paired with the alloy being

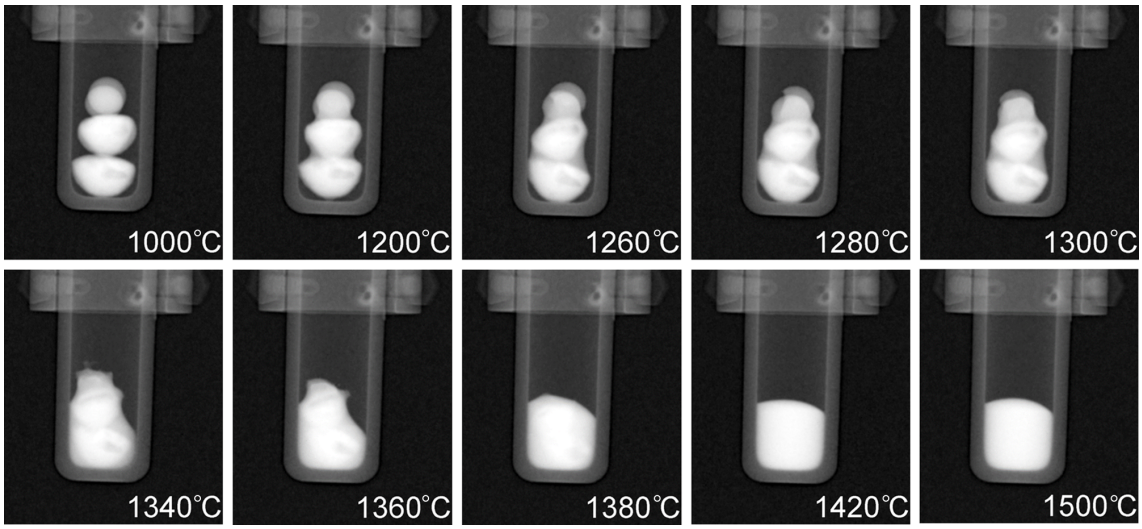

Figure 5.7: Radiographs taken at increasing temperatures of the CoCrCu + Ni buttons inside the alumina crucible in the HOT-A vacuum furnace. A full movie-like sequence of radiographs can be found in the original publication of this work.

in contact with the alumina crucible walls. The overall contrast of the sample is uniform throughout as opposed to the initial presence of the different contrast phases (CoCr-rich and Cu-rich) that are present in Figure 5.4.

5.4 Discussion

The CoCrCuNi alloy has been previously shown to solidify into a uniform dendritic microstructure from arc-melting [140], which is indicative that the microstructure evolved from a single-phase liquid as opposed to the large-scale macroscopic-phase separation that has been observed in similar alloys of CoCrCu [86] and CoCrCuFe [139]. However, there are no reported slow cooling solidification studies on the CoCrCuNi alloy. Previous neutron

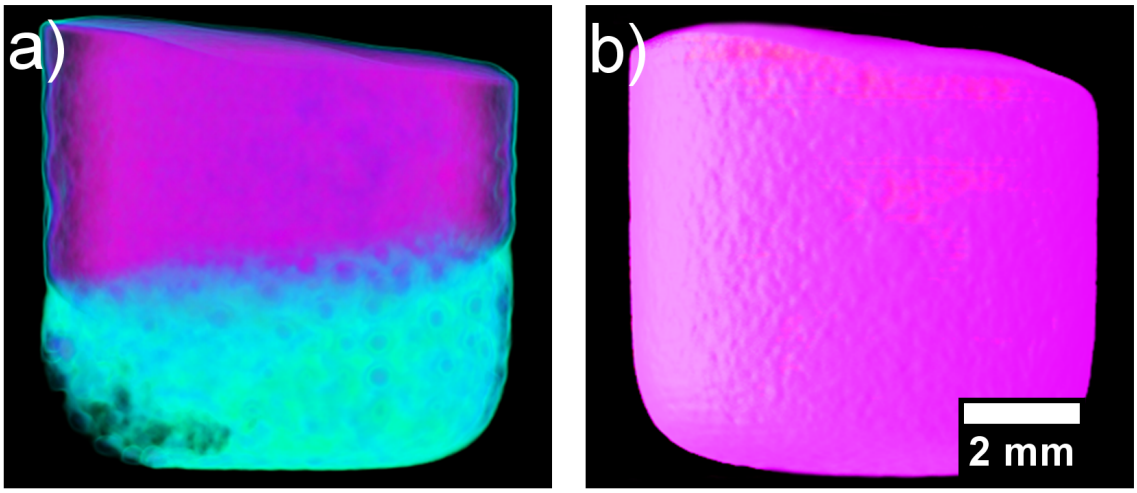

Figure 5.8: (**a**) Reconstructed computed tomography (CT) of the solidified heterogenous CoCrCu alloy, (**b**) Reconstructed CT of the solidified CoCrCuNi alloy.

imaging of the CoCrCu by the present authors resulted in neutron radiographs of the CoCrCu displaying the buttons melting and separating based on density [209]. The stacking of the liquid immiscible phases of CoCr-rich liquid and Cu-rich liquid was characterized by their differences in neutron attenuation. The same experiment was essentially repeated for this work with the equiatomic addition of Ni buttons such that the equiatomic CoCrCu becomes equiatomic CoCrCuNi once melting and dissolution has occurred. This allows for a more equilibrium solidification due to the slow cooling, as well as an opportunity to image the remixing of the immiscible CoCr-rich and Cu-rich liquid phases.

Figure 5.7 displays how the multiple attenuated phases dissolve into one phase, indicating that the previously immiscible CoCr-rich and Cu-rich phases in the CoCrCu alloy became miscible when equiatomic portions of Ni are added to the system. Although pure Ni has a melting point of 1455 °C, the molten Cu present on the surface of the heterogeneous CoCrCu buttons leads to the dissolving of the Ni buttons, which becomes more visible

in Figure 5.7 at 1260 °C. The CT images were processed using ImageJ software, and are presented in Figure 5.8. The CT of the alloys was reconstructed from the radiographs of the immiscible solid CoCrCu alloy (recreated from Ref. [209] with permission from the authors), and the solid CoCrCuNi HEA that was radiographed on a rotating stage for this study, which corresponds to the solid phase presented in the bottom right of Figure 5.6. The crucible was removed from the image after applying color thresholds to reveal the solid CoCrCuNi piece. The CT images represent the final solid forms of the alloys after the in-situ neutron imaging, having been removed from the furnace and imaged while still in the crucible.

Inspection through the cross-sections of the CoCrCuNi revealed no additional phases, indicating that the CoCrCuNi alloy had solidified from a single-phase liquid with no macroscopic-phase separations. This is in contrast to the large phase separation in CoCrCu visible in Figure 5.8a. For the CoCrCu alloy, the purple coloring indicates the CoCr-rich phase while the green coloring represents the Cu-rich phase. The same look-up tables (LUT) were applied in Figure 5.8b for the CoCrCuNi alloy, where no macroscopic liquid phase separation can be seen. The results indicate that Ni acts as a solubility pathway for the Cu-rich liquid phase to enter the solution with the overall melt.

Thermodynamic calculations for the CoCrCuNi alloy system were performed using Thermo-Calc software using the TCHEA3 thermodynamic database to generate an isopleth of $CoCrCuNi_x$ such that the left hand side of the diagram (0 at. % Ni) represents equiatomic CoCrCu while the right hand side of the phase diagram would represent pure Ni. The calculated isopleth present in Figure 5.9 displays the $CoCrCuNi_x$ system from x = 0 to

0.50 where equiatomic CoCrCuNi corresponds to 25 at. % Ni (0.25 mole fraction) which is indicated by a dotted line in Figure 5.9. The calculation of the isopleth for this system shows agreement with previous calculations [86] and experiment [209] for the left hand side of the isopleth (CoCrCu), as there is indeed a significant liquid state miscibility gap for the CoCrCu alloy. The calculations also show that there exists a single-phase liquid region above the miscibility gap until approximately 27.5 at. % Ni, which at percentages greater than this would result in a single phase in the molten state with no liquid phase separation at all.

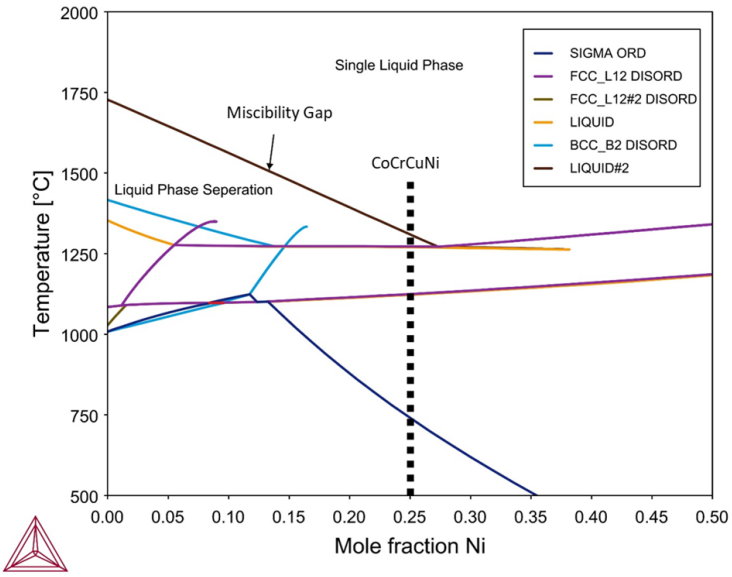

Figure 5.9: Calculated isopleth of the $CoCrCuNi_x$ system using Thermo-Calc software. Legend descriptions: SIGMA ORD = ordered σ phase, FCC_{L12} DISORD = disordered FCC phases, BCC_{B2} DISORD = disordered BCC phases.

The current experiment reached temperatures of 1500 °C and stayed at this tem-

perature to ensure good mixing between the phases. Slow cooling from 1500 °C to room temperature did not yield any changes in neutron attenuation of the CoCrCuNi liquid, which indicates that there was no observable macroscopic liquid phase separation during solidification of the CoCrCuNi alloy. The CT images presented in Figure 5.8 compare the equiatomic CoCrCu (Figure 5.8a) with the equiatomic CoCrCuNi (Figure 5.8b), and correspond to the left hand side of the isopleth in Figure 5.9 (0 at. % Ni) and the dotted line representing equiatomic CoCrCuNi (25 at. % Ni), respectively. The CT of CoCrCuNi in Figure 5.8b shows no macroscopic liquid phase separation, therefore the thermodynamic calculations show good agreement with the experiment, as the miscibility gap line in the calculated phase diagram in Figure 5.9 ends at 27.5 at. % Ni, and is very close to the experimental concentrations used in this study of 25 at. % Ni.

5.5 Summary

The field of high-entropy alloys continues to grow every year, and with this growth comes an enormous amount of never before seen alloy systems with unknown liquid state behavior. As previously shown, neutron imaging can be a very useful technique to elucidate the liquid state behavior of molten alloy systems. With the application of this technique to high-entropy alloys, in-situ imaging of liquid state miscibility has been observed for the first time with the equiatomic additions of Ni to the immiscible CoCrCu system. The current results show the following:

Neutron imaging can be utilized to image liquid state behavior in high-entropy alloys. Imaging was carried out on equiatomic CoCrCu buttons with equiatomic additions

of Ni such that when melting occurred between the alloying elements, full miscibility was achieved.

In-situ neutron imaging was successfully utilized to image in-situ alloying of Ni into an immiscible CoCrCu system. The synthesis of the CoCrCuNi alloy inside the high-temperature furnace was fully imaged via a movie-like sequence of carefully timed radiographs to display the melting/alloying process.

Previous neutron imaging experiments of CoCrCu show the liquid phase separation that occurs between CoCr and Cu. The added Ni in this system acts as a solubility pathway for Cu to enter the solution with the rest of the alloying elements.

In-situ neutron imaging of solidification can provide a novel solution to probe the liquid phases of calculated isopleths and provide valuable insight into the liquid state behavior of HEAs.

Chapter 6

Processing Pathway Effects in CoCrCuNi + X (Fe, Mn) High-Entropy Alloys

6.1 Abstract

A parallel study of mechanical alloying and solidification was carried out on FCC high-entropy alloys (HEAs) CoCrCuNi, CoCrCuFeNi, and CoCrCuMnNi to investigate the effects of each processing methods on the resulting microstructure, crystal structure, and microhardness. Elemental powders were mechanically alloyed followed by spark plasma sintering (SPS) at 800 °C and 900 °C to achieve densified discs, while arc-melting was carried out from bulk pieces of the elemental metals followed by furnace annealing at 800 °C and 900 °C for 5 hours. Both processing routes resulted in a primary FCC phase with secondary Cu-rich FCC segregation as interdendrites for the solidified alloys and particle boundaries for the SPS alloys, with the exception of a small amount of σ phase present in the SPS processed alloys. The solidification of the CoCrCuNi, CoCrCuFeNi, and CoCrCuMnNi HEAs resulted in typical dendritic microstructure, followed by the precipitation of a small Cr-rich phase in the CoCrCuMnNi alloy after annealing. The grain size of the mechanically alloyed powder was approximately 20 nm from Scherrers equation and the SPS processed HEAs consisted of a Cu-rich phase in the particle boundaries, forming cobblestone-like microstructure. The microhardness was examined in the as-cast, annealed, and SPS states. It was found that the SPS processed samples had an increased microhardness by a factor of 2.5. The following work was published in Ref. [281].

6.2 Introduction

The dominating synthesis route throughout the literature for the high-entropy alloys involves liquid-phase methods (predominantly arc-melting), however recent studies have

explored powder metallurgy approaches, particularly focused on the CoCrFeNi [282,283] and AlCoCrFeNi [284–286] HEAs. A recent study of the Al_xCoCrFeNi system comparing the phase composition of the arc-melted alloys vs. sintering of compacted powder indicated the formation of the same phases even though they were microstructurally different (dendritic vs particles/grains) [286].

One of the original HEA papers by Yeh et al. [3] dealt with the primary FCC phase CoCrCuFeNi alloy. Throughout the years, there have been many investigations into the CoCrCuFeNi alloy to understand its tendency for stable FCC phase formation. Such experiments include investigating the mechanical properties [159], recrystallization [150], rapid solidification [151], cold rolling [150, 280], sputter depositing of thin films [287], and liquid phase separation [139,152,153,239]. In order to further investigate phase formation in this alloy, phase predictions for CoCrCuFeNi using CALPHAD produced calculations leading to two FCC phases (CoFeNi-rich and Cu-rich) and two BCC phases (Co-Fe-rich and Cr-rich) [138], which differed from the dual phase FCC solid solution dendritic microstructures from the original solidification studies by Yeh et al. [3]. CALPHAD calculations in Ref. [138] also predicted solid solution phases in two similar alloys, CoCrCuNi (2 FCC + BCC) and CoCrCuMnNi (2FCC + BCC + HCP). However, upon mechanically alloying the CoCrCuNi alloy X-ray diffraction (XRD) analysis on CoCrCuNi, one FCC phase was observed [138]. Mechanical alloying studies of CoCrCuFeNi resulted in a nanostructured alloy, with primarily FCC phase with small amounts of BCC, followed by σ phase after spark plasma sintering (SPS) [266]. In a follow-up study, these authors mechanically alloyed CoCrCuNi and CoCrCuFeNi for 15 h, which resulted in a single FCC phase with small

amounts of BCC. Upon annealing at 1000 °C, the alloys resulted in FCC and σ phase [142]. Similarly, in a solidification study by the present group, alloys of CoCrCuNi, CoCrCuFeNi, and CoCrCuMnNi were prepared via arc-melting which resulted in the as-cast alloys having a two-phase microstructure: FCC dendrites and FCC interdendritic regions [140].

As the field of high-entropy alloys continues to grow, it is crucial to understand the role of processing in these new alloy systems. This work seeks to explore the differences in phase evolution in the processing of the CoCrCuNi, CoCrCuFeNi, and CoCrCuMnNi HEAs via mechanical alloying and spark plasma sintering compared to solidification and annealing. As much of the HEAs found in the literature are synthesized via arc-melting, and since arc-melting is not an equilibrium solidification route, the importance of studying the effects of heat treatment can help elucidate any equilibrium phases that may become present from the heat treatment process. Spark plasma sintering has been shown to increase the hardness in HEAs due to the nanocrystallinity obtained from mechanical alloying [142, 266, 288]. Comparing the phases obtained from heat treatment and SPS at the same temperatures is important for understanding the phases that are formed in HEAs.

6.3 Experimental Procedure

6.3.1 Solidification and Annealing

Equiatomic alloys of CoCrCuNi, CoCrCuFeNi and CoCrCuMnNi were prepared from elemental metallic pieces of purities Co $\geq$ 99.9%, Cr $\geq$ 99.99% , Cu $\geq$ 99.9%, Fe $\geq$ 99.97%, Mn $\geq$ 99.7%, and Ni $\geq$ 99.99% purchased from Alfa Aesar (Ward Hill, Massachusetts). The elemental manganese was pickled prior to alloying using concentrated

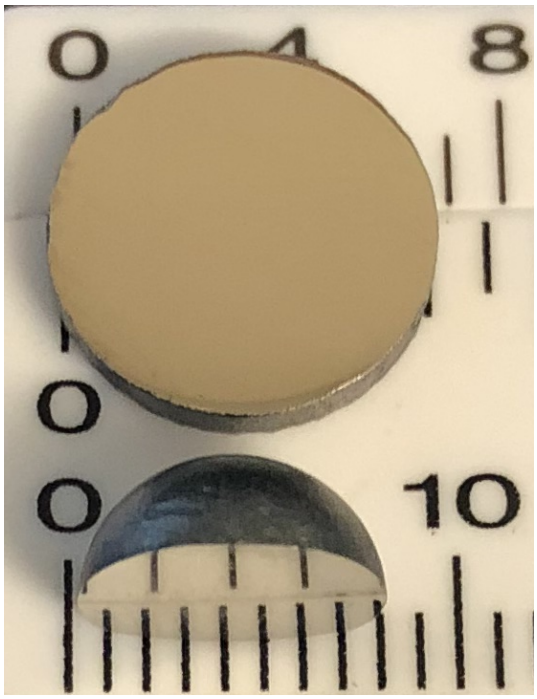

Figure 6.1: Image of a 10 mm HEA disc after spark plasma sintering (top) and a vertically cross sectioned arc-melted button (bottom).

HNO_3 in order to remove surface oxidation, rinsed with water, and stored in acetone until alloying. Samples were weighed to 1.5 g and arc-melted 4 times (flipped three times) on a water-cooled Cu hearth in a Ti-gettered argon atmosphere. The as-cast alloys were then annealed at 800 °C and 900 °C in a tube furnace for 5 h, followed by furnace cooling to room temperature.

6.3.2 Mechanical Alloying and Sintering

Powders of elemental purities Co $\geq$ 99.9%, Cr $\geq$ 99.8% , Cu $\geq$ 99.9%, Fe $\geq$ 99.8%, Mn $\geq$ 99.9%, and Ni $\geq$ 99.9% purchased from Atlantic Equipment Engineers (AEE) (Bergenfield, New Jersey) were mechanically alloyed to synthesize the equiatomic CoCr-

CuNi, CoCrCuFeNi, and CoCrCuMnNi alloys using a SPEX 8000D shaker mill using a hardened 440C stainless steel grinding vial set. The powders were milled with a ball to powder weight ratio of 5:1 using 1/4" stainless steel balls for 20 h. No process control agent was used as cold welding was not an issue with the CoCrCuFeNi and CoCrCuMnNi powders. However, for the CoCrCuNi powder, 1 wt. % stearic acid was used due to the higher fraction of Cu present in the powder. No contamination from the milling media was observed for the CoCrCuMnNi powder, and less than 3 at. % Fe contamination was found in the CoCrCuNi powder. Characterization of Fe contamination from the milling media cannot be determined in the CoCrCuFeNi alloy due to the nominal presence of Fe in the alloy. The milled powder was densified at 75 MPa and sintered with a 200 °C/min heating up to 600 °C followed by a 75 °C/min heating rate to a final temperature of 800 °C or 900 °C for five minutes using a Dr. Sinter LAB Jr. SPS to produce nominal 10 mm diameter by 1 mm thick discs (Fig. 6.1) for each sample.

6.3.3 Characterization

The arc-melted samples were cross-sectioned perpendicular to the chill surface and mounted in Conducto-mount Conductive Mounting Powder and abraded using SiC paper down to 5 μm followed by final polishing of 1, 0.3, and 0.05 μm with Al_2O_3 powder. The densified discs were polished along the face of the disc. Vickers microhardness tests were carried out on the polished surface of the samples using a Phase II Micro Vickers Hardness Tester (Model no. 900-931) at loads of 1 kg for 15 s. The average value of 10 indentations were used to describe the microhardness for each sample except in the case of CoCrCuFeNi annealed at 900 °C, where the average of 5 indentations was used due to sample size.

X-ray diffraction patterns were taken of the powder and flat polished samples using a PANalytical Empyrean Series 2 diffractometer with Cu K_α radiation. The X-ray data was acquired from 20° to 80 ° 2θ with a step size of 0.02° and step time of 40 s/step. The milled powders were also analyzed from 40° to 80° 2θ with a step size 0.02° and step time of 80s/step for higher resolution. Backscattered electron images (BEIs) and energy-dispersive X-ray spectroscopy (EDS) data were obtained from the alloys with an FEI NovaNanoSEM 450 scanning electron microscope.

6.4 Results & Discussion

6.4.1 Arc-melted and Annealed Samples

The arc-melting and solidification of the CoCrCuNi, CoCrCuFeNi, and CoCrCuMnNi alloys led to dendritic microstructures with Cu-rich interdendritic regions as discussed below. Energy-dispersive X-ray spectroscopy data for each of the as-cast samples can be found in Table 6.1. The phase fraction (%) of the dendritic phases of the CoCrCuNi, CoCrCuFeNi, and CoCrCuMnNi alloys were analyzed from the backscattered electron images of the microstructures using ImageJ. The dendritic phase consisted of approximately 85 %, 90 %, and 65 % of the CoCrCuNi, CoCrCuFeNi, and CoCrCuMnNi alloys respectively while the remaining amount of phase fraction is the interdendritic region.

CoCrCuNi

The as-cast CoCrCuNi solidified into CoCrNi-rich dendrites, rejecting the liquid rich in Cu to the interdenritic regions. The dendrites directionally solidified upwards from

the Cu-chill plate of the arc-melting furnace. The same sample was then annealed at 800 °C and 900 °C and returned to room temperature via furnace cooling. The overall morphology of the dendritic microstructure did not change after annealing, and is present as the dark grey dendritic and light grey interdendritic regions of Fig. 6.2a–c. The X-ray diffraction pattern for the CoCrCuNi alloy was indexed as dual FCC peaks and shown in Fig. 6.3, representing the crystal structures for the dendrite and interdendrite phases. The annealing of the CoCrCuNi sample lead to increased intensity for the 200 peak labeled in Fig. 6.3. This intensity of the 200 peak is most likely due to the way the sample was cut perpendicularly to the chill surface, perpendicular to the directionally solidified dendrite. Counter to the CALPHAD predictions given in Ref. [138], no BCC x-ray peaks were found in the diffraction pattern of the CoCrCuNi alloy.

The two FCC phases from the solidification of the alloy that are present are from the CoCrNi-rich and Cu-rich phases. Energy-dispersive X-ray spectroscopy (EDS) of these regions indicated an approximate stoichiometry of $CoCrCu_{0.5}Ni$ for the dendrites and ≈ 85 % Cu (15 at. % balance) for the interdendritic phase, shown in Table 6.1.

CoCrCuFeNi

The dendrites directionally solidified upwards from the Cu-chill plate of the arc-melting furnace shown in Fig. 6.2d. The as-cast dendritic duplex microstructures for the CoCrCuFeNi alloy shows agreement with the solidification microstructures observed in the literature [139, 140]. Annealing the alloys at 800 °C did not have an impact on the microstructure, as shown in Fig. 6.2e. Annealing of the sample at 900 °C also resulted in

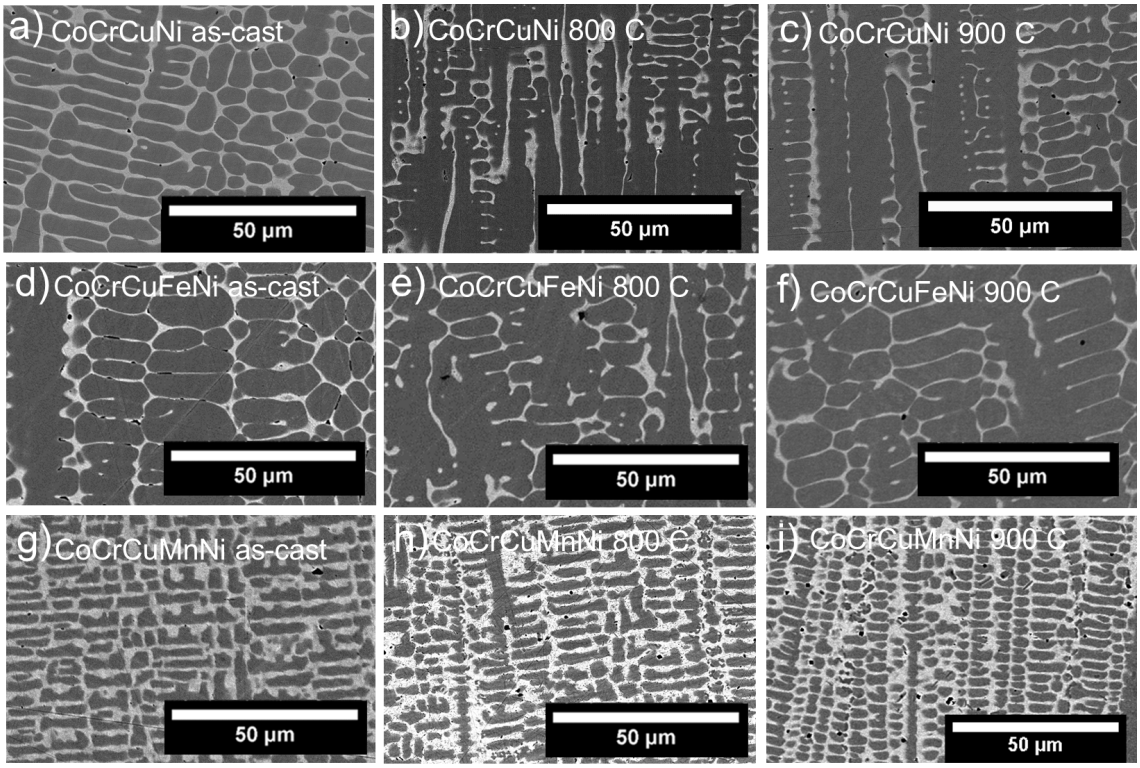

Figure 6.2: Backscattered electron images (BEIs) of the solidification processed HEAs a) CoCrCuNi as-cast, b) CoCrCuNi 800 °C anneal, c) CoCrCuNi 900 °C anneal, d) CoCrCuFeNi as-cast, e) CoCrCuFeNi 800 °C anneal, f) CoCrCuFeNi 900 °C anneal, g) CoCrCuMnNi as-cast, h) CoCrCuMnNi 800 °C anneal, i) CoCrCuMnNi 900 °C anneal.

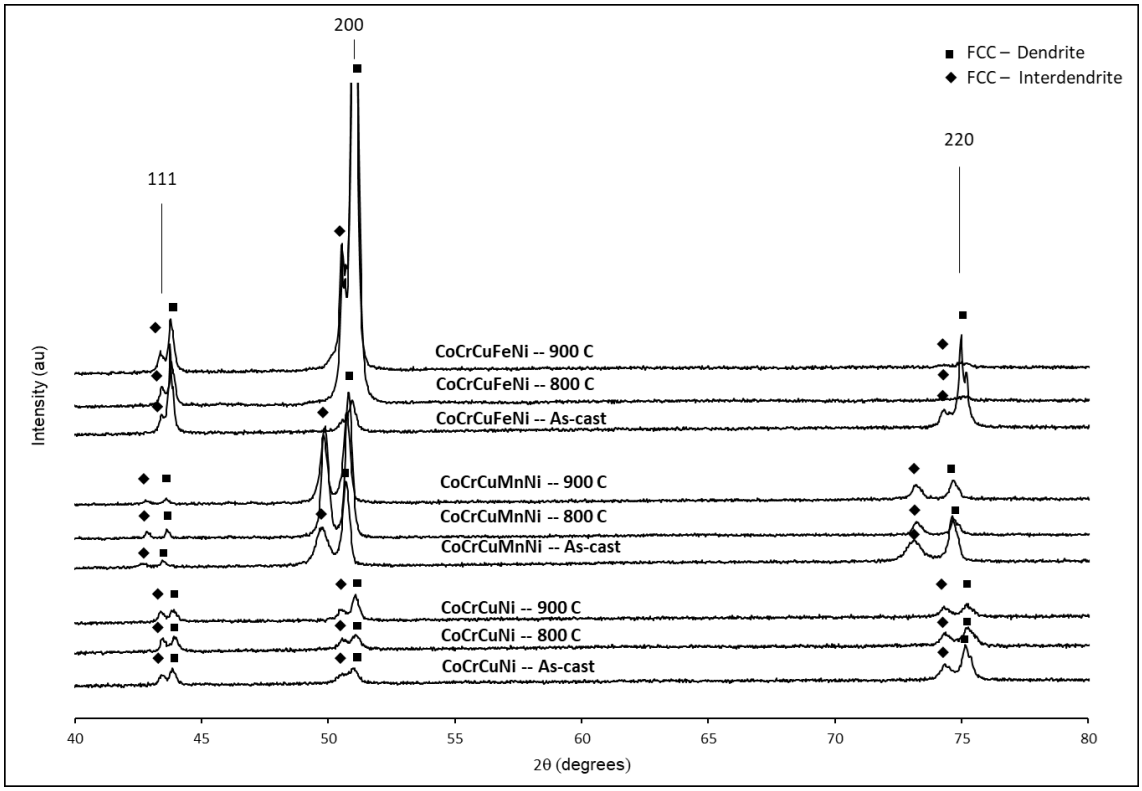

Figure 6.3: X-ray diffraction patterns of the CoCrCuNi, CoCrCuFeNi, and CoCrCuMnNi alloys in the as-cast condition and after annealing at 800 °C and 900 °C.

Table 6.1: Semi-quantitative analysis (at. %) for the energy-dispersive X-ray spectroscopy (EDS) data and corresponding microstructures of the as-cast CoCrCuNi, CoCrCuFeNi, and CoCrCuMnNi alloys. *Precipitates after 800 °C anneal.

Alloy	Region	Co	Cr	Cu	Fe	Mn	Ni
CoCrCuNi	Nominal	25	25	25	–	–	25
	Dendrite	31.4	30.0	14.3	–	–	24.3
	Interdendrite	4.1	4.0	84.1	–	–	7.9
CoCrCuFeNi	Nominal	20	20	20	20	–	20
	Dendrite	23.1	21.4	13.6	22.0	–	19.8
	Interdendrite	4.2	3.9	80.6	4.1	–	7.2
CoCrCuMnNi	Nominal	20	20	20	–	20	20
	Dendrite	29.8	31.7	8.6	–	11.2	18.7
	Interdendrite	8.2	7.2	43.4	–	23.0	18.3
	Precipitates*	24.1	38.2	14.8	–	13.1	9.9

no significant morphology changes or homogenization. As with the CoCrCuNi alloy, the intensity of the 200 reflection which was greater than the 111 reflection in the as-cast state in the XRD patterns also increased with annealing as labeled in Fig. 6.3. Similar to the solidification of the CoCrCuNi, the dendrites have approximately half the amount of Cu than the nominal equiatomic percentages present in the liquid (CoCrCuFeNi, 20 at. % each). The Cu-rich interdendrite is also similar to the interdendrite in CoCrCuNi, ($\sim$ 80 at. % Cu, 20 at. % balance). It appears that adding Fe to CoCrCuNi has no major effect on the microstructure or resultant FCC phases.

CoCrCuMnNi

The CoCrCuMnNi alloy solidified into very jagged dendritic microstructure with CoCrMnNi-rich dendrites and very large CuMnNi-rich interdendrites as shown in Fig. 6.2g. Annealing to 800 °C resulted in Cr-rich precipitates in the interdendritic regions in random

parts of the alloy, which can be seen as small darker grey regions around the dendrite periphery in Figs. 6.2h–i. Annealing to 900 °C led to rounding of the jagged dendrite arms visible in Fig. 6.2i, while still containing the Cr-rich precipitates, the composition of which is found in Table 6.1. The CoCrCuMnNi alloy also displayed two sets of FCC peaks similar to CoCrCuNi and CoCrCuFeNi in Fig. 6.3. The same intensity of the 200 reflection is present as the sample cross section was perpendicular to the directionally solidified dendrites in the same fashion as the CoCrCuNi and CoCrCuFeNi alloys. There is a much wider spacing between the peaks for the dendritic and interdendritic regions, as opposed to the CoCrCuNi and CoCrCuFeNi alloys. This is likely due to the interdendritic regions being rich in Mn and less Cu when compared to the CoCrCuNi and CoCrCuFeNi alloys, which have interdendritic Cu content $\geq$ 80 at. %. This leads to the dual FCC peaks being much more distinct, and are closer to published diffraction data of the CuMn binary alloy [289]. The interdendritic stoichiometry of $\sim$ Cu_2MnNi resulting in FCC phase supports the CALPHAD predictions for FCC phase in these percentages [132].

6.4.2 Mechanical Alloying and Spark Plasma Sintering

Mechanical alloying of the CoCrCuNi, CoCrCuFeNi, and CoCrCuMnNi HEAs from elemental powders resulted in broad single FCC phase diffraction patterns for all three of the alloys, as presented in Fig. 6.4. Using the Scherrer equation, $\tau = \frac{K\lambda}{\beta \cos\theta}$ (with K = 1) on the diffraction pattern in Fig. 6.4, approximate grain sizes for the HEA powders were determined to be around 18 nm, 16 nm, and 20 nm for CoCrCuNi, CoCrCuFeNi, and CoCrCuMnNi respectively. Archimedes' method was carried out using propylene glycol (ρ = 1.04 g/cm^3) to determine the density of the SPS samples compared to the theoretical

density from the rule of mixtures (based on volume fraction), and are presented in Table 6.2. All three alloys resulted in $\geq$ 94 % relative density compared to the theoretical value.

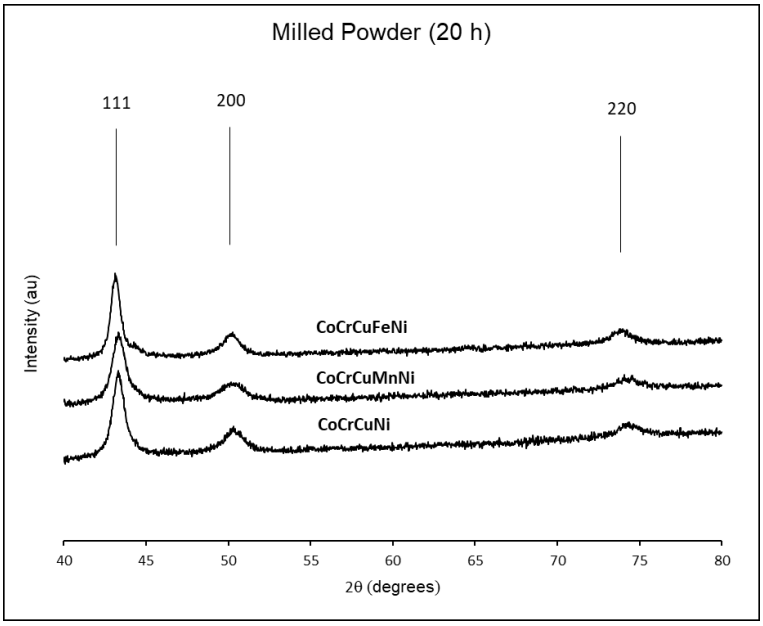

Figure 6.4: X-ray diffraction patterns of the CoCrCuNi, CoCrCuFeNi, and CoCrCuMnNi powders displaying FCC phase after ball milling for 20 h.

Table 6.2: Relative densities for the CoCrCuNi, CoCrCuFeNi and CoCrCuMnNi alloys after SPS using Archimedes' Method compared to the theoretical density using the rule of mixtures.

HEA	ρ (rule of mixtures)	800 °C	900 °C
CoCrCuNi	8.47 g/cm^3	7.96 g/cm^3 – 94.0 %	8.16 g/cm^3 – 96.3 %
CoCrCuFeNi	8.35 g/cm^3	7.84 g/cm^3 – 93.9 %	7.95 g/cm^3 – 95.3 %
CoCrCuMnNi	8.25 g/cm^3	7.86 g/cm^3 – 95.3 %	7.81 g/cm^3 – 94.7 %

CoCrCuNi

Spark plasma sintering of the CoCrCuNi powder lead to the microstructures present in Fig. 6.5a–b. The particles ($\approx 20 - 100$ μm) can be seen packed together as the darker contrast regions in Fig. 6.5a–b, surrounded by a very bright high Z-contrast phase along the boundaries of each particle. The EDS measurements for each of these regions yielded similar atomic percentages compared to solidified counterpart alloys, and are presented in Table 6.3. For example, the particle cores in Fig. 6.5a–b are near-equiatomic while darker particle edges are depleted in Cu and the interparticle regions (boundaries) are close to the atomic concentration of the interdendrite regions of this same alloy processed via arc-melting ($\approx$ 84 at. % Cu). The tabulated comparison between atomic percentages in each region can be found in Table 6.3. Sintering at 900 °C lead to a similar microstructures (Fig. 6.5b) to the microstructure of the 800 °C sintering (Fig. 6.5a). The Cu-rich boundary region can be seen in all of the spacing between the dark particles in a sort of cobblestone-like microstructure. The darker particle edges are randomly dispersed throughout the particles in Fig. 6.5a–b. This phase was revealed to be depleted in Cu while the adjacent particle boundary/interparticle regions are rich in Cu. The X-ray diffraction pattern of the CoCrCuNi alloy is presented in Fig. 6.6 along with the other two MA + SPS processed alloys. The X-ray diffraction pattern was indexed as two sets of FCC phases, as similar to the solidified CoCrCuNi alloy. There is a small peak present in the 800 °C pattern before the primary 111 FCC reflection, which is most likely the σ phase, which was observed for the CoCrCuFeNi alloy after SPS at 900 °C [266] and annealing at 1000 °C [142]. Recent studies have shown the appearance $Cr_{23}C_6$ phases in SPS of similar alloys of AlCoCrFe [288], how-

ever more advanced techniques such as transmission electron microscopy and atom probe tomography are required to accurately determine the C content that may be present as contamination in these alloys in order to accurately determine the nature of the small XRD peaks present in Fig. 6.6, and is outside the scope of this work.

CoCrCuFeNi

The 800 °C and 900 °C SPS of the CoCrCuFeNi HEA produced the same cobblestone like microstructure to the CoCrCuNi alloy, and is presented in Fig. 6.5c–d. Like the CoCrCuNi alloy, the dark contrast particles are near-equiatomic while the boundaries contained $\sim$ 85 % Cu, with the remaining elements being Co, Cr, Fe, and Ni, shown in Table 6.3. Unlike the dendrites in Fig. 6.2d–f, the main particle has double the at.% of Cu when compared to the primary dendrite of the solidified counterpart (Table 6.3). The same darker particle edge phase is also present in the CoCrCuFeNi alloy, and is also depleted in Cu and is present randomly throughout the edges of the majority particle phase of the SPS samples. The X-ray diffraction pattern for the alloy present in Fig. 6.6 also indicated two sets of FCC peaks like its solidified counterpart, however with the presence of an extra peak before the primary FCC 111 reflection, which was previously found to be σ phase for the SPS processing of this alloy at 900 °C in Ref. [266]. The darker Cu-depleted regions may be the small amount σ phase that are present in the XRD patterns however, more extensive research involving transmission electron microscopy is needed to accurately determine the crystal structure of this phase.

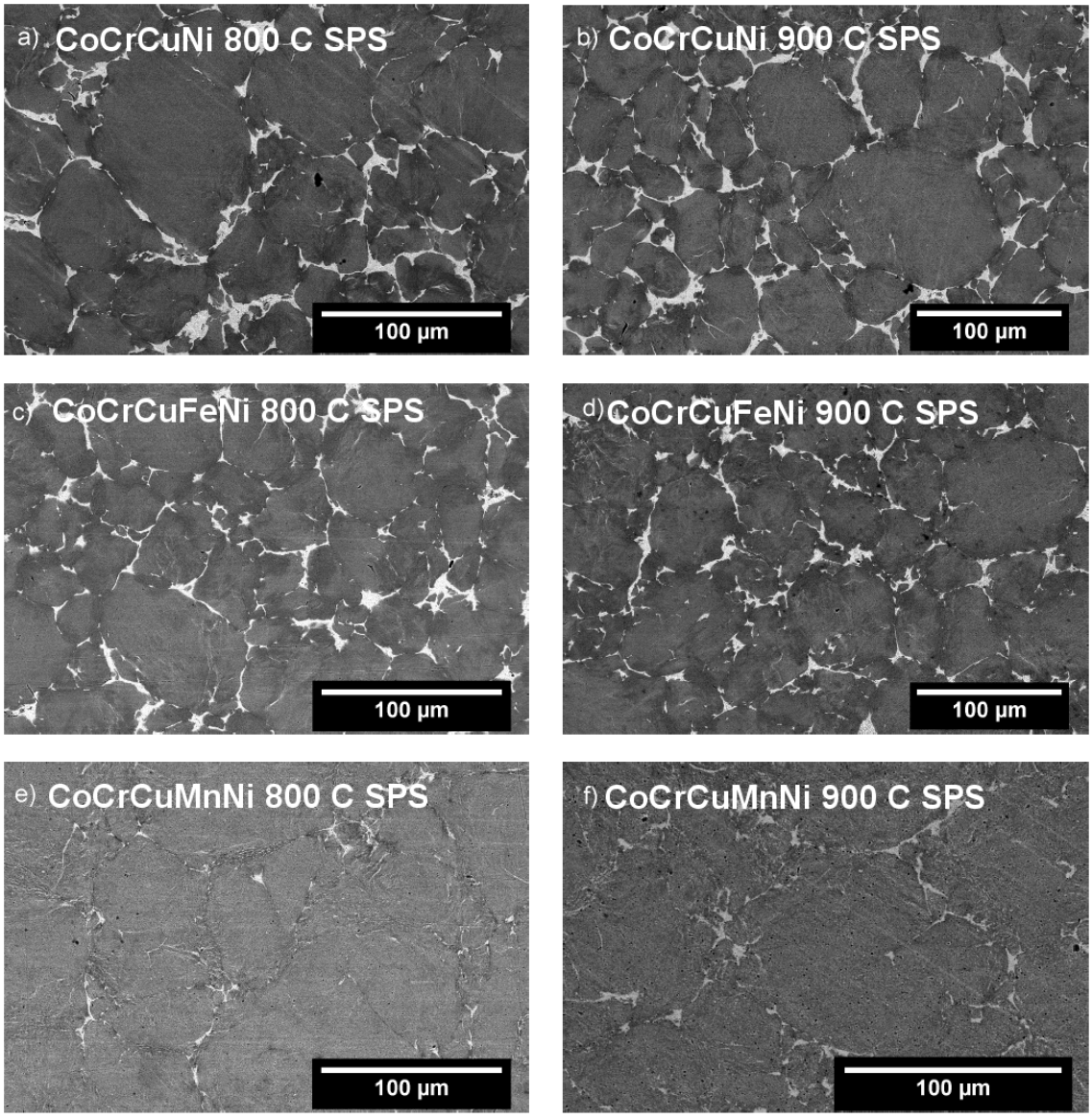

Figure 6.5: Backscattered electron images (BEIs) of the mechanically alloyed-SPS HEAs a) CoCrCuNi 800 °C, b) CoCrCuNi 900 °C c) CoCrCuFeN 800 °C, d) CoCrCuFeNi 900 °C, e) CoCrCuMnNi 800 °C, f) CoCrCuMnNi 900 °C.

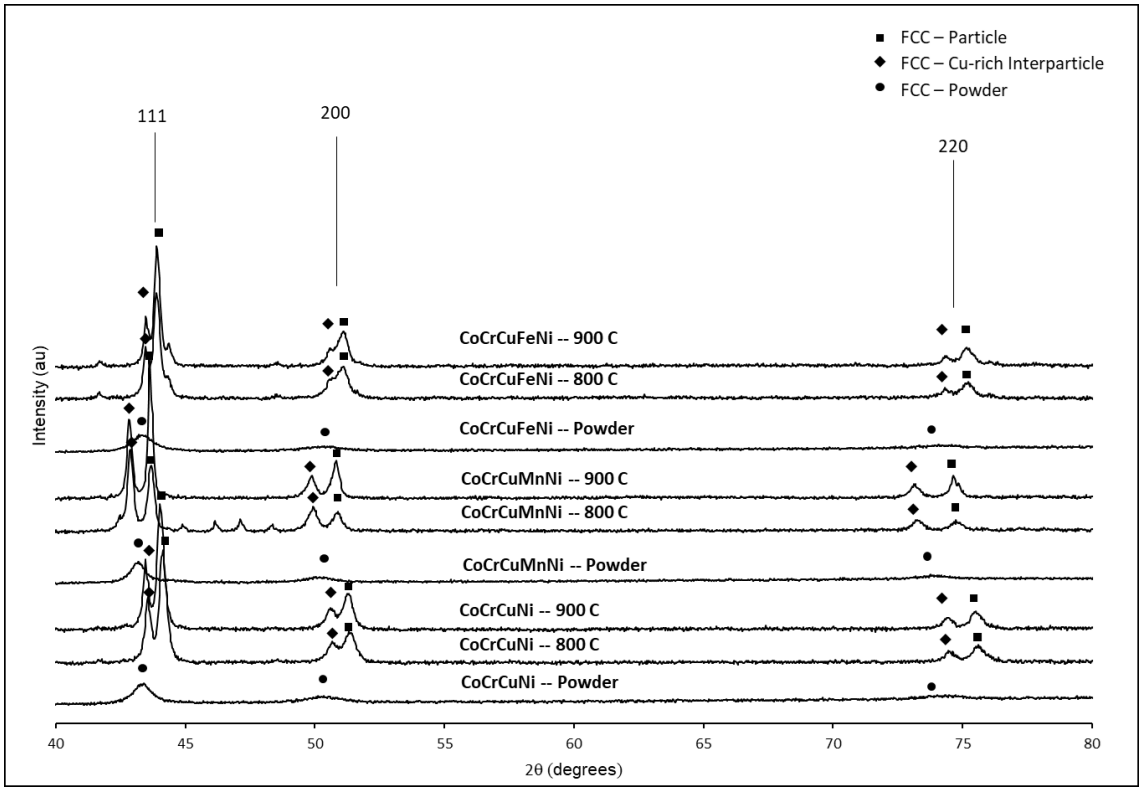

Figure 6.6: X-ray diffraction patterns of the CoCrCuNi, CoCrCuFeNi, and CoCrCuMnNi alloys after ball milling for 20h and subsequent SPS 800 °C and 900 °C.

CoCrCuMnNi

The SPS of the CoCrCuMnNi powder at 800 °C lead to the cobblestone-like microstructure as seen in CoCrCuNi and CoCrCuFeNi. However the particles are packed much closer together than the other two alloys. The main particle phase core appears to be mostly homogeneous, with a composition near nominal equiatomic concentration of the elements while also containing a Cu-depleted particle edge (Table 6.3). In this respect, the particles are distinctively different than the dendritic counterpart primary phase, as there is a significant decrease in Co, Cr, with an increase in Cu and Mn, somewhat resembling a near-equiatomic composition. The interparticle regions, however, are close to the atomic concentrations of the interdendrite regions of the solidified alloy counterpart. The X-ray diffraction pattern for the 800 °C SPS processed alloy shows a number of peaks between the FCC 111 and 200 reflections. These peaks may also be the σ phase observed for CoCrCuFeNi in Ref. [266], as no other intense peaks appear to be present at the higher scattering angles. However, this would need to be confirmed via TEM and is outside the scope of the present investigation. Sintering at 900 °C resulted in only two sets of FCC peaks, nearly identical to the solidified CoCrCuMnNi diffraction pattern in Fig. 6.3.

6.4.3 Microhardness

Vickers microhardness for all three HEAs was carried out on the as-cast, annealed, and SPS processed samples and are presented in Table 6.4. Minor differences (within the same order-of-magnitude) in the microhardness values were observed between the as-cast and solidified+annealed materials. When annealed to 800 °C, the microhardness decreased

Table 6.3: Comparison of the semi-quantitative analysis (at. %) from EDS obtained from the solidified and SPS microstructures. Dendrite and Interdendrite refer to the solidification microstructures in Fig. 6.2 while Particle Core, Particle Edge, and Boundary refer to the SPS processed microstructures in Fig. 6.5.

HEA	Solidification	SPS	SPS	Solidification	SPS
CoCrCuNi	Dendrite	Part. Core	Part. Edge	Interdendrite	Boundary
Co	31.4	23.2	33.0	4.1	4.1
Cr	30.0	23.6	31.1	4.0	2.0
Cu	14.3	26.9	7.59	84.1	84.2
Ni	24.3	22.3	28.3	7.9	9.8
CoCrCuFeNi	Dendrite	Part. Core	Part. Edge	Interdendrite	Boundary
Co	23.1	17.0	22.3	4.2	3.0
Cr	21.4	22.1	28.1	3.9	2.2
Cu	13.6	26.0	6.84	80.6	86.2
Fe	22.0	17.4	21.2	4.1	2.4
Ni	19.8	17.5	21.5	7.2	6.2
CoCrCuMnNi	Dendrite	Part. Core	Part. Edge	Interdendrite	Boundary
Co	29.8	18.6	24.1	8.2	6.4
Cr	31.7	19.6	24.0	7.2	3.3
Cu	8.6	24.7	15.7	43.4	46.9
Mn	11.2	18.6	18.0	23.0	23.3
Ni	18.7	18.4	18.2	18.3	20.2

from 1.76 ± 0.04 GPa to 1.65 ± 0.04 GPa in the CoCrCuNi alloy, and from 1.56 ± 0.05 GPa to 1.43 ± 0.03 GPa in the CoCrCuFeNi alloy. Is is believed that this decrease could be due to the annealing temperatures causing recovery and residual thermal stress relief. Similar observations were made in annealing studies, where the microhardness decreased in the CoCrCuFeNi [150, 280]. In contrast with the previous alloys the microhardness of CoCrCuMnNi alloy increased slightly from 2.11 ± 0.07 GPa to 2.26 ± 0.07 GPa after the 800 °C anneal and back to 2.09 ± 0.06 GPa post 900 °C anneal. Again, the decrease in microhardness is likely attributed to residual thermal stress relief during annealing.

The microhardness for the SPS processed HEAs yielded approximately double and in some cases by 2.5 times the microhardness of their as-cast and annealed counterparts. This increase in hardness can be attributed to Hall-Petch strengthening, as the aforementioned approximate grain size from Scherrer analysis of the milled powder were on the order of $\sim$ 20 nm. Further measurements using transmission electron microscopy will be carried out to validate the grain size range predicted by Scherrer's analyses in the HEAs processed by SPS. Hardness differences could also be due to micro scale morphology differences (such as dendrite arm spacing) and impurity pickup during mechanical alloying.

6.5 Summary

The resulting microstructures, crystal structures, and microhardness of CoCrCuNi, CoCrCuFeNi, and CoCrCuMnNi High-entropy alloys (HEAs) were investigated via solidification processing and subsequent annealing and mechanical alloying followed by spark plasma sintering. It was found that all processing routes resulted in a primary FCC phase,

Table 6.4: Vickers microhardness (GPa) for the CoCrCuNi, CoCrCuFeNi and CoCrCuMnNi samples in the as-cast and post-annealed/post SPS temperatures. Values for microhardness were averaged over 10 indentations. MA + SPS = Mechanically alloyed + spark plasma sintering.

Arc-melted	As-cast	800 °C	900 °C
CoCrCuNi	1.76 ± 0.04	1.77 ± 0.03	1.65 ± 0.04
CoCrCuFeNi	1.56 ± 0.05	1.47 ± 0.04	1.44 ± 0.03
CoCrCuMnNi	2.11 ± 0.07	2.26 ± 0.07	2.09 ± 0.06
MA + SPS	–	800 °C	900 °C
CoCrCuNi	–	4.42 ± 0.17	4.47 ± 0.22
CoCrCuFeNi	–	4.22 ± 0.16	4.22 ± 0.12
CoCrCuMnNi	–	5.12 ± 0.06	3.66 ± 0.04

while secondary FCC phases were found in the interdendrite regions of the solidified samples and at the particle boundaries of the SPS samples. Small amounts of σ phase were observed in the SPS processed alloys, but not in the cast counterparts. All three alloys solidified with dendritic microstructures that did not undergo any significant changes after annealing, with the exception of the CoCrCuMnNi alloy which had Cr-rich precipitates after annealing. The mechanically alloyed powder of all three alloys resulted in single FCC peaks and approximate grain sizes of 20 nm deduced from Scherrer's equation. When comparing the observed phases to the published CALPHAD predictions for these alloys, it can be difficult to confidently and comprehensively explain discrepancies between thermodynamic calculation and observed results. This is due to the many variables that dictate phase formation in these alloys.

Spark plasma sintering on all three samples resulted in a cobblestone-like microstructure with a Cu-rich phase in the particle boundaries. The microhardness for the

SPS alloys increased by a factor of ~ 2.5 when compared to their solidified counterparts. The processing of these alloys via SPS compared to solidification resulted in similar FCC phases and Cu-rich segregation, while doubling the microhardness when compared to the microhardness of the solidification processed HEAs.

Chapter 7

Duplex Phase Hexagonal-Cubic Multiprincipal Element Alloys with High Hardness

7.1 Abstract

We report on the influence of Mn additions on the microstructure and properties of (CoCrCuTi)Mn_x high-entropy alloys containing 5, 10, 15, and 20% Mn prepared by arc-melting. It was observed that the alloys containing less than 10 at. % Mn contained BCC dendrites and a Cu-rich face centered cubic (FCC) interdendritic matrix. In contrast, alloys containing Mn $\geq$ 10 at. %, consisted of a hexagonal dendritic Laves phase (C14, hexagonal, $P6_3/mmc$) with a Cu-rich FCC interdendritic matrix. The particular combination of $Co_{22}Cr_{18}Cu_{20}Mn_{16}Ti_{24}$ was also found to consists of Laves C14 phase hexagonal dendrites in a Cu-rich FCC interdendritic matrix with very small dispersed Ti-rich dendrites when compared to the non-uniform microstructures of the (CoCrCuTi)Mn_x with nominal Mn additions. The hexagonal dendritic phase of the composition $Co_{22}Cr_{18}Cu_{20}Mn_{16}Ti_{24}$ has very high Vickers mircohardness of 996.6 HV 0.01 while the Cu-rich interdendritic matrix has hardness of 457.3 HV 0.01 and overall hardness of both regions equaling 480.0 HV 1. The overall Rockwell hardness was found to be 43 HRC. The $Co_{22}Cr_{18}Cu_{20}Mn_{16}Ti_{24}$ composition was found to have high compressive strength of 1430 MPa and low wear rate of 2.64×10^{-5} $mm^3/m{\cdot}N$. Selected area electron diffraction of this alloy revealed the dendritic phase to be the hexagonal intermetallic Laves(2H)-$MgZn_2$, corresponding to space group $P6_3/mmc$ with lattice parameters approximated to be $a = 4.8$ Å and $c = 7.5$ Å based on fitting the d-spacing of the indexed patterns to previously published data on the Cr_2Ti intermetallic phase. Due to the high alternating hardness of the hexagonal dendritic microstructure and Cu-rich matrix of these alloys, they may be potential candidates for fracture resistant and wear-based applications due to their low density and high hardness.

Isopleths of the CoCrCuMnTi system were generated using the ThermoCalc software with TCHEA3 database and were used to help elucidate phase formation in these alloys.

7.2 Introduction

The search for single-phase solid solutions with exceptional mechanical properties has driven research in the field of multicomponent alloys over the past 15 years. The majority of the 3d transition metal HEAs in the literature typically consist of body centered cubic (BCC) and face centered cubic (FCC) crystallographic systems as well as B2 phase, σ phase, and other intermetallics [1–6, 22]. Many of these alloy systems exhibit high strength [30, 245, 290], wear resistance [4, 291–293], and corrosion resistance [294, 295], which make these multiprincipal element alloys potential candidates for engineering applications.

There is only a small fraction of hexagonal HEAs/MPEAs/CCAs compared to those with FCC and BCC crystal structure. The first attempt to create hexagonal HEAs stemmed from using elements containing stable room temperature hexagonal close packed (HCP) crystal structures, which ultimately led to the amorphization of the entire mixture for the BeCoMgTi and BeCoMgTiZn systems [296]. Shortly after, Li et al. synthesized AlCuMgMnZn which was found to be mainly composed of HCP and Al-Mn quasicrystal phases [297]. Using a CALPHAD approach, Gao et al. in 2013 predicted that CoOsReRu HEA would have HCP crystal structure [298], which was later experimentally verified by Gao in 2016 [299]. One of the first experimental observations of hexagonal crystal structure in an HEAs was found by Takeuchi et al. in 2014 with the arc-melting of heavy lanthanide HEAs DyGdLuTbY and DyGdLuTbTm [300]. This study demonstrated that simple solid

solutions in HEAs could exist in hexagonal closed packed structure. Later than year, Youssef et al. observed HCP crystal structure in a light metal HEA, which was observed when the as-milled FCC crystal structure of $AlLiMg_{0.5}ScTi_{1.5}$ was converted to HCP after annealing at 500 for 1 hour [301]. Since these discoveries, the amount of HEAs/MPEAs/CCAs that either have a majority hexagonal closed packed (HCP) or ordered hexagonal intermetallic phase are still very few, which are presented in Table 7.1. From the alloys shown in the table, only recently was the HCP phase seen in a purely 3d transition metal HEA with high pressure processing of the Cantor alloy, CoCrFeMnNi at 54 GPa where it was observed that the HCP phase was partially retained after depressurization [302]. Table 7.1 provides a summary of many hexagonal HEAs/MPEAs that contain precious metals [298,299,303] and rare-earth metals [300,301,304–308], which can be very costly for manufacturing purposes. As for 3d transition metal HEAs, there are yet to be any other hexagonal systems observed in the literature other than the high pressure processed Cantor alloy [302].

Recent work by the present group demonstrated a the presence of a large immiscibility in quaternary and quinary 3d transition metal MPEAs when the alloy contains equiatomic CoCrCu [140]. It was found that due to large stable liquid miscibility gap in equiatomic CoCrCu [86], specific alloying elements (Fe, Mn, Ni, V) would either shift the overall composition towards a single-phase liquid or liquid phase separation [209]. This liquid state immiscibility was then observed in-situ by the present authors using neutron imaging of the melting and remixing of phases when equiatomic CoCrCu is alloyed with Ni to make equiatomic CoCrCuNi [278]. Three MPEAs CoCrCuNi, CoCrCuFeNi, and CoCrCuMnNi from the previous study solidified with uniform dendritic microstructures,

Table 7.1: Multiprinicipal element alloys/high-entropy alloys containing hexagonal crystal structures. MA = Mechanical alloying, EML = Electromagnetic levitation, AM = Arc-melting, MS = Melt spinning. [1] = Atomic percentages: $Ir_{0.19}Os_{0.22}Re_{0.21}Rh_{0.20}Ru_{0.19}$. TD = Thermal decomposition of single-source precursors

Composition	Structure	Processing	Ref.
AlCrNbTiV	Laves (C14)	AM	[309]
AlCrNbTiVZr	Laves (C14)	AM	[309]
AlCuMgMnZn	HCP	IM	[297]
$AlLiMg_{0.5}ScTi_{1.5}$	HCP	MA + $\frac{500°C}{1\text{ hr}}$	[301]
CoCrFeMnNi	HCP	AM + 54.1 GPa	[302]
CoFeReRu	HCP	AM	[299]
CoOsReRu	HCP	CALPHAD	[298]
CrNiTiVZr	Laves (C14)	MS	[310]
DyGdHoTbY	Mg-type	EML	[304]
DyGdHoTbY	$P6_3/mmc$	EML	[307]
DyGdHoLuTb	$P6_3/mmc$	EML	[308]
DyGdLuTbY	HCP	AM	[300]
DyGdLuTbTm	HCP	AM	[300]
GdHoLaTbY	HCP	AM	[306]
HfLaScTiYZr	HCP	AM	[305]
IrOsReRhRu[1]	HCP	TD	[303]

indicating that the alloy most likely solidified from a single phase liquid as opposed to undergoing solidification after liquid phase separation. The dendritically solidifying CoCrCuNi, CoCrCuFeNi, and CoCrCuMnNi MPEAs contained duplex FCC microstructures, consisting of an FCC Cu-depleted dendritic phase and an FCC Cu-rich interdendritic matrix [140]. As for hexagonal crystal structure in these 3d transition metal systems, several studies indicate that CoCrMn is a hexagonal close packed system when Mn $\geq$ 4% [311,312]. Phase equilibrium studies [313] of the ternary CoCrTi system [102] indicate that both cubic (C15) and hexagonal (C36) Laves phases could exist, which extend from the Co-Ti binary side from Co_2Ti to the Cr-Ti binary side to Cr_2Ti with full solubility of Co and Cr through the isothermal section of the form $(Co,Cr)_2Ti$ when Ti remains $\sim$ 33 at. % [313].

In view of the above discussion, the objective of this work is to understand the microstructure, mechanical properties, and wear properties of CoCrCu-based alloys that contain Mn and Ti, as well as to establish the effects these alloying elements have on hexagonal crystal structure formation.

7.3 Experimental Procedure

In the present investigation, alloys combinations of Co, Cr, Cu, Mn, and Ti consisting of CoCrCuTi (0 at. % Mn), $(CoCrCuTi)_{95}Mn_5$ (5 at. % Mn), $(CoCrCuTi)_{90}Mn_{10}$ (10 at. % Mn), $(CoCrCuTi)_{85}Mn_{15}$ (15 at. % Mn), CoCrCuMnTi (20 at. % Mn), and $Co_{22}Cr_{18}Cu_{20}Mn_{16}Ti_{24}$ were prepared from raw elements of purities Co $\geq$ 99.9%, Cr $\geq$ 99.99% , Cu $\geq$ 99.9% , Mn $\geq$ 99.7%, and Ti $\geq$ 99.7% purchased from Alfa Aesar (Ward Hill, Massachusetts). Samples were weighed to 1.5 g and arc-melted 4 times (flipped three

times) on a water-cooled Cu hearth in a Ti-gettered argon atmosphere. The elemental manganese was pickled prior to alloying using concentrated HNO_3 in order to remove surface oxidation, rinsed with water, and stored in acetone until alloying. The arc-melted samples were vertically cross-sectioned and mounted in Conducto-mount Conductive Mounting Powder and abraded using SiC paper down to 5 μm and polished in steps of 1 μm, 0.3 μm, and 0.05 μm with Al_2O_3 powder and colloidal silica.

Vickers microhardness tests were carried out on the polished surface of the alloy samples using a Phase II Micro Vickers Hardness Tester (Model no. 900-931) at loads of 10 g for the dendrite/interdendrite regions, as it was observed that the indentations were small enough to fit inside dendrite and interdendrite region without touching the boundary of the other. However, 1 kg loads for 15 s were used across both regions and the average value of 10 indentations were used to describe the microhardness for each region. In addition to Vickers hardness, Rockwell hardness (HRC) tests were taken of a larger piece of the $Co_{22}Cr_{18}Cu_{20}Mn_{16}Ti_{24}$ alloy with a load of 150 kg using a Phase 2 Rockwell tester (Model no. 900-331D), for which the values were averaged over 5 indentations. Archimedes method was carried out using propylene glycol (ρ = 1.04 g/cm^3) to determine the density of the $Co_{22}Cr_{18}Cu_{20}Mn_{16}Ti_{24}$ alloy to be 7.05 g/cm^3.

X-ray diffraction patterns (XRD) were taken of the flat polished samples using a PANalytical Empyrean Series 2 diffractometer with Cu K_α radiation. The X-ray data for $Co_{22}Cr_{18}Cu_{20}Mn_{16}Ti_{24}$ was acquired from 20° to 100° with a step size of 0.02° and step time of 100s/step while the remaining alloys had a step time of 40s/step. Backscattered electron images (BEIs) and energy-dispersive X-ray spectroscopy (EDS) data were obtained with an

FEI NovaNanoSEM 450 scanning electron microscope. Transmission electron microscopy (TEM) samples were prepared with an FEI Quanta 3D 2009 SEM/FIB from the polished arc-melted buttons. TEM was performed on the samples with FEI TEM Tecnai12 and FEI STEM Titan Themis 300 operated at 300 keV equipped with a high-angle annular dark-field (HAADF) detector.

Compression specimens were cut from arc-melted buttons into 4 mm wide by 6 mm height pieces, where the long dimension of the compression sample is perpendicular to the bottom of the as-cast button. The alloy was then compressed using a strain rate of 5×10^{-3} mm/s. Dry reciprocating sliding wear tests were conducted using a NANOVEA Mechanical Tester in relative humidity of 46 % and room temperature of 21.5 . The parameters of the scratch test involved an applied load of 5 N using a 3 mm tungsten carbide ball, scratch length of 5 mm perpendicular to dendritic growth direction of the arc-melted sample, scratch speed of 200 mm/min, for 1000 cycles (full length of scratch and back, 5mm + 5mm). A diagram of the scratch tester is present in Fig. 7.1.

Equilibrium phase diagrams and Scheil solidification diagrams for the alloy system were calculated using the CALPHAD approach utilizing ThermoCalc software. The thermodynamic database used, high entropy alloy v3 (TCHEA3), is the newest iteration of a specialized database developed for complex compositions with multiple principal elements. It is important to note this database includes select elements from the periodic table for which the database as assessed particular binary and ternary systems that are used to extrapolate thermodynamic calculations of higher order systems. According to ThermoCalc, for the CoCrCuMnTi alloy system all possible binaries are critically assessed but out of the

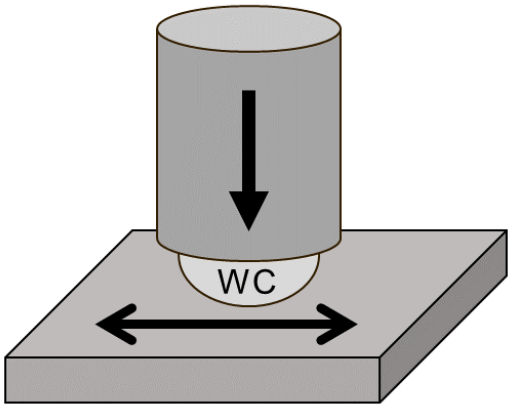

Figure 7.1: Diagram of scratch testing setup for the obtaining wear rate of the alloy against a WC ball.

ten ternary subsystems, only CoCrCu, CoCrTi, and CoCuMn are critically assessed and CoCuTi tentatively assessed; leaving the other six ternary subsystems unassessed in the current iteration of the database.

7.4 Results & Discussion

X-ray diffraction patterns of the as-cast alloys are presented in Fig. 7.2. The as-cast CoCrCuTi and $(CoCrCuTi)_{95}Mn_5$ contain two sets of BCC peaks and a set of FCC peaks. At Mn concentrations $\geq$ 10 at. %, the BCC phase disappears and is replaced by non-trivial peaks present in the diffraction pattern along with the FCC phase, which appears to be slightly shifted from the addition of Mn. The non-trivial peaks were indexed as Laves(C14/2H)-$MgZn_2$ structure type (space group 194, $P6_3/mmc$), corresponding to the Cr_2Ti diffraction pattern form [314].

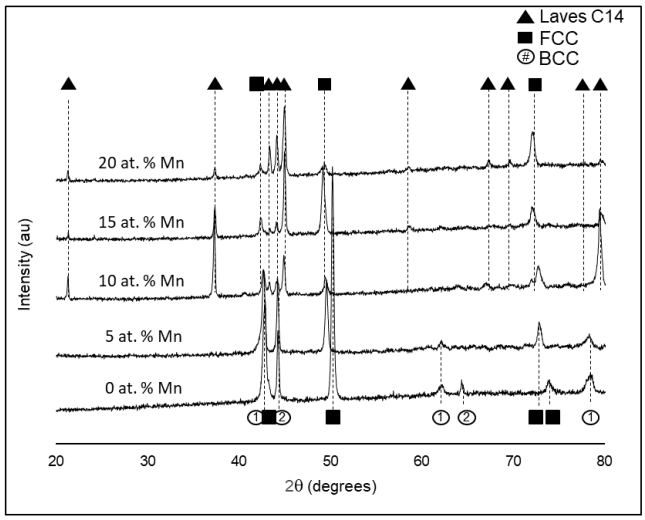

Figure 7.2: X-ray diffraction pattern of CoCrCuTi, $(CoCrCuTi)_{95}Mn_5$, $(CoCrCuTi)_{90}Mn_{10}$, $(CoCrCuTi)_{85}Mn_{15}$, and CoCrCuMnTi with corresponding peak labels.

Fig. 7.3 displays the diffraction pattern for the $Co_{22}Cr_{18}Cu_{20}Mn_{16}Ti_{24}$ alloy, however now with an additional peak present at approximately 29.5 2θ labeled as '*'. This peak is not present in any of the diffraction patterns for the Laves C14 or Laves C15 Cr_2Ti diffraction patterns [314]. This peak may be attributable to this phase, however more work is needed to understand if this peak belongs to a different phase and is outside of the scope of the present investigation.

7.4.1 Scanning Electron Microscopy

Varying Concentrations of Mn

The solidification of the CoCrCuTi sample resulted in microstructures consisting of two CoCrTi-rich dendritic regions and a Cu-rich interdendrite matrix which are shown by arrows in the backscattered electron image (BEI) in Fig. 7.4a. As the volume fraction of

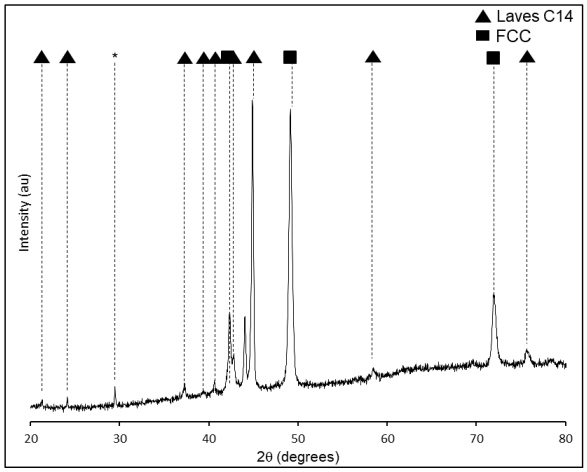

Figure 7.3: X-ray diffraction pattern of $Co_{22}Cr_{18}Cu_{20}Mn_{16}Ti_{24}$ displaying both Laves C14 and FCC peaks.

the two darkest phases are the majority of the sample, they are the phases responsible for the two sets of BCC peaks present in the XRD pattern in Fig. 7.2. The darkest contrast dendrites labeled D_{BCC1} are the first to solidify, which is inferred from the dendrite arms being encapsulated in the larger, lighter contrast dendrites labeled D_{BCC2}. The D_{BCC2} dendrites appear to form perictectically from the D_{BCC1} + remaining liquid, that is, once the peritectic phase completely surrounds the pro-peritectic phase, the liquid transforms to D_{BCC2}. The D_{BCC1} dendrites contain significantly more Cr than the D_{BCC2} dendrites, while the interdendrite regions contain mostly Cu (93 at. %). Therefore, the ID is attributed to the FCC peaks present in the CoCrCuTi diffraction pattern in Fig. 7.2 and is labeled as such in Fig. 7.4 as ID_{FCC}. The tabulated energy dispersive X-ray spectroscopy (EDS) data for each of the alloys in this study is presented in Table 7.2.

The addition of 5 at. % Mn to equiatomic CoCrCuTi to form $(CoCrCuTi)_{95}Mn_5$ resulted in the microstructure in Fig. 7.4b. The microstructure is similar to the CoCrCuTi alloy, however now present is a randomly dispersed Cr-rich dendrite ($\sim$ 83 at. % Cr), and is indicated in Fig. 7.4b by a white arrow and label D_{Cr}. The concentration of 10 at. % Mn to CoCrCuTi at 90% of the alloy, led to very clear hexagonal dendritic morphology of the CoCrTi-rich dendrites, which is indicated by the angled direction of the secondary dendrite arms as opposed to the perpendicular secondary dendrite arms found in the solidification of cubic systems. Like the previous compositions, the interdendritic region is also Cu-rich at 76.2 at. % Cu, similar to the previous alloys however with much more dispersed D_{Cr} throughout the material (Fig. 7.4c). From the XRD pattern in Fig. 7.2, the hexagonal Laves phase appears in place of the BCC phases when Mn is $\geq$ 10 at. %, and we attribute this phase to the majority dendritic phase present in Fig. 7.4c and is labeled D_{Laves}.

The nature of hexagonal dendritic growth which results in secondary dendrite arms that are not perpendicular to the primary arms. Inn cubic dendritic growth, the secondary and tertiary dendrite arms grow at 90 ngles from the primary dendrite arm. The overall volume fraction of D_{Cr} was too small to contribute peaks in the XRD pattern. Increasing the concentration of Mn to 15 at. % led to very similar microstructures (Fig. 7.4d) that were observed in Fig. 7.4c, however now with the presence of additional cubical dendrites that are rich in Ti ($\sim$ 49 at. % Ti). These Ti-rich dendrites are labeled as D_{Ti} and appear randomly throughout the microstructure. When equiatomic concentrations of each alloying element are added to form CoCrCuMnTi (20 at. % each), the system led to the microstructure in Fig. 7.4e, where the majority dendritic phase consisted of D_{Laves}, while the D_{Cr} dendrites

are dispersed randomly throughout the microstructure. The interdendritic phase, ID_{FCC} contained 77.6 at. % Cu and 20.4 at. % Mn.

$Co_{22}Cr_{18}Cu_{20}Mn_{16}Ti_{24}$

In an effort to reduce the D_{Cr} and D_{Ti} phases, such that the alloy only would only consist of the D_{Laves} and ID_{FCC} phases, the $Co_{22}Cr_{18}Cu_{20}Mn_{16}Ti_{24}$ was designed by measuring the atomic concentrations of bulk regions in the microstructure that had little to no D_{Cr} or D_{Ti}. This new composition is present in Fig. 7.4f and in lower magnification in Fig. 7.5 to illustrate the macrostructure. The composition led to very similar microstructures and phases to the previous combinations, however without the presence of the large D_{Cr} phase and contained a much smaller volume fraction of the D_{Ti} dendrites. The small black D_{Ti} dendrites are present throughout and appear to be first in the solidification process. The next to solidify is the CoCrTi-rich Laves phase dendrite which is the majority phase of the material. Image analysis of Fig. 7.5 using ImageJ to process the intensities of the contrasts between the phases results in the majority dendrite phase being approximately 85% of the alloy for the cross-section in Fig. 7.5. Solidification is completed upon freezing of the Cu-rich interdendritic liquid (70 at. % Cu).

7.4.2 Transmission Electron Microscopy

Fig. 7.6 displays a Z-contrast high-angle annular dark field (HAADF) image of the hexagonal dendrite D_{Laves} and FCC interdendrite region ID_{FCC}. Elemental mapping of the regions in Fig. 7.6 are consistent with the EDS data in Table 7.2.

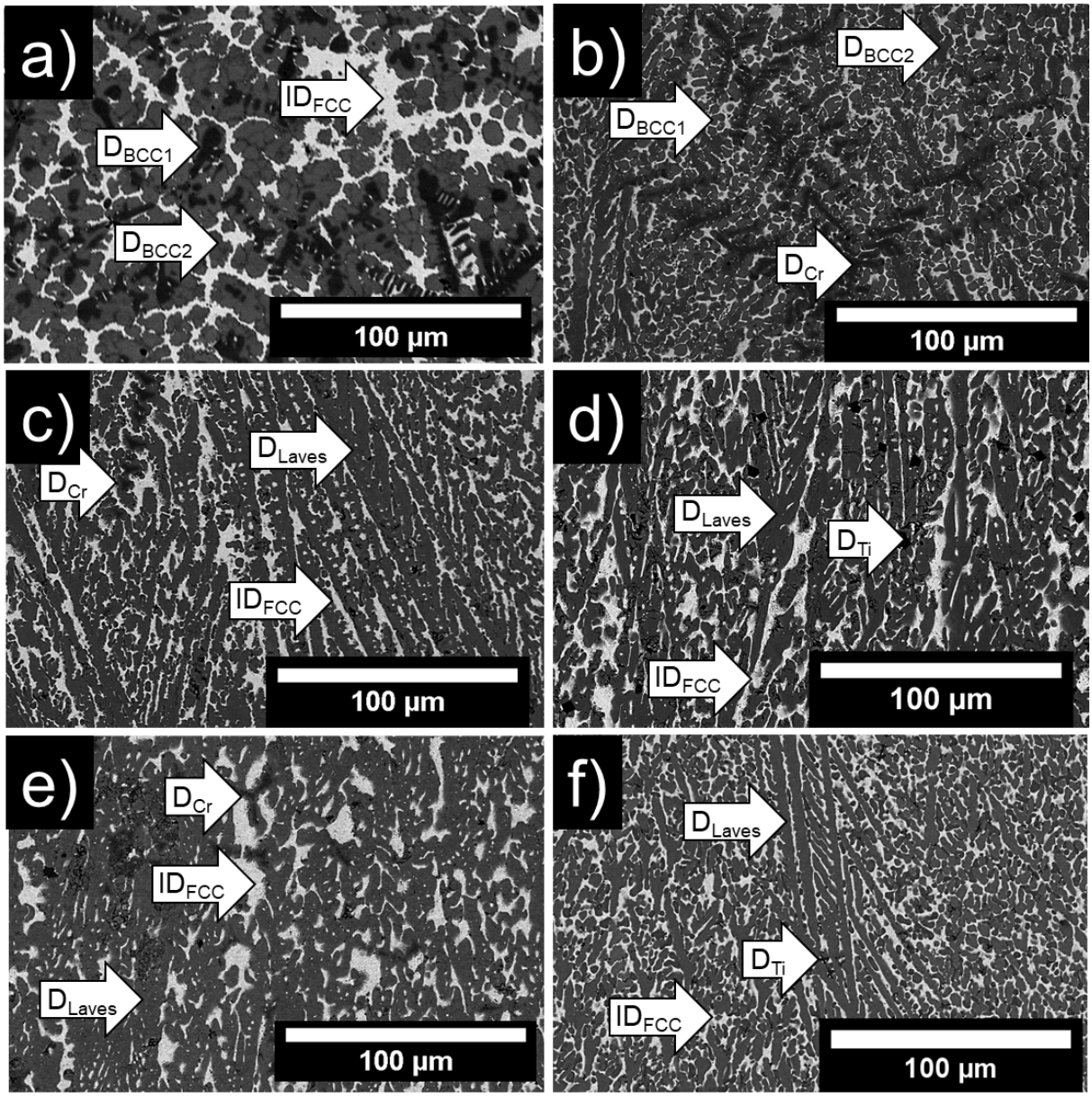

Figure 7.4: Backscattered electron images (BEIs) of alloys a) equiatomic CoCrCuTi (0 at. % Mn), b) $(CoCrCuTi)_{95}Mn_5$ c) $(CoCrCuTi)_{90}Mn_{10}$ d) $(CoCrCuTi)_{85}Mn_{15}$ e) CoCrCuMnTi, and the refined composition f) $Co_{22}Cr_{18}Cu_{20}Mn_{16}Ti_{24}$. D = dendrite, DC = dendrite core, DE = dendrite edge, ID = interdendrite

Table 7.2: Semi-quantitative analysis for the energy-dispersive X-ray spectroscopy (EDS) data and corresponding crystal structures for the (CoCrCuTi)Mn_x alloys and $Co_{22}Cr_{18}Cu_{20}Mn_{16}Ti_{24}$ in at. %.

Alloy	Region	Co	Cr	Cu	Mn	Ti e
CoCrCuTi	Nominal (at. %)	25.00	25.00	25.00	–	25.00
	Nominal (wt. %)	26.50	23.39	28.58	–	21.53
	D_{BCC1}	25.4	45.5	4.7	–	24.4
	D_{BCC2}	29.8	34.4	6.1	–	29.7
	ID_{FCC}	2.8	1.0	93.4	–	2.8
$(CoCrCuTi)_{95}Mn_5$	Nominal (at. %)	23.75	23.75	23.75	5.00	23.75
	Nominal (wt. %)	25.20	22.23	27.17	4.94	20.46
	D_{BCC1}	29.4	31.0	7.1	4.5	28.0
	D_{BCC2}	40.2	6.9	10.3	2.5	40.2
	D_{Cr}	6.9	83.1	1.1	2.9	6.0
	ID_{FCC}	3.5	3.0	79.3	10.8	3.4
$(CoCrCuTi)_{90}Mn_{10}$	Nominal (at. %)	22.50	22.50	22.50	10.00	22.50
	Nominal (wt. %)	23.89	21.07	25.75	9.89	19.40
	D_{Laves}	31.3	27.2	4.3	6.7	30.6
	D_{Cr}	5.7	83.7	0.1	4.8	5.2
	ID_{FCC}	4.4	4.1	76.2	10.8	4.6
$(CoCrCuTi)_{85}Mn_{15}$	Nominal (at. %)	21.25	21.25	21.25	15.00	21.25
	Nominal (wt. %)	22.57	19.91	24.34	14.85	18.33
	D_{Laves}	28.2	28.4	3.3	11.0	29.0
	D_{Cr}	10.1	64.9	5.1	9.9	10.0
	D_{Ti}	23.9	17.7	3.2	6.5	48.7
	ID_{FCC}	7.3	1.9	60.7	23.7	6.4
CoCrCuMnTi	Nominal (at. %)	20.00	20.00	20.00	20.00	20.00
	Nominal (wt. %)	21.25	18.75	22.92	19.81	17.26
	D_{Laves}	27.2	27.1	7.2	10.4	28.1
	D_{Cr}	6.5	78.5	1.2	8.1	5.8
	D_{Ti}	–	–	–	–	≥ 50
	ID_{FCC}	0.8	0.7	77.6	20.4	0.7
$Co_{22}Cr_{18}Cu_{20}Mn_{16}Ti_{24}$	Nominal (at. %)	22.50	17.70	19.90	15.80	24.00
	Nominal (wt. %)	23.99	16.67	22.89	15.67	20.78 –
	D_{Laves}	26.6	27.6	3.3	12.8	29.9
	D_{Ti}	23.2	16.4	3.4	6.7	50.5
	ID_{FCC}	3.8	2.9	70.0	19.1	4.3

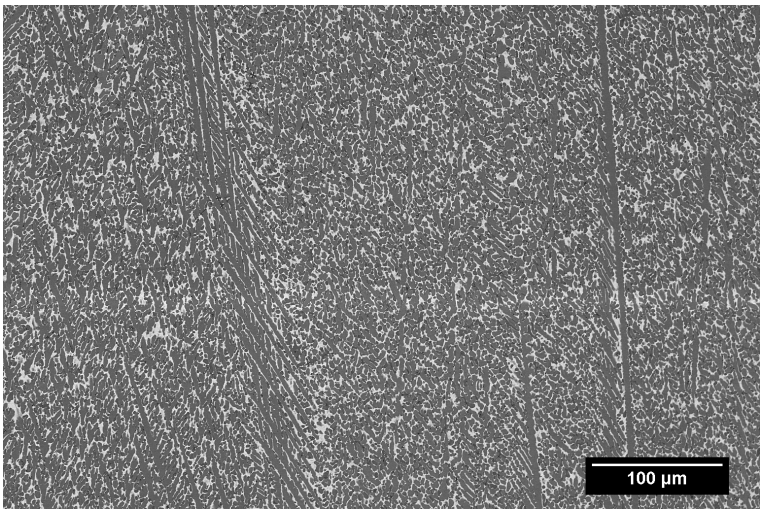

Figure 7.5: Backscattered electron image of $Co_{22}Cr_{18}Cu_{20}Mn_{16}Ti_{24}$ displaying the overall macrostructure of the system. The darker regions are the dendrites while the lighter regions are the Cu-rich interdendrite.

Analysis of the selected area electron diffraction (SAED) patterns in Fig. 7.6 of the $Co_{22}Cr_{18}Cu_{20}Mn_{16}Ti_{24}$ alloy revealed the crystal structure of the majority dendrite phase to be consistent with the Laves C14 crystal structure studied in Ref. [314]. The diffraction pattern in Fig. 7.6b is of the [0001] zone axis and displays perfect hexagonal symmetry such that the angle between the diffraction spots are 60° while Figs. 7.6c-d display zone axes $[10\bar{1}2]$ and $[\bar{2}112]$ respectively. The d-spacing of the directions in the SAED patterns are consistent with a structure form of Cr_2Ti with Laves(2H)-$MgZn_2$ structure type, corresponding to space group $P6_3/mmc$ (194) [314]. The lattice parameters of the system are estimated to be $a \approx 4.8$ Å and $c \approx 7.5$ Å with c/a ratio ≈ 1.56, based on fitting the d-spacing of the indexed patterns to the published data in Ref. [314]. The angles between the zone axes are presented below:

$\angle([1000], [10\bar{1}2]) = 29.0°$

$\angle([1000], [1123]) = 32.6°$

$\angle([1123], [1\bar{2}16]) = 50.3°$

$\angle([1\bar{2}16], [1\bar{2}11]) = 14.9°$

$\angle([1\bar{2}11], [\bar{2}112]) = 43.9°$

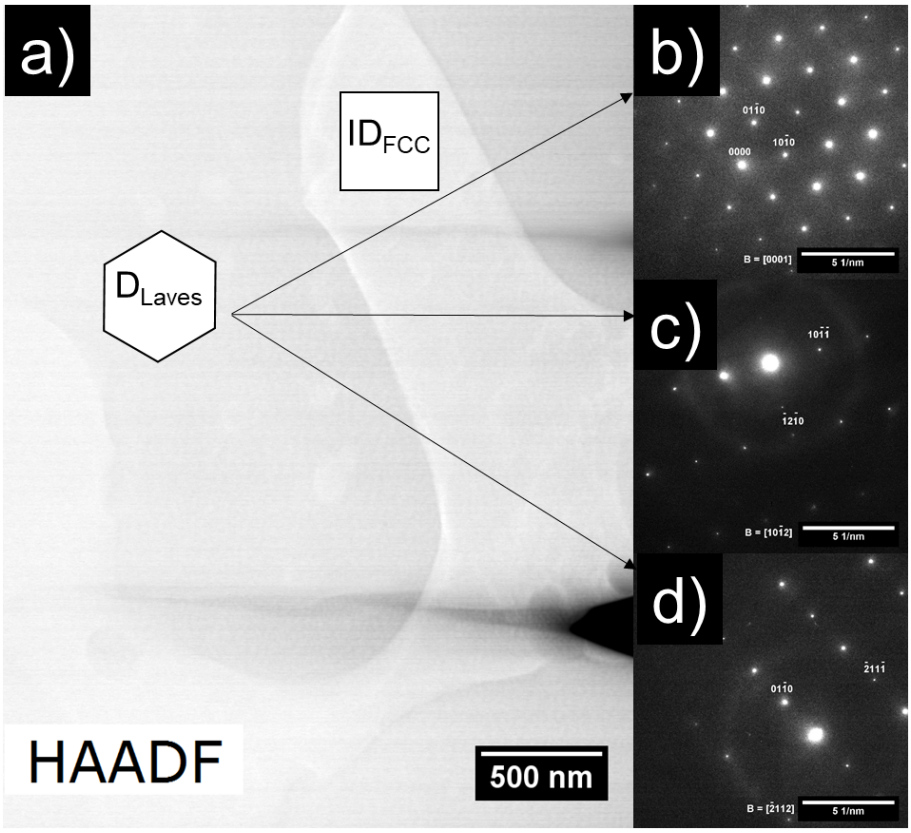

Figure 7.6: a) High-angle annular dark field image (HAADF) of dendrite/interdendrite regions of $Co_{22}Cr_{18}Cu_{20}Mn_{16}Ti_{24}$. Selected area diffraction (SAED) patterns corresponding to b) [0001] c) $[10\bar{1}2]$, and d) $[\bar{2}112]$ zone axes.

As the main dendrites have an approximate composition of $Co_{27}Cr_{28}Cu_3Mn_{13}Ti_{30}$, the structure form of Cr_2Ti may actually be of the form $(Co,Cr,Cu,Mn)_2Ti$, which is similar to the predicted solubility of Co and Cr in the ternary CoCrTi, where the Laves phases extend in solubility from Co_2Ti to Cr_2Ti in the form of $(Co,Cr)_2Ti$ as predicted by Zhou et al. [313]. In this case, the Cu and Mn could be randomly substituting positions of the Co and Cr due to their similar atomic size. However, more extensive TEM studies are needed to determine their specific positions and is beyond the scope of this current investigation. The crystal system for the small D_{Ti} dendrites dispersed throughout the sample were analyzed in the same fashion and found to be of CsCl-type structure corresponding to space group $Pm\bar{3}m$ (221) [315].

7.4.3 Thermodynamic Calculations

The calculated isopleth for $CoCrCuMn_xTi$ is presented in Fig. 7.7. There are significant differences when comparing this equilibrium calculation to the XRD patterns and SEM-EDS analysis of the select $CoCrCuMn_xTi$ alloys reported above. The most prominent feature of the isopleth is an apparent liquid phase separation across the entire compositional range from equiatomic CoCrCuTi to equiatomic CoCrCuMnTi. This prediction is not supported by the current experimental observations of any of the $CoCrCuMn_xTi$ alloys which did not exhibit any microstructural signs of liquid phase separation. Across the composition at the liquidus temperature the solid phase predicted is a $(Co\text{-}Cr)_2Ti$ type cubic C15 laves phase while a $(Co\text{-}Cr\text{-}Mn)_2Ti$ hexagonal C14 laves has increasing stability as Mn is increased. At intermediate temperatures between the liquidus and solidus, there is a Cr-rich BCC predicted and finally at the solidus a copper rich FCC phase resulting from

the liquid phase separation. At lower temperatures the laves phases are not predicted to be stable and decompose into a Cr-rich BCC phase and a CoTi type ordered B2. As Mn is increased, CALPHAD predicts it will segregate to both Cr-rich BCC and Cu-rich FCC.

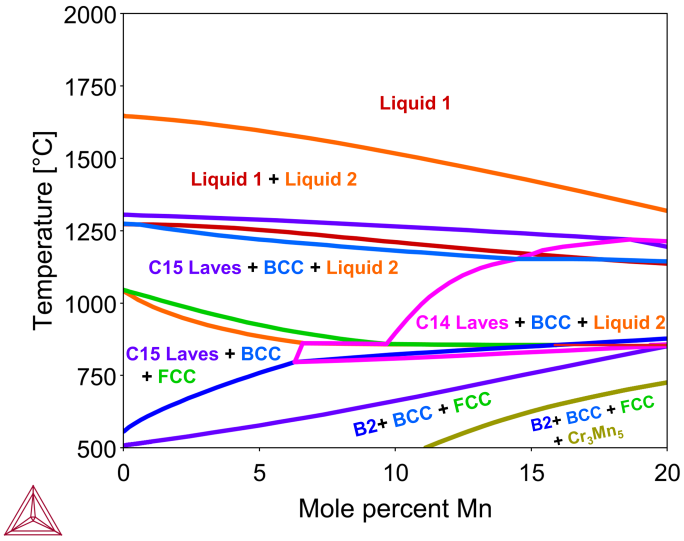

Figure 7.7: Calculated isopleth for the $CoCrCuMn_xTi$ alloy system up to 20 at. % Mn

A step diagram for the $Co_{22}Cr_{18}Cu_{20}Mn_{16}Ti_{24}$ alloy is presented in Fig. 7.8, where the mole fraction of individual phases is a function of temperature. The red and orange lines present in Fig. 7.8 represent the liquid phases predicted in the alloy. At approximately 1400 , the first solid phase predicted is the $(CoCrMn)_2Ti$ type Laves C14 phase which is also accompanied by an increase in the CuMn-rich liquid phase (solute rejection to the interdendritic liquid). Again there is a liquid phase separation present in the step diagram that is not in agreement with the experimental results as the microstructure showed no signs of spherical phase separations in the microstructure [55]. At roughly 850 , the Cu rich liquid solidifies into an FCC phase while a Cr-rich BCC is predicted as a small mol fraction of

the system. Eventually the Laves C14 phase is predicted to decompose sharply and convert to ordered CoTi type B2 phase and a Cr-rich disordered BCC phase. Two intermetallic phases Cr_3Mn_5 and $Co_{10}Cu_{57}Ti_{33}$ are predicted at the lower temperature range of the plot which are most likely inaccessible in experiment due to limited diffusion kinetics at those temperatures. Comparing the high temperature solid equilibrium phases predicted to the XRD and EDS of $Co_{22}Cr_{18}Cu_{20}Mn_{16}Ti_{24}$ there is reasonable agreement with the major phases.

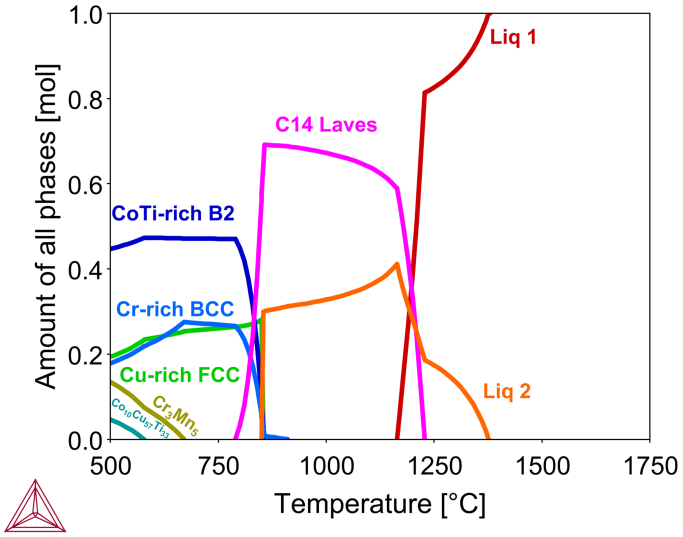

Figure 7.8: Calculated equilibrium step diagram for the $Co_{22}Cr_{18}Cu_{20}Mn_{16}Ti_{24}$ alloy presenting the relative amounts of each equilibrium phase as a function of temperature.

7.4.4 Mechanical & Wear Properties

The microhardness of the $Co_{22}Cr_{18}Cu_{20}Mn_{16}Ti_{24}$ composition was averaged over 10 indentations across the length of the sample for each of the regions examined and are

summarized in Table 7.3. The majority phase dendrite D_{Laves} was found to be 996.6 ± 57.2 HV 0.01 while the interdendritic region ID_{FCC} has microhardness of 457.3 ± 87.0 HV 0.01. Indentations over bulk regions yielded an average microhardness of 480 ± 21.4 HV 1. The dendritic morphology of this material results in an alternating ∼ 2:1 hardness between the two majority phases, where the D_{Laves} dendrite is twice as hard as the ID_{FCC} interdendrite. Rockwell hardness tests were also carried out over average regions of a bulk sample which resulted in a hardness of 43 ± 2.0 HRC averaged over 5 indentations.

Table 7.3: Hardness corresponding to each phase in $Co_{22}Cr_{18}Cu_{20}Mn_{16}Ti_{24}$. Hardness of the bulk areas were under a 1 kg load, while the D_{Laves} and ID_{FCC} were measured with a 10 g load. *Rockwell indentations for the bulk were taken across average areas of the large sample, and smaller features were not measured due to their relative size to the HRC indenter. Therefore, HRC listed above for the D and ID regions are converted from Vickers to Rockwell using the measured HV 0.01 values.

Region	Vickers	Rockwell
Bulk	480.2 ± 21.4 HV 1	43 ± 2.0 HRC
D_{Laves}	996.6 ± 57.2 HV 0.01	(68 HRC)*
ID_{FCC}	457.3 ± 87.0 HV 0.01	(46 HRC)*

The compressive strength for the $Co_{22}Cr_{18}Cu_{20}Mn_{16}Ti_{24}$ alloy was measured to be 1430 MPa followed by fracture with no appreciable plastic deformation, and is presented in Fig. 7.9.

The main mode of wear for the test in this study was determined to be abrasive wear with large amounts of fragmentation, the wear tracks of which are presented in Fig.

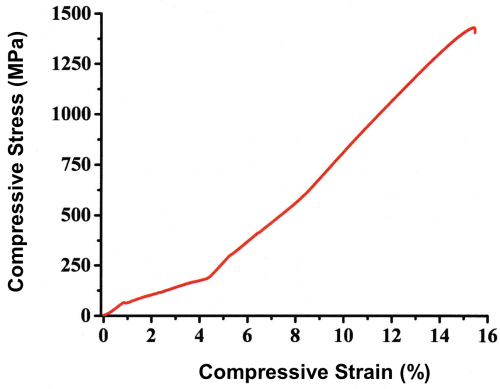

Figure 7.9: Compressive stress-strain curve for the $Co_{22}Cr_{18}Cu_{20}Mn_{16}Ti_{24}$ alloy.

7.10. The wear track on the $Co_{22}Cr_{18}Cu_{20}Mn_{16}Ti_{24}$ alloy from the 3 mm WC ball is very jagged, likely resulting from the brittleness of the material, previously indicated from the lack of plastic deformation during compression testing. Large amounts of cracking can be seen in several locations at the very end of the wear track in Fig. 7.10a, where there are visible dark cracks, as well as the middle of the wear track in Fig. 7.10b. The wear track also appears to be uneven in the normal direction, which may also be a result of brittleness of the sample. The wear rate was calculated using the Archard equation (Eq. 7.1) [316],

$$\kappa = \frac{V_w}{S \cdot N} \left(\frac{mm^3}{m \cdot N} \right) \tag{7.1}$$

where κ is the wear coefficient, V_w is the volume loss, S is the sliding distance, and N is the normal load. The wear rate for this material was calculated to be 2.64 $\times$ 10^{-5} mm^3/m·N which is comparable to wear rate in MPEA/HEA systems $Al_{0.2}Ti_{0.75}CoCrFeNi$ [317] (worn against WC) and $Al_{0.6}CoCrFeNi$ [293] (worn against steel) and an order of magnitude lower than the CoCrFeMnNi and $Al_{0.1}CoCrFeNi$ HEAs [318] (worn against Si_3N_4). The alternat-

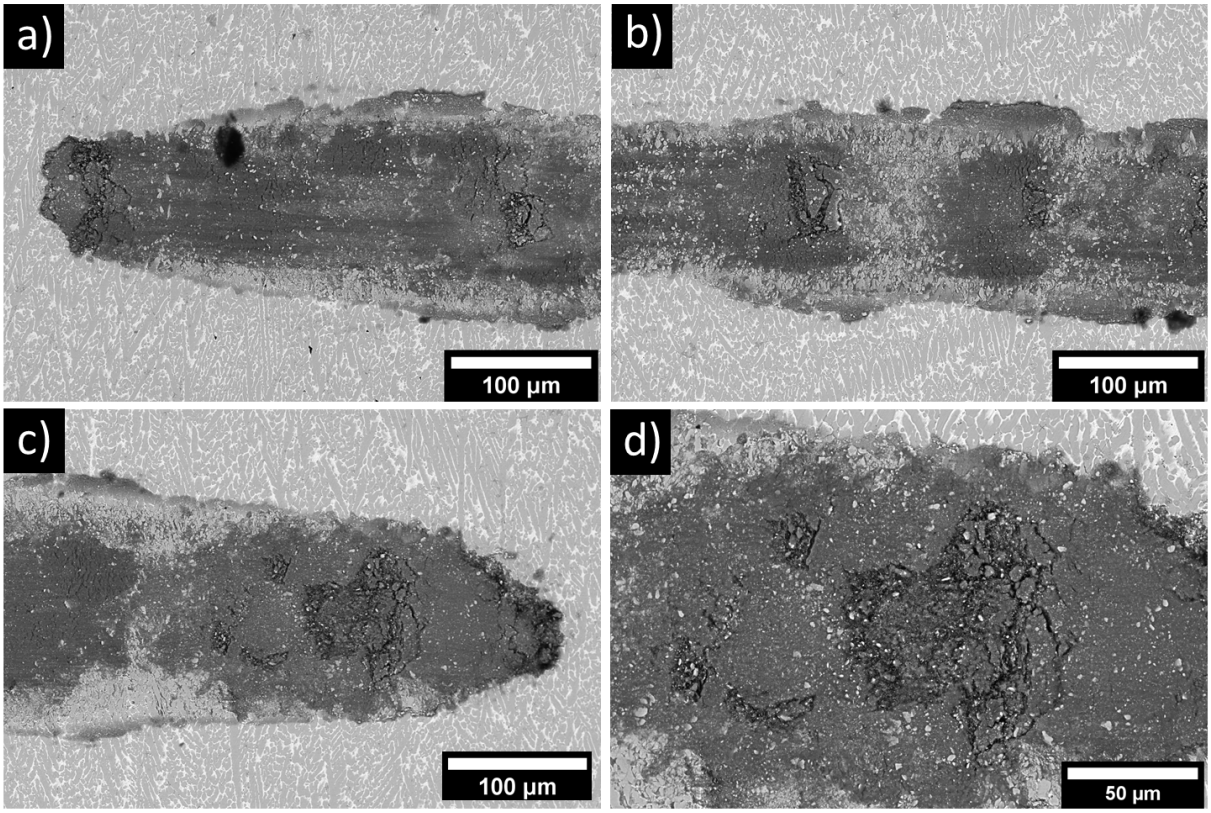

Figure 7.10: Backscattered electron images of the a) edge of the wear track, b) middle of the wear track, c) opposite edge of the wear track, d) magnification of the cracking at the opposite edge of the wear track.

ing 2:1 hardness of the dendritic hexagonal Laves phase and the Cu-rich FCC interdenritic may have potential for wear and fracture-resistant applications, as the Cu-rich matrix may have the potential to blunt crack propagation. However, this is not readily apparent from the micrographs in Fig. 7.10 and is outside of the scope of this present investigation.

7.5 Summary

Below, the findings of the investigation into the CoCrCuMnTi alloy system are summarized:

- Alloys of CoCrCuTi, $(CoCrCuTi)_{95}Mn_5$, $(CoCrCuTi)_{90}Mn_{10}$, $(CoCrCuTi)_{85}Mn_{15}$, and CoCrCuMnTi were investigated to understand the critical Mn concentration for the formation of Laves C14 phase in these systems.

- The results indicate for the first time that MPEAs consisting of purely 3d transition metals can solidify with a majority hexagonal phase from arc-melting when Mn is higher than 10 at. %.

- The results show reasonable agreement with the ThermoCalc predictions of the phases in these alloys, however several factors may be responsible for the discrepancy between the CALPHAD predictions and experimental observations, two of which being: (1) out of the ten ternary subsystems of CoCrCuMnTi, only CoCrCu, CoCrTi, and CoCuMn are critically assessed and CoCuTi tentatively assessed; leaving the other six ternary subsystems unassessed in the current iteration of the database which may lead to incorrect predictions and (2) due to the fast-cooling rates of the arc-melting process

some of the low temperature phases may not have had time to form.

- The alloy composition of $Co_{22}Cr_{18}Cu_{20}Mn_{16}Ti_{24}$ was designed by using EDS analysis to determine atomic concentrations in areas of the CoCrCuMnTi alloy that only contained the dendritic Laves phase and FCC interdendritic phase. This alloy was found to have considerable dendritic hardness.

- For the $Co_{22}Cr_{18}Cu_{20}Mn_{16}Ti_{24}$ alloy there exists a $\sim$ 2:1 Vickers hardness between the Laves phase dendrites (996 HV 0.01) and FCC interdendrites (457 HV 0.01) while the overall Vickers hardness of the material is 480 HV 1, which may have the potential for fracture and wear-resistant applications as the Cu-rich FCC phase could be potentially more ductile than the hexagonal intermetallic primary phase.

- The extremely hard Laves phase dendrites in contrast to the Cu-rich FCC interdendritic matrix may fall under the classification of a type of metal matrix composite. The $Co_{22}Cr_{18}Cu_{20}Mn_{16}Ti_{24}$ alloy Rockwell hardness of 43 HRC and relatively high compressive strength of 1430 MPa with moderate density of 7.05 g/cm^3 could potentially be harnessed for wear based applications, as the relatively small in-air wear rate of 2.64×10^{-5} mm^3/m·N could be improved with tailoring of the interdendritic regions of the material to be larger or smaller depending on the application.

Chapter 8

Solidification Processing and Cooling Rate Effects on Hexagonal Multiprincipal Element Alloys

8.1 Abstract

The solidification microstructures of the hexagonal $Co_{22}Cr_{18}Cu_{20}Mn_{16}Ti_{24}$ HEA were studied via electromagnetic levitation processing (EML) to elucidate the solidification microstructures and phase formation in this alloy. Differential scanning calorimetry (DSC) of a small piece of the alloy displayed three distinct peaks at 905 °C, 1205 °C, and 1295 °C which were used to determine processing temperatures. Multiple duplicates of the $Co_{22}Cr_{18}Cu_{20}Mn_{16}Ti_{24}$ alloys were synthesized using arc-melting to produce spherical 1.5 g buttons, which were then processed via EML. The samples were remelted and solidified in the following (4) conditions: (1) Solidification via drop casting directly from superheated temperatures, (2) interrupting slow solidification in the magnetic field via drop casting, (3) interrupting slow re-melting in the magnetic field via drop casting, and (4) solidified slowly in the magnetic field. Scanning electron microscopy (SEM), X-ray diffraction (XRD), transmission electron microscopy (TEM), and atom probe tomography (APT) were carried out for microstructural characterization. When solidified with a slow cooling rate, these alloys tend to form CoTi-rich dispersed dendrites that appear in random locations of the alloy. It was found that high cooling rates of led to the suppression of the randomly dispersed CoTi-rich dendrites.

8.2 Introduction

The majority of the high-entropy alloys [1–6] in the literature tend to form cubic phases, while the hexagonal phase has only been observed in a handful of HEA systems, such as those primarily containing Lanthanide elements [300, 304, 306] and platinum group

elements [299, 303, 305], which tend to be costly in their manufacturing. These hexagonal HEAs form either disordered HCP or ordered Laves phases, although alloys composed of a majority hexagonal phase tend to be brittle which limits their applications as structural materials. The first observation of a hexagonal phase in a 3d transition metal HEA was by Tracy et al., during high pressure processing of the Cantor alloy, CoCrFeMnNi when pressurized up to 54.1 GPa [302]. Although a portion of the hexagonal phase partially reverted to FCC after depressurization in the Cantor alloy, the authors suggested that the high pressure processing can potentially lead to overcoming the strength vs. ductility trade-off by tailoring the amount of HCP in the FCC CoCrFeMnNi alloy [302].

A previous study of HEAs by the present group demonstrated the formation of a primary hexagonal Laves (C14) dendritic phase with Cu-rich FCC interdendritic regions in the as-cast CoCrCuMnTi multiprincipal element alloys (MPEAs), referred to by the authors as Chromantium. In addition, a particular combination of the elements in Chromantium with atomic concentrations of $Co_{22}Cr_{18}Cu_{20}Mn_{16}Ti_{24}$ displayed the most uniform dendritic microstructure, with as-cast hardness of 43 HRC/480 HV 1, with very high Vickers microhardness of the dendritic phase of $\sim$ 1000 HV 0.01. The scope of the present work is to further investigate the effects of levitation processing on the microstructure of the $Co_{22}Cr_{18}Cu_{20}Mn_{16}Ti_{24}$ alloy to better understand its novel crystal structure and morphology.

8.3 Methods

8.3.1 Arc-melting and Electromagnetic Levitation Processing

Alloys consisting of $Co_{22}Cr_{18}Cu_{20}Mn_{16}Ti_{24}$ were prepared from raw elements of purities Co $\geq$ 99.9%, Cr $\geq$ 99.99% , Cu $\geq$ 99.9% , Mn $\geq$ 99.7%, and Ti $\geq$ 99.7% purchased from Alfa Aesar (Ward Hill, Massachusetts). Samples were weighed to 1.5 g and arc-melted 3 times (flipped two times) on a water-cooled Cu hearth in a Ti-gettered argon atmosphere. The elemental manganese was pickled prior to alloying using concentrated HNO_3 in order to remove oxides, rinsed with water, and stored in acetone until alloying. The arc-melted samples were electromagnetically levitated by the use of induction coils for electromagnetic levitation (EML) processing of 1.5 g alloy buttons (Fig. 8.1), as described in Ref. [319].

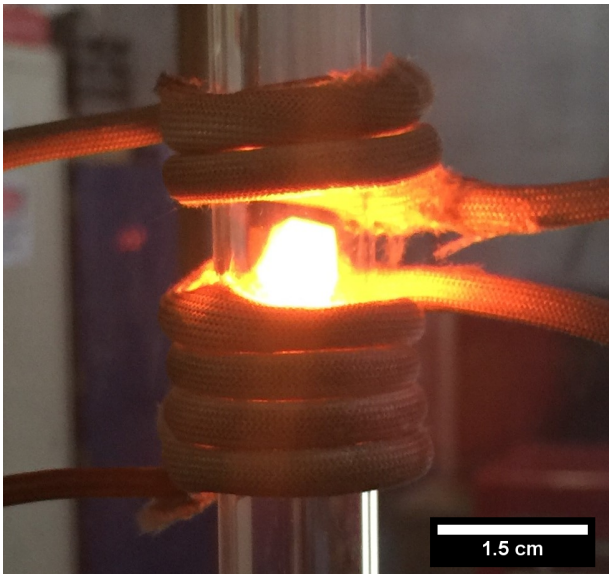

Figure 8.1: Electromagnetic levitation apparatus setup with a glowing hot metal enclosed within a quartz tube, suspended in a magnetic field.

Heating and cooling of the alloys were controlled via flow of He inside the quartz tube, due to the thermal conductivity of He allowing for fast conduction of heat during the induction melting process. The samples were levitated using a 20 kW, 300 kHz - 8 MHz high frequency generator, melted in an Ar/He environment inside of a quartz tube, and cast onto a Cu chill. The thermal history of the alloys was recorded with a Metis M3 2-color pyrometer with temperature range of 500 - 1800 °C, shown in Fig. 8.2. The alloys were solidified (4) different ways using the EML apparatus after a series of melting and solidification cycles: (1) Cast from a completely molten state at $\sim$ 1750 °C onto a Cu chill, (2) Cast during solidification (fast quenching by interrupting slow solidification, during cooling) at $\sim$ 1250 °C onto a Cu chill, (3) cast during melting (fast quenching by interrupting slow re-melting, during heating) at $\sim$ 1225 °C onto a Cu chill, and (4) solidified in the magnetic field while levitated and dropped out of the magnetic field as a solid at $\sim$ 1080 °C.

8.3.2 Differential Scanning Calorimetry

Differential scanning calorimetry (DSC) of the arc-melted $Co_{22}Cr_{18}Cu_{20}Mn_{16}Ti_{24}$ was carried out using a NETZSCH 404F3 DSC. Small chunks were broken off a larger piece of the alloy button and placed into 85 μL alumina DSC pans for the analysis. The DSC scans were made from room temperature to 1400 °C at a heating rate of 10 °C/min. The measurement was repeated three times. As there were no peaks observed under 900 °C, the heating curve displayed in Fig. 8.3 is representative of all the DSC measurements.

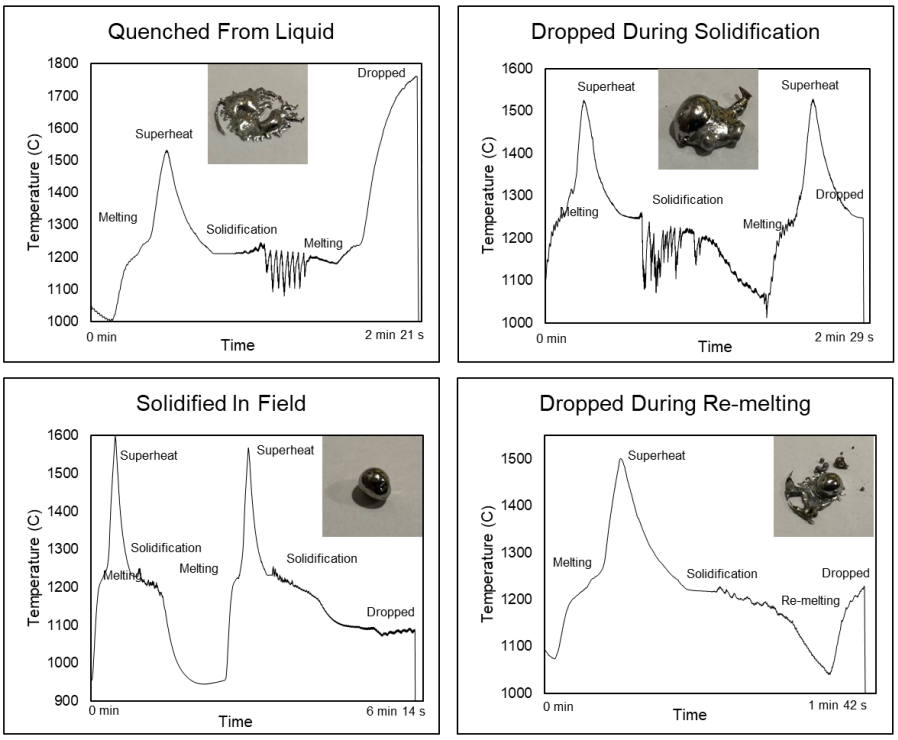

Figure 8.2: Thermal history and pictures of the $Co_{22}Cr_{18}Cu_{20}Mn_{16}Ti_{24}$ samples after EML processing. Note, the jagged portion of the curves in the Quenched From Liquid and Dropped During Solidification cases were from the sample moving in and out of view of the pyrometer in the magnetic field and not from the sample itself.

8.3.3 Microstructural Characterization

Scanning Electron Microscopy and X-ray Diffraction

For microstructural analysis, the EML processed samples were cross-sectioned parallel to the dendritic growth direction which was normal to the cooling substrate (with the exception of the sample solidified in the magnetic field, as there were no preferred growth directions). The solidified samples were mounted in Conducto-mount Conductive Mounting Powder and abraded using SiC paper down to 5 μ and polished with 1 μm Al_2O_3 powder.

The final polishing was done using 0.05 μm colloidal silica. Backscattered electron images (BEIs) and energy-dispersive X-ray spectroscopy (EDS) data were obtained from the polished samples with an FEI NovaNanoSEM 450 scanning electron microscope. As the sample that was solidified during levitation was suitable in size for X-ray diffraction (XRD), diffraction patterns were taken of the flat polished sample using a PANalytical Empyrean Series 2 diffractometer with Cu K_α radiation. The X-ray data for the alloy was acquired from 40° to 80° with a step size of 0.02° at 100s/step.

Scanning Transmission Electron Microscopy

Interface coherence were characterized using FEI Titan 300 transmission electron microscopy (TEM) at 300 kV accelerating voltage. STEM samples were taken from the cross section and prepared via an FEI quanta dual beam focused ion beam (FIB) using the lift out method. Oxide growths were also characterized with this method.

Atom Probe Tomography

High resolution chemical characterization was done by atom probe tomography (APT). APT needles were also prepared via FIB lift out and polishing with Ga ions. The ion beam thinning was carried out in multiple steps, beginning with 30 kV ions and ending with 5 kV ions to reduce surface damage caused by higher energy ions [320]. The final needle tip diameter of the atom probe specimen was 50-80 nm. The APT experiments were carried out in voltage evaporation mode with 25 % pulse fraction and 200 kHz frequency at sample temperature 40 K and evaporation rate of 0.5 % using LEAP 400XHR local electrode atom probe system from CAMECA Instruments Inc. Reconstruction of the APT data was

performed using IVAS software and the needle specimen's tip profile and shank angle were determined using a high magnification SEM image taken after final ion polishing.

8.4 Results

8.4.1 Differential Scanning Calorimetry

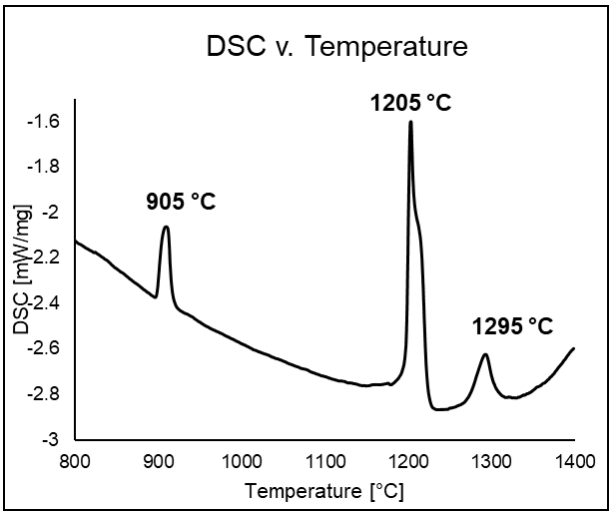

Figure 8.3: The 3rd differential scanning calorimetry measurement displaying three peaks during the heating cycle.

A representative differential scanning calorimetry (DSC) heating curve for a small 19.5 mg piece of $Co_{22}Cr_{18}Cu_{20}Mn_{16}Ti_{24}$ is shown in Fig. 8.3. There are three peaks present at 905 °C, 1205 °C, and 1295 °C. There were no peaks present in the heating curve below the first peak at 905 °C. As presented later, the interdendritic regions of this alloy are predominantly CuMn-rich, therefore the first peak at 905 °C is most likely the onset of melting of the interdendritic phase. The largest peak is at 1205 °C, and is the onset of

melting of the majority dendritic (Laves C14) phase, followed by a rather small peak at 1295 °C, which will be addressed during discussion of the microstructure and solidification process. Visual inspection of the alumina DSC crucibles after the measurement displayed that the sample had fully melted from the initial chunk.

8.4.2 Electromagnetic Levitation Processing

The calibration of 2-color pyrometers is dependent upon the emissivity slope correction factor for each material under study. As there is no emissivity data for the Chromantium alloys, obtaining the melting range temperatures from the DSC curve in Fig. 8.3 allowed for the calibration of the Metis M3 2-color pyrometer via melting a duplicate $Co_{22}Cr_{18}Cu_{20}Mn_{16}Ti_{24}$ button and adjusting the emissivity slope such that the accurate temperatures could be achieved. Once the system was calibrated to read the accurate temperatures, duplicate samples were electromagnetically levitated, melted, and solidified in (4) ways, presented in Fig. 8.2: (1) Quenched from a superheated state at around 1750 °C, referred to as Quenched From Liquid, (2) Casting the alloy during solidification (solid + liquid, mushy zone) at around 1250 °C referred to as Dropped During Solidification, (3) Casting the sample during re-melting at around 1225 °C referred to as Dropped During Re-melting, and (4) Solidification in the magnetic field, referred to as Solidified In Field. The arc-melted buttons were solidified and remelted a minimum of three times during electromagnetic levitation prior to solidification in the aforementioned fashions. The thermal histories of the samples present in Fig. 8.2 display the shape of the cast alloys related to their thermal history. The picture of the splat in the Quenched From Liquid curve demonstrates that the liquid solidified upon impact with the Cu chill plate, while the Solidified

In Field thermal history displays a picture of a spherical like piece, demonstrating that the alloy was a solid prior to dropping it out of the magnetic field, confirmed with pyrometry of temperatures below the melting point obtained from DSC. The picture of the Dropped During Solidification sample shows semi-solid shape, such that the alloy had a partial spherical shape and a partial splat shape, which is in agreement with the casting condition of being dropped during solidification from the thermal history of the sample. The alloy that was Dropped During Re-melting also displays the same semi-solid shape as the Dropped During Solidification sample, however, the spherical shape is a remnant of the previous solidification cycle while the splat-like pieces were the portion of the sample that began to melt. During EML, only the 1205 °C onset of melting was observed, with the exception of a small shoulder appearing in the Dropped During Solidification curve at around 1300 °C. This may be the 3rd peak in the DSC curve, however, it is not immediately clear if the curve shoulder was caused via fluctuations in the sample position during EML processing.

8.4.3 Microstructure

Quenched From The Liquid State

The Quenched From Liquid sample was cast onto the Cu chill from a completely molten state, as presented in Fig. 8.2. The splat was cross-sectioned perpendicular to the splat (parallel to dendritic growth) and a flat polished side was used for microstructural analysis, presented in Fig. 8.4. The backscattered electron image (BEI) in Fig. 8.4a displays a large bulk region of the sample where the splat initially made contact with the Cu chill. The dendritic growth direction is indicated by the arrow in Fig. 8.4a, and very small

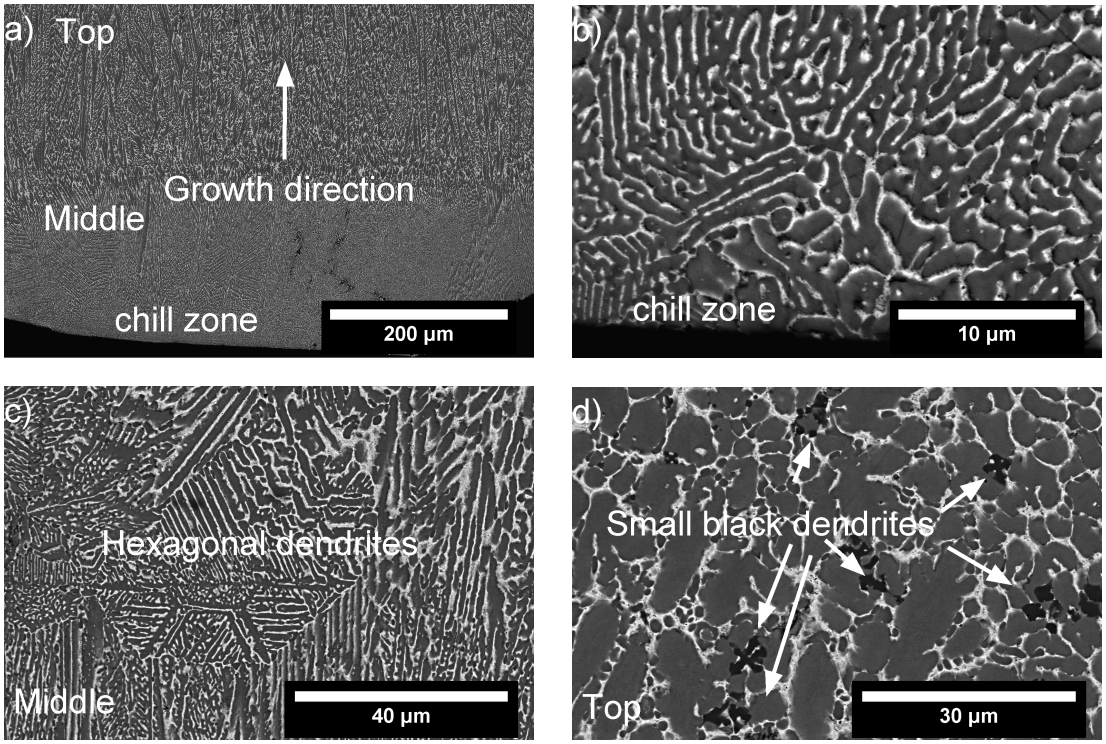

Figure 8.4: Backscattered electron images (BEIs) of a vertical cross section of the alloy after being dropped from a completely molten state around 1750 °C. a) Macroscopic view of the cast bottom to the middle of the sample, b) Higher magnification of the chill-zone (cast bottom), c) dendritic growth morphology towards the middle of the sample in between the chill and the surface of the solid, and d) dendritic morphology near the surface of the solid.

Table 8.1: Semi-quantitative analysis (at. %) for the energy-dispersive X-ray spectroscopy (EDS) data normalized for the elements in $Co_{22}Cr_{18}Cu_{20}Mn_{16}Ti_{24}$. Average atomic percentages for each region are presented.

Region	Co	Cr	Cu	Mn	Ti
Nominal (at. %)	22.50	17.70	19.90	15.80	24.00
Hexagonal Dendrite	29.47	27.21	2.98	10.49	29.84
Interdendrite	3.93	1.22	73.86	16.98	4.02
Darker Dendrite	25.00	17.48	2.32	5.57	49.62
Black Dendrites	10.58	7.86	2.83	8.31	70.42

dendrites can be seen near the labeled chill zone. The dendrite arm spacing significantly changed at approximately 200 μm above the chill zone, indicating a change in cooling rate. The micrograph in Fig. 8.4b displays a higher resolution image of the dendrites near the chill zone, with secondary dendrite arm spacing (S-DAS) of approximately 0.5 μm. The center of the splat is presented in Fig. 8.4c, where the hexagonal dendritic shapes are present near the center of the micrograph, which is indicative of hexagonal dendritic morphology. The S-DAS of these dendrites range from 1 – 5 μm, with an average width of 3.3 μm. Towards the top of the sample (Fig. 8.4d), the S-DAS become much larger, ranging up to 7 μm. Also present near the top of the solid are small faceted black dendrites, labeled such, with an atomic concentration of $\sim$ 70 at. % Ti measured from EDS. These small black dendrites were only near the top of the sample where solidification was not as rapid. The average atomic composition of the dendritic/interdendritic phases are presented in Table 8.1, where the dendrites are primarily CoCrTi-rich, with approximately 11 at. % Mn. The interdendritic phase consists of $\approx$ 74 % Cu and 17 % Mn, with a small amount of Co, Cr, and Ti.

Dropped During Solidification

The BEIs of the Dropped During Solidification sample are presented in Fig. 8.5. This sample was dropped by interrupting the full solidification process and quenching during visible thermal arrest of the pyrometer temperature readings, indicated in the thermal history curve in Fig. 8.2. The micrographs display intermixed large and small dendrites, labeled Zones 1 and 2, respectively, with similar atomic compositions to the dendrite/interdendritic phases in the Quenched From Liquid case. The S-DAS in Zone 1 vary from 2 μm to 7 μm (Table 8.3), indicating that that the larger dendrites in Fig. 8.5a were allowed more time for solidification, while the smaller dendrites in Zone 2 most likely grew upon impact with the Cu chill. Fig. 8.5b displays a region of the majority hexagonal dendrites and the surrounding Cu-rich matrix. A darker dendritic phase is present in various portions of the sample near the larger coarse dendrites, and is labeled in Fig. 8.5b. Elemental analysis using EDS reveals the darker dendrite to be approximately 50 at. % Ti, 25 at. % Co with smaller concentrations of the remaining components. The morphology of the dendrite implies that it floated freely throughout the single phase liquid, as it is not constrained by any of the majority dendritic growth. There is also indication of the darker dendritic phase solidification taking place first, as the tip of the darker dendrite can be seen as a starting point for the nucleation of the majority medium-gray hexagonal dendritic phase, and is labeled in Fig. 8.5b. The darker dendrite arm can be seen as the starting point for the medium-gray (majority phase) dendrites in Fig. 8.5b, as they grow radially away from the tip of the darker dendrite. As this sample was cast during an interrupted slow solidification at around 1250 °C, it appears that this darker dendrite phase was already solidified when

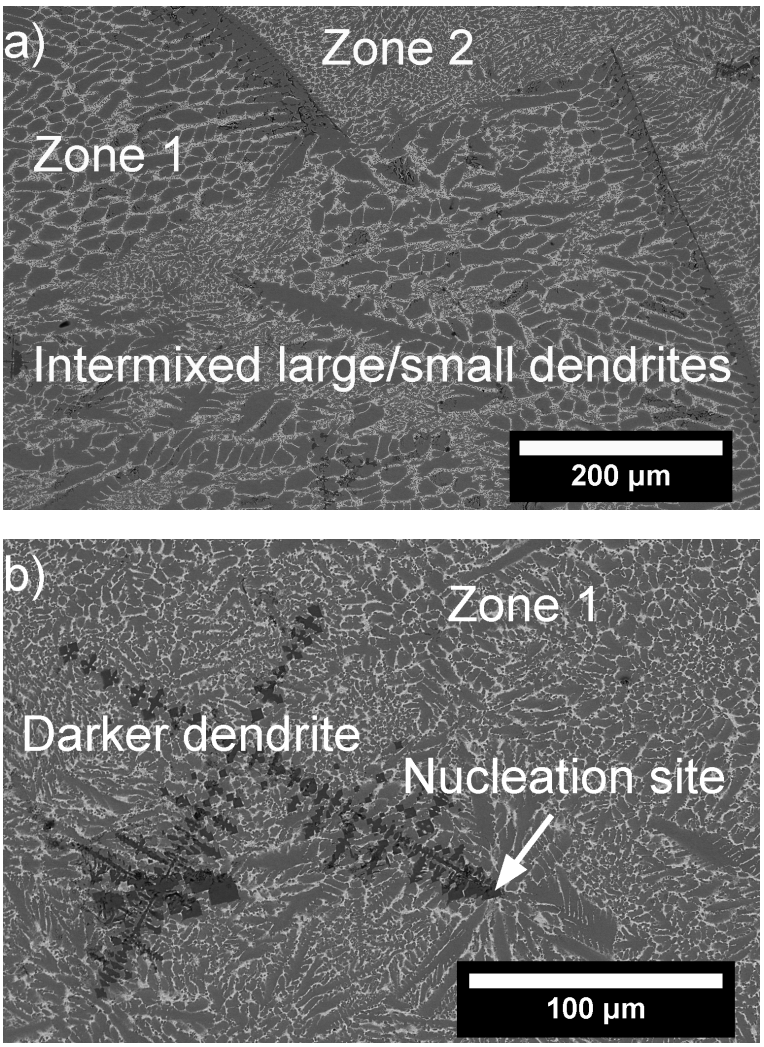

Figure 8.5: Backscattered electron images (BEIs) of a vertical cross section of the alloy after being dropped during solidfiication at around 1250 °C.

dropped out of the magnetic field. The DSC curve present in Fig. 8.3 displays a peak at 1295 °C, therefore, this may be attributable to melting/solidification point of this darker dendritic phase and will be discussed later. Transmission electron microscopy (TEM) of the Dropped During Solidification sample is presented in Fig. 8.7 with all three phases from Zone 1 are presented in higher resolution.

EDS maps (Fig. 8.6) were taken of an average bulk region without the presence of the darker dendrites to illustrate the composition differences between the dendrite and interdendritic phases. The maps for Co and Ti are slightly more rich than the map of Cr, which indicates they are also more present in the interdendritic region than Cr, which was confirmed via the EDS analysis of each phase in Table 8.1. The EDS map of only Cu contributions shows little presence in the majority dendrite phase, which is in agreement with the alloys presented in the previous chapter, where there was approximately 3 at. % Cu in each dendrite.

Atom probe tomography (APT) was carried out on the Darker Dendrite phase of the Dropped During Solidification sample to determine an accurate chemical composition of this phase. The results of the APT measurements are presented in Fig. 8.8, which includes elemental mapping of the APT tip, a 1D composition profile of the APT tip, and the mass spectrum for all of the elements in the chemical analysis. The highest concentration of ions from the APT measurements are from Ti, followed by Co, Cr, and O, the values of which are presented in Table 8.2.

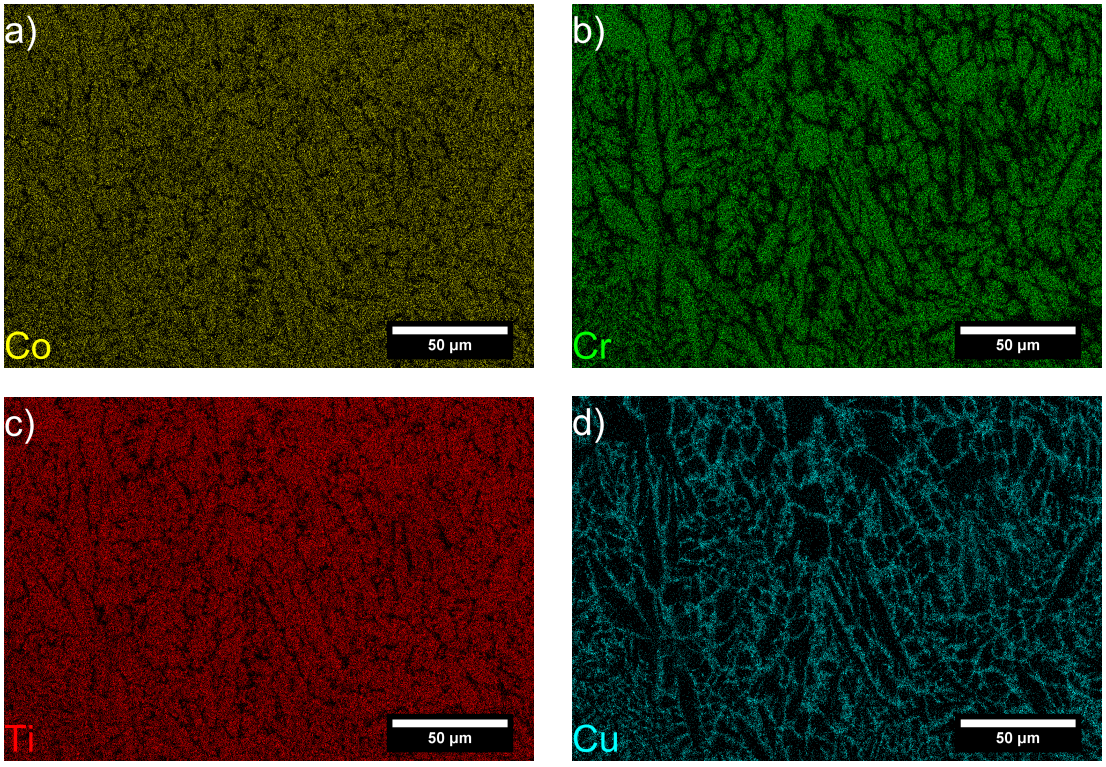

Figure 8.6: Energy dispersive X-ray spectroscopy (EDS) maps of the dendrite/interdendrite region in the alloy dropped during solidification. Colored EDS maps correspond to a) Co, b) Cr, c) Ti, and d) Cu. Manganese map not shown as it is distributed evenly amongst the two phases.

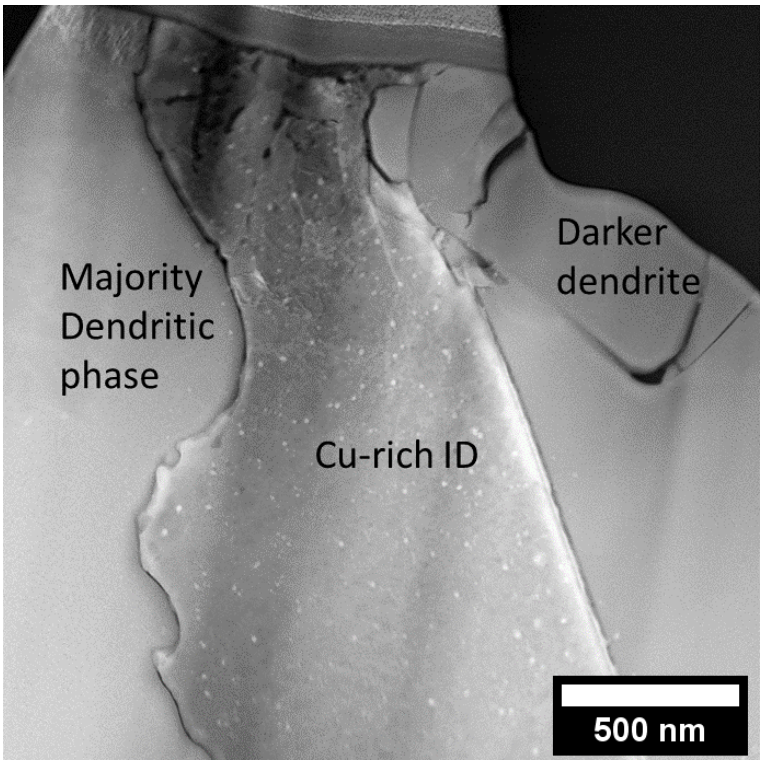

Figure 8.7: TEM image of all three phases from Zone 1.

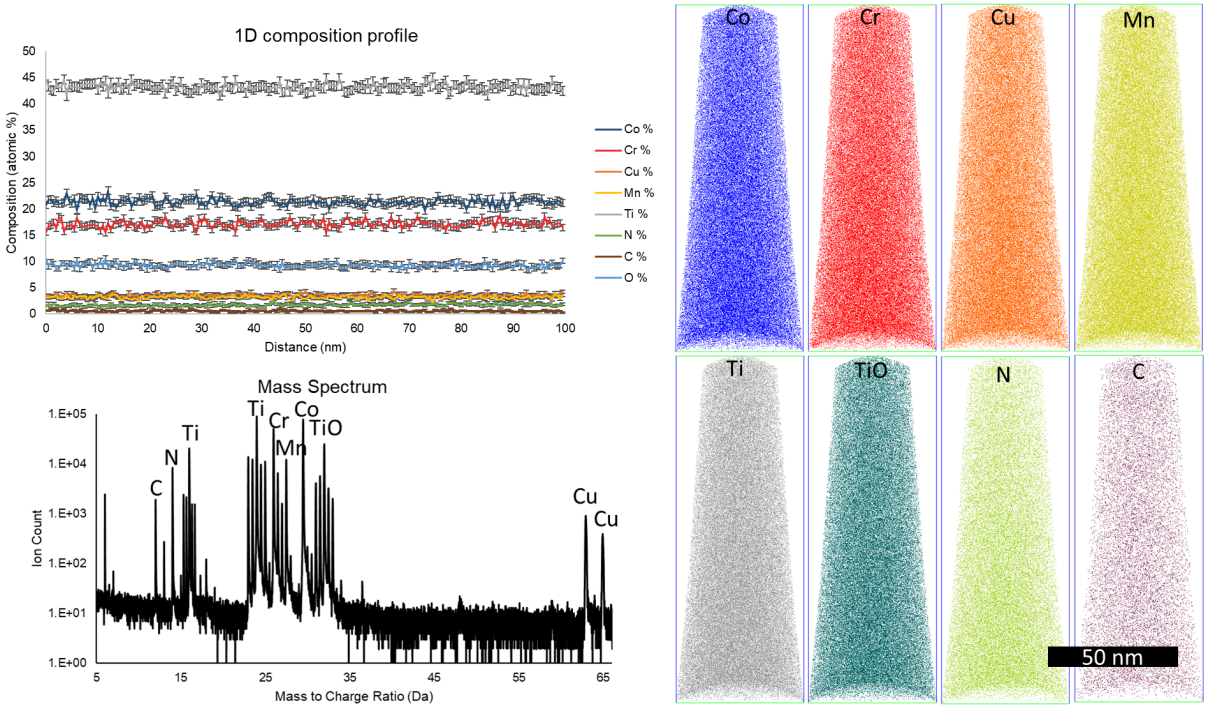

Figure 8.8: Atom probe tomography (APT) data from the Darker Dendrite phase consisting of a 1D composition profile of the atom probe tip, elemental mapping of the atom probe tip, and the mass spectrum from the APT measurements.

Table 8.2: Chemical analysis of the APT tip of the Darker Dendrite phase.

Element	Ions	At. %
Ti	1423799	43.15
Co	710754	21.54
Cr	568037	17.21
O	304621	9.23
Cu	115223	3.49
Mn	104987	3.18
N	55061	1.67
C	17428	0.53

Solidified In The Magnetic Field

The sample that was slowly solidified while levitating in the magnetic field (Solidified In Field) was found to have the largest S-DAS ($\sim$ 17 μm, measured from the dendrite arms in Fig. 8.9c), indicative of a slower solidification process, displayed in Fig. 8.9. The darker faceted dendrites that were observed in the Dropped During Solidification casting are also present in this microstructure, labeled as such in Fig. 8.9. The dendrites appear to have no preferred growth direction, as the alloy was solidified while in electromagnetic levitation. The darker faceted dendrites were floating freely in the liquid, frozen in the present microstructure, unperturbed by the growth of the majority phase dendrites. The majority phase dendrites were previously found to be of hexagonal Laves C14 phase ($P6_3/mmc$) crystal structure, while the interdendritic matrix was found to be FCC. These results were validated with additional XRD, presented in Fig. 8.10. The presence of the darker faceted dendrites with sharp edges indicate that they were first solidify, as they were free to grow into the melt.

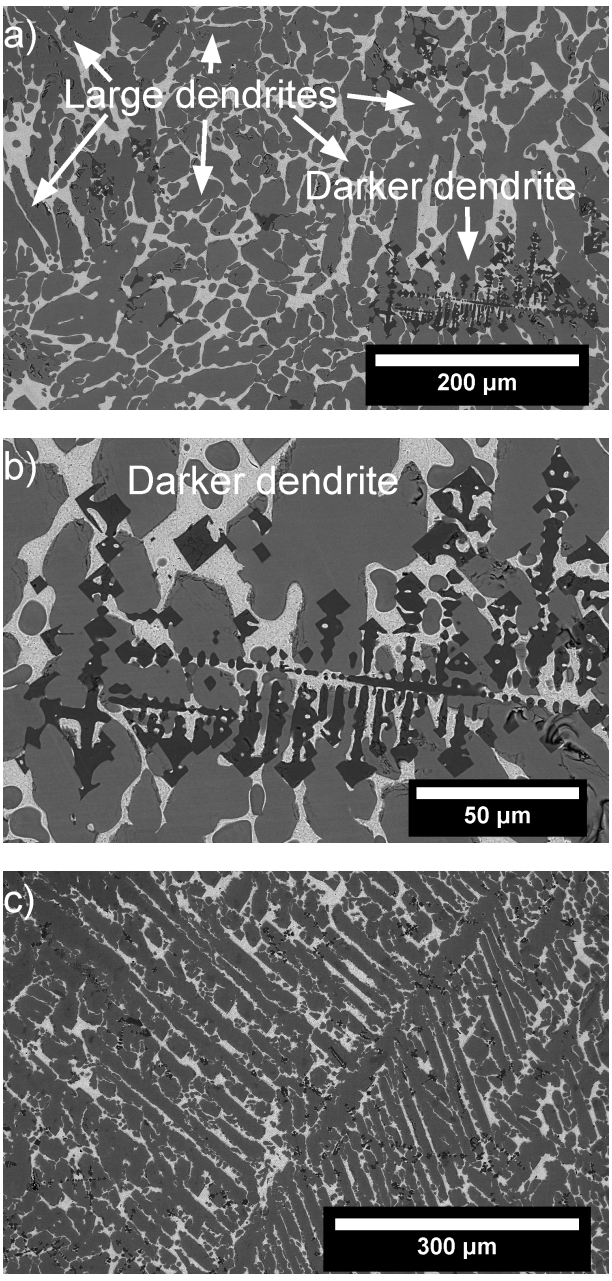

Figure 8.9: BEIs of a cross section of $Co_{22}Cr_{18}Cu_{20}Mn_{16}Ti_{24}$ after being dropped from levitation from a solid state around 1080 °C. a) Coarse broken hexagonal phase dendrites with smaller floating darker dendrites b) higher magnification of darker dendrite c) low magnification of a large hexagonal phase dendrite displaying secondary arms.

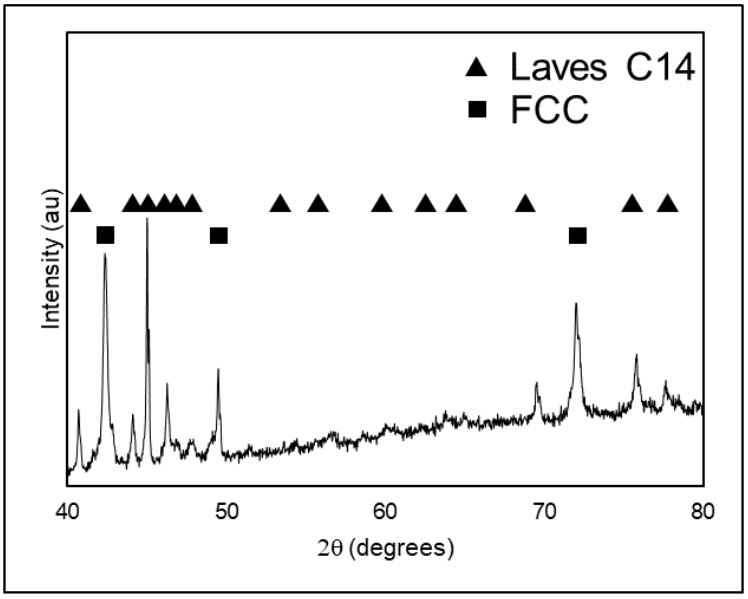

Figure 8.10: X-ray diffraction patterns of a cross section of $Co_{22}Cr_{18}Cu_{20}Mn_{16}Ti_{24}$ after being dropped from levitation from a solid state around 1080 °C. X-ray diffraction from 40° to 80° 2θ.

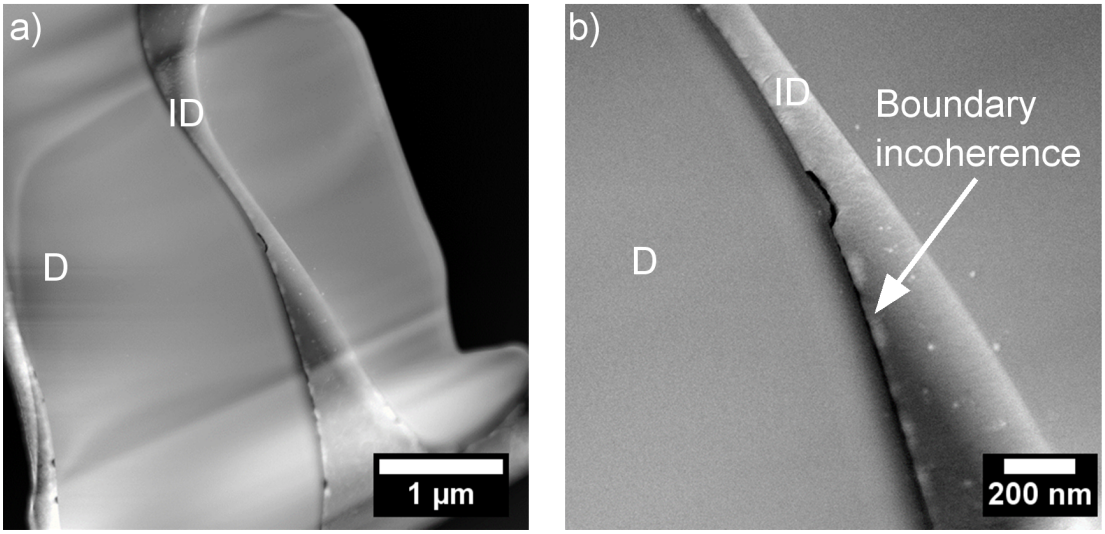

Figure 8.11: a) Scanning transmission electron microscopy (STEM) images of the Solidified in Field Laves dendritic and Cu-rich interdendritic phase, b) higher resolution STEM illustrating boundary incoherence between the two phases.

Scanning transmission electron microscopy (STEM) of the Solidified in Field sample is presented in Fig. 8.11, where a cross section of the Laves C14 dendritic phase (D) and the Cu-rich interdendritic phase (ID) are presented in Fig. 8.11a. Higher resolution STEM in Fig. 8.11b indicates what appears to be boundary incoherence between the Laves dendritic phase and the interdendritic phase.

Dropped During Melting

The microstructure of the sample, Dropped During Re-melting, is present in Fig. 8.12. The microstructure is mixed between the melted portion of the sample that solidified during drop casting from a semi-solid state and the leftover microstructure from the previous

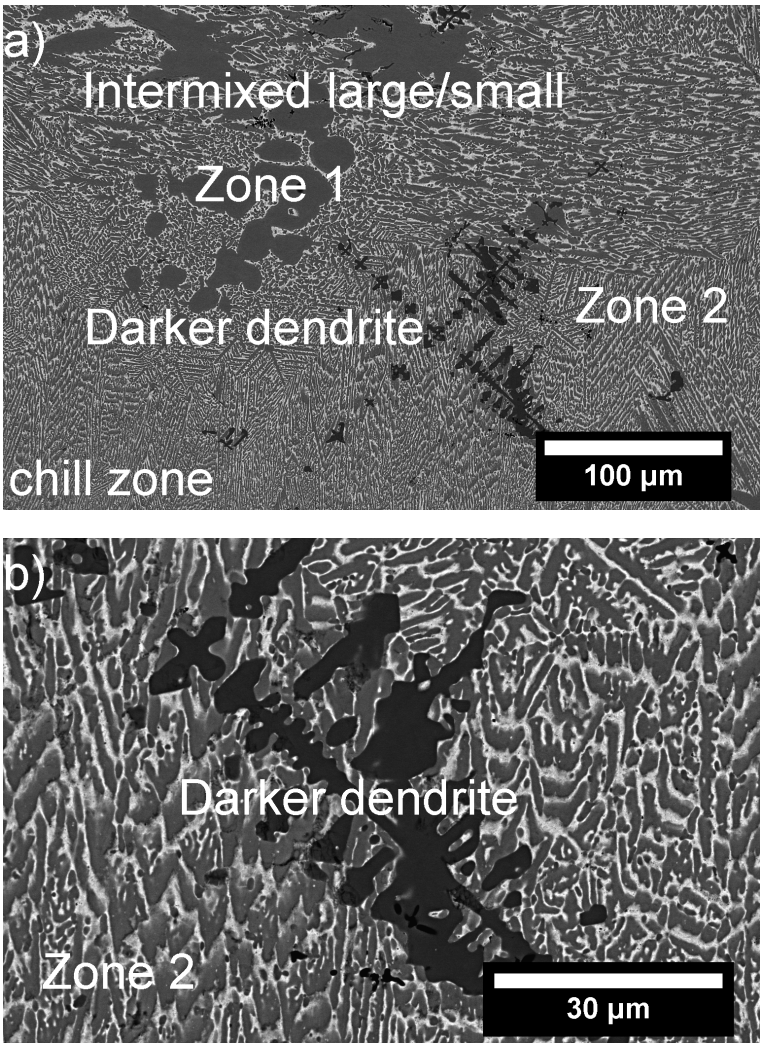

Figure 8.12: Backscattered electron images (BEIs) of a vertical cross section of the alloy after being dropped during melting at around 1225 °C.

solidification cycle. During re-melting, the structure goes through coarsening of the solid in the solid + liquid range. Nevertheless, the large dendrites in Zone 1 have similar morphology to those in the Solidified in Field process (Table 8.3) and were remnants of the previous solidification microstructure. The smaller sharper dendrites aimed upward from the chill zone were from the molten portion of the semi-solid coming into contact with the Cu chill during casting. The secondary dendrite arm spacing near the chill in this sample were similar in length to the dendrites formed from the cast sample that was dropped from the completely molten state (Table 8.3). The darker faceted dendrite present in Fig. 8.12b is not as sharp and defined as the darker dendrites present in the Dropped During Solidification (Fig. 8.5b) and Solidified In Field (Fig. 8.9b) solidification processes. The rounding of the edges indicate that this phase became mushy during melting, but did not fully dissolve in the surrounding liquid. The S-DAS of the majority medium gray phase (Laves C14 phase) is very small ($\sim 1.5\ \mu$m), and surrounds the darker faceted dendrite. The hexagonal dendrites also display an upward growth direction, which indicates that this region was fully molten except for the darker dendrite.

8.5 Discussion

8.5.1 Solidification Microstructures

The DSC curve in Fig. 8.3 displays three sets of peaks; 905 °C, 1205 °C, and 1295 °C. Based on volume fraction of the first two peaks of 905 °C and 1205 °C, these are the melting events for the interdendritic (FCC) and majority dendrite phases ($P6_3/mmc$). The last peak at 1295 °C is smaller than the first two, and based on the solidification

microstructures presented for each of the solidification processes, this peak is attributable to the small faceted darker dendritic phases. The darker dendrites are only present in regions with slow cooling in all the samples, such as near the top of the Quenched From Liquid case (Fig. 8.4d), the marked Zone 1 in the Dropped During Solidification (Fig. 8.5b), and everywhere throughout the Solidified in Field sample (Fig. 8.9). However, the darker faceted dendrite is present in Zone 2 of the Dropped During Melted case. As temperatures during remelting of this sample did not surpass 1295 °C, it is possible that this phase remained mostly solid, floating in the newly melted liquid prior to being dropped out of the magnetic field and cast onto the Cu chill. This can be seen by comparing the microstructure of the darker dendrite in the Solidified in Field sample, present in Fig. 8.9b to the microstructure of the Dropped During Re-melting sample in Fig. 8.12b. The Solidified in Field sample was allowed to solidify in the magnetic field with a cooling rate of $\sim$ 1 K/s. The same cooling rate was applied during the previous solidification cycle in the Dropped During Re-melting case, as shown in Fig. 8.2. Therefore, the same microstructure would have been present in the Dropped During Re-melting case had it been dropped out of the magnetic field prior to re-melting. However, the Dropped During Re-melting sample was allowed to partially melt, and was quenched onto the flat Cu chill before reaching full melting, as shown by the semi-solid shape in Fig. 8.2. The last phase to melt in this case would have been the darker faceted dendrites, however due to quenching taking place before temperatures of 1295 °C were reached, the liquid surrounding these floating dendrites solidified relatively rapidly, trapping this phase in a frozen region of fast cooling (Zone 2). The small dendrites in Zone 2 of Fig. 8.12 have S-DAS comparable to the Quenched From Liquid case, as presented in

Table 8.3. Due to the very high oxygen content in this phase (9.23 at. % O measured with APT), it may have formed from either residual oxygen present in the melting environment as Ti has a very high affinity for oxidation at high temperatures, or from any surface oxides that were initially present on the Ti or Mn prior to alloying.

Dendrite Arm Spacing and Cooling Rates

The cooling rate of an alloy as temperatures lead toward solidification affects the dendrite arm spacing (DAS). Various solidification processes such as arc-melting can have cooling rates up to 100 K/s, whereas EML processing and casting onto a Cu chill can have cooling rates $\sim$ 1000 K/s [188]. Measuring the DAS can provide insight into the cooling rate of an alloy, as DAS can be described as function of cooling rate, as shown in Eq. 8.1.

$$\text{DAS} = k\varepsilon^{-n} \tag{8.1}$$

where DAS is in units of μm, ε is the cooling rate in K/s, k is a constant for a given alloy, and n is generally 1/2 for primary DAS and ranges from 1/3 to 1/2 for secondary DAS [321]. By measuring the secondary dendrite arm spacing (S-DAS) from Fig. 8.9c, the cooling rate ε from the thermal history of the samples solidified in the magnetic field, such as the case of the Solidified In Field sample in Fig. 8.2, and using $n = 1/2$, we can approximate k for the alloys in this study (k = 16.01).

The secondary DAS was measured for the four solidification processes, and using k obtained from Eq. 8.1, the approximate cooling rates, ε, were calculated for the solidification microstructures of the EML processed samples presented in Table 8.3.

Table 8.3: Seconday dendrite arm spacing (DAS) and approximate cooling rates (ε) of each region in $Co_{22}Cr_{18}Cu_{20}Mn_{16}Ti_{24}$ from each EML processing route. QFL = Quenched from liquid, SIF = Solidified in field, DDS = Dropped during solidification, DDM = Dropped during melting.

Processing	Region	DAS (μm)	ε (K/s)	Black/Dark Dendrites
QFL	Near Chill	0.5	10^3	Not Present
	Middle	3.3	25	Not Present
	Top	6.9	5	Present
SIF	Average	16.7	1	Present
DDS	Coarse Dendrites	7.1	5	Present
	Small Dendrites	1.8	75	Not Present
DDM	Coarse Dendrites	17.1	1	Present
	Small Dendrites	1.4	130	Not Present

Examining the microstructure of the sample Quenched From Liquid, present in Fig. 8.4, there are three areas (chill zone, middle, and top) with different dendritic morphologies and S-DAS. By measuring the S-DAS of the three regions, approximations for cooling rate of each region were made using Eq. 8.1. Fig. 8.13 display S-DAS as a function of cooling rate (ε) and distance from the chill zone, and cooling rate (ε) as a function of distance from the chill zone. As the liquid coming into contact with the Cu chill zone experiences local supercooling and is the first area to solidify, the cooling rates are very high which leads to rapid heterogeneous nucleation of a thin layer of randomly oriented grains [322]. The cooling rate of the liquid coming into contact with the chill for the Quenched From Liquid sample was calculated to be on the order of 10^3 K/s, which is in agreement with the cooling rates described in Ref. [188]. The cooling rate slowed down further away from the chill, which also leads to coarsening of the dendrites and increased DAS and S-DAS. The top of the sample displays the largest S-DAS, indicative of a slow cooling rate.

Near the top of the sample, the small black Ti-rich dendrites are present (Fig. 8.4b), whereas they are missing in the areas with relatively fast cooling (chill zone, middle in Fig. 8.4a. This is also the case in Zone 2 of the Dropped During Solidification sample, where the slow cooling rate of $\sim$ 1 K/s was interrupted via quenching onto a Cu-chill. The areas of slow cooling (Zone 1) show presence of the darker faceted dendrites, which are morphologically and chemically similar to the smaller black faceted dendrites present near the top of the Quenched From Liquid sample, the differences in formation of however, require further investigation. All of the fast cooled regions in the samples lack the presence of the darker and small black faceted dendrites, therefore it appears that fast quenching suppresses the appearance of this phase, noted by the lack thereof in Fig. 8.4a–c and Zone 2 in Fig. 8.5a. In short, it appears that the floating darker dendrite and small black dendrite phases are skipped when solidification is fast, and is presented pictorially in Fig. 8.14. Further computational methods are recommended to more accurately understand the thermodynamics of the solidification process in these alloys.

8.5.2 Thermodynamic Interpretation

Calculations for enthalpy of mixing H^{ϕ}_{mix} of the resulting phases were carried out using each solidified phases' elemental atomic percentages obtained from EDS. The calculated mixing enthalpy of the phases were obtained from the binary interactions between liquid metal elements as described in the sub-regular solution modification of Miedema's method in Takeuchi et al., where these values were initially calculated for metallic glass formability [167]. The calculated mixing enthalpies for the alloys in this study were obtained

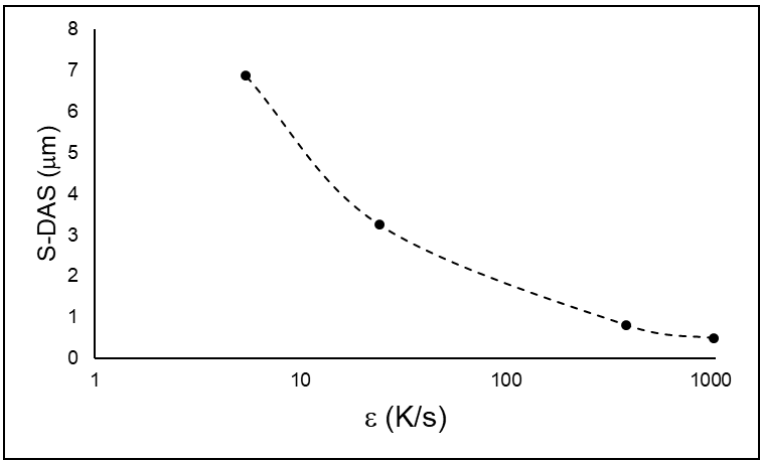

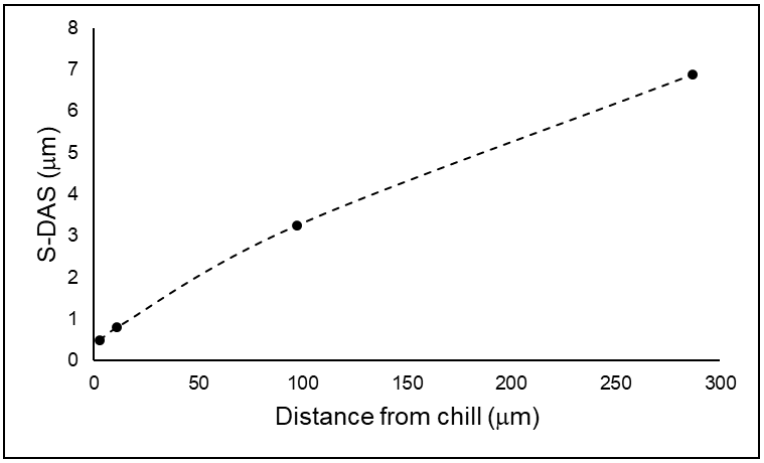

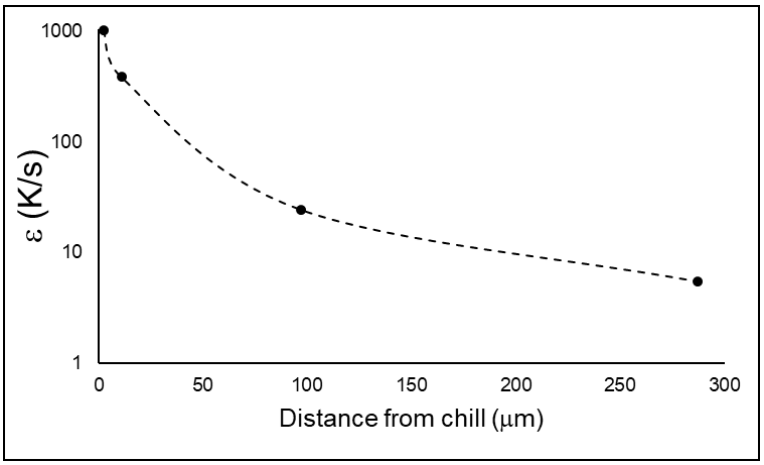

Figure 8.13: Graphs of S-DAS as a function of cooling rate ε and distance from chill, and cooling rate ε as a function of distance from chill for the Quenched From Liquid sample.

Table 8.4: Enthalpy of mixing H^{ϕ}_{mix} (kJ/mol) calculated using the atomic percentages obtained via EDS of the dendritic phases found in $Co_{22}Cr_{18}Cu_{20}Mn_{16}Ti_{24}$.

Phase	H^{ϕ}_{mix}
Liquid	-8.0
Laves Dendrite	-15.6
Darker Dendrite	-19.0
Small Black Dendrite	-12.8

from Eq. 8.2, where $H^{\phi}_{c_i,c_j} = 4\Omega_{ij}c_ic_j$ for the ith and jth elements at $A_{0.5}B_{0.5}$ concentrations from the tables for Ω_{ij} in Ref. [167].

$$H_{\phi} = \sum_{i=1, i\neq j}^{n} H^{\phi}_{c_i,c_j} \tag{8.2}$$

Atomic percentages for the calculation of H^{ϕ}_{mix} of the solidified phases were obtained from the post-mortem microstructural analysis EDS data for each phase. For the overall H^{ϕ}_{mix} calculation of the liquid, the authors assume the liquid is single phase. The calculated values for H^{ϕ}_{mix} are presented in Table 8.4.

Although these calculations are rough approximations for mixing enthalpy, microstructural analysis of the solidification process indicates that the darker dendrites solidified first, followed by the majority phase hexagonal Laves dendrite and lastly the leftover Cu-rich liquid to the interdendritic regions. It is not immediately clear if the small faceted black dendrites are broken off pieces of the darker faceted dendrites, and further investigation is needed to understand the formation of this small amount of phase. The approximate values for H^{ϕ}_{mix} show that the darker dendrites are slightly more attractive and likely to form than the Laves phase dendrites, which results in the hexagonal dendrites growing from

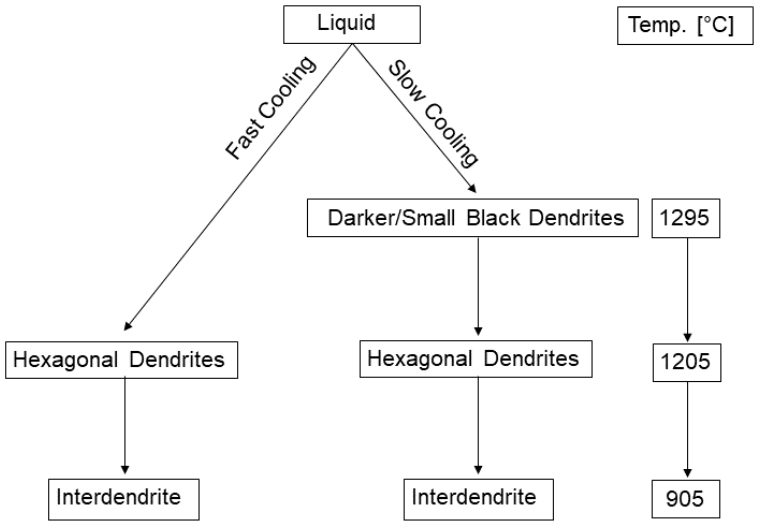

Figure 8.14: Diagram of the solidification process in this study of the $Co_{22}Cr_{18}Cu_{20}Mn_{16}Ti_{24}$ MPEA.

the remaining liquid after the Darker Dendrite forms. It appears that the floating darker dendrite and small black dendrite phases are skipped when solidification is fast, and is presented pictorially in Fig. 8.14. Further computational methods are recommended to more accurately understand the thermodynamics of the solidification process in these alloys.

8.6 Summary

The solidification microstructures of the Laves/FCC phase $Co_{22}Cr_{18}Cu_{20}Mn_{16}Ti_{24}$ MPEA were studied via electromagnetic levitation processing (EML). Differential scanning calorimetry (DSC) of a small chunk of the alloy displayed three distinct peaks at 905 °C, 1205 °C, and 1295 °C which were used to calibrate a 2-color pyrometer for temperature measurement for EML processing and casting. Duplicate alloys of $Co_{22}Cr_{18}Cu_{20}Mn_{16}Ti_{24}$

were arc-melted to achieve 1.5 g buttons for EML processing. The buttons were electromagnetically levitated and melted, and were either dropped from the completely molten state, dropped during solidification, dropped during re-melting, or solidified in the magnetic field and dropped from the solid state. The results of which are summarized below:

- It was found that when the alloy was allowed to solidify in the magnetic field, small CoTi-rich dendrites formed freely in the melt prior to the majority hexagonal Laves dendritic phase, while solidification is finished upon freezing of the interdendritic regions. When correlating the dendritic morphology and temperature of casting with the DSC curve, it is our observation that the small CoTi-rich phase is DSC peak observed at 1295 °C.

- X-ray diffraction of the alloy that was solidified in the magnetic field is in agreement with the diffraction data in the previous chapter for the hexagonal and FCC phases.

- Secondary dendrite arm spacing (S-DAS) was measured for each of the solidified samples, and cooling rates were approximated for each of the regions in the alloy. The regions with faster cooling rates and small S-DAS lacked any floating CoTi-rich (darker) dendrites, therefore fast cooling appears to suppress this phase when the liquid is cooled at a rate of $\gtrapprox 10^2$ K/s.

Overall, when processed via electromagnetic levitation, the predominant dendritic phase of the material remains to be the hexagonal Laves C14 phase, which is novel among the high-entropy alloys. The interdendritic phase is an FCC CuMn-rich matrix, which may result in this material having desirable toughness, as the as-cast hardness from arc-melting these materials were previously found to have high hardness.

Chapter 9

Conclusions

A summary of each chapter is presented below, as well as general conclusions reached about each section with relation the overall hypothesis regarding liquid state mixing in these alloys. These summaries are intended to recap each of the chapters such that they can summarize the main findings and contributions of this work.

9.1 Chapters 1 & 2: Summary of Literature Review and Experimental Techniques

The field of high-entropy, complex concentrated, and multiprincipal element alloys is very young, and with every year, more research groups are adopting high-entropy alloy research in the quest for new and exciting materials. Strictly defining nomenclature for these alloys can be restrictive and might hinder progress towards more exploratory alloy combinations and compositions. The potential for these materials have not fully been realized, simply due to the billions of potential combinations of alloys that can arise from mixing elements in non-equiatomic proportions.

The empirical approaches for the predictions of stable single phases are honest attempts to understand the phase formation in these complex alloy systems. However, the ability to make successful predictions has always been a challenge for the materials scientist, and I believe more collaborative work between computational and experimental groups may provide a path forward for further understanding of these systems as the current methodologies can only provide rough approximations for phase prediction in the HEAs.

Liquid phase separation in metallic systems has been extensively studied since the 20th century, and LPS in alloys can be interpreted via positive mixing enthalpy interac-

tions between the alloying elements. However these are thermodynamic interpretations of liquid-liquid phase separations in metallic systems. In order to understand the atomistic causes of liquid phase separation in alloys, there may be potential for an answer via a more chemistry related approach via the study of molecular dynamics and orbital theory. Recent calculations for the enthalpy of alloy formation in alloys and intermetallic compounds are shown to be related to polar bonding and charge transfer between the metallic alloying elements [323]. In Ref. [323], Liu states that "Alloys can be significantly polar, with internal and surface dipoles comparable to organic compounds and minerals." [323].

Many of the alloys in the literature have been prepared via solidification based methods such as arc-melting, induction melting, and levitation melting. The same metallurgical techniques used for conventional alloys can be applied for the synthesis and processing of high-entropy alloys, which is why there is such a vast amount of research conducted on these materials. Powder metallurgical processing can also be used to make HEAs, as shown in this work, the processing of HEA powder can lead to the same crystallographic phases and increased hardness when compared to identical compositions made via solidification based methods.

9.2 Chapter 3: Solidification Microstructures and Calculated Mixing Enthalpies in CoCrCu Containing Alloys

Of the 16 alloy combinations of the CoCrCu + X system, X being the remaining combinations of the 3d transition metals up to quinary alloy combinations, CoCrCuNi, CoCrCuTi, CoCrCuFeNi, CoCrCuMnNi, CoCrCuMnTi, and CoCrCuTiV solidified den-

dritically resulting in FCC solid solutions of both the dendritic and interdendritic regions for the Ni containing alloys and BCC, HCP, and FCC phases for the Ti-containing alloys. The alloys of CoCrCuTi and CoCrCuTiV were found to have (2) sets of BCC dendritic phases, with a Cu-rich FCC interdendritic matrix. CoCrCuMnTi was found to be duplex HCP/FCC, while CoCrCuFeTi also contained the HCP phase but exhibited severe liquid phase separation. The remaining samples all underwent a melt separation into Cu-rich and Cu-lean liquids.

The results show that the enthalpy of mixing, ΔH_{mix} for each of the dendritic regions are more negative than the calculations for their nominal equiatomic concentrations, indicating that the approximation for ΔH_{mix} using Miedema's scheme for sub-regular solutions displays a correlation between negative mixing enthalpy and single phase liquid formation in these alloys. However, it should be noted that even though the summation of binary alloy mixing enthalpies may have a negative ΔH_{mix}, binaries within the calculation that have a very large positive mixing enthalpy (such as alloys with Cu) may lead to segregation of the alloy that has the highest mixing enthalpy across the binaries to liquid phase separated regions. When comparing the mixing enthalpies of the possible combinations of mixing enthalpies of all the alloying elements, approximations can be made as to whether the resulting mixture will contain Cu-rich and Cu-lean phases, however cannot distinguish if this separation will occur in the interdendritic region or a completely phase separated globule.

The results indicate that positive mixing enthalpy contributions in the 3d transition metal quaternary and quinary HEAs are mostly due to the influence of Cu in the melt.

From this work, it is clear that since Cu leads to liquid phase separation in these alloys, that the much more negative enthalpy contributions from the other alloying elements bring the overall mixing enthalpy down and allow for Cu liquid solubility, such as the cases for the 6 dendritically solidifying HEAs in this study.

9.3 Chapters 4 & 5: In-Situ Imaging of Molten Alloys Using Cold Neutrons

By utilizing neutron imaging, liquid phase separation of the CoCrCu system was observed. The CoCrCu system has been shown to have a stable miscibility gap at temperatures up to 1500 . This technique can be applied to other alloy systems provided that the neutron transmission of the alloying elements are dissimilar enough to see a contrast between the multiple phases.

With the application of this technique to high-entropy alloys, in-situ imaging of liquid state remixing has been observed for the first time with the equiatomic additions of Ni to the immiscible CoCrCu system. After solidification had finished, there were no indications from the CT scans that Cu had segregated anywhere in the melt. When comparing the results to the CALPHAD prediction for the liquid state behavior in CoCrCuNi, we see that the results are in reasonable agreement with the prediction for a single phase liquid in this system.

This technique also provides a way to potentially image casting processes by constructing crucibles that simulate various cast shapes. After solidification has finished, the use of computed tomography (CT) can be applied with the cold neutrons and a rotating

sample stage to look for impurities or voids within the cast. This method can be applied to study fundamental liquid state behavior in complex alloy systems, such as the high-entropy alloys. By using neutron imaging of the liquid phase, it can provide invaluable information about the alloy system as well as other systems that contain miscibility gaps and is not solely specific to liquid metals.

9.4 Chapter 6: Processing Pathway Effects in CoCrCuNi + X (Fe, Mn) High-Entropy Alloys

The resulting microstructures, crystal structures, and microhardness of CoCrCuNi, CoCrCuFeNi, and CoCrCuMnNi High-entropy alloys (HEAs) were investigated via solidification processing and subsequent annealing and mechanical alloying followed by spark plasma sintering. It was found that all processing routes resulted in a primary FCC phase, while secondary FCC phases were found in the interdendrite regions of the solidified samples and at the particle boundaries of the SPS samples. Small amounts of σ phase were observed in the SPS processed alloys, but not in the cast counterparts. All three alloys solidified with dendritic microstructures that did not undergo any significant changes after annealing, with the exception of the CoCrCuMnNi alloy which had Cr-rich precipitates after annealing. The mechanically alloyed powder of all three alloys resulted in single FCC peaks and approximate grain sizes of 20 nm deduced from Scherrer's equation. When comparing the observed phases to the published CALPHAD predictions for these alloys, it can be difficult to confidently and comprehensively explain discrepancies between thermodynamic calculation and observed results. This is due to the many variables that dictate phase formation.

Spark plasma sintering on all three samples resulted in a cobblestone-like microstructure with a Cu-rich phase in the particle boundaries. The microhardness for the SPS alloys increased by a factor of ~ 2.5 when compared to their solidified counterparts. The processing of these alloys via SPS compared to solidification resulted in similar FCC phases and Cu-rich segregation, while doubling the microhardness when compared to the microhardness of the solidification processed HEAs.

These results show that significant differences in mechanical properties, microstructure, and crystallographic phase can be achieved by varying the processing route for these alloys. The results also show that nanocrystalline HEAs are possible via the use of spark-plasma sintering techniques.

9.5 Chapters 7 & 8: Hexagonal-Cubic Multiprincipal Element Alloys with High Hardness

Intermetallic-alloy 3d transition metal MPEAs with considerable dendritic hardness were prepared via arc-melting. Alloys of:

- CoCrCuTi
- $(CoCrCuTi)_{95}Mn_5$
- $(CoCrCuTi)_{90}Mn_{10}$
- $(CoCrCuTi)_{85}Mn_{15}$
- CoCrCuMnTi

- $Co_{22}Cr_{18}Cu_{20}Mn_{16}Ti_{24}$

were investigated to understand the critical Mn concentration for the formation of Laves C14 phase in these alloys. The results indicate for the first time that MPEAs consisting of purely 3d transition metals can solidify with a majority hexagonal phase from arc-melting. Atomic percentages of $\geq 10\%$ Mn when added to CoCrCuTi leads to Laves phase dendrites with small amounts of Ti-rich dendrites and a Cu-rich interdendritic region.

Using EDS analysis of the most uniform regions in the equiatomic CoCrCuMnTi composition, the alloy composition of $Co_{22}Cr_{18}Cu_{20}Mn_{16}Ti_{24}$ was found to have the most reproducible uniform as-cast dendritic microstructure with a uniform Cu-rich interdendritic matrix. There exists a $\sim$ 2:1 Vickers hardness between the Laves phase dendrites (996 HV 0.01) and FCC interdendrites (457 HV 0.01) while the overall Vickers hardness of the material is 480 HV 1, which may have the potential for fracture and wear-resistant applications as the Cu-rich FCC phase could be potentially more ductile than the hexagonal intermetallic primary phase. The extremely hard Laves phase dendrites in contrast to the Cu-rich FCC interdendritic matrix may fall under the classification of a type of metal matrix composite. The $Co_{22}Cr_{18}Cu_{20}Mn_{16}Ti_{24}$ alloy Rockwell hardness of 43 HRC and relatively high compressive strength of 1430 MPa with moderate density of 7.05 g/cm^3 could potentially be harnessed for wear based applications, as the relatively small in-air wear rate of 2.64×10^{-5} mm^3/m·N could be improved with tailoring of the interdendritic regions of the material to be larger or smaller depending on the application.

The solidification microstructures of the Laves/FCC phase $Co_{22}Cr_{18}Cu_{20}Mn_{16}Ti_{24}$ MPEA were then studied via electromagnetic levitation processing (EML). Differential scan-

ning calorimetry (DSC) of a small chunk of the alloy displayed three distinct peaks at 905 °C, 1205 °C, and 1295 °C which were used to determine EML processing and casting temperatures. The alloy was electromagnetically levitated and melted, and were either dropped from the completely molten state, dropped during solidification, dropped during re-melting, or solidified in the magnetic field and dropped from the solid state. It was found that when the alloy was allowed to solidify in the magnetic field, small CoTi-rich dendrites formed freely in the melt prior to the majority hexagonal Laves dendritic phase, while solidification is finished upon freezing of the interdendritic regions. The morphology of the CoTi-rich dendrites imply they were first to solidify, and when correlating the dendritic morphology and temperature of casting with the DSC curve, it is our conclusion that this phase is responsible for the DSC peak observed at 1295 °C.

Secondary dendrite arm spacing (S-DAS) was measured for each of the solidified samples, and cooling rates were approximated for each of the regions in the alloy. The regions with faster cooling rates and small S-DAS lacked any floating CoTi-rich (darker) dendrites, therefore fast cooling appears to suppress this phase when the liquid is cooled at a rate of $\sim 10^3$ K/s. Overall, when processed via electromagnetic levitation, the predominant dendritic phase of the material remains to be the hexagonal Laves C14 phase, which is rare among the high-entropy alloys. The interdendritic phase is an FCC CuMn-rich matrix, which may result in this material having desirable toughness, as the as-cast hardness from arc-melting these materials were previously found to have high hardness.

Bibliography

[1] B. Cantor, I. T. H. Chang, P. Knight, and A. J. B. Vincent, "Microstructural development in equiatomic multicomponent alloys," *Materials Science Engineering A*, vol. 375-377, pp. 213–218, 2004. 2, 4, 5, 6, 13, 14, 15, 16, 43, 56, 57, 60, 107, 171, 195

[2] J.-W. Yeh, S.-K. Chen, S.-J. Lin, J.-Y. Gan, T.-S. Chin, T.-T. Shun, C.-H. Tsau, and S.-Y. Chang, "Nanostructured High-Entropy Alloys with Multiple Principal Elements: Novel Alloy Design Concepts and Outcomes," *Advanced Engineering Materials*, vol. 6, no. 5, pp. 299–303, 2004. 2, 4, 13, 32, 56, 57, 60, 64, 107, 120, 171, 195

[3] J.-W. Yeh, S.-J. Lin, T.-S. Chin, J.-Y. Gan, S.-K. Chen, T.-T. Shun, C.-H. Tsau, and S.-Y. Chou, "Formation of simple crystal structures in Cu-Co-Ni-Cr-Al-Fe-Ti-V alloys with multiprincipal metallic elements," *Metallurgical and Materials Transactions A*, vol. 35, no. 8, pp. 2533–2536, 2004. 2, 4, 5, 6, 26, 41, 43, 44, 56, 60, 107, 130, 131, 149, 171, 195

[4] C.-y. Hsu, J.-w. Yeh, S.-k. Chen, and T.-t. Shun, "Wear resistance and high-temperature compression strength of Fcc CuCoNiCrAl0.5Fe alloy with boron addition," *Metallurgical and Materials Transactions A*, vol. 35, no. 5, pp. 1465–1469, 2004. 2, 4, 56, 107, 171, 195

[5] P. Huang and J. Yeh, "Multi-Principal Element Alloys with Improved Oxidation and Wear Resistance for Thermal Spray Coating," *Advanced Engineering Materials*, vol. 6, no. 1-2, pp. 74–78, 2004. 2, 4, 56, 107, 171, 195

[6] T. K. Chen, M. S. Wong, T. T. Shun, and J. W. Yeh, "Nanostructured nitride films of multi-element high-entropy alloys by reactive DC sputtering," *Surface and Coatings Technology*, vol. 200, no. 188-189, pp. 193–200, 2004. 2, 4, 56, 107, 171, 195

[7] D. B. Miracle, "Critical Assessment 14: High entropy alloys and their development as structural materials," *Materials Science and Technology*, vol. 31, no. 10, pp. 1142–1147, 2015. 2, 3

[8] D. Miracle, J. Miller, O. Senkov, C. Woodward, M. Uchic, and J. Tiley, "Exploration and Development of High Entropy Alloys for Structural Applications," *Entropy*, vol. 16, no. 1, pp. 494–525, 2014. 2, 5

[9] A. M. Manzoni and U. Glatzel, "New multiphase compositionally complex alloys driven by the high entropy alloy approach," *Materials Characterization*, no. April, pp. 0–1, 2018. 2, 4, 9, 34

[10] J. W. Yeh, "Recent progress in high-entropy alloys," *Annales de Chimie: Science des Materiaux*, vol. 31, no. 6, pp. 633–648, 2006. 2, 7, 15, 57

[11] O. Maulik, D. Kumar, S. Kumar, S. K. Dewangan, and V. Kumar, "Structure and properties of lightweight high entropy alloys: A brief review," *Materials Research Express*, vol. 5, no. 5, 2018. 3, 9

[12] Y. Lu, Y. Dong, S. Guo, L. Jiang, H. Kang, T. Wang, B. Wen, Z. Wang, J. Jie, Z. Cao, H. Ruan, and T. Li, "A promising new class of high-temperature alloys: Eutectic high-entropy alloys," *Scientific Reports*, vol. 4, pp. 1–5, 2014. 3

[13] M. H. Tsai, "Physical properties of high entropy alloys," *Entropy*, vol. 15, no. 12, pp. 5338–5345, 2013. 4

[14] M. C. Gao, "Progress in High-Entropy Alloys," *Jom*, vol. 65, no. 12, pp. 1964–1965, 2013. 4

[15] M. C. Gao, "Progress in High-Entropy Alloys," *Jom*, vol. 66, no. 10, pp. 1964–1965, 2014. 4

[16] M. H. Tsai and J. W. Yeh, "High-entropy alloys: A critical review," *Materials Research Letters*, vol. 2, no. 3, pp. 107–123, 2014. 4, 9

[17] Y. Zhang, T. T. Zuo, Z. Tang, M. C. Gao, K. A. Dahmen, P. K. Liaw, and Z. P. Lu, "Microstructures and properties of high-entropy alloys," *Progress in Materials Science*, vol. 61, no. October 2013, pp. 1–93, 2014. 4, 9, 34

[18] R. Kozak, A. Sologubenko, and W. Steurer, "Single-phase high-entropy alloys - An overview," *Zeitschrift fur Kristallographie*, vol. 230, no. 1, pp. 55–68, 2015. 4, 9

[19] M. C. Gao, "Progress in High Entropy Alloys," *Jom*, vol. 67, no. 10, pp. 2251–2253, 2015. 4

[20] E. J. Pickering and N. G. Jones, "High-entropy alloys: a critical assessment of their founding principles and future prospects," *International Materials Reviews*, vol. 61, no. 3, pp. 183–202, 2016. 4, 9

[21] Y. F. Ye, Q. Wang, J. Lu, C. T. Liu, and Y. Yang, "High-entropy alloy: challenges and prospects," *Materials Today*, vol. 19, no. 6, pp. 349–362, 2016. 4, 9

[22] D. B. Miracle and O. N. Senkov, "A critical review of high entropy alloys and related concepts," *Acta Materialia*, vol. 122, pp. 448–511, 2017. 4, 5, 8, 9, 18, 31, 32, 34, 57, 58, 59, 107, 108, 171

[23] S. Praveen and H. S. Kim, "High-Entropy Alloys: Potential Candidates for High-Temperature Applications – An Overview," *Advanced Engineering Materials*, vol. 20, no. 1, pp. 1–22, 2018. 4, 9, 34

[24] B. Murty, J. Yeh, and S. Ranganathan, *High-Entropy Alloys*. London: Butterworth-Heinemann, 1st ed., 2014. 4

[25] D. Fisher, *High-Entropy Alloys - Microstructures and Properties*. Zurich: Trans Tech Publications, materials ed., 2015. 4

[26] S. Maiti, *Local Structure and Properties of Refractory High-Entropy Alloys: High-Entropy Alloys Critically Analyzed From A More Fundamental Point of View*. Saarbrücken: Lambert Academic Publishing, 2016. 4

[27] C. Zhang and M. C. Gao, *High-Entropy Alloys: Fundamentals and Applications*. 2016. 4, 34

[28] F. Tian, L. Varga, and V. Levente, *Theoretical Design of Single Phase High-Entropy Alloys*. Saarbrücken: Lambert Academic Publishing, 1st ed., 2017. 4

[29] A. Raj, *HEA: High Entropy Alloys*. CreateSpace Independent Publishing Platform, 2017. 4

[30] C.-J. Tong, Y.-L. Chen, J.-W. Yeh, S.-J. Lin, S.-K. Chen, T.-T. Shun, C.-H. Tsau, and S.-Y. Chang, "Mechanical Performance of the AlxCoCrCuFeNi High-Entropy Alloy System with Multiprincipal Elements," *Metallurgical and Materials Transactions A*, vol. 36, no. 4, pp. 881–893, 2005. 5, 171

[31] C.-J. Tong, Y.-L. Chen, J.-W. Yeh, S.-J. Lin, S.-K. Chen, T.-T. Shun, C.-H. Tsau, and S.-Y. Chang, "Microstructure characterization of Al x CoCrCuFeNi high-entropy alloy system with multiprincipal elements," *Metallurgical and Materials Transactions A*, vol. 36, no. 4, pp. 881–893, 2005. 5, 13

[32] L. J. Santodonato, Y. Zhang, M. Feygenson, C. M. Parish, M. C. Gao, R. J. K. Weber, J. C. Neuefeind, Z. Tang, and P. K. Liaw, "Deviation from high-entropy configurations in the atomic distributions of a multi-principal-element alloy.," *Nature communications*, vol. 6, p. 5964, 2015. 5

[33] A. Munitz, M. Kaufman, M. Nahmany, N. Derimow, and R. Abbaschian, "Microstructure and mechanical properties of heat treated Al 1.25 CoCrCuFeNi high entropy alloys," *Materials Science and Engineering: A*, vol. 714, no. September 2017, pp. 146–159, 2018. 5

[34] X. Yang and Y. Zhang, "Prediction of high-entropy stabilized solid-solution in multi-component alloys," *Materials Chemistry and Physics*, vol. 132, no. 2-3, pp. 233–238, 2012. 5, 20, 63

[35] O. N. Senkov, J. D. Miller, D. B. Miracle, and C. Woodward, "Accelerated exploration of multi-principal element alloys for structural applications," *Calphad: Computer Coupling of Phase Diagrams and Thermochemistry*, vol. 50, pp. 32–48, 2015. 5, 107

[36] M. C. Troparevsky, J. R. Morris, P. R. C. Kent, A. R. Lupini, and G. M. Stocks, "Criteria for predicting the formation of single-phase high-entropy alloys," *Physical Review X*, vol. 5, no. 1, pp. 1–6, 2015. 5

[37] I. Toda-Caraballo and P. Rivera-Díaz-del Castillo, "A criterion for the formation of high entropy alloys based on lattice distortion," *Intermetallics*, vol. 71, pp. 76–87, 2016. 5, 22, 107

[38] F. Tancret, I. Toda-Caraballo, E. Menou, and P. E. J. R. Díaz-Del-Castillo, "Designing high entropy alloys employing thermodynamics and Gaussian process statistical analysis," *Materials & Design*, vol. 115, pp. 486–497, 2017. 5

[39] Tazuddin, N. Gurao, and K. Biswas, "In the quest of single phase multi-component multiprincipal high entropy alloys," *Journal of Alloys and Compounds*, vol. 697, pp. 434–442, 2017. 5

[40] W. Sun, X. Huang, and A. A. Luo, "Phase formations in low density high entropy alloys," *Calphad: Computer Coupling of Phase Diagrams and Thermochemistry*, vol. 56, no. September 2016, pp. 19–28, 2017. 5

[41] M. H. Tsai, J. H. Li, A. C. Fan, and P. H. Tsai, "Incorrect predictions of simple solid solution high entropy alloys: Cause and possible solution," *Scripta Materialia*, vol. 127, pp. 6–9, 2017. 5, 15

[42] S. Guo, "Phase selection rules for cast high entropy alloys: an overview," *Materials Science and Technology*, vol. 31, no. 10, pp. 1223–1230, 2015. 9, 15, 17, 21, 59, 63

[43] C. Chattopadhyay, A. Prasad, and B. S. Murty, "Phase prediction in high entropy alloys – A kinetic approach," *Acta Materialia*, vol. 153, pp. 214–225, 2018. 9

[44] C. R. LaRosa, M. Shih, C. Varvenne, and M. Ghazisaeidi, "Solid solution strengthening theories of high-entropy alloys," *Materials Characterization*, vol. 151, no. February, pp. 310–317, 2019. 9

[45] A. Abu-Odeh, E. Galvan, T. Kirk, H. Mao, Q. Chen, P. Mason, R. Malak, and R. Arróyave, "Efficient exploration of the High Entropy Alloy composition-phase space," *Acta Materialia*, vol. 152, pp. 41–57, 2018. 9

[46] S. A. Kube, S. Sohn, D. Uhl, A. Datye, A. Mehta, and J. Schroers, "Phase selection motifs in High Entropy Alloys revealed through combinatorial methods: Large atomic size difference favors BCC over FCC," *Acta Materialia*, vol. 166, pp. 677–686, 2019. 9

[47] Z. Li, S. Zhao, R. O. Ritchie, and M. A. Meyers, "Mechanical properties of high-entropy alloys with emphasis on face-centered cubic alloys," *Progress in Materials Science*, vol. 102, no. December 2018, pp. 296–345, 2019. 9

[48] W. Li, P. K. Liaw, and Y. Gao, "Fracture resistance of high entropy alloys: A review," *Intermetallics*, vol. 99, no. May, pp. 69–83, 2018. 9

[49] C. Peiyong, L. E. E. Chanho, W. Shao-yu, S. Mohsen, L. J. J, D. K. A, J. I. A. Haoling, X. I. E. Xie, C. Bilin, Y. E. H. Jien-wei, T. Che-wei, Y. Tao, and L. P. K, "Fatigue behavior of high-entropy alloys : A review," *Sci China Tech Sci*, vol. 61, no. 2, pp. 168–178, 2018. 9

[50] H. Y. Diao, R. Feng, K. A. Dahmen, and P. K. Liaw, "Fundamental deformation behavior in high-entropy alloys: An overview," *Current Opinion in Solid State and Materials Science*, vol. 21, no. 5, pp. 252–266, 2017. 9

[51] J. Chen, X. Zhou, W. Wang, B. Liu, Y. Lv, W. Yang, D. Xu, and Y. Liu, "A review on fundamental of high entropy alloys with promising high–temperature properties," *Journal of Alloys and Compounds*, vol. 760, pp. 15–30, 2018. 9

[52] Y. Shi, B. Yang, and P. Liaw, "Corrosion-Resistant High-Entropy Alloys: A Review," *Metals*, vol. 7, no. 2, p. 43, 2017. 9

[53] X. H. Yan, J. S. Li, W. R. Zhang, and Y. Zhang, "A brief review of high-entropy films," *Materials Chemistry and Physics*, vol. 210, pp. 12–19, 2018. 9

[54] W. Li, P. Liu, and P. K. Liaw, "Microstructures and properties of high-entropy alloy films and coatings: A review," *Materials Research Letters*, vol. 6, no. 4, pp. 199–229, 2018. 9

[55] N. Derimow and R. Abbaschian, "Liquid Phase Separation in High-Entropy Alloys — A Review," *Entropy*, vol. 20, no. 11, pp. 1–19, 2018. 9, 131, 187

[56] Z. Pei, "An overview of modeling the stacking faults in lightweight and high-entropy alloys: Theory and application," *Materials Science and Engineering A*, vol. 737, no. September, pp. 132–150, 2018. 9

[57] A. McNaught and A. Wilkinson, *IUPAC. Compendium of Chemical Terminology, 2nd ed.* Oxford: Oxford, 2nd ed., 1997. 10

[58] K. Ishida and T. Nishizawa, "The Co-Cr (Cobalt-Chromium) system," *Bulletin of Alloy Phase Diagrams*, vol. 11, no. 4, pp. 357–370, 1990. 12, 101

[59] D. J. Chakrabarti and D. E. Laughlin, "The Cr-Cu (Chromium-Copper) system," 1984. 12

[60] N. A. Gokcen, "The Cu-Mn (copper-manganese) system," *Journal of Phase Equilibria*, vol. 14, no. 1, pp. 76–83, 1993. 12

[61] J. F. Smith, "The Fe-V (Iron-Vanadium) system," *Bulletin of Alloy Phase Diagrams*, vol. 5, no. 2, pp. 184–194, 1984. 12

[62] T. Nishizawa and K. Ishida, "The Co-Cu (Cobalt-Copper) system," *Bulletin of Alloy Phase Diagrams*, vol. 5, no. 2, pp. 161–165, 1984. 12, 57, 108

[63] J. O. Andersson and B. Sundman, "Thermodynamic properties of the CrFe system," *Calphad*, vol. 11, no. 1, pp. 83–92, 1987. 12

[64] Y. Iguchi, G. Katona, C. Cserhati, G. Langer, and Z. Erdelyi, "On the miscibility gap of Cu-Ni system," no. November, 2016. 12

[65] H. Okamoto, "Mn-Ni (manganese-nickel)," *Journal of Phase Equilibria and Diffusion*, vol. 28, no. 4, pp. 406–407, 2007. 12

[66] T. Nishizawa and K. Ishida, "The Co-Fe (Cobalt-Iron) system," *Bulletin of Alloy Phase Diagrams*, vol. 5, no. 3, pp. 250–259, 1984. 12

[67] E. A. Brandes and R. F. Flint, "The Cr-Mn (Chromium-Manganese) system," *Bulletin of Alloy Phase Diagrams*, vol. 2, no. 1, pp. 104–105, 1981. 12

[68] H. Okamoto, "Cu-Ti (Copper-Titanium)," *Journal of Phase Equilibria*, vol. 26, no. 3, pp. 549–550, 2002. 12

[69] J. L. Murray, "The Mn-Ti (Manganese-Titanium) system," *Bulletin of Alloy Phase Diagrams*, vol. 2, no. 3, pp. 334–343, 1981. 12

[70] K. Ishida and T. Nishizawa, "The Co-Mn (Cobalt-Manganese) system," *Bulletin of Alloy Phase Diagrams*, vol. 11, no. 2, pp. 125–137, 1990. 12

[71] P. Nash, "The Cr-Ni (Chromium-Nickel) System," *Bulletin of Alloy Phase Diagrams*, vol. 7, no. 5, pp. 466–476, 1986. 12

[72] J. F. Smith and O. N. Carlson, "The Cu-V (Copper-Vanadium) system," *Bulletin of Alloy Phase Diagrams*, vol. 2, no. 3, pp. 348–351, 1981. 12

[73] H. Okamoto, "Mn-V (Manganese-Vanadium)," *Journal of Phase Equilibria*, vol. 13, no. 5, pp. 575–576, 1992. 12

[74] T. Nishizawa and K. Ishida, "The Co-Ni (Cobalt-Nickel) system," *Bulletin of Alloy Phase Diagrams*, vol. 4, no. 4, pp. 390–395, 1983. 12

[75] H. Okamoto, "Cr-Ti (Chromium-Titanium)," *Journal of Phase Equilibria*, vol. 23, no. 4, pp. 382–383, 2000. 12

[76] V. T. Witusiewicz, F. Sommer, and E. J. Mittemeijer, "Reevaluation of the Fe-Mn phase diagram," *Journal of Phase Equilibria and Diffusion*, vol. 25, no. 4, pp. 346–354, 2004. 12

[77] D. Le, C. Colinet, P. Hicter, and A. Pasturel, "Theoretical description of phase equilibrium in the nickel-titanium system," *Journal of Physics: Condensed Matter*, vol. 3, no. 50, pp. 9965–9974, 1991. 12

[78] J. Murray, "The Co-Ti (Cobalt-Titanium) System Co-Ti," *Bulletin of Alloy Phase Diagrams*, vol. 3, no. 1, pp. 74–85, 1982. 12

[79] J. F. Smith, D. M. Bailey, and O. N. Carlson, "The Cr-V (Chromium-Vanadium) system," *Bulletin of Alloy Phase Diagrams*, vol. 2, no. 4, pp. 469–473, 1982. 12

[80] G. V. Raynor and V. G. Rivlin, "The Fe-Ni (Iron-Nickel) system," *Bulletin of Alloy Phase Diagrams*, vol. 2, no. 1, p. 102, 1981. 12

[81] J. Smith, "The Ni-V (Nickel-Vanadium) System," *Bulletin of Alloy Phase Diagrams*, vol. 3, no. 3, pp. 342–349, 1982. 12

[82] J. F. Smith, "The Co-V (Cobalt-Vanadium) System," *Journal of Phase Equilibria*, vol. 12, no. 3, pp. 324–331, 1991. 12

[83] Y. Y. Chuang, R. Schmid, and Y. A. Chang, "Thermodynamic analysis of the iron-copper system I: The stable and metastable phase equilibria," *Metallurgical Transactions A*, vol. 15, no. 10, pp. 1921–1930, 1984. 12, 28, 57, 108

[84] J. L. Murray, "The Fe-Ti (Iron-Titanium) system," *Bulletin of Alloy Phase Diagrams*, vol. 2, no. 3, pp. 320–334, 1981. 12

[85] J. Murray, "The Ti-V (Titanium-Vanadium) System 47.88," *Bulletin of Alloy Phase Diagrams*, vol. 2, no. 1, pp. 48–55, 1981. 12

[86] X. J. Liu, Z. P. Jiang, C. P. Wang, and K. Ishida, "Experimental determination and thermodynamic calculation of the phase equilibria in the Cu – Cr – Nb and Cu – Cr – Co systems," *Journal of Alloys and Compounds*, vol. 478, no. 422, pp. 287–296, 2009. 13, 31, 32, 41, 42, 58, 60, 64, 100, 108, 109, 111, 117, 121, 124, 131, 132, 137, 141, 144, 172

[87] E. Josso, "Iron-Cobalt-Vanadium Alloys: A Critical Study of the Phase Diagrams in Relation to Magnetic Properties," *IEEE Transactions on Magnetics*, vol. MAG-10, no. 2, pp. 161–165, 1974. 13

[88] V. Ivanchenko, "Chromium-Iron-Titanium," *Landolt-Bornstein*, vol. New Series, pp. 1–17, 2008. 13

[89] H. Masumoto, S. Sawaya, and M. Kikuchi, "H. Nonferromagnetic Elinvar-Type Alloys in the Mn-Cu-V System," *Transactions of the Japan Institue of Metals*, vol. 17, no. 2, pp. 111–115, 1976. 13

[90] V. Raghavan, "Co-Cr-Fe (cobalt-chromium-iron)," *Journal of Phase Equilibria*, vol. 15, no. 5, pp. 524–525, 1994. 13, 101

[91] K. P. Gupta, "The Co-Mn-Ni (Cobalt-Manganese-Nickel) system," *Journal of Phase Equilibria*, vol. 20, no. 5, pp. 527–532, 1999. 13

[92] V. Ivanchenko, "Chromium-Iron-Vanadium," *Landolt-Bornstein*, vol. New Series, pp. 1–18, 2008. 13

[93] K. P. Gupta, "The Cu-Ni-Ti (Copper-Nickel-Titanium) System," *Journal of Phase Equilibria*, vol. 23, no. 6, pp. 541–547, 2002. 13

[94] K. Adachi, "Co-Cr-Mn," in *Landolt-Bornstein 3d, 4d and 5d Elements, Alloys and Compounds* (H. Wijn, ed.), vol. 19A, p. 438, Springer Materials, 1986. 13

[95] "Co-Mn-Ti Isothermal Section of Ternary Phase Diagram: Datasheet from "PAULING FILE Multinaries Edition – 2012" in SpringerMaterials (http://materials.springer.com/isp/phase-diagram/docs/c_0925260)." 13

[96] "Cr-Mn-Ni Isothermal Section of Ternary Phase Diagram: Datasheet from "PAULING FILE Multinaries Edition – 2012" in SpringerMaterials (http://materials.springer.com/isp/phase-diagram/docs/c_0200767)." 13

[97] J. Schramm, "Copper-Nickel-Vanadium Alloy," *Patent 3364082*, vol. USA, no. Jan. 16, 1968. 13

[98] S. Yang, M. Jiang, H. Li, Y. Liu, and L. Wang, "Assessment of Co-Cr-Ni ternary system by CALPHAD technique," *Rare Metals*, vol. 31, no. 1, pp. 75–80, 2012. 13, 99

[99] K. Gupta, "The Co-Mn-V (Cobalt-Manganese-Vanadium) System," *Journal of Phase Equilibria & Diffusion*, vol. 25, no. 6, pp. 566–569, 2004. 13

[100] L. Y. Chen, C. H. Li, K. Wang, H. Q. Dong, X. G. Lu, and W. Z. Ding, "Thermodynamic modeling of Ti-Cr-Mn ternary system," *Calphad: Computer Coupling of Phase Diagrams and Thermochemistry*, vol. 33, no. 4, pp. 658–663, 2009. 13

[101] H. P. Ng, A. Devaraj, S. Nag, C. J. Bettles, M. Gibson, H. L. Fraser, B. C. Muddle, and R. Banerjee, "Phase separation and formation of omega phase in the beta matrix of a Ti-V-Cu alloy," *Acta Materialia*, vol. 59, no. 8, pp. 2981–2991, 2011. 13

[102] K. P. Gupta, "The Co-Cr-Ti System (Cobalt-Chromium-Titanium)," *Journal of Phase Equilibria*, vol. 22, no. 1, pp. 52–60, 2001. 13, 174

[103] G. Cacciamani and P. Riani, "Cobalt – Nickel – Titanium," *Landolt-Bornstein*, vol. New Series, pp. 169–177, 2006. 13

[104] "Cr-Mn-V Isothermal Section of Ternary Phase Diagram: Datasheet from "PAULING FILE Multinaries Edition – 2012" in SpringerMaterials (http://materials.springer.com/isp/phase-diagram/docs/c_2000205)." 13

[105] L. Zhang, Y. Du, H. Xu, S. Liu, Y. Liu, F. Zhengc, N. Dupin, H. Zhou, and C. Tang, "Phase equilibria and thermal analysis in the Fe-Mn-Ni system," *International Journal of Materials Research*, vol. 100, no. 2, pp. 160–175, 2009. 13

[106] C. Zhao, C.C., Yu, Y., Liu, X.J., Wang, "Experimental Determination of Phase Equilibria in the Co-Cr-V Ternary System," *Journal of Phase Equilibria and Diffusion*, vol. 33, no. 3, pp. 189–194, 2012. 13, 101

[107] "Co-Ni-V Liquidus Projection of Ternary Phase Diagram: Datasheet from "PAULING FILE Multinaries Edition – 2012" in SpringerMaterials (http://materials.springer.com/isp/phase-diagram/docs/c_0206472)." 13

[108] B. Hu, Y. Du, J. C. Schuster, W. Sun, S. Liu, and C. Tang, "Thermodynamic modeling of the Cr-Ni-Ti system using a four-sublattice model for ordered/disordered bcc phases," *Thermochimica Acta*, vol. 578, pp. 35–42, 2014. 13

[109] C. Craighead, O. Simmons, and L. Eastwood, "Ternary Alloys of Titanium," *Journal of Metals*, vol. Transactio, pp. 514–538, 1950. 13

[110] A. Munitz, R. Abbachian, C. Cotler, and C. Shacham, "Liquid Phase Separation in Cu-Co-Fe and Cu-Fe-Ni-Cr Alloys," *High Temperature Materials and Processes*, vol. 15, no. 13, pp. 187–194, 1996. 13, 26, 29, 31, 41, 43, 58, 108

[111] G. J. Zhou, J. G. Tang, Y. Zhou, W. K. An, and A. H. Cai, "Phase equilibria in the Co-Ti-V system at 873 K," *Journal of Alloys and Compounds*, vol. 602, pp. 49–52, 2014. 13

[112] S. K. Singh and K. P. Gupta, "The Cr-Ni-V System," *Journal of Phase Equilibria*, vol. 16, no. 2, pp. 129–136, 1995. 13

[113] J. Darby and P. A. Beck, "Sigma- Phase in Certain Ternary Systems With Vanadium," *Journal of Metals*, vol. Transactio, no. January, pp. 69–72, 1957. 13

[114] C. P. Wang, X. J. Liu, I. Ohnuma, R. Kainuma, and K. Ishida, "Thermodynamic assessments of the Cu-Mn-X (X: Fe, Co) systems," *Journal of Alloys and Compounds*, vol. 438, no. 1-2, pp. 129–141, 2007. 13

[115] C. P. Wang, X. J. Liu, I. Ohnuma, R. Kainuma, and K. Ishida, "Phase equilibria in Fe-Cu-X (X: Co, Cr, Si, V) ternary systems," *Journal of Phase Equilibria*, vol. 23, no. 3, pp. 236–245, 2002. 13, 26, 29, 31, 41

[116] G. Ghosh, "Thermodynamic and kinetic modeling of the Cr-Ti-V system," *Journal of Phase Equilibria*, vol. 23, no. 4, pp. 310–328, 2002. 13

[117] G. Cacciamani, J. De Keyzer, R. Ferro, U. E. Klotz, J. Lacaze, and P. Wollants, "Critical evaluation of the Fe-Ni, Fe-Ti and Fe-Ni-Ti alloy systems," *Intermetallics*, vol. 14, no. 10-11, pp. 1312–1325, 2006. 13

[118] D. Y. Zang, H. P. Wang, F. P. Dai, D. Langevin, and B. Wei, "Solidification mechanism transition of liquid Co-Cu-Ni ternary alloy," *Applied Physics A: Materials Science and Processing*, vol. 102, no. 1, pp. 141–145, 2011. 13

[119] W. DeBoskey, *SIGMA PHASE IN THE TERNARY SYSTEMS CHROMIUM-COBALT-COPPER AND CHROMIUM-MANGANESE-COOPER*. Master of science, Virginia Polytechnic Institute, 1955. 13

[120] C. Zhao, S. Yang, Y. Lu, Y. Guo, C. Wang, and X. J. Liu, "Experimental investigation and thermodynamic calculation of the phase equilibria in the Fe-Ni-V system," *CALPHAD: Computer Coupling of Phase Diagrams and Thermochemistry*, vol. 46, pp. 80–86, 2014. 13

[121] Y. M. Wang, H. S. Liu, L. Zhang, F. Zheng, and Z. P. Jin, "The isothermal section of the Co-Cu-Ti ternary system at 1023 K by using diffusion triple technique," *Materials Science and Engineering A*, vol. 431, pp. 184–190, 2006. 13

[122] G. Ghosh, "Chromium – Copper – Nickel," *Landolt-Bornstein*, vol. Non-Ferrou, no. Part 2, pp. 210–221, 2007. 13

[123] I. Egry, J. Brillo, and T. Matsushita, "Thermophysical properties of liquid Cu-Fe-Ni alloys," *Materials Science and Engineering A*, vol. 413-414, pp. 460–464, 2005. 13

[124] V. Raghavan, "Fe-Ti-V (Iron-Titanium-Vanadium)," *Journal of Phase Equilibria and Diffusion*, vol. 32, no. 4, pp. 1–2, 2011. 13

[125] X. J. Liu, Y. Yu, Y. H. Liu, W. L. Huang, Y. Lu, Y. H. Guo, and C. P. Wang, "Experimental Investigation and Thermodynamic Calculation of the Phase Equilibria in the Co-Cu-V Ternary System," *Journal of Phase Equilibria and Diffusion*, vol. 38, no. 5, pp. 733–742, 2017. 13

[126] "Cr-Cu-Ti Liquidus Projection of Ternary Phase Diagram: Datasheet from "PAULING FILE Multinaries Edition – 2012" in SpringerMaterials (http://materials.springer.com/isp/phase-diagram/docs/c_0925481)." 13

[127] H. Bo, L. I. Duarte, W. J. Zhu, L. B. Liu, H. S. Liu, Z. P. Jin, and C. Leinenbach, "Experimental study and thermodynamic assessment of the Cu-Fe-Ti system," *Calphad: Computer Coupling of Phase Diagrams and Thermochemistry*, vol. 40, pp. 24–33, 2013. 13

[128] K. P. Gupta, "The Mn-Ni-Ti (Mangenese-Nickel-Titanium) System — Update," *Journal of Phase Equilibria*, vol. 24, no. 4, pp. 371–372, 2003. 13

[129] a. Baruj, a. F. Guillermet, M. Sade, and C. A. Bariloche, "The fcc/hcp Relative Phase Stability in the Fe-Mn-Co System:Martensitic Transformation Temperatures,Assessment of Gibbs Energies and Thermodynamic Calculation of To Lines," *Journal De Physique IV*, vol. 7, pp. C5–405, 1997. 13

[130] Y. K. Yoo, Q. Xue, Y. S. Chu, S. Xu, U. Hangen, H. C. Lee, W. Stein, and X. D. Xiang, "Identification of amorphous phases in the Fe-Ni-Co ternary alloy system using continuous phase diagram material chips," *Intermetallics*, vol. 14, no. 3, pp. 241–247, 2006. 13

[131] J. Vrestal, "Chromium-Iron-Manganese," *Landolt-Bornstein*, vol. 11D4, pp. 1–19, 2008. 13

[132] J. Miettinen, "Thermodynamic description of the Cu-Mn-Ni system at the Cu-Ni side," *Calphad: Computer Coupling of Phase Diagrams and Thermochemistry*, vol. 27, no. 2, pp. 147–152, 2003. 13, 158

[133] B. M. Enomoto, "The Mn-Ti-V System," *Journal of Phase Equilibria*, vol. 13, no. 4, pp. 417–420, 1992. 13

[134] Y. Pan, C. Chen, Y. Du, C. Yuan, and F. Luo, "Experimental Investigation and Thermodynamic Calculations of the Co-Fe-Ti System," *Journal of Phase Equilibria and Diffusion*, vol. 38, no. 1, pp. 5–16, 2017. 13

[135] J. Tomiska, "The system Fe-Ni-Cr: Revision of the thermodynamic description," *Journal of Alloys and Compounds*, vol. 379, no. 1-2, pp. 176–187, 2004. 13

[136] H. Masumoto, S. Sawaya, and M. Kikuchi, "Elinvar Characteristics of Nonferromagnetic Mn-Cu-Ti and Mn-Cu-Zr Alloys," *Transactions of the Japan Institue of Metals*, vol. 24, no. 11, pp. 765–772, 1983. 13

[137] M. D. Dolan, M. A. Kochanek, C. N. Munnings, K. G. McLennan, and D. M. Viano, "Hydride phase equilibria in V-Ti-Ni alloy membranes," *Journal of Alloys and Compounds*, vol. 622, pp. 276–281, 2015. 13

[138] A. Durga, K. C. Hari Kumar, and B. S. Murty, "Phase formation in equiatomic high entropy alloys: CALPHAD approach and experimental studies," *Transactions of the Indian Institute of Metals*, vol. 65, no. 4, pp. 375–380, 2012. 13, 60, 63, 130, 149, 154

[139] A. Munitz, M. Kaufman, and R. Abbaschian, "Liquid phase separation in transition element high entropy alloys," *Intermetallics*, vol. 86, pp. 59–72, 2017. 13, 43, 57, 60, 64, 72, 81, 83, 100, 108, 109, 117, 131, 141, 149, 154

[140] N. Derimow and R. Abbaschian, "Solidification microstructures and calculated mixing enthalpies in CoCrCu containing alloys," *Materials Today Communications*, vol. 15, no. February, pp. 1–10, 2018. 13, 31, 41, 42, 43, 56, 131, 132, 141, 150, 154, 172, 174

[141] C. H. Tsau, "Phase transformation and mechanical behavior of TiFeCoNi alloy during annealing," *Materials Science and Engineering A*, vol. 501, no. 1-2, pp. 81–86, 2009. 13

[142] S. Praveen, B. S. Murty, and R. S. Kottada, "Phase evolution and densification behavior of nanocrystalline multicomponent high entropy alloys during spark plasma sintering," *Jom*, vol. 65, no. 12, pp. 1797–1804, 2013. 13, 60, 150, 160

[143] C. P. Lee, C. C. Chang, Y. Y. Chen, J. W. Yeh, and H. C. Shih, "Effect of the aluminium content of AlxCrFe1.5MnNi0.5 high-entropy alloys on the corrosion behaviour in aqueous environments," *Corrosion Science*, vol. 50, no. 7, pp. 2053–2060, 2008. 13

[144] M.-H. Tsai, K.-Y. Tsai, C.-W. Tsai, C. Lee, C.-C. Juan, and J.-W. Yeh, "Criterion for Sigma Phase Formation in Cr- and V-Containing High-Entropy Alloys," *Materials Research Letters*, vol. 1, no. May 2014, pp. 207–212, 2013. 13

[145] S. Guo, C. Ng, Z. Wang, and C. T. Liu, "Solid solutioning in equiatomic alloys: Limit set by topological instability," *Journal of Alloys and Compounds*, vol. 583, pp. 410–413, 2014. 13

[146] F. He, Z. Wang, Q. Wu, J. Li, J. Wang, and C. T. Liu, "Phase separation of metastable CoCrFeNi high entropy alloy at intermediate temperatures," *Scripta Materialia*, vol. 126, pp. 15–19, 2017. 13, 99

[147] F. He, Z. Wang, Q. Wu, S. Niu, J. Li, J. Wang, and C. T. Liu, "Solid solution island of the Co-Cr-Fe-Ni high entropy alloy system," *Scripta Materialia*, vol. 131, no. January, pp. 42–46, 2017. 13, 99

[148] F. Otto, Y. Yang, H. Bei, and E. P. George, "Relative effects of enthalpy and entropy on the phase stability of equiatomic high-entropy alloys," *Acta Materialia*, vol. 61, no. 7, pp. 2628–2638, 2013. 13, 60, 109

[149] M. X. Ren, B. S. Li, and H. Z. Fu, "Formation condition of solid solution type high-entropy alloy," *Transactions of Nonferrous Metals Society of China (English Edition)*, vol. 23, no. 4, pp. 991–995, 2013. 13, 21

[150] N. Park, I. Watanabe, D. Terada, Y. Yokoyama, P. K. Liaw, and N. Tsuji, "Recrystallization Behavior of CoCrCuFeNi High-Entropy Alloy," *Metallurgical and Materials Transactions A*, vol. 46, no. 4, pp. 1481–1487, 2015. 13, 57, 64, 109, 131, 149, 166

[151] N. Liu, P. Wu, P. Zhou, Z. Peng, X. Wang, and Y. Lu, "Rapid solidification and liquid-phase separation of undercooled CoCrCuFexNi high-entropy alloys," *Intermetallics*, vol. 72, pp. 44–52, 2016. 13, 43, 44, 57, 64, 109, 131, 149

[152] W. Wang, L. Hu, S. Luo, L. Meng, D. Geng, and B. Wei, "Liquid phase separation and rapid dendritic growth of high-entropy CoCrCuFeNi alloy," *Intermetallics*, vol. 77, pp. 41–45, 2016. 13, 43, 44, 57, 58, 64, 109, 131, 149

[153] P. H. Wu, N. Liu, P. J. Zhou, Z. Peng, W. D. Du, X. J. Wang, and Y. Pan, "Microstructures and liquid phase separation in multicomponent CoCrCuFeNi high entropy alloys," *Materials Science and Technology*, vol. 0836, no. May, pp. 1–5, 2016. 13, 43, 44, 57, 64, 109, 131, 149

[154] B. Ren, Z. X. Liu, D. M. Li, L. Shi, B. Cai, and M. X. Wang, "Effect of elemental interaction on microstructure of CuCrFeNiMn high entropy alloy system," *Journal of Alloys and Compounds*, vol. 493, no. 1-2, pp. 148–153, 2010. 13

[155] A. K. Mishra, S. Samal, and K. Biswas, "Solidification behaviour of Ti-Cu-Fe-Co-Ni high entropy alloys," *Transactions of the Indian Institute of Metals*, vol. 65, no. 6, pp. 725–730, 2012. 13

[156] Y. Zhang, Y. J. Zhou, J. P. Lin, G. L. Chen, and P. K. Liaw, "Solid-solution phase formation rules for multi-component alloys," *Advanced Engineering Materials*, vol. 10, no. 6, pp. 534–538, 2008. 13

[157] T. T. Shun, L. Y. Chang, and M. H. Shiu, "Microstructures and mechanical properties of multiprincipal component CoCrFeNiTix alloys," *Materials Science and Engineering A*, vol. 556, pp. 170–174, 2012. 13

[158] D. Tabachnikova, V. Podolskiy, M. O. Laktionova, N. A. Bereznaia, M. A. Tikhonovsky, and A. S. Tortika, "Mechanical properties of the CoCrFeNiMnVx high entropy alloys in temperature range 4.2–300 K," *Journal of Alloys and Compounds*, vol. 698, pp. 501–509, 2017. 14

[159] X. F. Wang, Y. Zhang, Y. Qiao, and G. L. Chen, "Novel microstructure and properties of multicomponent CoCrCuFeNiTix alloys," *Intermetallics*, vol. 15, no. 3, pp. 357–362, 2007. 14, 60, 109, 130, 149

[160] N. D. Stepanov, D. G. Shaysultanov, G. A. Salishchev, M. A. Tikhonovsky, E. E. Oleynik, A. S. Tortika, and O. N. Senkov, "Effect of v content on microstructure and mechanical properties of the CoCrFeMnNiVx high entropy alloys," *Journal of Alloys and Compounds*, vol. 628, pp. 170–185, 2015. 14

[161] Y. J. Zhou, Y. Zhang, Y. L. Wang, and G. L. Chen, "Microstructure and compressive properties of multicomponent Alx(TiVCrMnFeCoNiCu)100-x high-entropy alloys," *Materials Science and Engineering A*, vol. 454-455, pp. 260–265, 2007. 14, 60, 109

[162] S. Fang, X. Xiao, L. Xia, W. Li, and Y. Dong, "Relationship between the widths of supercooled liquid regions and bond parameters of Mg-based bulk metallic glasses," *Journal of Non-Crystalline Solids*, vol. 321, no. 1-2, pp. 120–125, 2003. 16

[163] S. Guo, C. Ng, J. Lu, and C. T. Liu, "Effect of valence electron concentration on stability of fcc or bcc phase in high entropy alloys," *Journal of Applied Physics*, vol. 109, no. 10, 2011. 16, 63, 99

[164] S. Guo and C. Liu, "Phase stability in high entropy alloys: Formation of solid-solution phase or amorphous phase," *Progress in Natural Science: Materials International*, vol. 21, no. 6, pp. 433–446, 2011. 17, 63

[165] A. R. Miedema, "A simple model for alloys I," *Philips Technical Review*, vol. 33, no. 6, pp. 149–160, 1973. 19, 27, 59

[166] A. Takeuchi and A. Inoue, "Metallic Glasses By Atomic Size Difference, Heat of Mixing and Period of Constituent Elements and Its Application To Characterization of the Main Alloying Element," *Materials Transactions*, vol. 46, no. 12, pp. 2817–2829, 2005. 19, 27, 61

[167] A. Takeuchi and A. Inoue, "Mixing enthalpy of liquid phase calculated by miedema's scheme and approximated with sub-regular solution model for assessing forming ability of amorphous and glassy alloys," *Intermetallics*, vol. 18, no. 9, pp. 1779–1789, 2010. 19, 27, 28, 61, 62, 65, 221, 223

[168] H. Hardy, "A "sub-regular" solution model and its application to some binary alloy systems," *Acta Metallurgica*, vol. 1, pp. 202–209, 1953. 19, 27, 61

[169] D. J. M. King, S. C. Middleburgh, A. G. McGregor, and M. B. Cortie, "Predicting the formation and stability of single phase high-entropy alloys," *Acta Materialia*, vol. 104, pp. 172–179, 2016. 21, 107

[170] F. Zhang, C. Zhang, S. Chen, J. Zhu, W. Cao, and U. Kattner, "An understanding of high entropy alloys from phase diagram calculations," *Calphad*, vol. 45, pp. 1–10, 2014. 22

[171] B. W. Mott, "Liquid immiscibility in metal systems," *Philosophical Magazine*, vol. 2, no. 14, pp. 259–283, 1957. 24

[172] B. Mott, "Immiscibility in Liquid Metal Systems," *Journal of Materials Science*, vol. 3, pp. 424–435, 1968. 24

[173] L. Ratke and S. Diefenbach, "Liquid immiscible alloys," *Materials Science and Engineering R*, vol. 15, no. 7-8, pp. 263–347, 1995. 24, 25, 35

[174] L. Ratke, G. Korekt, and S. Drees, "Solidification of Immiscible Alloys," in *ESA Symposium Proceedings on 'Space Station Utilisation'*, (Darmstadt), pp. 247–251, European Space Agency, 1996. 24

[175] R. N. Singh and F. Sommer, "Segregation and Immiscibility in Liquid Binary Alloys," *Reports on Progress in Physics*, vol. 60, pp. 57–150, 1997. 24, 25

[176] C. W. Bale, E. Bélisle, P. Chartrand, S. A. Decterov, G. Eriksson, A. E. Gheribi, K. Hack, I. H. Jung, Y. B. Kang, J. Melançon, A. D. Pelton, S. Petersen, C. Robelin, J. Sangster, P. Spencer, and M. A. Van Ende, "FactSage thermochemical software and databases, 2010–2016," *Calphad: Computer Coupling of Phase Diagrams and Thermochemistry*, vol. 55, pp. 1–19, 2016. 24, 31

[177] A. Munitz and R. Abbaschian, "Liquid separation in Cu-Co and Cu-Co-Fe alloys solidified at high cooling rates," *Journal of Materials Science*, vol. 33, no. 14, pp. 3639–3649, 1998. 26, 28, 29, 31, 41

[178] D. I. Kim and R. Abbaschian, "The metastable liquid miscibility gap in Cu-Co-Fe alloys," *Journal of Phase Equilibria*, vol. 21, no. 1, pp. 25–31, 2000. 26, 29, 31, 41, 58, 108

[179] M. Bamberger, A. Munitz, L. Kaufman, and R. Abbaschian, "Evaluation of the stable and metastable Cu-Co-Fe phase diagrams," *Calphad: Computer Coupling of Phase Diagrams and Thermochemistry*, vol. 26, no. 3, pp. 375–384, 2002. 26, 29, 31, 41

[180] C.-D. Cao and G. P. Görler, "Direct Measurement of the Metastable Liquid Miscibility Gap in Fe–Co–Cu Ternary Alloy System," *Chinese Physics Letters*, vol. 22, no. 2, pp. 482–484, 2005. 26, 29, 31, 41, 58, 108

[181] I. Yamauchi, T. Irie, and H. Sakaguchi, "Metastable liquid separation in undercooled Fe-Cu and Fe-Cu-Si melts containing a small B concentration and their solidification structure," *Journal of Alloys and Compounds*, vol. 403, no. 1-2, pp. 211–216, 2005. 26, 29, 31, 57, 108

[182] A. Munitz, A. M. Bamberger, S. Wannaparhun, and R. Abbaschian, "Effects of supercooling and cooling rate on the microstructure of Cu-Co-Fe alloys," *Journal of Materials Science*, vol. 41, no. 10, pp. 2749–2759, 2006. 26, 29, 31, 41

[183] S. Curiotto, R. Greco, N. H. Pryds, E. Johnson, and L. Battezzati, "The liquid metastable miscibility gap in Cu-based systems," *Fluid Phase Equilibria*, vol. 256, no. 1-2, pp. 132–136, 2007. 26, 28, 29, 31, 41

[184] A. Munitz, A. Venkert, P. Landau, M. J. Kaufman, and R. Abbaschian, "Microstructure and phase selection in supercooled copper alloys exhibiting metastable liquid miscibility gaps," *Journal of Materials Science*, vol. 47, pp. 7955–7970, 2012. 26, 28, 29, 31, 40, 41, 57, 58, 108

[185] N. Liu, F. Liu, W. Yang, Z. Chen, and G. C. Yang, "Movement of minor phase in undercooled immiscible Fe-Co-Cu alloys," *Journal of Alloys and Compounds*, vol. 551, pp. 323–326, 2013. 26, 29, 31, 41

[186] Y. Nakagawa and D. L. E. S. Systemes, "LIQUID SYSTEMS IN COPPER-IRON IN THE SUPERCOOLED AND COPPER-COBALT STATE * According to the recent report on the phase diagrams , cl) both the Cu-Fe and Cu-Co systems are miscible in all proportions in the liquid ph & se . It should be mentioned , howeve," *Acta Metallurgica*, vol. 6, pp. 704–711, 1958. 28

[187] A. Munitz and R. Abbaschian, "Two-melt separation in supercooled Cu-Co alloys solidifying in a drop-tube," *Journal of Materials Science*, vol. 26, no. 23, pp. 6458–6466, 1991. 28, 57, 108

[188] A. Munitz, S. P. Elder-Randall, and R. Abbaschian, "Supercooling effects in Cu-10 Wt Pct Co alloys solidified at different cooling rates," *Metallurgical Transactions A*, vol. 23, no. 6, pp. 1817–1827, 1992. 28, 29, 57, 108, 219, 220

[189] A. Munitz and R. Abbaschian, "Microstructure of Cu-Co Alloys Solidified at Various Supercoolings," *Metallurgical and Materials Transactions A*, vol. 27, no. December, pp. 4049–4059, 1996. 28

[190] M. B. Robinson, D. Li, T. J. Rathz, and G. Williams, "Undercooling, liquid separation and solidification of Cu-Co alloys," *Journal of Materials Science*, vol. 34, no. 15, pp. 3747–3753, 1999. 28

[191] M. Kolbe and J. R. Gao, "Liquid phase separation of Co-Cu alloys in the metastable miscibility gap," *Materials Science and Engineering A*, vol. 413-414, pp. 509–513, 2005. 28, 35

[192] S. Curiotto, N. H. Pryds, E. Johnson, and L. Battezzati, "Liquid-liquid phase separation and remixing in the Cu-Co system," *Metallurgical and Materials Transactions A: Physical Metallurgy and Materials Science*, vol. 37, no. 8, pp. 2361–2368, 2006. 28

[193] W. Yang, Z. Xu, Z. Wang, S. Li, F. Liu, and G. Yang, "Microstructure morphology and solute segregation in nonequilibrium solidification of metastable immiscible Cu50Co50 alloy," *Procedia Engineering*, vol. 27, no. 2011, pp. 1518–1523, 2012. 28

[194] Y. K. Zhang, J. Gao, C. Yang, M. Kolbe, S. Binder, and D. M. Herlach, "Asynchronous crystallization behavior of Co-rich droplets in phase-separated Cu-Co alloys," *Materials Letters*, vol. 73, pp. 56–58, 2012. 28, 57, 108

[195] Y. Zhang, J. Gao, H. Yasuda, M. Kolbe, and G. Wilde, "Particle size distribution and composition in phase-separated Cu75Co25 alloys under various magnetic fields," *Scripta Materialia*, vol. 82, pp. 5–8, 2014. 28, 57, 108

[196] S.-H. Si, H. Zhang, Y.-Z. He, M.-X. Li, and S. Guo, "Liquid Phase Separation and the Aging Effect on Mechanical and Electrical Properties of Laser Rapidly Solidified Cu100-xCrx Alloys," *Metals*, vol. 5, no. 4, pp. 2119–2127, 2015. 28

[197] O. E. Jegede, R. F. Cochrane, and A. M. Mullis, "Metastable monotectic phase separation in Co – Cu alloys," *Journal of Materials Science*, vol. 53, no. 16, pp. 11749–11764, 2018. 28

[198] A. Munitz, "Liquid separation effects in Fe-Cu alloys solidified under different cooling rates," *Metallurgical Transactions B*, vol. 18, no. 3, pp. 565–575, 1987. 28

[199] A. Munitz, "Metastable liquid phase separation in tungsten inert gas and electron beam copper/stainless-steel welds," *Journal of Materials Science*, vol. 30, no. 11, pp. 2901–2910, 1995. 28, 57, 108

[200] C. P. Wang, X. J. Liu, Y. Takaku, I. Ohnuma, R. Kainuma, and K. Ishida, "Formation of core-type macroscopic morphologies in Cu-Fe base alloys with liquid miscibility gap," *Metallurgical and Materials Transactions A: Physical Metallurgy and Materials Science*, vol. 35 A, no. 4, pp. 1243–1253, 2004. 28

[201] Y. Z. Chen, F. Liu, G. C. Yang, X. Q. Xu, and Y. H. Zhou, "Rapid solidification of bulk undercooled hypoperitectic Fe-Cu alloy," *Journal of Alloys and Compounds*, vol. 427, no. 1-2, pp. 3–7, 2007. 28, 57, 108

[202] Y. K. Zhang, J. Gao, D. Nagamatsu, T. Fukuda, H. Yasuda, M. Kolbe, and J. C. He, "Reduced droplet coarsening in electromagnetically levitated and phase-separated Cu-Co alloys by imposition of a static magnetic field," *Scripta Materialia*, vol. 59, no. 9, pp. 1002–1005, 2008. 28, 35, 57, 108

[203] N. Liu, "Investigation on the phase separation in undercooled Cu-Fe melts," *Journal of Non-Crystalline Solids*, vol. 358, no. 2, pp. 196–199, 2012. 28

[204] J. T. Zhang, Y. H. Wang, X. C. Cui, and J. B. Lin, "The growth and congregation of minor phase in immiscible Cu-Fe alloys," *Medziagotyra*, vol. 19, no. 4, pp. 373–376, 2013. 28, 57, 108

[205] J. Zhang, X. Cui, and Y. Wang, "Liquid phase separation in immiscible Cu–Fe alloys," *International Journal of Cast Metals Research*, vol. 31, no. 2, pp. 87–92, 2018. 28

[206] Y. A. Chang, D. Goldberg, and J. P. Neumann, "Phase diagrams and thermodynamic properties of ternary copper-silver systems," *Journal of Physical and Chemical Reference Data*, vol. 6, no. 3, pp. 621–674, 1977. 31

[207] K. Taguchi, H. Ono-Nakazato, and T. Usui, "Liquid Immiscibility in Fe–Cu–B System," *ISIJ International*, vol. 46, no. 1, pp. 633–636, 2006. 31

[208] J. B. Guo, C. D. Cao, S. L. Gong, R. B. Song, X. J. Bai, J. Y. Wang, J. B. Zheng, X. X. Wen, and Z. B. Sun, "Rapid solidification of Cu60Co30Cr10alloy under different conditions," *Transactions of Nonferrous Metals Society of China (English Edition)*, vol. 23, no. 3, pp. 731–734, 2013. 31, 32

[209] N. Derimow, L. Santodonato, R. Mills, and R. Abbaschian, "In-Situ Imaging of Liquid Phase Separation in Molten Alloys Using Cold Neutrons," *Journal of Imaging*, vol. 4, no. 1, p. 5, 2018. 31, 38, 41, 106, 125, 132, 136, 137, 142, 143, 144, 172

[210] N. Liu, F. Liu, Z. Chen, G. Yang, C. Yang, and Y. Zhou, "Liquid-phase Separation in Rapid Solidification of Undercooled Fe-Co-Cu Melts," *Journal of Materials Science and Technology*, vol. 28, no. 7, pp. 622–625, 2012. 31, 41

[211] B. A. A. Dreval, L. A., Turchanin, M. A., Abdulov, A. R., "Thermodynamic assessment of the Cu-Fe-Cr phase diagram," *Chemistry of Metals and Alloys*, vol. 3, no. 2010, pp. 132–139, 2010. 31

[212] T. Nagase, M. Matsumoto, and Y. Fujii, "Microstructure of Ti-Nb-Ag Immiscible Alloys with Liquid Phase Separation," *Microscopy*, vol. 66, no. August, p. i22, 2017. 31

[213] C. P. Wang, X. J. Liu, I. Ohnuma, R. Kainuma, K. Ishida, and S. M. Hao, "Phase equilibria in the Cu-Fe-Mo and Cu-Fe-Nb systems," *Journal of Phase Equilibria*, vol. 21, no. 1, pp. 54–62, 2000. 31

[214] L. Bo, S. Li, L. Wang, D. Wu, M. Zuo, and D. Zhao, "Liquid-liquid phase separation and solidification behavior of Al55Bi36Cu9monotectic alloy with different cooling rates," *Results in Physics*, vol. 8, pp. 1086–1091, 2018. 31

[215] D. Zhao, R. Liu, D. Wu, L. Bo, and L. Wang, "Liquid-liquid phase separation and solidification behavior of Al-Bi-Sb immiscible alloys," *Results in Physics*, vol. 7, pp. 3216–3221, 2017. 31

[216] W. Wang, X. Zhang, L. Li, and B. Wei, "Dual solidification mechanisms of liquid ternary Fe-Cu-Sn alloy," *Science China: Physics, Mechanics and Astronomy*, vol. 55, no. 3, pp. 450–459, 2012. 31

[217] H. X. Liu, C. P. Wang, Y. Yu, X. J. Liu, Y. Takaku, I. Ohnuma, R. Kainuma, and K. Ishida, "Experimental investigation and thermodynamic calculation of the phase equilibria in the Al-Bi-Sn ternary system," *Journal of Phase Equilibria and Diffusion*, vol. 33, no. 1, pp. 9–19, 2012. 31

[218] R. Dai, J. F. Zhang, S. G. Zhang, and J. G. Li, "Liquid immiscibility and core-shell morphology formation in ternary Al-Bi-Sn alloys," *Materials Characterization*, vol. 81, pp. 49–55, 2013. 31

[219] X. Sun, M. Li, P. Jia, and H. Geng, "Liquid–liquid phase equilibrium in ternary immiscible Al–Bi–Sn melts," *Physics and Chemistry of Liquids*, vol. 54, no. 6, pp. 740–746, 2016. 31

[220] L. Wang, S. Li, L. Bo, D. Wu, and D. Zhao, "Liquid-liquid phase separation and solidification behavior of Al-Bi-Sn monotectic alloy," *Journal of Molecular Liquids*, vol. 254, pp. 333–339, 2018. 31

[221] W. Zhai, H. M. Liu, and B. Wei, "Liquid phase separation and monotectic structure evolution of ternary Al62.6Sn28.5Cu8.9 immiscible alloy within ultrasonic field," *Materials Letters*, vol. 141, pp. 221–224, 2015. 31

[222] J. Dantzig and M. Rappaz, *Solidification*. Lausanne: EPFL Press, 2nd ed., 2016. 32

[223] Y. Takamatsu, H. Esaka, and K. Shinozuka, "Liquid-phase separation in the interdendritic region after growth of primary β-Sn in undercooled Sn-2.8Ag-0.3Cu melt," *Journal of Electronic Materials*, vol. 41, no. 8, pp. 2035–2044, 2012. 34

[224] A. Munitz, S. Samuha, E. Brosh, S. Salhov, N. Derimow, and R. Abbaschian, "Liquid phase separation phenomena in Al 2.2 CrCuFeNi 2 HEA," *Intermetallics*, vol. 97, no. April, pp. 77–84, 2018. 34, 41, 43

[225] A. Kamio, S. Kumai, and H. Tezuka, "Solidification structure of monotectic alloys," *Materials Science and Engineering A*, vol. 146, no. 1-2, pp. 105–121, 1991. 35

[226] Z. Fan, S. Ji, J. Zhang, Z. Fan, S. Ji, and J. Zhang, "Processing of immiscible metallic alloys by rheomixing process," *Materials Science and Technology*, vol. 17:7, pp. 837–842, 2001. 35

[227] J. Barry Andrews, "Low Gravity Containerless Processing of Immiscible Gold Rhodium Alloy," *NASA Technical Report*, vol. N87-16745, 1986. 35

[228] L. Ratke, G. Korekt, and S. Drees, "Phase separation and solidification of immiscible metallic alloys under low gravity," *Advances in Space Research*, vol. 22, no. 8, pp. 1227–1236, 1998. 35

[229] B. C. Luo, X. R. Liu, and B. Wei, "Macroscopic liquid phase separation of Fe-Sn immiscible alloy investigated by both experiment and simulation," *Journal of Applied Physics*, vol. 106, no. 5, 2009. 35

[230] W. Q. Lu, S. G. Zhang, and J. G. Li, "Depressing liquid phase separation and macrosegeregation of Fe–Sn immiscible alloys by Cu alloying," *Materials Science and Technology*, vol. 30, no. 2, pp. 231–235, 2014. 35

[231] U. S. Hsu, U. D. Hung, J. W. Yeh, S. K. Chen, Y. S. Huang, and C. C. Yang, "Alloying behavior of iron, gold and silver in AlCoCrCuNi-based equimolar high-entropy alloys," *Materials Science and Engineering A*, vol. 460-461, pp. 403–408, 2007. 40, 43, 60

[232] A. Munitz, M. Kaufman, J. Chandler, H. Kalaantari, and R. Abbaschian, "Melt separation phenomena in CoNiCuAlCr high entropy alloy containing silver," *Materials Science and Engineering: A*, vol. 560, pp. 633–642, 2013. 40, 43

[233] H. Zhang, W. Wu, Y. He, M. Li, and S. Guo, "Formation of core – shell structure in high entropy alloy coating by laser cladding," *Applied Surface Science*, vol. 363, pp. 543–547, 2016. 41

[234] S. Guo, C. Ng, and C. T. Liu, "Anomalous solidification microstructures in Co-free Al xCrCuFeNi2 high-entropy alloys," *Journal of Alloys and Compounds*, vol. 557, pp. 77–81, 2013. 41

[235] J. He, N. Mattern, J. Tan, J. Z. Zhao, I. Kaban, Z. Wang, L. Ratke, D. H. Kim, W. T. Kim, and J. Eckert, "A bridge from monotectic alloys to liquid-phase-separated bulk metallic glasses: Design, microstructure and phase evolution," *Acta Materialia*, vol. 61, no. 6, pp. 2102–2112, 2013. 43

[236] A. A. Kündig, M. Ohnuma, D. H. Ping, T. Ohkubo, and K. Hono, "In situ formed two-phase metallic glass with surface fractal microstructure," *Acta Materialia*, vol. 52, no. 8, pp. 2441–2448, 2004. 43

[237] K. Ziewiec, G. Garze, T. Czeppe, B. Artur, and K. Ruebenbauer, "Microstructure and phase transformations in a liquid immiscible Fe60Cu20P10Si5B5 alloy," *Intermetallics*, vol. 69, pp. 47–53, 2016. 43

[238] P. H. Wu, N. Liu, W. Yang, Z. X. Zhu, Y. P. Lu, and X. J. Wang, "Microstructure and solidification behavior of multicomponent CoCrCuxFeMoNi high-entropy alloys," *Materials Science and Engineering A*, vol. 642, pp. 142–149, 2015. 43, 45, 60, 63, 109, 130, 131

[239] T. Guo, J. Li, J. Wang, Y. Wang, H. Kou, and S. Niu, "Liquid-phase separation in undercooled CoCrCuFeNi high entropy alloy," *Intermetallics*, vol. 86, pp. 110–115, 2017. 43, 45, 131, 149

[240] Z. Peng, N. Liu, S. Y. Zhang, P. H. Wu, and X. J. Wang, "Liquid-phase separation of immiscible CrCuxFeMoyNi high-entropy alloys," *Materials Science and Technology*, vol. 33, no. 11, pp. 1352–1359, 2017. 43, 45

[241] S. Elder and G. J. Abbaschian, "Supercooling and Rapid Solidification using EM Levitation," in *Principles of Solidification and Materials Processing*, p. 299, Delhi: Oxford and IBH Publishing Co. Pft. Ltd., 1990. 44, 53

[242] S. Wang, Z. Chen, L. C. Feng, Y. Y. Liu, P. Zhang, Y. Z. He, Q. Q. Meng, and J. Y. Zhang, "Nano-phase formation accompanying phase separation in undercooled CoCrCuFeNi-3 at.% Sn high entropy alloy," *Materials Characterization*, vol. 144, no. April, pp. 516–521, 2018. 45, 131

[243] C. Y. Hsu, T. S. Sheu, J. W. Yeh, and S. K. Chen, "Effect of iron content on wear behavior of AlCoCrFexMo0.5Ni high-entropy alloys," *Wear*, vol. 268, no. 5-6, pp. 653–659, 2010. 45

[244] C. Y. Hsu, W. R. Wang, W. Y. Tang, S. K. Chen, and J. W. Yeh, "Microstructure and mechanical properties of new AlCoxCrFeMo 0.5Ni high-entropy alloys," *Advanced Engineering Materials*, vol. 12, no. 1-2, pp. 44–49, 2010. 45

[245] J. M. Zhu, H. F. Zhang, H. M. Fu, A. M. Wang, H. Li, and Z. Q. Hu, "Microstructures and compressive properties of multicomponent AlCoCrCuFeNiMox alloys," *Journal of Alloys and Compounds*, vol. 497, no. 1-2, pp. 52–56, 2010. 45, 60, 171

[246] W. von Bolton, "Das Tantal un die Tantallampe von Siemens & Halske," *Zeitschrift Fur Elektrochemie*, vol. 11, no. 43, pp. 705–764, 1905. 48

[247] G. Cabane, "(No Title)," *Journal of Nuclear Energy*, vol. 6, pp. 269–274, 1958. 48

[248] G. Geach and F. Jones, "(No Title)," *Journal of Less-Common Metals*, vol. 1, p. 56, 1959. 48

[249] R. Bunshah, "Melting, Casting, and Distillation Techniques Which Minimuze Crucible Contamination," in *Techniques of Materials Reserach Vol. 1*, vol. Techniques, New York, London, Sydney, Toronto: Interscience Publishers, a division of John Wiley and Sons, 1968. 49, 52

[250] O. Muck, "Levitation of Solid or Molten Conductors," *Patent 42204*, vol. Germany, no. Oct. 30, 1923. 50

[251] W. Lovell, "Electromagnetic Levitation," *Patent 2400869*, vol. USA, no. May 28, 1946. 50

[252] W. Lovell, "Electromagnetic Levitation," *Patent 2566221*, vol. USA, no. Aug. 28, 1951. 50

[253] E. C. Okress, D. M. Wroughton, G. Comenetz, P. H. Brace, and J. C. R. Kelly, "Electromagnetic levitation of solid and molten metals," *Journal of Applied Physics*, vol. 23, no. 5, pp. 545–552, 1952. 51

[254] E. Okress and D. M. Wroughton, "Electromagnetic Levitation," *Iron Age*, vol. 170, p. 83, 1952. 51

[255] D. Wroughton, E. Okress, P. Brace, G. Comenetz, and J. C. R. Kelly, "A Technique for Eliminating Crucibles in Heating and Melting Metals," *Journal of the Electrochemical Society*, vol. 99, no. 5, pp. 205–211, 1952. 51

[256] L. Lacy, M. Robinson, T. Rathz, N. Evans, and R. Bayuzick, "Materials Processing in the Reduced Gravity Environment of Space," tech. rep., Elsevier Science Publishing Co., New York, 1982. 53

[257] G. Amaya, J. Patchett, and G. Abbaschian, "Grain Refinement in Castings and Welds," in *The Metallurgical Society of AIME*, p. 51, 1983. 53

[258] D. McDevitt and G. Abbaschian, "Electromagnetic Levitation," *Microstructural Science*, vol. 11, p. 125, 1983. 53

[259] R. Bayuzick, W. Hofmeister, and M. Robinson, "Undercooled Alloy Phases," *Metallurgical Society*, p. 207, 1987. 53

[260] E. Ethridge, J. Theiss, P. Curreri, and G. Abbaschian, "TM-82565," *NASA Technical Report*, 1983. 53

[261] M. Bonvalot, P. Courtois, P. Gillon, and R. Tournier, "Magnetic levitation stabilized by eddy currents," *Journal of Magnetism and Magnetic Materials*, vol. 151, no. 1-2, pp. 283–289, 1995.

[262] E. C. Ethridge, P. A. Curreri, J. Theiss, and G. J. Abbaschian, "Technique for the efficient and reproducible fabrication of electromagnetic levitation coils," *Review of Scientific Instruments*, vol. 55, no. 11, pp. 1859–1861, 1984. 53

[263] S. Curiotto, L. Battezzati, E. Johnson, M. Palumbo, and N. Pryds, "The liquid metastable miscibility gap in Cu-based systems," *Fluid Phase Equilibria*, vol. 43, no. 9, pp. 3253–3258, 2007. 57, 108

[264] T. W. Ellis, I. E. Anderson, H. L. Downing, and J. D. Verhoeven, "Deformation-processed wire prepared from gas-atomized Cu-Nb alloy powders," *Metallurgical Transactions A*, vol. 24, no. 1, pp. 21–26, 1993. 58, 108

[265] A. Munitz, M. J. Kaufman, J. P. Chandler, H. Kalaantari, and R. Abbaschian, "Melt separation phenomena in CoNiCuAlCr high entropy alloy containing silver," *Materials Science and Engineering A*, vol. 560, pp. 633–642, 2013. 60

[266] S. Praveen, B. S. Murty, and R. S. Kottada, "Alloying behavior in multi-component AlCoCrCuFe and NiCoCrCuFe high entropy alloys," *Materials Science and Engineering A*, vol. 534, pp. 83–89, 2012. 60, 149, 150, 160, 161, 164

[267] B. S. Li, Y. P. Wang, M. X. Ren, C. Yang, and H. Z. Fu, "Effects of Mn, Ti and V on the microstructure and properties of AlCrFeCoNiCu high entropy alloy," *Materials Science and Engineering A*, vol. 498, no. 1-2, pp. 482–486, 2008. 60

[268] S. Singh, N. Wanderka, B. Murty, U. Glatzel, and J. Banhart, "Decomposition in multi-component AlCoCrCuFeNi high-entropy alloy," *Acta Materialia*, vol. 59, no. 1, pp. 182–190, 2011. 60, 63

[269] J. W. Yeh, S. Y. Chang, Y. D. Hong, S. K. Chen, and S. J. Lin, "Anomalous decrease in X-ray diffraction intensities of Cu-Ni-Al-Co-Cr-Fe-Si alloy systems with multi-principal elements," *Materials Chemistry and Physics*, vol. 103, no. 1, pp. 41–46, 2007. 60

[270] Z. Wang, X. Wang, H. Yue, G. Shi, and S. Wang, "Microstructure, thermodynamics and compressive properties of AlCoCrCuMn-x (x=Fe, Ti) high-entropy alloys," *Materials Science and Engineering A*, vol. 627, pp. 391–398, 2015. 60, 63

[271] Z. Hu, Y. Zhan, G. Zhang, J. She, and C. Li, "Effect of rare earth Y addition on the microstructure and mechanical properties of high entropy AlCoCrCuNiTi alloys," *Materials and Design*, vol. 31, no. 3, pp. 1599–1602, 2010. 60

[272] C. T. Liu, "Physical metallurgy and mechanical properties of ductile ordered alloys (Fe, Co, Ni)3 V," *International Metals Reviews*, vol. 29, pp. 168–194, jan 1984. 63

[273] J. H. Zhu, P. K. Liaw, and C. T. Liu, "Effect of electron concentration on the phase stability of NbCr 2 -based Laves phase alloys," *Materials Science and Engineering A*, vol. 239-240, pp. 260–264, 1997. 63

[274] M. G. Poletti and L. Battezzati, "Electronic and thermodynamic criteria for the occurrence of high entropy alloys in metallic systems," *Acta Materialia*, vol. 75, pp. 297–306, 2014. 63

[275] J. Li, W. Jia, J. Wang, H. Kou, D. Zhang, and E. Beaugnon, "Enhanced mechanical properties of a CoCrFeNi high entropy alloy by supercooling method," *Materials and Design*, vol. 95, pp. 183–187, 2016. 99

[276] A. Munitz, S. Salhov, G. Guttmann, N. Derimow, and M. Nahmany, "Heat treatment influence on the microstructure and mechanical properties of AlCrFeNiTi0.5 high entropy alloys," *Materials Science and Engineering: A*, vol. 742, no. July 2018, pp. 1–14, 2019. 102

[277] I. S. Anderson, R. L. McGreevy, and H. Z. Bilheux, *Neutron Imaging and Applications*. 2009. 110, 134

[278] N. Derimow, L. J. Santodonato, B. E. Macdonald, B. Le, E. J. Lavernia, and R. Abbaschian, "In-Situ Imaging of Molten High-Entropy Alloys Using Cold Neutrons," *Journal of Imaging*, vol. 5, no. 2, p. 29, 2019. 130, 172

[279] B. Wu, Z. Xie, J. Huang, J. Lin, Y. Yang, L. Jiang, J. Huang, G. Ye, C. Zhao, S. Yang, and B. Sa, "Microstructures and thermodynamic properties of high-entropy alloys CoCrCuFeNi," *Intermetallics*, vol. 93, no. April 2017, pp. 40–46, 2018. 131

[280] L. J. Zhang, J. T. Fan, D. J. Liu, M. D. Zhang, P. F. Yu, Q. Jing, M. Z. Ma, P. K. Liaw, G. Li, and R. P. Liu, "The microstructural evolution and hardness of the equiatomic CoCrCuFeNi high-entropy alloy in the semi-solid state," *Journal of Alloys and Compounds*, vol. 745, pp. 75–83, 2018. 131, 149, 166

[281] N. Derimow, T. Clark, C. Roach, S. Mathaudhu, and R. Abbaschian, "Processing pathway effects in CoCrCuNi+X (Fe, Mn) high-entropy alloys," *Philosophical Magazine*, vol. 99, no. 15, pp. 1899–1913, 2019. 148

[282] P. Sathiyamoorthi, J. Basu, S. Kashyap, K. G. Pradeep, and R. S. Kottada, "Thermal stability and grain boundary strengthening in ultrafine-grained CoCrFeNi high entropy alloy composite," *Materials and Design*, vol. 134, pp. 426–433, 2017. 149

[283] R. B. Mane and B. B. Panigrahi, "Comparative study on sintering kinetics of as-milled and annealed CoCrFeNi high entropy alloy powders," *Materials Chemistry and Physics*, pp. 1–8, 2017. 149

[284] A. Zhang, J. Han, J. Meng, B. Su, and P. Li, "Rapid preparation of AlCoCrFeNi high entropy alloy by spark plasma sintering from elemental powder mixture," *Materials Letters*, vol. 181, pp. 82–85, 2016. 149

[285] S. Mohanty, T. N. Maity, S. Mukhopadhyay, S. Sarkar, N. P. Gurao, S. Bhowmick, and K. Biswas, "Powder metallurgical processing of equiatomic AlCoCrFeNi high entropy alloy: Microstructure and mechanical properties," *Materials Science and Engineering A*, vol. 679, no. September 2016, pp. 299–313, 2017. 149

[286] J. Cieslak, J. Tobola, K. Berent, and M. Marciszko, "Phase composition of AlxFeNi-CrCo high entropy alloys prepared by sintering and arc-melting methods," *Journal of Alloys and Compounds*, vol. 740, pp. 264–272, 2018. 149

[287] B. R. Braeckman and D. Depla, "Structure formation and properties of sputter deposited Nb x - CoCrCuFeNi high entropy alloy thin fi lms," *Journal of Alloys and Compounds*, vol. 646, pp. 810–815, 2015. 149

[288] S. Praveen, A. Anupam, R. Tilak, and R. S. Kottada, "Phase evolution and thermal stability of AlCoCrFe high entropy alloy with carbon as unsolicited addition from milling media," *Materials Chemistry and Physics*, vol. 210, pp. 57–61, 2018. 150, 160

[289] R. Dean, J. Long, T. Graham, E. Potter, and E. Hayes, "The Cu-Mn equilibrium system," *Transactions of the American Society for Metals*, vol. 34, pp. 443–464, 1945. 158

[290] Y. J. Zhou, Y. Zhang, Y. L. Wang, and G. L. Chen, "Solid solution alloys of AlCoCrFeNiTix with excellent room-temperature mechanical properties," *Applied Physics Letters*, vol. 90, no. 18, p. 181904, 2007. 171

[291] M.-R. Chen, S.-J. Lin, J.-W. Yeh, M.-H. Chuang, S.-K. Chen, and Y.-S. Huang, "Effect of vanadium addition on the microstructure, hardness, and wear resistance of

Al0.5CoCrCuFeNi high-entropy alloy," *Metallurgical and Materials Transactions A*, vol. 37, no. 5, pp. 1363–1369, 2006. 171

[292] M.-H. Chuang, M.-H. Tsai, W.-R. Wang, S.-J. Lin, and J.-W. Yeh, "Microstructure and wear behavior of AlxCo1.5CrFeNi1.5Tiy high-entropy alloys," *Acta Materialia*, vol. 59, no. 16, pp. 6308–6317, 2011. 171

[293] M. Chen, X. H. Shi, H. Yang, P. K. Liaw, M. C. Gao, J. A. Hawk, and J. Qiao, "Wear behavior of Al0.6CoCrFeNi high-entropy alloys: Effect of environments," *Journal of Materials Research*, vol. 33, no. 19, pp. 3310–3320, 2018. 171, 190

[294] Y. L. Chou, J. W. Yeh, and H. C. Shih, "The effect of molybdenum on the corrosion behaviour of the high-entropy alloys Co1.5CrFeNi1.5Ti0.5Mox in aqueous environments," *Corrosion Science*, vol. 52, no. 8, pp. 2571–2581, 2010. 171

[295] C. P. Lee, Y. Y. Chen, C. Y. Hsu, J. W. Yeh, and H. C. Shih, "The Effect of Boron on the Corrosion Resistance of the High Entropy Alloys Al[sub 0.5]CoCrCuFeNiB[sub x]," *Journal of The Electrochemical Society*, vol. 154, no. 8, p. C424, 2007. 171

[296] Y. L. Chen, C. W. Tsai, C. C. Juan, M. H. Chuang, J. W. Yeh, T. S. Chin, and S. K. Chen, "Amorphization of equimolar alloys with HCP elements during mechanical alloying," *Journal of Alloys and Compounds*, vol. 506, no. 1, pp. 210–215, 2010. 171

[297] R. Li, J. C. Gao, and K. Fan, "Microstructure and Mechanical Properties of MgMnAlZnCu High Entropy Alloy Cooling in Three Conditions," *Materials Science Forum*, vol. 686, pp. 235–241, jun 2011. 171, 173

[298] M. Gao and D. Alman, "Searching for Next Single-Phase High-Entropy Alloy Compositions," *Entropy*, vol. 15, no. 12, pp. 4504–4519, 2013. 171, 172, 173

[299] M. C. Gao, B. Zhang, S. M. Guo, J. W. Qiao, and J. A. Hawk, "High-Entropy Alloys in Hexagonal Close-Packed Structure," *Metallurgical and Materials Transactions A: Physical Metallurgy and Materials Science*, vol. 47, no. 7, pp. 3322–3332, 2016. 171, 172, 173, 196

[300] A. Takeuchi, K. Amiya, T. Wada, K. Yubuta, and W. Zhang, "High-Entropy Alloys with a Hexagonal Close-Packed Structure Designed by Equi-Atomic Alloy Strategy and Binary Phase Diagrams," *Jom*, vol. 66, no. 10, pp. 1984–1992, 2014. 171, 172, 173, 195

[301] K. M. Youssef, A. J. Zaddach, C. Niu, D. L. Irving, and C. C. Koch, "A novel low-density, high-hardness, high-entropy alloy with close-packed single-phase nanocrystalline structures," *Materials Research Letters*, vol. 3, no. 2, pp. 95–99, 2014. 172, 173

[302] C. L. Tracy, S. Park, D. R. Rittman, S. J. Zinkle, H. Bei, M. Lang, R. C. Ewing, and W. L. Mao, "High pressure synthesis of a hexagonal close-packed phase of the high-entropy alloy CrMnFeCoNi," *Nature Communications*, vol. 8, no. May, pp. 1–6, 2017. 172, 173, 196

[303] K. V. Yusenko, S. Riva, P. A. Carvalho, M. V. Yusenko, S. Arnaboldi, A. S. Sukhikh, M. Han, and S. A. Gromilov, "First hexagonal close packed high-entropy alloy with outstanding stability under extreme conditions and electrocatalytic activity for methanol oxidation," *Scripta Materialia*, vol. 138, pp. 22–27, 2017. 172, 173, 196

[304] M. Feuerbacher, M. Heidelmann, and C. Thomas, "Hexagonal High-entropy Alloys," *Materials Research Letters*, vol. 3, pp. 1–6, 2015. 172, 173, 195

[305] A. Takeuchi, K. Amiya, T. Wada, and K. Yubuta, "Dual HCP structures formed in senary ScYLaTiZrHf multi-principal-element alloy," *Intermetallics*, vol. 69, pp. 103–109, 2016. 172, 173, 196

[306] Y. J. Zhao, J. W. Qiao, S. G. Ma, M. C. Gao, H. J. Yang, M. W. Chen, and Y. Zhang, "A hexagonal close-packed high-entropy alloy: The effect of entropy," *Materials and Design*, vol. 96, pp. 10–15, 2016. 172, 173, 195

[307] R. Soler, A. Evirgen, M. Yao, C. Kirchlechner, F. Stein, M. Feuerbacher, D. Raabe, and G. Dehm, "Microstructural and mechanical characterization of an equiatomic YGdTbDyHo high entropy alloy with hexagonal close-packed structure," *Acta Materialia*, vol. 156, pp. 86–96, 2018. 172, 173

[308] S. Vrtnik, J. Lužnik, P. Koželj, A. Jelen, J. Luzar, M. Krnel, Z. Jagličić, A. Meden, M. Feuerbacher, and J. Dolinšek, "Magnetic phase diagram and magnetoresistance of Gd–Tb–Dy–Ho–Lu hexagonal high-entropy alloy," *Intermetallics*, vol. 105, no. March 2018, pp. 163–172, 2019. 172, 173

[309] N. Yurchenko, N. Stepanov, and G. Salishchev, "Laves-phase formation criterion for high-entropy alloys," *Materials Science and Technology (United Kingdom)*, vol. 33, no. 1, pp. 17–22, 2017. 173

[310] T. P. Yadav, S. Mukhopadhyay, S. S. Mishra, N. K. Mukhopadhyay, and O. N. Srivastava, "Synthesis of a single phase of high-entropy Laves intermetallics in the Ti–Zr–V–Cr–Ni equiatomic alloy," *Philosophical Magazine Letters*, vol. 97, no. 12, pp. 494–503, 2017. 173

[311] H. Song, S.-y. Hong, S.-j. Kwon, T.-d. Lee, and K.-h. Shin, "HCP Structured CoCrMn Underlayer for Co-Based," *IEEE Transactions on Magnetics*, vol. 36, no. 5, pp. 2300–2302, 2000. 174

[312] H. Song, K.-H. Shin, and S.-J. Kwon, "Crystallographic texture evolution of hexagonal CoCrMn thin films depending on the Mn content and processing parameters," *Journal of Magnetism and Magnetic Materials*, vol. 226-230, pp. 1666–1668, 2001. 174

[313] P. Zhou, Y. Peng, B. Hu, S. Liu, Y. Du, S. Wang, G. Wen, and W. Xie, "A thermodynamic description of the CoCrTi ternary system over the entire composition and temperature range," *Calphad: Computer Coupling of Phase Diagrams and Thermochemistry*, vol. 41, no. June 2013, pp. 42–49, 2013. 174, 186

[314] W. Elliott, R.P., Rostoker, "The occurence of Laves-type phases among transition elements," in *Transactions of the American Society for Metals*, vol. 50, pp. 617–633, 1958. 177, 178, 184

[315] Y. Aoki, T. Nakamichi, and M. Yamamoto, "Magnetic properties of cobalt-titanium alloys with the CsCl-Type structure," *Journal of the Physical Society of Japan*, vol. 27, no. 6, pp. 1455–1458, 1969. 186

[316] J. F. Archard, "Contact and rubbing of flat surfaces," *Journal of Applied Physics*, vol. 24, no. 8, pp. 981–988, 1953. 190

[317] B. Gwalani, A. V. Ayyagari, D. Choudhuri, T. Scharf, S. Mukherjee, M. Gibson, and R. Banerjee, "Microstructure and wear resistance of an intermetallic-based Al0.25Ti0.75CoCrFeNi high entropy alloy," *Materials Chemistry and Physics*, pp. 1–10, 2017. 190

[318] A. Ayyagari, C. Barthelemy, B. Gwalani, R. Banerjee, T. W. Scharf, and S. Mukherjee, "Reciprocating sliding wear behavior of high entropy alloys in dry and marine environments," *Materials Chemistry and Physics*, vol. 210, no. 210, pp. 162–169, 2018. 190

[319] G. J. Abbaschian and M. C. Flemings, "Supercooling and Structure of Levitation Melted Fe-Ni Alloys," *Metallurgical Transactions A*, vol. 14, no. 5, pp. 1147–1157, 1983. 197

[320] K. Thompson, D. Lawrence, D. J. Larson, J. D. Olson, T. F. Kelly, and B. Gorman, "In situ site-specific specimen preparation for atom probe tomography," *Ultramicroscopy*, vol. 107, no. 2-3, pp. 131–139, 2007. 200

[321] M. C. Flemings, *Solidification Processing*. New York: McGraw-Hill, 1st ed., 1974. 219

[322] M. E. Glicksman, *Principles of Solidification: An Introduction to Modern Casting and Crystal Growth Concepts*. New York: Springer-Verlag, 1 ed., 2011. 220

[323] J. Liu, E. Tennessen, J. Miao, Y. Huang, J. M. Rondinelli, and H. Heinz, "Understanding Chemical Bonding in Alloys and the Representation in Atomistic Simulations," *Journal of Physical Chemistry C*, vol. 122, no. 26, pp. 14996–15009, 2018. 228